Wisconsin
Space Grant Consortium

Proceedings of the 23rd Annual
Wisconsin Space Conference

Global Climate Change Impacts on Lake Michigan

August 15-16, 2013
Marquette University
Milwaukee Wisconsin

For information about the programs of the Wisconsin Space Grant Consortium, contact the Program Office or any of the following individuals:

Wisconsin Space Grant Consortium
University of Wisconsin-Green Bay
2420 Nicolet Drive
Green Bay, WI 54311-7001
Tel: (920)465-2108; Fax: (920)465-2376
www.uwgb.edu/wsgc

Director
R. Aileen Yingst
University of Wisconsin-Green Bay
(920)465-2327; yingsta@uwgb.edu

Program Manager
Tori Nelson
University of Wisconsin-Green Bay
(920)465-5078; nelsont@uwgb.edu

Chair, WSGC Advisory Council and Institutional Representative
Mike LeDocq
Western Technical College
(608)785-4745 ; ledocqm@westerntc.edu

WSGC Associate Director for Scholarships/Fellowships
Lindsay McHenry
University of Wisconsin-Milwaukee
(414)229-3951; lmchenry@uwm.edu

WSGC Associate Director for Student Satellite Programs
William Farrow
Milwaukee School of Engineering
(414)277-2241; farroww@msoe.edu

WSGC Associate Director for Research Infrastructure
Gubbi R. Sudhakaran
University of Wisconsin-La Crosse
(608)785-8431; sudhakar.gubb@uwlax.edu

WSGC Associate Director for Higher Education
John Borg
Marquette University
(414)288-7519; john.borg@marquette.edu

WSGC Associate Director for Aerospace Outreach
Shelley Lee
Wisconsin Department of Public Instruction
(608)266-3319; shelley.lee@dpi.state.wi.us

WSGC Associate Director for Special Initiatives
Nicole Wiessinger
Wisconsin Department of Transportation
(608)266-8177; nicole.wiessinger@dot.wi.gov

WSGC Associate Director for Industry Program
Eric Rice
Orbital Technologies Corporation
(608)827-5000; ricee@orbitec.com

Global Climate Change Impacts on Lake Michigan

23rd Annual Wisconsin Space Conference
August 15-16, 2013
Host: Marquette University
Milwaukee, Wisconsin

Edited by: Tori Nelson, Program Manager, Wisconsin Space Grant Consortium
Todd Zimmerman, University of Wisconsin-Stout
Harald Schenk, University of Wisconsin-Sheboygan
Glenn Spiczak, University of Wisconsin-River Falls
Amy Prevost, BTCI
Karin Borgh, BTCI
Coggin Heeringa, Crossroads at Big Creek

Cover by: Shelby Weber, Student Assistant, Wisconsin Space Grant Consortium

Layout by: Brittany Luedtke, Office Coordinator, Wisconsin Space Grant Consortium

Published by: Wisconsin Space Grant Consortium
University of Wisconsin-Green Bay

Wisconsin Space Grant Consortium
University of Wisconsin - Green Bay
Green Bay, WI 54311

May, 2014

Preface and Acknowledgements

It is with profoundly mixed feelings that I approach the writing of this, my last Proceedings preface as the Director of the Wisconsin Space Grant Consortium. The year I took over the Directorship of the WSGC, NASA was still reeling from the dual loss of Mars Climate Orbiter and Mars Polar Lander, a loss that many attributed to the "Faster, Better, Cheaper" philosophy that was the agency's motto at the time. Deep Space 2 had also gone missing. The 2001 Mars lander had been mothballed; there were no plans to use this half-built lander. The plans for planetary missions were all under review. My field of planetary science was on the ropes.

Fast-forward fourteen years. Mars Odyssey, Mars Reconnaissance Orbiter, the Mars Exploration Rovers Spirit and Opportunity, the Mars Science Laboratory Curiosity, and Lunar Reconnaissance Orbiter all successfully launched and executed their primary missions (all but Spirit are still going strong). Cassini arrived at Saturn; the Huygens probe soft-landed on the surface of Saturn's moon Titan; NEAR and Deep Space 1 encountered the bodies Eros, Braille and Borrelley; Stardust acquired the first samples from a comet; Deep Impact purposely impacted into comet Tempel 1; MESSENGER began its mapping mission of Mercury; the New Horizons mission launched to the dwarf planet Pluto; Juno launched to Jupiter; and MAVEN launched to Mars. And these are only some of the planetary missions with which NASA was and is involved.

What does this fantastic turnaround teach us? It certainly reminds us that out of great failure can come great progress, as long as you are willing to bravely face and learn from those failures. But more salient here is the fact that every great endeavor is in process — it is always in a state of becoming. Such is true for the WSGC. From 17 members struggling under a small Program Grant, we have grown to 41 members across the state, representing every congressional district, working together to best utilize the funds from our higher-level Designated Grant. The statewide and Midwest regional Collegiate Rocket Competitions, the First Nations Launch, the Elijah High-Altitude Balloon programs, and the greatly expanded NASA student intern program, all started and grew strong within the last ten years. Slowly but surely, the WSGC has changed, and continues to change, the face of aerospace education and research in Wisconsin. This volume represents the best of those game-changing, "becoming" activities.

The Wisconsin Space Grant Consortium office especially thanks our most excellent host for this conference, Marquette University, starting with Conference lead Professor Christopher Stockdale, Associate Director for Higher Education Professor John Borg, and the Marquette staff of volunteers who kept our schedule moving smoothly. We are grateful as well for the work of our session moderators for their conscientious work and their strong support for our students. Our keynote speakers are also to be thanked for adding so much to our conference: Professor J. Val Klump, Senior Scientist and Director of the Great Lakes Water Institute, whose topic was "What Lies Ahead for the Future of Freshwater and Our Great Lakes," and Professor Hector Bravo, Chair of Civil Engineering and Mechanics, University of Wisconsin-Milwaukee, who spoke to us about "Two Case Studies on Effects of Climate Variability and Climate Change on the

Laurentian Great Lakes." Finally, we extend our thanks to all those who contributed papers to this volume. The students, educators, faculty and other professionals who have put their best effort into this Proceedings are the ones who advance our Consortium, our state, our country and our species into the next frontier.

As a final note, I want to extend my personal, heartfelt gratitude to the Institutional Representatives and Associate Directors — all volunteers — of the Wisconsin Space Grant Consortium. Fourteen years ago, I was a freshly-minted graduate student with little experience, but lots of enthusiasm and a deep and abiding love for the national Space Grant program. The Advisory Council and Executive Committee members were patient with my mistakes, supported me unfailingly through my very steep learning curve, and gave generously of their time, experience and talents to the WSGC. We became friends as well as colleagues, and for that I will always consider myself incredibly fortunate. Thanks to all, I can't wait to see what you and the WSGC become. And as always….

Forward!

R. Aileen Yingst, Ph.D.
Director

Wisconsin Space Grant

Consortium Programs for 2013

Student Programs

- Undergraduate Scholarship
- Undergraduate Research
- Graduate Fellowship
- Dr. Laurel Salton Clark Memorial Graduate Fellowship
- University Sounding Rocket Team Competition
- Student High-Altitude Balloon Launch
- Student High-Altitude Balloon Payload
- Student High-Altitude Balloon Instrument Development
- Industry Member Internships
- NASA ESMD Internships
- NASA Academy Leadership Internships
- NASA Centers/JPL Internships
- NASA Reduced/Gravity Team Launches
- Relevant Student Travel

(see detailed descriptions on next page)

Research

The Research Infrastructure Program provides Research Seed Grant Awards to faculty and staff from WSGC Member and Affiliate Member colleges and universities to support individuals interested in starting or enhancing space- or aerospace-related research program(s).

Higher Education

The Higher Education Incentives Program is a seed-grant program inviting proposals for innovative, value-added, higher education teaching/training projects related to space science, space engineering, and other space- or aerospace-related disciplines. The Student Satellite Program including Balloon and Rocket programs is also administered under this program.

Industry Program

The WSGC Industry Program is designed to meet the needs of Wisconsin Industry member institutions in multiple ways including:

1) the Industry Member Internships (listed under students above),

2) the Industry/Academic Research Seed Program designed to provide funding and open an avenue for member academia and industry researchers to work together on a space-related project, and

3) the Industrial Education and Training Program designed to provide funding for industry staff members to keep up-to-date in NASA-relevant fields.

Aerospace Outreach Program

The Aerospace Outreach Program provides grant monies to promote outreach programs and projects that disseminate aerospace and space-related information to the general public, and support the development and implementation of aerospace and space-related curricula in Wisconsin classrooms. In addition, this program supports NASA-trained educators in teacher training programs.

Special Initiatives

The Special Initiatives Program is designed to provide planning grants and program supplement grants for ongoing or new programs which have space or aerospace content and are intended to encourage, attract, and retain under-represented groups, especially women, minorities and the developmentally challenged, in careers in space- or aerospace-related fields.

Wisconsin Space Conference

The Wisconsin Space Conference is an annual conference featuring presentations of students, faculty, K-12 educators and others who have received grants from WSGC over the past year. The Conference allows all to share their work with others interested in Space. It also includes keynote addresses, and the announcement of award recipients for the next year.

Regional Consortia

WSGC is a founding member of the Great Midwest Regional Space Grant Consortia. The Consortia consists of eight members, all Space Grants from Midwest and Great Lakes States.

Communications

WSGC web site www.uwgb.edu/wsgc provides information about WSGC, its members and programs, and links to NASA and other sites.

Contact Us

Wisconsin Space Grant Consortium
University of Wisconsin–Green Bay
2420 Nicolet Drive, MAC A307
Green Bay, Wisconsin 54311-7001
Phone: (920) 465-2108
Fax: (920) 465-2376
E-mail: wsgc@uwgb.edu
Website: www.uwgb.edu/wsgc

WSGC

Wisconsin Space Grant Consortium

Student Programs for 2013

Undergraduate Scholarship Program
Supports outstanding undergraduate students pursuing aerospace, space science, or other space-related studies or research.

Undergraduate Research Awards
Supports qualified students to create and implement a small research study of their own design during the summer or academic year that is directly related to their interests and career objectives in space science, aerospace, or space-related studies.

Graduate Fellowships
Support outstanding graduate students pursuing aerospace, space science, or other interdisciplinary space-related graduate research.

Dr. Laurel Salton Clark Memorial Graduate Fellowship
In honor of Dr. Clark, Columbia Space Shuttle astronaut and resident of Wisconsin, this award supports a graduate student pursuing studies in the fields of environmental or life sciences, whose research has an aerospace component.

University Sounding Rocket Team Competition
Provides an opportunity and funding for student teams to design and fly a rocket that excels at a specific goal that is changed annually.

High School Sounding Rocket Team Competition
For high school students. This program is in its initial stages. It mimics the university competition.

Student High-Altitude Balloon Instrument Development
Students participate in this instrument development program through engineering or science teams. Working models created by the students will be flown on high-altitude balloons.

Student High-Altitude Balloon Payload/ Launch Program
The Elijah Project is a high-altitude balloon program in which science and engineering students work in integrated science and engineering teams, to design, construct, launch, recover and analyze data from a high-altitude balloon payload. These balloons travel up to 100,000 ft., considered "the edge of space." Selected students will join either a launch team or a payload design team.

Industry Member Internships
Supports student internships in space science or engineering for the summer or academic year at WSGC Industry members co-sponsored by WSGC and Industry partners.

NASA ESMD Internships
Supports student internships at NASA centers or WSGC industry members that tie into NASA's Exploration Systems Mission Directorates.

NASA Academy Leadership Internships
This summer internship program at NASA Centers promotes leadership internships for college juniors, seniors and first-year graduate students and is co-sponsored by participating state Space Grant Consortia.

NASA Centers/JPL Internships
Supports WSGC students for research internships at NASA Centers or JPL.

NASA Reduced Gravity Program
Operated by the NASA Johnson Space Center, this program provides the unique "weightless" environment of space flight for test and training purposes. WSGC student teams submit reduced gravity experiments to NASA and, if selected, get to perform their experiments during a weightless environment flight with the support of WSGC.

Relevant Student Travel
Supports student travel to present their WSGC-funded research.

23rd Annual Conference
TABLE OF CONTENTS

Single-Photon Detection using a Quantum-Dot-Gated Resonant RLC Circuit, Tyler Nickel, Physics Department, University of Wisconsin- La Crosse; Yann Talhouarne, Physics Department, University of Wisconsin- La Crosse; Andrew Prudhom, Physics Department, University of Wisconsin- La Crosse; Richard Allenby, Physics Department, University of Wisconsin- La Crosse; Eric Gansen, Physics Department, University of Wisconsin- La Crosse

Part 4: Chemistry and Biosciences

Soft X-Ray EPMA Analyses of Lunar Fe-Si Compounds, Philip Gopon, PhD Student, Department of Geoscience, University of Wisconsin- Madison

Coacervates as Prebiotic Reactors, Vera Kolb, Professor, Department of Chemistry, University of Wisconsin- Parkside

Part 5: Team Projects

Balloon Payload and Launch Team:
Trent Cybela, University of Wisconsin- Platteville
Daniel Kass, Milwaukee School of Engineering Falls
Amber Koeune, Milwaukee School of Engineering
Nathaniel Pedigo, Milwaukee School of Engineering
Alana Tirimacco, Milwaukee School of Engineering

1st Place in Rocket Competition – Engineering
Team Whoosh Generator, Milwaukee School of Engineering
James Ihrcke
Eric Johnson
Victoria Falcon
Christopher Larson
Kirsti Pajunen

2nd Place in Rocket Competition – Engineering
Team Jarts, Milwaukee School of Engineering
Cameron Schulz
Joe Hintz
Eric Logisz
Brett Foster

Part 6: Engineering

Reliability Analysis of Light Emitting Diode Technologies for Cabin Lighting in Manned Space Flight Applications, Todd Treichel, Chairman, AIAA- Wisconsin Section and Senior Systems Engineer, Orbital Technologies Corporation

New Capabilities and Discovered Interconnectivities for a Curriculum-Integrated Multicourse Model Rocketry Project, Dr. Matthew J. Traum, Assistant Professor, Department of Mechanical Engineering; Dr. Vincent C. Prantil, Associate Professor; Dr. William Farrow, Associate Professor; Dr. Hope Weiss, Assistant Professor, Department of Mechanical Engineering, Milwaukee School of Engineering

Dynamic Dynamometry to Characterize Disk Turbines for Space-Based Power, Zhiyuan Yang, Undergraduate Researcher, Department of Mechanical Engineering, Milwaukee School of Engineering; Dr. Matthew Traum, Assistant Professor, Department of Mechanical Engineering, Milwaukee School of Engineering

Nitrogen Phase Separation at Terminal Velocity to Inform Design of Future Microgravity Cryogenic Rankine Power Cycles, Roberto J. Fernandez, Undergraduate Researcher, Department of Mechanical Engineering, Milwaukee School of Engineering; Dr. Matthew Traum, Assistant Professor, Department of Mechanical Engineering, Milwaukee School of Engineering

Part 7: Planetary Geology and Astronomy

Lassen Volcanic Fumaroles and Hot Springs, Lindsay McHenry, Associate Professor, Department of Geosciences, University of Wisconsin- Milwaukee

Dynamics of One-Dimensional Self-Gravitating Systems Using Hermite-Legendre Polynomials, Eric Barnes, Associate Professor, Department of Physics, University of Wisconsin- La Crosse; Robert Ragan, Department of Physics, University of Wisconsin- La Crosse

Examining Supernova Remnant GSH054-00+003, Cheuk Man Lo, Undergraduate Student, Department of Physics, University of Wisconsin- La Crosse

Appendix A: 23rd Annual Conference 2013 Program

23rd Annual Conference
Part One

K-12 Education &
General Public Outreach

Elementary rocket Launch II

Judy Schieble

Spaceport Sheboygan
Elementary Rocket Chair

Abstract

The Elementary Rocket Launch Program is sponsored by Spaceport Sheboygan. Spaceport Sheboygan is a knowledge center of interactive science / space exhibits, programs for students and the public. Through hands-on activity of rocket construction for students develop teamwork and critical thinking skills; applying STEM concepts.

Program Background

The elementary rocket launch has been a lead-up program to rocketry using space to teach science and math concepts. The program is offered to 4th & 5th graders in the Sheboygan County during the month of May. We have added a 2-station tracking component to emphasize a math component to the program. A drawing of the students' rocket flight was generated from the data collected from the rocket's launch. Students received a picture, showing the direction and height of his / her rocket a week after the event.

We introduced bottle rocketry a couple of years ago as one of the options the student could participate in at the elementary rocket launch. Some of the students did both the bottle and model rocket construction. The scheduling of the students to do both in the event was a little difficult. As a committee, we decided to make the bottle rocket component a separate event. Thus, it would allow students do both and concentrate on them separately.

For two years, a - 5th grade teacher at Oostburg Elementary has been doing a week long, 2-liter plastic bottle rocket unit in her science curriculum. She has created her own data sheet for the students to collect their data. This teacher has introduced critical thinking and teamwork for her students into this unit. I have assisted this teacher every year in this week - long bottle rocket unit.

Program Evaluation

The Elementary Rocket Launch program has been successful over a decade allowing 4th & 5th graders of the Sheboygan County to construct model rockets, launch them and see how high they go. Over the years we experienced a declined in a number of students, but we are pleased with the inclusive quality of science and math components.

We have added a larger model rocket for the 5th graders; thus the student who chooses to participate as a 4th & 5th grade would be building 2 different rockets. Enhancing the quality of the program, we have the optical 2-station tracking for 6th graders to utilize to collect the data. This math component adds to the STEM part of the program.

Putting the Bottle rocket program as a separate component to the program gave the elementary rocket program a new direction as we placed it in the classroom. It gave the teachers a chance to place it in their science curriculum. Even with a set of directions, the students came up with many different designs for the rocket. Thus, the technology and engineering components of STEM incorporated. The teacher constructed data sheets for the students to collect: pressure, angle of the launch, and results of each flight. Due to the results, the teacher emphasized to the student, that only one variable was changed on each launch or trial.

As of this year, we had 5 new teachers include the bottle rocket activity in their science curriculum. So, that gives us total of 6 elementary / middle school teachers who are using space to teach science. I assisted each teacher on the rocket construction day and the launch day. Those new teachers only did it one or two days and worked on one goal: either distance or accuracy.

One new component that was added to the Elementary rocket program was the straw rocket launcher activity. The straw rocket would be used at the lower elementary grades where the teacher can implement it as a class activity or student group work. The amount of the time available in their school year and the level of the students determined which way the class went.

The straw rocket activity allows the teacher and the students to apply STEM in any degree. Two, second grade teachers did it as a class- activity. The teacher constructed the straw rocket, generated the activity and the students helped collect and complied the data of the experiment. Three 4th grade teachers discussed the concepts of force, motion and engineering with their classes. Students were then given the materials to design their rocket and predict their results on their data sheets.

After the students conducted and collected their data, a graph of their data was generated. Bases on their data, the teacher then changed one variable and the students had to predict the results. Using critical thinking and analysis of the data, most students were correct on the outcome of the straw rocket's flight.

A third piece of equipment was purchased with the grant money, a tripod bottle rocket launcher. Due to the short time left in the school year, only one 5th grade teacher was able to experiment with the bottle launcher. The purpose of this equipment was to see the different parts of the 'flight of the rocket'; including being able to deploy the parachute of the rocket, after the rocket has reached 'apogee' in

its flight. The variables that were used in the other bottle rocket unit can still be addressed here.

At the middle school grades, the class can calculate average acceleration for the flight of the rocket. This concept would have to be mastered in the class and practiced in sample problems before it is applied to this activity. The students should be aware of other factors as it affected the data collected.

Future Outcomes

For the Elementary Model Rocket program, we would like to extend the 5th grade portion of the program to offer a 'payload' rocket as well as just a level II rocket kit. The 5th grade student would design a payload for his/her rocket, launch the rocket and see the results of his / her design. Optical tracking would be measured.

As for the straw and bottle rocket activities, we would like to hold teacher workshops at Spaceport Sheboygan. Our goals would be to instruct teachers in the use of the equipment in their science curriculum, to review which teaching standards are covered and how they are mastered in the activity.

We would work with the beginning activities, discussing how the activity can be changed to incorporate upper level knowledge, critical thinking skills and other disciplines. Teachers, who would be new to this kind of activity, will become comfortable with this kind of hands-on learning activity, going on to experience success with their students. Experienced teachers will fell confident about taking the activity to a higher level of learning, meeting state standards and integrating it with other disciplines.

Rocket Science for Educators Workshop for Science Technology Engineering and Mathematics

Todd H. Treichel[1]
American Institute of Aeronautics and Astronautics (AIAA) – Wisconsin

& Orbital Technologies Corporation, Madison, Wisconsin 53717

The Wisconsin AIAA chapter has leveraged the talent of its members to provide a variety of outreach opportunities for precollege aged students. Hands-on demonstrations, visual aids, and real-life space flight examples provide a foundation for bringing pre-college aged students face-to-face with space-related science, designed hardware, technology, and potential benefits; increased interest in aerospace and space related fields that lead to study at the university level followed by career. The Rocket Science for Educators program consists of a workshop used to assist schools in implementing rocket science into respective math or science curriculums. Grant assistance provided by the Wisconsin Space Grant Consortium (WSGC) makes this workshop possible. Participating educators attend a weekend workshop and receive a set of rocket science materials that they may take back to their respective schools. This workshop is taught by aerospace professionals where they provide a unique opportunity for teachers to provide meaningful activities in their classrooms and improve student performance in the fields of science, technology, engineering, and mathematics.

Nomenclature

AIAA	=	American Institute for Aeronautics and Astronautics
CG	=	Center of gravity
CM	=	Center of mass
G	=	Acceleration force due to gravity
V	=	Velocity
MSOE	=	Milwaukee School of Engineering
NASA	=	National Aeronautics and Space Administration
ORBITEC	=	Orbital Technologies Corporation
STEM	=	Science Technology Engineering and Mathematics
WSGC	=	Wisconsin Space Grant Consortium

I. Introduction

THE Wisconsin section of AIAA is based in Madison, Wisconsin and has a current membership of approximately 95 members and has recently won the 2013 *Harry Staubs Pre-College Outreach Award.* The award is presented annually to sections that have developed and implemented an outstanding pre-college (K–12) outreach program that provides quality educational resources for teachers in science, technology, engineering, and mathematics (STEM) subject areas. In 2010, 2011, and 2012 AIAA-Wisconsin was awarded a WSGC outreach grant and successfully administered a *Rocket Science for Educators* workshop for K-12 educators in Madison, DePere, and Milwaukee, Wisconsin respectively.

II. Goals and Value of Project

A decline in both the quantity and quality of students pursuing careers in STEM is widely noted in policy reports, the press, education, and government. Fears of increasing global competition compound the perception that

[1] Senior Systems Engineer, Space Center, 1212 Fourier Drive, Madison, Wisconsin, USA,

there has been a drop in the supply of high-quality students moving up through the STEM pipeline in the United States. A recent article published on February 12, 2010, by the Milwaukee Journal Sentinel, reveals the following (Miller, 2010):

> *Grade school science teachers aren't doing* the *best job of informing their students about careers in science and engineering, according to a new survey of students from the American Society for Quality (ASQ). The survey of more than 1,110 students, which was done in December 2009, tried to discover how well teachers translate their knowledge and passion for science to getting children excited about engineering and science careers. It found that 63% of students think their teachers are not doing a good job of talking to them about engineering careers, and 42% said their teachers aren't good at showing them how science can be used in a career.*
> *Among the survey's findings:*

- *85% of students said their teachers deserve at least a "B" grade when it comes to knowledge about science topics, and 55% gave them an "A."*
- *Nearly one third of students give their teachers a "C" or lower for making science more exciting and fun to learn and assigning fun hands-on projects in the classroom.*
- *Students in grades 3-6 rate their science teachers higher for making science exciting and hands-on than students in grades 7-12 rate their science teachers.*
- *72% of students in 3-12 grades think a person needs to do well in science and math to get a good paying job in the future.*
- *As students get older (7-12 grades) however, they are less likely to believe that science and math are necessary to getting a good paying job.*

The Wisconsin AIAA chapter has leveraged the talent of its members to provide a variety of outreach opportunities for precollege aged students. Hands-on demonstrations, visual aids, and real-life space flight examples provide a foundation for bringing pre-college aged students face-to-face with space-related science, designed hardware, technology, and the potential benefits; increased interest in aerospace and space related fields that lead to study at the university level followed by career. Section officers discussed and reviewed a compilation of various outreach projects summarizing a three year period covering 2006 – 2008. A survey form was constructed in an attempt to measure effectiveness of outreach efforts.

In 2009 the Wisconsin AIAA conducted a series of workshops on Physics of Propulsion and Space Flight. To test the effectiveness of these workshops, participants were asked to participate in a pre and post workshop survey. Survey results are summarized in Figure 1 where students sampled, grades six through eight, considered math and science important but only 60% were interested in STEM subjects. At the conclusion of the workshop series, students again were surveyed where a 35% increase in STEM interest resulted. Over the last century, America's economy has shifted from an agricultural and industrial focus to one that requires greater scientific and mathematical knowledge as well as technological expertise. According to the Bureau of Labor Statistics, of the thirty fastest growing occupations projected for 2016, twenty-two of them are in STEM related fields. AIAA Wisconsin members and involved teachers were intrigued by these measureable results. Thus, causing the development of an educational outreach program that reaches out to K-12 teachers.

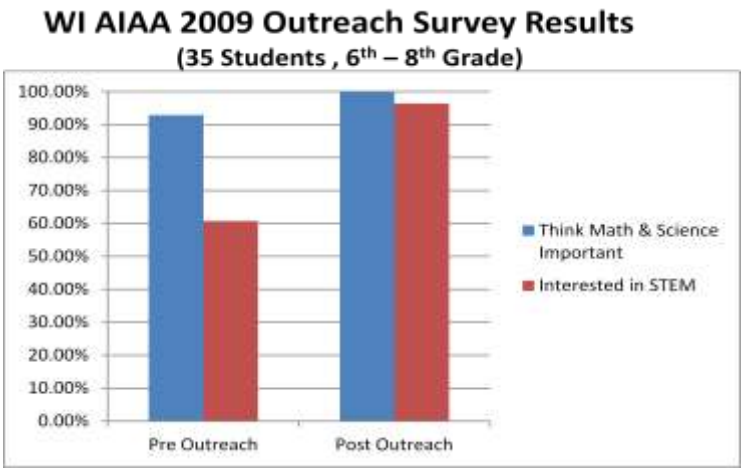

Figure 1. 2009 outreach survey summary.

The goal of the *Rocket Science for Educators* workshop is to assist schools in implementing rocket science into respective math or science curriculums. A proposal was submitted to the Wisconsin Space Grant Consortium (WSGC) to assist with funding the newly designed program. The *Rocket Science for Educators* workshop was designed specifically for educators from public and private institutions and those educators experienced with teaching math or science subjects. Participating educators attend a weekend workshop and receive a set of rocket science materials that they may take back to their respective schools for use and implementation. A workshop taught by aerospace professionals provides a unique opportunity for teachers to provide meaningful activities in their classrooms and improve student performance in the fields of science, technology, engineering, and mathematics.

III. Rocket Science for Educators

The WSGC grant funded Rocket Science for Educators workshops contained between twelve and fourteen educators who were recruited to attend a rocket science workshop at no charge. Workshop attendees consisted of math, science, art, and special needs teachers from K-12 institutions, where the origins of various participants are illustrated in Figure 2. The first workshop was conducted at Orbital Technologies Corporation (ORBITEC), located in Madison, the second workshop at East DePere High School located in DePere, and the third workshop was held at Milwaukee School of Engineering (MSOE) in Milwaukee, Wisconsin. The workshops utilized aerospace topics to

Figure 2. Geographical origins of workshop participants.

provide STEM education to educators for preparing today's students for tomorrow's jobs allowing them to be competitive in an increasingly global economy.

Figure 3. Rocket design simulation software and reference materials.

Table 1 illustrates workshop topics and how each topic relates to an educational discipline. Lectures and hands on activities were conducted including design, construction, planned experimentation, altitude analysis and differential pressure, static rocket engine firing, and the launching of a payload capable rocket. Key airframe and propulsion topics were discussed describing center of mass (CM), center of gravity (CG), velocity (V), and g- force (G) considerations for flight stability. At the close of the workshop, instructors provided constructive feedback accompanied by a short competency quiz to demonstrate participants' mastery of course subject matter. Educators were issued an achievement plaque and a set of materials that can be used for implementation into their respective math or science curriculums. Curriculum adaptable aerospace reference material, rocket design and simulation software license, and rocket construction material (see Figure 4) were provided to each participant completing the workshop. Highlights of the workshop consisted of a series of lectures which included demonstration (static) firing of potassium nitrate solid fuel, composite solid fuel, and hybrid rocket engines (see Figure 5).

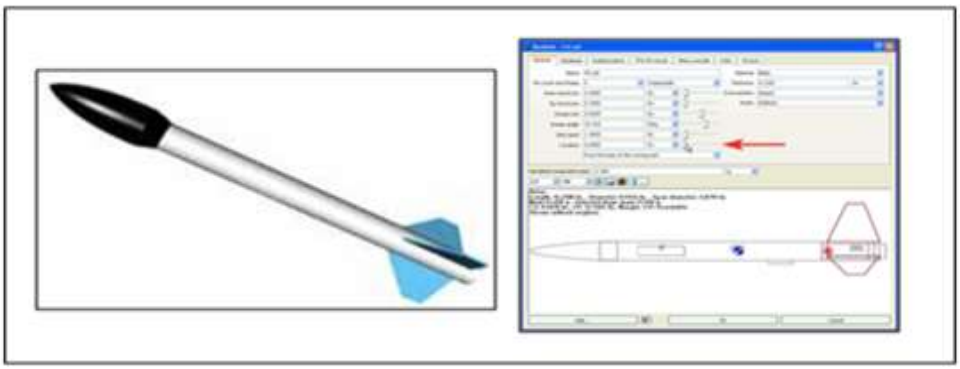

Figure 4. RockSim software design and simulation.

Safety rules for storage and handling of propellant materials was discussed and making a science project out of home-made rocket engines was discouraged for reasons of safety. Extensive time was spent using RockSim design software to demonstrate rocket design techniques, 3D imaging, and flight simulation followed by construction and flight of a payload capable rocket. RockSim is a computer program that allows you to design any size rocket, and then simulate its flight to see how high, and how fast it will fly. Prior to teachers building their payload capable rockets, an analysis of various payload weights were conducted with different engine thrust parameters to determine if the actual flight would be stable and safe to launch. The purpose of lectures, demonstrations, and take-home materials was to provide educators with educational tools that:

1. Provide basic knowledge of aerospace engineering and rockets.
2. Provide rocket design and simulation software training and user license.
3. Ability to conduct flight experiments using an electronic altimeter.
4. Allows educator to have access to reference material for rocket propulsion.
5. Provide knowledge of how to build an electric powered launch pad.
6. Assure safety and enable educator with skills to properly conduct a rocket launch for educational groups.
7. Build interest and excitement about STEM.
8. Provide an opportunity for hands-on experiences with STEM subjects by designing, building, launching, and recovering payload capable rocket.
9. Raise student educational aspirations, knowledge of STEM, and interest in pursuing a career in aerospace.
10. Improve teaching of STEM subjects by collaborating with teacher preparation and professional development activities.

Figure 5. Static firing of rocket engines.

Table 1. Rocket science for educator's workshop curriculum.

Education Module	Aerodynamics & Physics	Chemistry of Propulsion	Geometry & Measurement	Computer Aided Design	Design Simulation	Modeling	Electronics & Circuitry	Scientific Inquiry	Problem Solving	Communication	Graphic Design & Development
Newton's Laws	X		X						X		
Principles of Flight	X		X	X	X						
Rocket Engines	X	X	X	X	X	X	X				
Rocket Stability	X	X	X	X	X	X					
Techniques of Rocket Design	X	X	X	X	X	X		X	X	X	
Payload Science	X	X	X	X	X	X	X	X	X	X	X
Recovery	X		X	X	X	X		X	X	X	X
Planned Experimentation	X	X	X	X	X	X		X	X	X	
Rocket Construction			X	X	X	X	X		X	X	X
Engineering Change Mgt.			X	X	X	X	X		X	X	X
Safety Procedures		X					X			X	
Weather	X				X			X	X	X	
Launch Pad & Controls	X		X				X			X	
Analysis & Reporting								X	X	X	X

The purpose of workshop presentations was to give teachers a strong foundation in rocketry, understand the physics and science behind rocket propulsion, and bring a motivating set of materials and subject matter back to their classrooms. A particular emphasis on rocket propulsion and rocket stability was contained in take-home binder to accompany rocket propulsion discussions, talks about the physics, how rockets produce thrust, the types of propellants used in rockets, characteristics of high and low thrust motors, the nomenclature for rocket motors, the thrust curve, and how to select the best type of engine for a rocket and desired mission.

At the conclusion of launching the various payloads a post-launch review was conducted to discuss lessons learned and the process of corrective actions for improvement and future experimentation. Prior to adjournment of each workshop, a survey was administered to test workshop effectiveness where each educator was asked to score the workshop for relevance and fit-for-use within their respective curriculums. The scoring scale was 1 – 10, where 1 indicates that they should have stayed home and 10 indicating that the workshop exceeded expectations. Workshop survey results are illustrated in Figure 6, Figure 7, and Figure 8 respectively. An average score between 8.9 and 9.4 over the three separate workshops revealed a worthwhile effort and a desire among AIAA Wisconsin section members to pursue this type of outreach effort in the future.

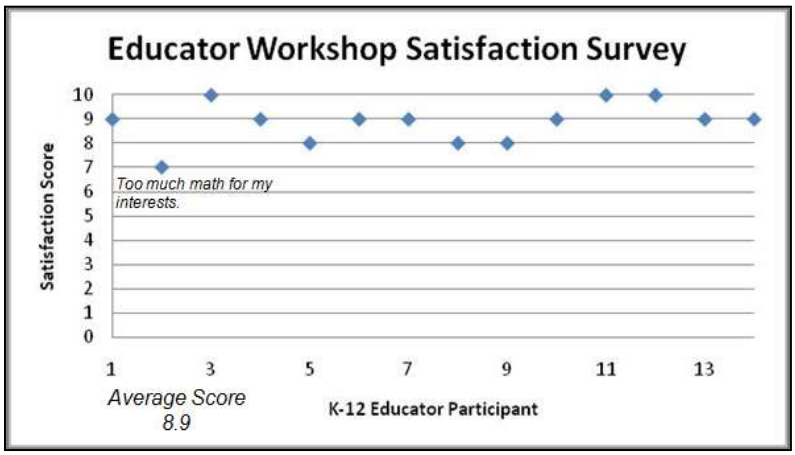

Figure 6. 2010 Rocket Science for Educators workshop survey results.

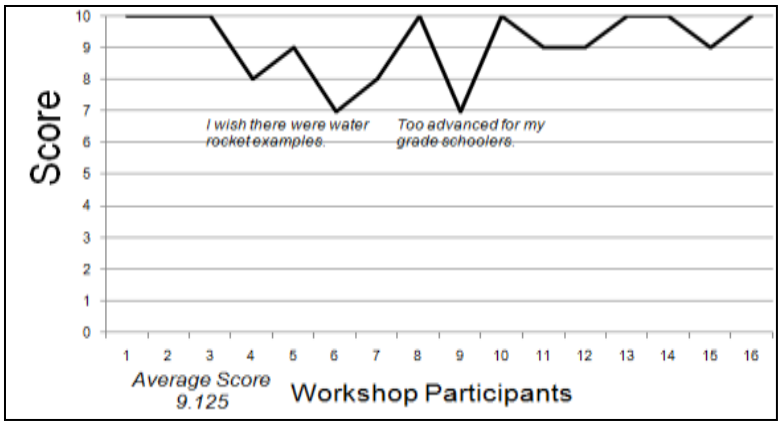

Figure 7. 2011 Rocket Science for Educators workshop survey results.

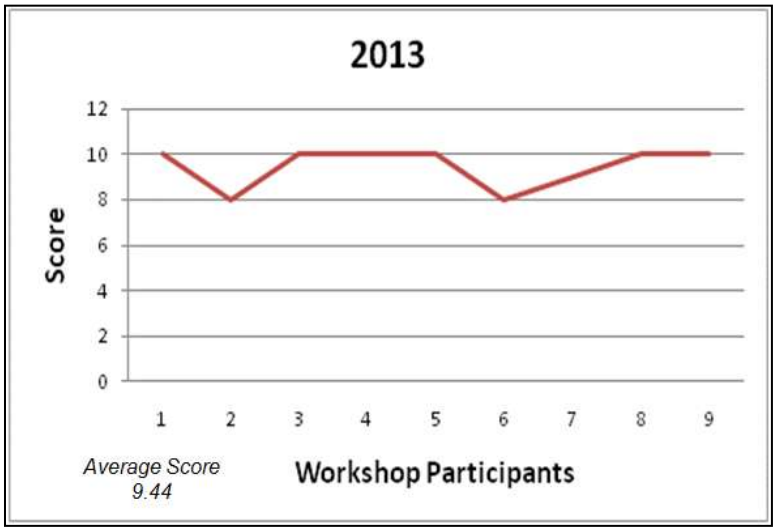

Figure 8. 2012 Rocket Science for Educators workshop survey results.

IV. Conclusion

In June 2011 the 14 educator workshop participants were contacted and asked to respond to five questions about their use of workshop materials and most importantly if respective activities improved student interest in STEM. Out of the 14 educators 11 responded to the survey and *yes* answers were recorded and are illustrated in Figure 9.

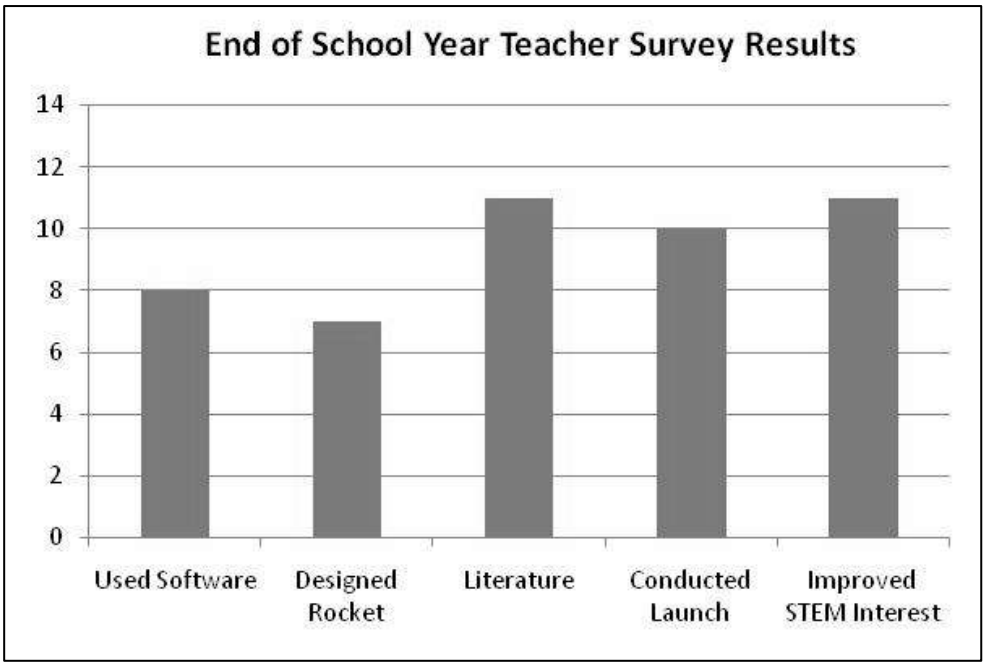

Figure 9. End of school year survey results from educators.

The following are two examples cited from workshop participants in the end of school year surveys:

> ***2010:*** *I used the book and materials we were given to help me gain more confidence before I had my students assemble rockets for launching. I had never done this at school and had wanted to for a long time. The experience with the rockets during the workshop really made me have enough knowledge to give it a try with my students.*
>
> *I used the RockSim software with several classes. My advanced reading group read "Rocket Boys" (grade 7/8) and then launched rockets. We used RockSim to look at what would happen to the Rockets during flight. In both of my Earth Science classes (grade 7) we launched rockets in the spring, and again used RockSim to predict what would happen. It predicted that one of the rockets would launch and then crash to the ground nosecone first. That is what actually happened. Also several of my advanced science students spent time using the software on their own, it was very exciting for them and encouraged them to work on some rockets at home.*
>
> *Building and launching rockets is always exciting for my students. This is a great science experience because we have successes and failures just like in all science experimentation! The students feel so empowered when they get a chance to make scientific decisions and then test what they build. We have great discussion about how scientists make building and experimentation decisions. Anytime students are actively building and experimenting they are inspired and ready to learn. Students that don't always show interest in science are active participants with hands-on activities like rocket building and launching.*

> ***2012:*** *I'm noticing as the years go by, fewer kids build things. They use their hands for video games, but to actually build a rocket and understand why it does what it does is so valuable. So I just wanted to say thanks again for the AIAA rocket construction and launch. It makes such a difference in getting kids to see math and science outside of a textbook and to put a real world interest at work with my students goes along way with inspiring them with math and science topics.*

The International Journal of Science Education published a study researching students' attitudes about scientific professions. Researchers asked high school students to rate their attitudes toward scientific professions and describe why or why they would not consider a STEM related career. The study revealed that participants, across both sexes, considered scientific professions to be less creative and less people-oriented than other more popular career choices. The Hofstra University study concluded that students may be led away from STEM careers by common misperceptions that science is difficult, uncreative, and socially isolating. Researchers stated that finding ways to encourage students to seek STEM careers continues to challenge teachers, career counselors, and mentors (Masnick, Valenti, Cox, & Osman, 2010). Let's face it, astronauts make science cool. They are the NFL football players of science. This high powered rocket project demonstrates the *coolness* of science by connecting student eyes, ears, and fingers to a real rocket flight vehicle and experiences that will inspire future interests.

A simple, compelling philosophy drives AIAA Wisconsin's commitment to math, science, and technology education. Make it exciting, make it empowering, and make it fun. The Rocket Science for Educators workshop is a far-reaching program that targets precollege students, and the educators who inspire them. Learning starts with a teacher, a curious student, and fun in the classroom. The AIAA sponsored *Rocket Science for Educators* workshop provide educators with first-hand experience and training from real aerospace professionals that will spark students' excitement about machines … space … aviation … how things work…. flying … and why things happen. In short, all the facets of math and science. Please feel free to contact the author if you are interested in learning more about this STEM workshop.

References

1. Chiaverini, M. J., Kuo, K. K. (2007). *Fundamentals of hybrid rocket combustion and propulsion*. Reston, VA: AIAA Press.

2. Fortescue, P., Stark, J., Swinerd, G. (2003). *Spacecraft systems engineering* (4th ed.). West Sussex, England: John Wiley and Sons Ltd.

3. Masnick, A. M., Valenti, S. S., Cox, B. D., & Osman, C. J. (2010, March). A multidimensional scaling analysis of student attitudes about science careers. *International Journal of Science Education*, 32 (5), 653-667.

4. Miller, S. A. (2010, February 14). Engineers step up for STEM next week. *Milwaukee Journal Sentinel*, pp. A37.

5. RockSim software. *Model rocket design and simulation software* (Ver. 9.0). Purchased from: www.apogeerockets.com. Colorado Springs, CO: Apogee Components.

6. Van Milligan, T. S. (1995). *Developing Creativity Using Model Rockets to Teach the Techniques of Problem Solving*. Colorado Springs, CO: Apogee Components.

7. Van Milligan, T. S. (2008). *Model rocket design and construction* (3rd ed.). Oregon, IL: Quality Books, Inc.

Teaching Teachers through Outreach

Coggin Heeringa

Crossroads at Big Creek, Inc.

Abstract

Elementary and middle school teachers participated in workshops and credit and/or non-credit classes designed to increase their content knowledge and to introduce age-appropriate activities which will prepare the next generation for careers in the STEM disciplines. Each of the classes and workshops were scheduled along with a public outreach event, giving teachers experience in demonstrating the activities.

Background

For the past five years, Crossroads at Big Creek, through an arrangement with the University of Wisconsin-Green Bay Education Outreach program, has offered teacher education classes in astronomy. We have been able to attract teachers by offering stipends with generous funding from the Wisconsin Space Grant Consortium.

When we began offering these classes, we focused primarily on content, assuming that most teachers were not up to date on current astronomical understandings. We discovered that most teachers lacked any background at all, and in fact, were quite confused by the materials presented in two dimensional reference books . Unfortunately, their misunderstandings were being passed on to the children if astronomy was presented at all. A surprising number of teachers avoided teaching space related topics altogether because they did not feel prepared.

Educational Offerings

We discovered that the best way to teach teachers was to actually have them participate in the hands-on activities that were intended for children. We also learned that if teachers had tried (rather than just read or hear about) the demonstrations themselves, they were more likely to use them in the classroom.

Offering generous scholarship /stipends of $200 usually worked in recruiting teachers for our credit classes. For workshops we tied instruction to subjects teachers were already presenting and to encourage participation, we offered a free dinner, a program with free teaching materials, <u>and</u> we invited teachers to bring their significant offers and their children if they so desired.

Having kids at the workshops was a game changer! Teachers could see how engaged children became while doing the activities. And once they had seen kids in action, teacher were eager to present the activities to their students and/or to bring their classes to Crossroads for field trips.

We now schedule our workshops and classes to coincide with the outreach activities of the Door Peninsula Astronomical Society. Teachers are still offered a scholarship/stipend and free meal, but we now offer an addition $20 if the teacher will stay and present activities to the general public during Astronomy Days or special events such as the Transit of Venus.

This is a win-win. Teachers are more far likely to encourage their students to attend DPAS outreach activities if they will be presenting. Because they are experienced in working with children, teachers are outstanding presenters during our programs. And best of all, after becoming thoroughly familiar with the activities, teachers are far more likely use them in their own classrooms.

In 2012, we directly reached 23 teachers, but we continued to provide services to teachers who have participated in previous years.

Results

We do not have the staff to do extensive follow-up activities to determine the impact of our classes and we certainly cannot determine long range outcomes such the number of students who eventually go on the pursue STEM careers. However, we have seen a significant increase in the number of teachers who schedule astronomy field trips to Crossroads and we can tell by the questions of the students whether or not a teacher has participated in our programs.

We were simple amazed when a third grade student asked if the asteroids were on the same plane as the planets and another wanted to know if a comet was coming at Saturn, would it be swallowed up by the planet or caught in the rings.

We do hope to continue to offer kind of teacher training in the future as teachers struggle to grasp and teach the concepts covered by the New Generation Standards for Science.

This project has been made possible with a grant from the Wisconsin Space Grant Consortium and with assistance from University of Wisconsin-Green Bay Education Outreach and the Door Peninsula Astronomical Society.

The Next Generation Science Standards are Coming to Wisconsin

Shelley Lee

Wisconsin Department of Public Instruction

Abstract

The Wisconsin Space Grant Consortium provided the state science leadership team with a grant that funded a meeting of the state appointed science leadership team. Occurring at a critical time, the team was able to respond to a draft the of the Next Generation Science Standards on behalf of science teachers around the state. The team then was able to develop a comprehensive plan of implementation for the standards.

Through a collaborative state-led process, new K–12 science standards have been developed that are rich in content and practice and arranged in a coherent manner across disciplines and grades to provide all students an internationally benchmarked science education. Developed by Achieve, Inc. *Next Generation Science Standards* (NGSS) are based on the *Framework for K–12 Science Education* published by the National Research Council. These standards were derived from contemporary science education research and pedagogical practices. They represent the essential science content that all students should know and understand in order to be successful in this contemporary and global society.

State Superintendent Tony Evers appointed a science leadership team whose make-up consisted of K-12 educators, higher education faculty, technical college faculty, and community members from around the state. He charged this team with the task of responding to all NGSS drafts on behalf of the state. They accomplished this by gathering feedback from every CESA through listening and preview sessions. The team was also charged with developing state level implementation plan, which is now being implemented.

The Wisconsin Space Grant Consortium funded a January 2013 leadership team meeting. It was held in Green Bay and Dr. Aileen Yingst, the space grant director, was the keynote. The funds for the meeting came at a strategic time because the second draft of the NGSS was just released. The leadership team was able to develop a cogent and appropriate response to the draft that reflected what was important for students to know and understand in Wisconsin science education. The leadership team also developed the state's NGSS implementation plan during this meeting that was a reflection on NASA's STEM initiatives.

As a result of this meeting, the following activities took place:

- The leadership team had a clear picture of the NGSS.
- The state superintendent's cabinet was briefed on the NGSS.
- Over 600 educators attended a preview session conducted by the leadership team that were held in various locations around the state.

The Wisconsin Department of Public Instruction is grateful to the Wisconsin Space Grant Consortium for funding one of the science leadership team meetings. Without space grant's support the Next Generation Science Standards would not be a reality in Wisconsin. To date, over 1,500 teachers of science and administrators have been exposed to the NGSS; this is the result of that January meeting.

References:

CESA conversations as recorded by Kevin Anderson, conference call facilitator. April 2013.

Garet, M. Proter, A., Desimone, L. et al., 2001. *What makes professional development effective?* Results from a National Sample of Teachers. *American Educational Research Journal 38* no. 4: 915-945.

Moon, J., Michaels, S., & Reiser, B.J. (2013, November 30, 2012). Science standards require a teacher-learning rethink, Commentary. *Education Week*. Retrieved from http://www.edweek.org/ew/articles/2012/11/30/13moon.h32.html

National Research Council. (2007). *Taking science to school: Learning and teaching science in grades K-8*. Washington, DC: National Academies Press.

National Research Council. (2012). *A framework for K-12 science education: Practices, crosscutting concepts, and core ideas*. Washington, DC: National Academies Press.

NGSS Lead States. (2013). *Next Generation Science Standards: For states, by states*. Washington, DC: The National Academies Press.

Wisconsin Department of Public Instruction. 2012. *Wisconsin science leadership team needs assessment results*, unpublished.

23rd Annual Conference
Part Two

Physics, Astronomy & Meteorology

When Galaxies Collide:
The Search for Low-frequency Gravitational Wave Backgrounds in the Universe

Sydney J. Chamberlin

The Leonard E. Parker Center for Gravitation, Cosmology & Astrophysics
Department of Physics, University of Wisconsin-Milwaukee
Milwaukee, WI USA

Introduction

Gravitational waves (GWs) are a predicted feature of General Relativity (GR). These waves, which are tiny ripples in the fabric of space-time, appear as wavelike solutions to the vacuum Einstein equation, and are the only prediction from GR that have not yet been directly observed. In the past few decades, large scale efforts aimed at detecting these elusive waves have increasingly gained momentum: a direct observation of GWs will provide an entirely new mechanism for learning more about the structure and evolution of astrophysical objects in our universe, as well as the cosmology that underlies the universe itself.

Gravitational radiation may be generated by a number of interesting astrophysical and cosmological sources. Compact objects (specifically, asymmetric or bumpy rotating objects) such as neutron stars, supernovae, and mergers of compact binary objects are just a few of the potential sources of this radiation. In this work, we are interested in low-frequency GWs (10^{-9} Hz–10^{-6} Hz) which are thought to be generated primarily by supermassive black hole binaries (SMBHBs) with masses ($M \gtrsim 10^9 M_\odot$) Jaffe and Backer [2003], Sesana et al. [2008, 2009].

In this presentation, we describe the type of GW signal that we are searching for, and explain how pulsars may be used to aid in the detection of this signal. We present a package of software algorithms and tools that we have extensively developed to use for our detection efforts, and point out some future tasks that need to be accomplished. For additional details, readers are encouraged to keep an eye out for our upcoming publication on this work (Chamberlin et al.).

Detecting GW backgrounds with pulsar timing arrays

Millisecond pulsars are among the most stable clocks in the universe. Observations of the radio signals being emitted by these pulsars are in fact so precise that they can be more accurate than an atomic clock. The high precision of pulsar timing observations is what allows pulsars to be used in GW searches: a GW, if present between the Earth and a pulsar,

The author extends thanks to the Wisconsin Space Grant Consortium for funding this work through a graduate fellowship.

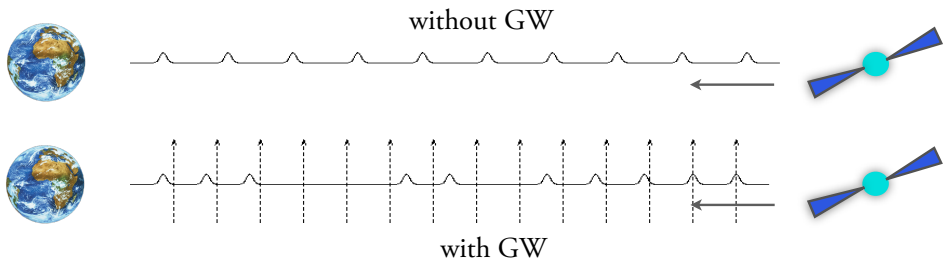

Figure 1: Two images showing the travel of a pulse-train from the pulsar to the Earth. In the top image, no GWs are present and the signals are timed as precisely as at any other time. In the lower image, dashed arrows represent areas in which a passing GW could cause a redshift in the pulse-train, and cause signals to arrive delayed or early at the Earth.

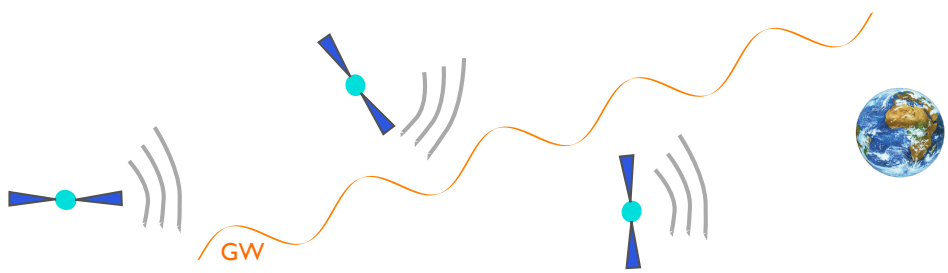

Figure 2: This figure demonstrates how a passing GW will effect the pulse-train from multiple pulsars. This effect will be correlated in a very unique way, allowing for a GW detection to take place.

will cause a redshift in the pulsar's radio pulse-train that is detectable at the Earth (see Fig. 1).

The quantity that is actually measured by radio astronomers is called the *timing residual*, which is defined as the difference between the actual and expected time-of-arrival (TOA) of the pulse at the Earth:

$$r(t) = \mathrm{TOA}_{\mathrm{actual}} - \mathrm{TOA}_{\mathrm{expected}}. \tag{1}$$

The observation of a single pulsar's timing residual $r(t)$ doesn't allow for any way to extract information about a passing GW signal, however, because it is impossible to tell whether a GW-induced redshift or some other effect is causing the delay of the signal. Instead of a single pulsar, an *array* of well-timed pulsars across the sky is used (hence the term pulsar timing array, or PTA). The idea, first proposed by Hellings and Downs [1983], is that the passing GW induces *uniquely correlated* changes in the pulsars' signals (see Fig. 2). Given an array of pulsars, therefore, a direct detection of GWs is possible. Several collaborations exist across the globe to take part in this effort: the North American Nanohertz Gravitational

Wave Observatory (NANOGrav), the European Pulsar Timing Array (EPTA) and the Parkes Pulsar Timing Array (PPTA) together form an international collaboration, the International Pulsar Timing Array (IPTA) which is working towards a direct observation of GWs.

The stochastic background

In this work, we are not concerned with the gravitational radiation emitted by a single astrophysical source, but instead a *bath* of background gravitational radiation. Such a bath, or background, is caused not by a single source but by a very large number of independent and individually unresolvable sources. For our expected dominant source of GWs – SMBHBs – such background could form (for instance) from the collision of galaxies throughout the universe. Electromagnetic observations, such as those from the Hubble Deep Field, have made it apparent that a very large number of galaxies and galactic collisions have taken place over the universe's lifetime. The GWs emitted by each of these events together form a background of gravitational radiation, in much the same way as the Cosmic Microwave Background forms a background of electromagnetic radiation thoughout the universe.

This background of GWs is typically referred to as the *stochastic* GW background, and is the type of gravitational radiation that we seek to detect in this work.

Detection algorithms

This project has involved the development of statistical data analysis tools and techniques aimed at extracting the GWs (that are hopefully) present in pulsar timing data. The primary feature of the statistical analysis involves the unique Hellings and Downs correlation between pulsar signals and is called the *optimal detection statistic*. This statistic conveys the level of confidence that a GW signal is present in the data.

Starting with pulsar TOA data, the timing residuals $r(t)$ are determined. To make this transition, known effects (pulsar spin-down, interstellar medium effects, etc.) are taken into account using sophisticated software techniques. A series of Python and C codes then take the timing residual data from the PTAs, and calculate the optimal detection statistic. This formalism also provides a robust method for generating frequentist upper limits in the data (see Fig. 3 for details on how this is accomplished).

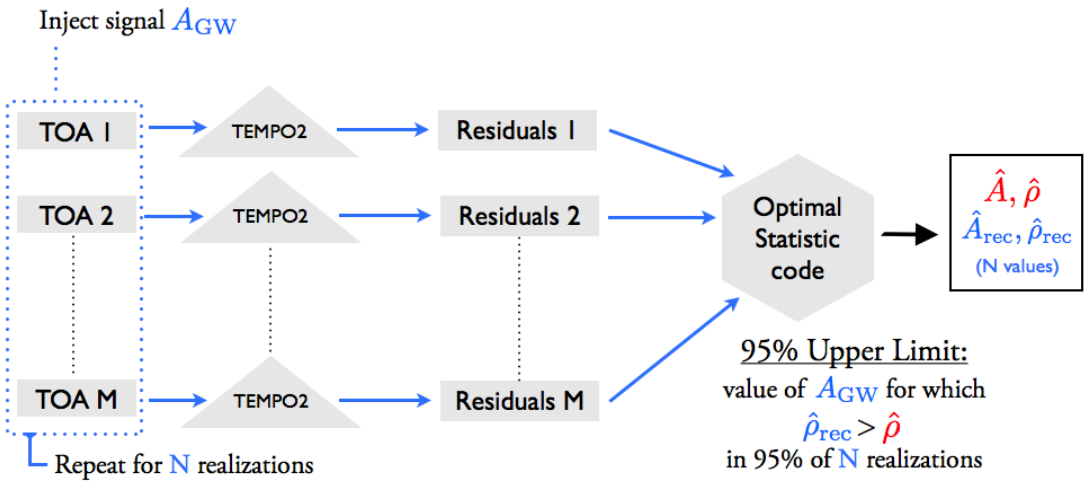

Figure 3: This schematic displays the elements of the stochastic GW detection pipeline. Assuming a PTA consisting of M pulsars, M timing residuals are obtained with the software Tempo2 Hobbs et al. [2006]. The M timing residuals then undergo a series of calculations resulting in a value for the detection statistic, $\hat{A}$, and signal-to-noise ratio $\hat{\rho}$. Examining this statistic gives a measure of confidence as to whether a signal is present in the data. Fake GW signals can then be injected into the data for some large number of realizations, N, and the same analysis performed for the data with injections to obtain $\hat{A}_{\rm rec}$ and $\hat{\rho}_{\rm rec}$. The 95% upper limits are obtained by finding the value of injected signal for which the recovered statistic $\hat{A}_{\rm rec}$ exceeded the initial value of the statistic $\hat{A}$ in 95% of the realizations.

Conclusion

A direct detection of GWs will open a new observational window on the universe, and illuminate new science in a way that traditional electromagnetic observations cannot. Here, we have presented efforts aimed at detecting a stochastic GW background, which is generated by a large number of independent, individually unresolvable sources. We have discussed the manner in which pulsars may be used to detect GWs, and briefly introduced the software developments that we have undertaken to aid in GW detection efforts.

References

A. H. Jaffe and D. C. Backer. Gravitational Waves Probe the Coalescence Rate of Massive Black Hole Binaries. 583:616–631, February 2003. doi: 10.1086/345443.

A. Sesana, A. Vecchio, and C. N. Colacino. The stochastic gravitational-wave background from massive black hole binary systems: implications for observations with Pulsar Timing Arrays. 390:192–209, October 2008. doi: 10.1111/j.1365-2966.2008.13682.x.

A. Sesana, A. Vecchio, and M. Volonteri. Gravitational waves from resolvable massive black hole binary systems and observations with Pulsar Timing Arrays. 394:2255–2265, April 2009. doi: 10.1111/j.1365-2966.2009.14499.x.

S. J. Chamberlin, J. D. E. Creighton, P. Demorest, J. Ellis, L. Price, and X. Siemens. A Practical Application of the Optimal Statistic for Stochastic Gravitational Wave Background Searches in Pulsar Timing Data. *In Preparation; to be submitted to Physical Review D.*

R. W. Hellings and G. S. Downs. Upper limits on the isotropic gravitational radiation background from pulsar timing analysis. 265:L39–L42, February 1983. doi: 10.1086/183954.

G. B. Hobbs, R. T. Edwards, and R. N. Manchester. TEMPO2, a new pulsar-timing package - I. An overview. 369:655–672, June 2006. doi: 10.1111/j.1365-2966.2006.10302.x.

Searching for Continuous Gravitational Waves with Pulsar Timing Arrays: Detection and Characterization

Jusitn Ellis

The Leonard E. Parker Center for Gravitation, Cosmology & Astrophysics
Department of Physics, University of Wisconsin-Milwaukee
Milwaukee, WI USA

Abstract

Gravitational Waves (GWs) are tiny ripples in the fabric of space-time predicted by Einsteins theory of General Relativity. Pulsar timing arrays (PTAs) offer a unique opportunity to detect low frequency GWs in the near future. Such a detection would be complementary to both LISA and LIGO GW efforts. In this frequency band, the expected source of GWs are Supermassive Black Hole Binaries (SMBHBs) and they will most likely form in an ensemble creating a stochastic GW background with the possibility of a few nearby/massive sources that will be individually resolvable. A direct detection of GWs will open a new window into the fields of astronomy and astrophysics by allowing us to constrain the coalescence rate of SMBHBs, providing further tests on the theory of General Relativity, and giving us access to properties of black holes not accessible by current astronomical techniques. Here we will discuss the development of a robust detection pipeline for single resolvable GW sources that is fully tailored to the unique aspects of PTA data analysis.

Introduction

In the next few years pulsar timing arrays (PTAs) are expected to detect gravitational waves (GWs) in the frequency range 10^{-9} Hz–10^{-7} Hz. Potential sources of GWs in this frequency range include supermassive black hole binary systems (SMBHBs) Sesana et al. (2008), cosmic (super)strings Olmez et al. (2010), inflation Starobinsky (1979), and a first order phase transition at the QCD scale Caprini et al. (2010). The community has thus far mostly focused on stochastic backgrounds produced by these sources, however; sufficiently nearby single SMBHBs may produce detectable continuous waves with periods on the order of years and masses in the range $10^8 M_\odot$–$10^9 M_\odot$ Wyithe & Loeb (2003); Sesana et al. (2009); Sesana & Vecchio (2010). The concept of a PTA, an array of accurately timed millisecond pulsars, was first conceived of over two decades ago Romani (1989); Foster & Backer (1990). Twenty years later three main PTAs are in full operation: the North American Nanohertz Observatory for Gravitational waves (NANOGrav; Jenet et al. (2009)), the Parkes Pulsar Timing Array (PPTA; Manchester (2008)), and the European Pulsar Timing Array (EPTA; Janssen et al. (2008)). The three PTAs collaborate to form the International Pulsar Timing Array (IPTA; Hobbs et al. (2010)).

Many authors have focused on determining the parameter accuracy that we may hope to extract from a future detection of a continuous GW from a SMBMB. Corbin & Cornish (2010) have developed a Bayesian Markov Chain Monte-Carlo (MCMC) data analysis algorithm for

JE is partially funded by the Wisconsin Space Grant Consortium and the NSF through PIRE award number 0968126.

parameter estimation of a SMBHB system in which the perturbation due to the GW at the pulsar is taken into account in the detection scheme, thereby increasing the signal-to-noise-ratio (SNR) and improving the accuracy of the GW source location on the sky. Recently, Lee et al. (2011) have developed parameter estimation techniques incorporating the pulsar term and have placed limits on the minimum detectable amplitude of a continuous GW source.

In this article, we will briefly review detection and characterization techniques developed for analysis of real PTA data (Ellis, 2013).

Methods

The GW signal from a SMBHB in a circular orbit measured at the earth can be described by 8 parameters: 2 *intrinsic* to the binary and 5 that are *extrinsic* and depend on our line of sight to the binary. The intrinsic parameters are the total mass and orbital separation (or equivalently the period of the binary, though Kepler's 3rd law) of the binary system and the extrinsic parameters are the sky location of the binary, initial phase at the time of observation, distance to the binary and orientation of the binary in the sky projected onto our line of sight. Since we are using the pulsars as our GW detector we must know the distance to the pulsars in order to correctly measure the GW parameters. However, typical pulsar distance uncertainties are on the order of tens of percent (Verbiest et al., 2012), in order to attain phase coherence in our search algorithm, we must allow the pulsar distance to vary as a search parameter as well.

Our parameter space will be at least 9-dimensional for a PTA comprised of one pulsar and we will gain another parameter for every pulsar that is used in the search. For typical PTAs (20 pulsars), this means that the parameter space will be ~ 28 dimensional. For this reason we have chosen to use a Markov Chain Monte-Carlo (MCMC) algorithm to perform our search and parameter estimation. MCMC is a stochastic sampling method that will efficiently explore large parameter spaces and map out the probability distribution function (pdf) for the model parameters. This is accomplished through the Metropolis-Hastings algorithm that allows the sampler to focus on high probability areas of parameter space while still exploring the entire prior volume. Next we will describe how this algorithm is used to search the parameter space for the maximum likelihood values, map out the pdfs of all parameters and make statements about the detection of GWs in our data set.

Characterization

Our goal is to measure both intrinsic and extrinsic parameters of the SMBMB through GW observations. To do this we must explore the large parameter space of the GW parameters in addition to the pulsar distances themselves. To efficiently locate the global maximum in the parameter space we make use of parallel tempering. Parallel tempering involves running several MCMC chains in parallel each evaluating the likelihood function of our data raised to some power $1/T$, where T ranges from 1 to $T_{\max}$, where $T = 1$ represents the true likelihood function and higher temperatures are a flatter version of the true likelihood function. This allows the hotter chains to explore the likelihood surface much more quickly and the algorithm then communicates information from the hotter chains back down to the $T = 1$ chain. Further discussion of the setup of parallel tempering is beyond the scope of this document, suffice it to say that this step is critical in locating the maximum likelihood quickly. We have simulated a moderately strong GW source and have run our analysis. Figure 1 shows that the algorithm quickly locates the maximum likelihood and injected parameters.

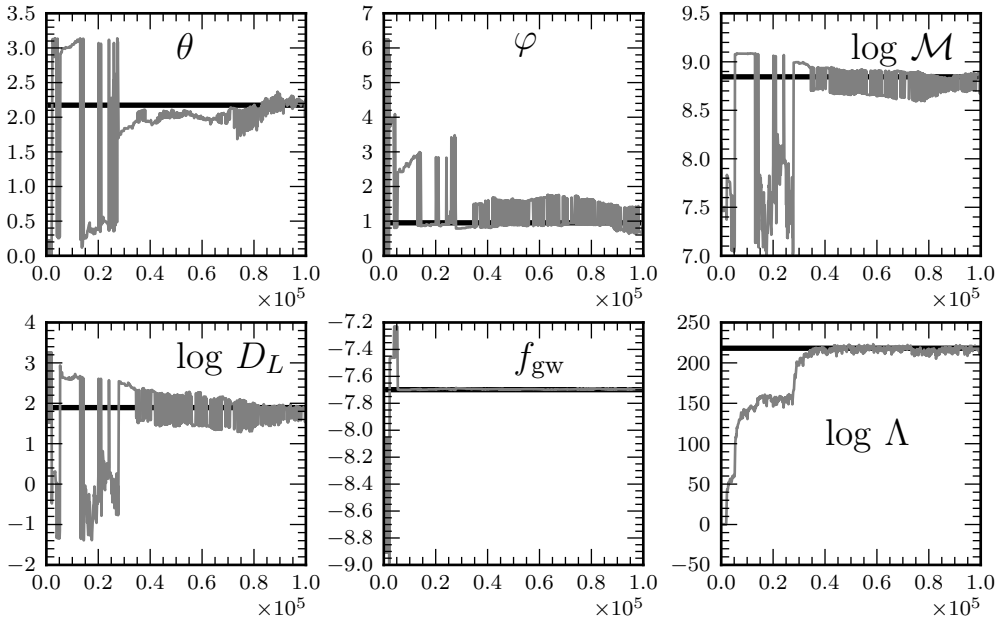

Figure 1: Trace plots for the measurable parameters (the inclination angle, initial phase and polarization angle are not well constrained for this realization) for an SNR=20 injection for the first 10^5 steps. In all cases the green line represents the injected parameters and the blue is the chain trace. We can see that the parallel tempering scheme has allowed us to locate the global maxima of the log-likelihood and all parameters within the first $\sim 6 \times 10^4$ steps.

Once we have located the maximum likelihood we can begin to collect samples of the pdfs of the model parameters. This phase of the algorithm is called the characterization phase. During this phase we will learn about any correlations among parameters or about any multimodal structure in the likelihood surface. As an example, we show the 2-d pdfs of the sky location and mass and distance to the source in Figure 2.

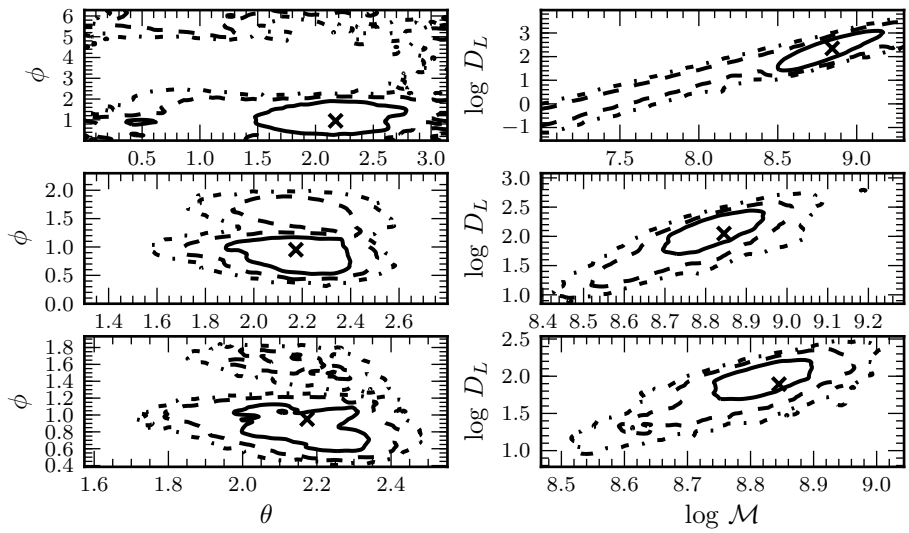

Figure 2: Marginalized 2-D posterior pdfs in the sky coordinates (θ, ϕ) and the log of the chirp mass and distance $(\log \mathcal{M}, \log D_L)$ for injected SNRs of 7, 14, and 20 shown from top to bottom. Here the injected GW source is in the direction of the Fornax cluster with chirp mass $\mathcal{M} = 7 \times 10^8 M_\odot$. The distance to the source is varied to achieve the desired SNR. Here the "$\times$" marker indicates the injected parameters and the solid, dashed and dot-dashed lines represent the 1, 2, and 3 sigma credible regions, respectively.

Here we see that we can recover the sky location with a smaller error box for louder GW signals. In addition, with a louder signal we can break the degeneracy between the mass of the system and distance to the source.

Detection

Above, we have shown that we are able to characterize the parameters of the SMBHB source if it is loud enough in our data. In this section we will review how we evaluate the evidence for the presence of a GW in our PTA data set. In Bayesian statistics we directly compare the evidence for a model with and without a GW source. In practice computing the Bayes factor is quite difficult because it involves integrating the full dimensional probability distribution function over all model parameters. As mentioned above in our case the parameter space

can be up to 28 dimensions or even higher. We have made us of the parallel chains that we have run in the characterization phase to compute the evidence via a thermodynamic integration scheme (see e.g. Littenberg & Cornish (2009) and references therein). After we have computed the evidence for a model with and without a GW signal, we can then construct the ratio of the GW model to the non-GW model, this is known as the Bayes factor. In many cases a Bayes factor larger than 100 is considered decisive evidence and we will adopt that convention here. Figure 3 shows the log of the Bayes factor as a function of the injected signal-to-noise ratio (SNR) for the same noise realization.

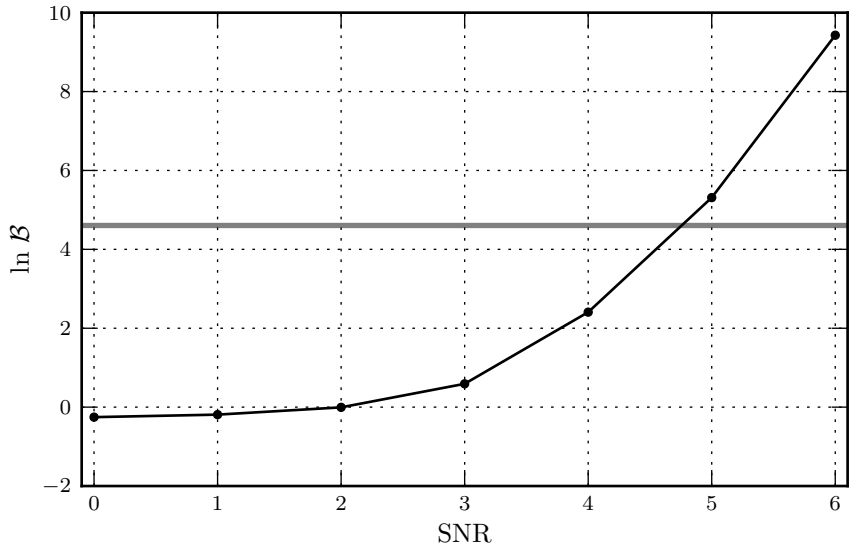

Figure 3: Log of the Bayes factor plotted against injected SNR for the same signal and noise realization. The green horizontal line is the threshold in the log of the Bayes factor in which we can claim a detection and the blue points are the log Bayes factor calculated from thermodynamic integration.

Here we see that the log Bayes factor increases with injected SNR as expected and that a detection is claimed around the SNR ~ 5 mark. However, note that this curve can change dramatically based on noise realization.

Conclusion

In this document, we have reviewed recent progress in the development of a pipeline for detection and characterization of continuous GW sources in PTA data. This algorithm quickly locates the global maximum in parameter space in the search phase, characterizes the GW parameters in the characterization phase, and evaluates the evidence and Bayes factor in the final evaluation stage. In the future we plan on optimizing this algorithm in order to get the quickest possible run time. We also plan to include for the possibility

of multiple continuous GW source as opposed to the current default of assuming only one source.

References

Caprini, C., Durrer, R., & Siemens, X. 2010, D82, 063511

Corbin, V., & Cornish, N. J. 2010, arXiv:1008.1782

Ellis, J. 2013, ArXiv e-prints

Foster, R. S., & Backer, D. C. 1990, 361, 300

Hobbs, G., et al. 2010, Classical and Quantum Gravity, 27, 084013

Janssen, G. H., Stappers, B. W., Kramer, M., Purver, M., Jessner, A., & Cognard, I. 2008, in American Institute of Physics Conference Series, Vol. 983, 40 Years of Pulsars: Millisecond Pulsars, Magnetars and More, ed. C. Bassa, Z. Wang, A. Cumming, & V. M. Kaspi, 633–635

Jenet, F., et al. 2009, arXiv:0909.1058

Lee, K. J., Wex, N., Kramer, M., Stappers, B. W., Bassa, C. G., Janssen, G. H., Karuppusamy, R., & Smits, R. 2011, 414, 3251

Littenberg, T. B., & Cornish, N. J. 2009, 80, 063007

Manchester, R. N. 2008, in American Institute of Physics Conference Series, Vol. 983, 40 Years of Pulsars: Millisecond Pulsars, Magnetars and More, ed. C. Bassa, Z. Wang, A. Cumming, & V. M. Kaspi, 584–592

Olmez, S., Mandic, V., & Siemens, X. 2010, Phys.Rev., D81, 104028

Romani, R. 1989, in NATO ASI Series, Series C, Vol. 262, Timing Neutron Stars, ed. H. Ögelman & E. van den Heuvel (Dordrecht, Netherlands; Boston, U.S.A.: Kluwer), 113–117

Sesana, A., & Vecchio, A. 2010, 81, 104008

Sesana, A., Vecchio, A., & Colacino, C. N. 2008, 390, 192

Sesana, A., Vecchio, A., & Volonteri, M. 2009, 394, 2255

Starobinsky, A. A. 1979, JETP Lett., 30, 682

Verbiest, J. P. W., Weisberg, J. M., Chael, A. A., Lee, K. J., & Lorimer, D. R. 2012, 755, 39

Wyithe, J. S. B., & Loeb, A. 2003, 590, 691

A sounding rocket payload experiment on zero gravity fuel gauging using modal analysis

Kevin M. Crosby[1,†], Eric Ireland[1], Kevin Lubick[1], Steven Mathe[1], Steven Metallo[1], Rudy Werlink[2]
[1]Carthage College, Kenosha, WI, USA [2]NASA Kennedy Space Center, Florida, USA
(rudy.werlink-1@nasa.gov) [†]
Corresponding author: kcrosby@carthage.edu

Abstract

For the past three years Carthage Space Sciences faculty and students have been developing Experimental Modal Analysis (EMA) techniques for use in microgravity fuel gauging of spacecraft propellant tanks. Our experiments were initially conducted on parabolic flights in which periods of microgravity of 20 seconds can be obtained. Parabolic flights were necessary to demonstrate the effectiveness of the technique in a relevant environment, but the short period of microgravity available during each parabola is insufficient to probe the resolution of the technique for settled, non-sloshing propellant. Here we report the results of an experiment in which the EMA technique is implemented in a sounding rocket payload developed through participation in the RockSat-C program of the Colorado and Virginia Space Grant Consortia.

Introduction

Low gravity propellant mass gauging is identified in NASA′s Exploratory Systems Architecture Study as a critical path objective [NASA, 2005]. The future of manned spaceflight beyond LEO relies in part on the development of accurate and robust methods of mass gauging in both settled and unsettled propellant states.

Traditional methods of fuel gauging require the presence of an external gravity field. Such methods typically rely on a buoyant force acting on a surface level indicator (e.g., the fuel gauge used in automobile gas tanks) or a measurement of effective capacitance of a probe in partial contact with the liquid. Such methods are not effective under microgravity conditions where the liquid surface position and shape is unrelated to the volume of liquid in the tank.

Fuel volume estimation on spacecraft instead use indirect gauging methods including equation-of-state estimations (for pressurized systems), measurement of spacecraft dynamics, and burn-time integration. Equation of state estimations require that the propellant tank be pressurized by a known volume of pressurant (typically helium). The pressure and temperature of the ullage volume in the tank is monitored as propellant is burned and the volume of the ullage and therefore of the remaining propellant is calculated based on the appropriate equation of state (usually the ideal gas law). This method, while effective, requires the additional hardware of pressurant tanks, pumps, valves and other hardware necessary to transfer pressurant to the propellant tanks. At launch costs exceeding $10,000/kg this additional hardware reduces the payload volume and substantially increases mission cost [NASA, 2008].

An alternative method of propellant gauging is to provide a known impulse to the spacecraft by a timed burn of thrusters. By measuring the craft's dynamic response to the impulse (acceleration

and final velocity), an estimate of the spacecraft's total average mass during the burn can be calculated using Newton's Laws. By subtracting the fixed mass of the spacecraft, the mass of fuel left in the tanks can be estimated. This method has the distinct disadvantage of burning additional propellant to make the measurement.

Finally, burn-time integration is a book-keeping method in which careful records of all thruster firings are recorded and the total propellant usage is estimated via assumptions about the propellant use during each burn. This method requires no additional hardware but is subject to large uncertainties resulting from the guesswork involved in assumptions about operating performance in the thrusters.

Beginning in 2011, the Carthage Space Sciences group has worked on an alternative technique utilizing Experimental Modal Analysis (EMA) methods and real-time data reduction methods to gauge the volume of liquid in model spacecraft propellant tanks. Our previous work on parabolic flights has demonstrated viability of the technique and provided a rough estimate of the resolution in volume measurement possible with the technique [Mathe *et al.*, 2012].

The short duration of microgravity available on parabolic flights (approximately 20 seconds per parabola) results in unsettled liquid sloshing continuously throughout the microgravity portions of the parabolic flight. In contrast, the propellant in a spacecraft such as a satellite in orbit around the earth, will generally be in a settled, non-sloshing state. To probe the resolution of the EMA method for settled fuel states, we proposed to the Wisconsin Space Grant Consortium to provide funding to implement the EMA gauging experiment on a sounding rocket where the smaller tank size and the ≈ 4 minutes of microgravity result in a liquid in mechanical equilibrium with its containment vessel.

The RockSat-C program allows student-faculty teams to propose, design and build experiments of their own conception for flight on a Terrier-Orion sounding rocket at NASA's Wallops Flight Facility on Wallops Island, VA [Koehler, 2013]. Details of the Terrier-Orion flight profile are discussed in the following sections.

Experimental Modal Analysis

EMA involves the application of acoustic forces to test structures. Natural resonances of the test structure are excited by the applied force, and sensors affixed to the structure record the amplitude of the acoustic response across the range of resonating frequencies [Brandt, 2011].

The acoustic forces applied to the structure can be in the form of discrete impacts, continuous white-noise functions, or chirp functions. In the present experiment, we use broad-band white noise. A white noise spectrum consists of all frequencies within a specified range with each frequency component having the same spectral power. By introducing every possible driving frequency to the tank, we are guaranteed that the full set of structural resonant frequencies is present within the applied signal. Therefore, natural vibrational modes of the structure will be excited resulting in an increased amplitude in sensor response at the excited mode frequencies.

In order to record and isolate the resonant frequencies of the tank, two non-invasive sensors are

attached to the tank. One sensor is located close to the actuator that provides the input spectrum of white noise frequencies. We refer to this sensor as the ”monitor” as it generally reproduces the input spectrum with very little resonant mode amplification. A second sensor located far from the monitor produces an output that consists of the attenuated white noise spectrum with the resonant frequencies preferentially excited.

In the EMA method, Fast Fourier Transforms (FFT) of the monitor and sensor signals are computed and the ratio of sensor to monitor FFTs is derived to construct the Frequency Response Function (FRF). The FRF, in effect, normalizes the signal FFT by the monitor FFT and therefore isolates those frequency components that only appear in the signal sensor. In this way, the resonant modes of the tank are isolated and extracted from the applied white noise spectrum. Modal techniques can therefore be used as real-time diagnostics of structural properties. Fluid loading increases the effective mass of the loaded structure, resulting in a decrease in the structure's resonant frequencies. The essential experimental concept is represented in Fig. 1.

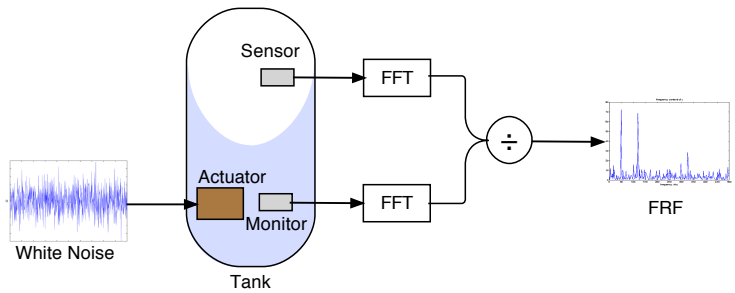

Figure 1: Experiment concept. A PZT patch actuator is adhered to a small experimental tank partially filled with water. Broadband white noise is introduced to the tank through the actuator. The Frequency Response Function is computed from the FFTs derived from the sensor and monitor signals.

Experiment Objectives

The central objective of the experiment is to continuously record signal and monitor response of a model propellant tank driven by a white noise spectrum throughout the duration of the Terrier-Orion flight profile. Continuous recording of monitor and sensor signals satisfies the minimum success criteria for the project, but the larger analysis goal is to correlate shifts in the resonant mode frequencies with change in fill fraction. Because we have demonstrated fill-fraction resolution of better than 5% with sloshing liquid in the parabolic flights, in the sounding rocket project in which we anticipated a settled fluid state, we hoped to push this resolution below 1% (to resolve fill fractions that differed by no more than 1% of the total tank volume).

Sounding Rocket Mission Profile

The Terrier Mk12-Improved Orion Sounding Rocket is configured with a first stage Terrier Mk12 motor providing 15037 lb of thrust over a burn time of 5.2 seconds, a second stage Improved Orion motor with 8273 lb of thrust over a burn time of 25.4 seconds, and two experiment bays with 9 payload canisters. The fifteen minute flight profile of the Terrier Orion rocket is illustrated

in Fig. 2. The period of free-fall during which data acquisition occurs is between the end of the Orion stage burn at T + 40 sec. and T + 312 sec. Apogee for the flight was at 73 miles and time approximately T + 168 sec. The flight trajectory from launch Pad 1 at the Wallops Island Launch Facility is illustrated in Fig. 3.

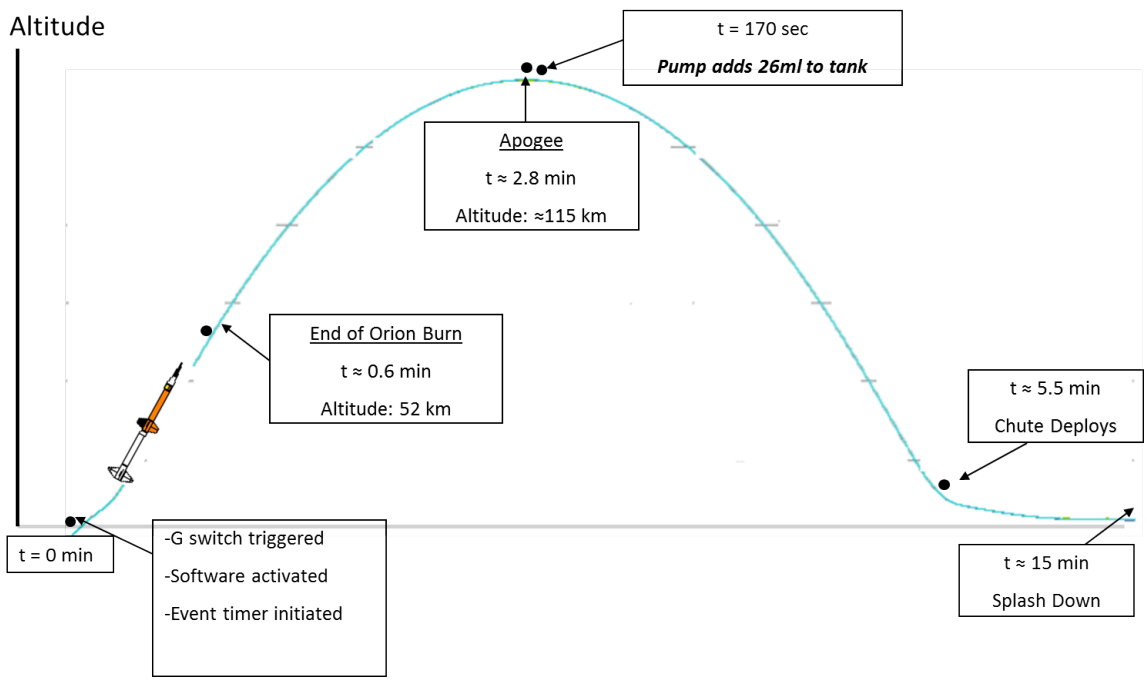

Figure 2: Terrier Orion Sounding Rocket flight profile

Launch accelerations exceed 25 g shortly after ignition of the first stage and the vehicle is moving at its maximum speed of 1300 m/s at the end of second stage burnout. Payload separation from motors occurs at T + 125 sec. The vehicle launches from a launch rail set at 89°.

Concept of Operations

The concept of operation for the experiment is illustrated in Fig. 1. The experiment protocol has our 1419 ml experimental tank initially filled with 160 ml of water corresponding to a fill fraction of 11%. Once in the zero-g portion of the flight trajectory, EMA data is continuously recorded. Approximately halfway through the flight trajectory, a solenoid valve opens and a micro-pump initiates the transfer of 26 ml of water from a reservoir bladder into the experimental tank, providing a fill change of approximately 1.8% of the total tank volume. A flow sensor measures the total amount of liquid exchanged between fill bladder and tank.

Experiment Design

Our payload was divided into four subsystems: structural, electronics / software, hydraulic, and sensors.

Figure 3: Sounding rocket flight trajectory from Wallops Island Flight Facility.

The sensor subsystem consists of two identical PZT (lead zirconate titanate) transducers, one serving as the monitor and one as the signal sensor. An actuator driven by a piezo signal amplifier in turn driven by a white noise generator provides a broad band excitation signal to the experimental tank. A hydraulics subsystem consisting of solenoid valve, micro-pump and two fluid reservoirs exchanges liquid and air with the experimental tank. The electronics subsystem consists of two micro controllers, a white noise signal generator, a four channel analog-to-digital converter (ADC), a four channel digital-to-analog converter (DAC) for voltage and data conversions, and Compact Flash (CF) format data storage, as well as latch and activation circuits for experiment initiation. Each subsystem is detailed in brief below.

Structural Subsystem

The heart of the Structural Subsystem consists of a cylindrical tank of 5.5 inch diameter and of 4 inch height. This experimental tank holds the water (our propellant simulant) and has the PZT transducers affixed to the outside surface. Two 1/4-inch NPT ports are located on top of the tank for filling and draining. Above the tank rests a deck, which we call the hanger, for holding hydraulic components including the pump, solenoid valves and water bladders. The hanger is supported by pillars, which we call secondary standoffs, in order to mechanically isolate the tank from the rest of the structure. A secondary containment vessel envelops the tank and hanger. Mounted above the secondary containment vessel is a polycarbonate plate to hold the electronic components. Finally, the RockSat payload canister which serves as the external sheath to the payload is bolted to the electronics plate by five standoffs. The canister is also bolted to the bottom of the secondary containment baseplate.

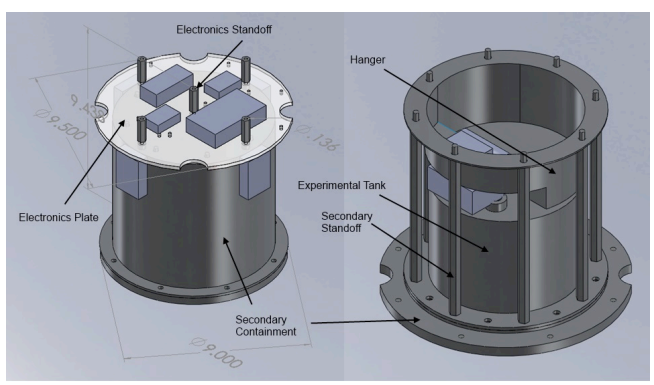

Figure 4: Structural subsystem consisting of experimental tank, electronics deck, support structure and secondary containment vessel.

Sensor Subsystem

The sensors and the actuator (also a PZT transducer) are affixed to the experimental tank by means of a thin double-sided adhesive. The sensors convert mechanical vibrations of the tank to proportional voltage signals at the level of 100s of mV.

The actuator is driven by a white noise signal amplified by a compact piezo driver that steps up the TTL signal from the white noise generator to a proportional signal with an RMS voltage of ± 200V.

Electronics Subsystem

The main functions of the Electronics Subsystem are to send a pre-recorded white noise signal to the actuator, to store signals from the sensor and monitor to a flash disk, and to control the event timer for the pump and solenoid valve. The electronics are powered by four 6V nickel metal hydride (NiMH) rechargeable battery packs wired in a series of two parallel circuits to produce an output voltage of 12VDC.

The latch circuit board regulates the power activation. In accordance with the Wallops Flight Facility Sounding Rocket Program Guidelines, activation occurs when both Wallops Flight Facility shorts the remove-before-flight (RBF) connection and when the g-switch is activated by launch acceleration. Power is then distributed to the relay circuits, white noise amplifier, and the 12 to 5V and 12 to 3V power regulators.

Upon activation of the g-switch by launch accelerations, the TIP triggers the mini SD card player. A prerecorded .ad4 file containing reference tones and the white noise signal is sent from the SD card player to the Piezo Amplifier for distribution to the actuator PZT. The signals from the sensor and monitor are processed by a separate micro controller (a Tern B-Engine) that handles on-board analog-to-digital conversion and data storage via a Compact Flash (CF) card. The B-Engine has an onboard ADC that samples at a rate of 32,000 samples per second. The TIP also regulates the timing of fill changes and handles event timing for the duration of the flight. Software development for both TIP and B-Engine was in C.

At sample rates of 32kHz, The Nyquist frequency for the experiment is 16 kHz, well above the highest frequencies (5 kHz) reliably detected in the resonance spectrum of the experimental tank.

Hydraulics Subsystem

The key elements of the hydraulics chain are illustrated in Fig. 5. A flexible bladder containing 50 ml of water is connected by tubing to a flow totalizer, solenoid valve, flow pump and to the experimental tank. An identical flexible bladder is used to equilibrate pressure in the tank during fill-changes.

The tank itself has two 1/4-inch NPT ports for connection to bladder and reservoir. A 24V micro-pump transfers water at a rate of around 1.0 liter/min. between bladder and tank. The pump is activated simultaneously with the opening of a solenoid valve. Both the valve and the pump remain powered for ≈ 2 seconds to transfer the 26 ml of water from bladder to tank.

The integrated payload experiment is shown in Fig. 6. Fully assembled and loaded with water, the payload weighs 20.0 lb and fully occupies one payload canister.

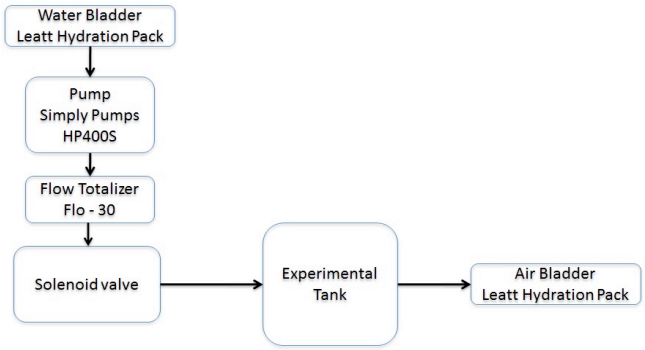

Figure 5: Hydraulic flow loop.

Figure 6: Fully assembled payload canister before wire assemblies are staked down for launch and RockSat canister is attached.

Flight and Ground Data

Prior to developing the sounding rocket payload experiment, the authors flew EMA fuel gauging experiments on parabolic aircraft using a larger cylindrical tank of volume 7.5 liters. The resonant mode peaks in the larger tank are distinguishable with a frequency resolution of around 1-2 Hz - at the limit of our sampling resolution. In contrast, the mode structure for the sounding rocket payload experiment has a lower frequency resolution of around 20 Hz. Fig. 7 shows a typical FRF obtained from the sounding rocket payload from which we can identify three primary modes which we label from lowest frequency to highest P1, P2, P3.

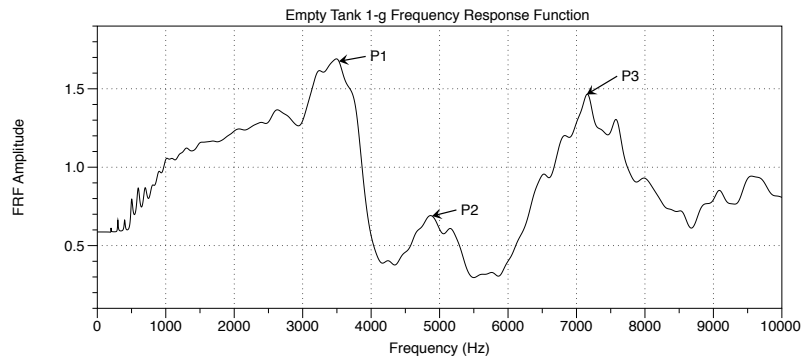

Figure 7: Sample Frequency Response Function for the empty tank. The frequencies P1, P2 and P3 were tracked throughout ground testing. Peak P2 was tracked through across two fill levels during flight.

The dependence of resonant mode P2 on fill level is shown in Fig. 8 for both ground (1-g) testing and for the two fill fractions used in the sounding rocket flight. Error bars for the ground data are standard errors obtained over a dozen sampling windows at each fill fraction. Standard errors for the flight data are not defined because of the small number of samples taken in flight.

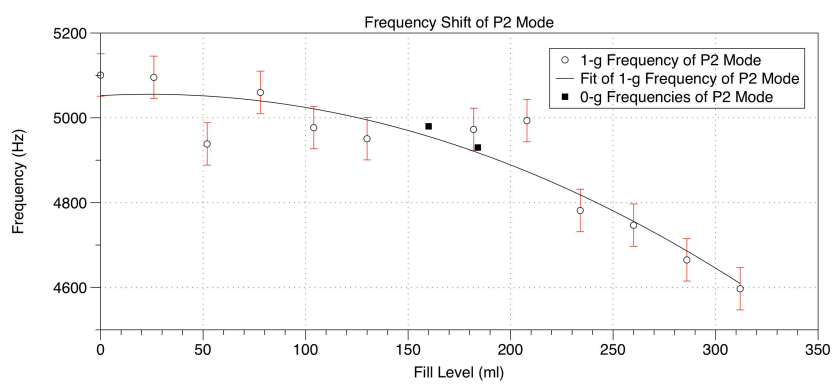

Figure 8: Cumulative data for peak frequencies as a function of fill level for both ground testing and for the two fill levels obtained during sounding rocket flight. Error bars are obtained from standard errors in ground testing data.

The relatively brief flight of the sounding rocket does not afford the opportunity to explore a large number of fill changes, but the flight data are suggestive, nonetheless. Mode shifts at the two fill levels obtained in zero-g do follow the anticipated trend. Mass-loading of the tank structure as a

result of added liquid should indeed result in decreasing resonant mode frequency as fill level is increased and this is what is observed in both ground and flight data.

Summary and Conclusions

EMA is an effective technique in real-time tracking of resonant mode shifts as a result of fill-level changes in a tank under arbitrary gravity states. Previous work has established that the EMA method can be used to infer fill-level changes of less than a few percent of tank volume under sloshing, zero-g conditions. The present study demonstrates that fill fraction changes of around 5% are potentially resolvable in a small cylindrical tank under zero-g conditions. The sounding rocket payload is also subject to spin about its vertical (symmetry) axis at a rate of about 5 Hz, and no confounding effects of this spin state were observed in the flight data.

EMA is a robust and viable method of inferring liquid volume in a spacecraft propellant tank in zero-g and has several advantages over existing methods of propellant gauging: EMA-based gauging is non-invasive, requires no additional hydraulics and can be performed in real-time with minimal computational overhead. Propellant tanks with integrated PZT sensors and minimal signal processing systems may one day replace the bulky pressurized systems currently in use in most gauging-critical spacecraft systems.

Acknowledgments

The authors gratefully acknowledge the Wisconsin Space Grant Consortium for financial support. The authors also acknowledge the useful contributions made by Prof. Brant Carlson.

References

[NASA, 2005] NASA Exploration Systems Architecture Study Final Report, available at `http://www.nasa.gov/exploration/news/ESAS_report.html`.

[NASA, 2008] Advanced Space Transportation Program: Paving the Highway to Space, available at `http://www.nasa.gov/centers/marshall/news/background/facts/astp.html`.

[Mathe *et al.*, 2012] Mathe, S., Anderson, K., Bakkum, K., Lubick, L., Robinson, J., Weiland, D., Werlink, R., Crosby, K.M. (2012). Modal Evaluation of Fluid Volume in Spacecraft Propellant Tanks. *Proceedings of the 22nd Annual Wisconsin Space Conference*.

[Koehler, 2013] RockSat Student Payload Experiment Program (2013). Information available at `http://spacegrant.colorado.edu/national-programs/rs-c-2014-home`.

[Brandt, 2011] Brandt, A. (2011). *Noise and vibration analysis: Signal analysis and experimental procedures*. Hoboken NJ: Wiley.

Physics: A student's guide through the great texts

Kerry Kuehn
Department of Physics; Wisconsin Lutheran College, Milwaukee[1]

Abstract

During the past decade, I have developed and taught a unique and challenging four-semester introductory physics curriculum at Wisconsin Lutheran College (WLC) based on the careful reading, analysis and discussion of selections from foundational texts in physics and astronomy. This curriculum is designed to encourage a critical and circumspect approach to natural science, while also developing a suitable foundation for advanced coursework in physics. It is scheduled to be published by Springer as a textbook/anthology around 2014.

Introduction

The motivation for this project was, at least in part, necessity: WLC is a small liberal arts institution located in Milwaukee. As such, we simply cannot offer the same range of courses as a large institutions might: *Physics for engineers, Physics of music, Physics for pre-meds, Physics of sports, etc.* So what kind of physics curriculum would be appropriate and profitable for a broad constituency of students, given WLC's limited resources? The solution: using classic texts. These texts are classics precisely because they address timeless questions in a thoughtful manner. For instance: both the beginning student and the seasoned scholar can profitably study Sophocles' Antigone–the former for plot and character development, the latter for ethics and political philosophy.

Standard physics textbooks do not make use of classic texts. Their pedagogical method is typically as follows: (1) present accepted laws, usually in the form of one or more equations, (2) provide example problems so students can avoid common conceptual errors, and (3) illustrate the relevance of the laws in contemporary industrial or diagnostic problems. While this method is efficient in preparing students for certain standardized tests, or in solving straightforward problems, it tends to mask how science is actually done: science is presented as an accomplished fact and prescribed problems revolve around technological applications of accepted laws.

In making use of classic texts, the pedagogical emphasis is rather different. Students are encouraged to (1) evaluate competing scientific theories, (2) understand concepts in context, rather than memorize modern terms, and (3) identify assumptions and their implications. Moreover, basing a physics curriculum on classic texts allows topics to arise naturally in the context of a continuing scientific dialogue.

[1] This work was supported by a grant from the Higher Education Program of the Wisconsin Space Grant Consortium and also from the Faculty Development Program of Wisconsin Lutheran College.

The textbook which I am developing has three main audiences. First, college and university students. It could be used as a primary textbook for discussion-style natural science classroom or as a supplementary textbook for courses in the history or philosophy of science. Second: advanced home-schooled and high-school students. It could aid senior-level home-schoolers looking for a bridge into college-level work or as a primary textbook for senior-level courses in physics, astronomy or history. Third: practicing physical scientists, social scientists, humanists and motivated lay-readers. It could serve as a structured review of foundational texts.

Project Activities

Evaluation, selection and acquisition of source texts. There were two primary criteria in selecting texts to include in the book: every selection must be significant for development of physical theory and every selection must be appropriate for beginning undergraduates or advanced high-school students. Student research and editorial assistants were involved at this stage of the project in, first, assembling a bibliography of english translations for each text and, second, evaluating articles which review the quality of the translation. These considerations informed the final decision on what to include.

In the following two tables are shown the text selections and topics included in Volume 1 of the textbook. The first table is for Part 1 of Volume 1; it is focused broadly on the themes of astronomy and cosmology. The second table is for Part 2 of Volume 1; it is focused on the themes of space, time and motion.

Volume 2, which is not described in this report, focuses on the themes of *electricity, magnetism, light* and *atoms, nuclei and matter*.

UNIT	AUTHOR	TEXT (TOPICS)
1	Aristotle	*On the heavens* (geocentrism, natural motion of elements)
2	Ptolemy	*The Almages*t (precision geocentrism)
3	Bede	*The reckoning of time* (astronomy & calendars)
4	Waldseemüller	*Introduction to cosmography* (astronomy & cartography)
5	Copernicus	*On the revolutions of the heavenly spheres* (heliocentrism)
6	Kepler	*Epitome of Copernican astronomy* (physical astronomy)
7	Galileo	*The starry messenger* (telescopic observations)
8	Herschel	*Outlines of astronomy* (stellar parallax)

UNIT	AUTHOR	TEXT (TOPICS)
9	Leavitt	*Harvard college observatory circular* (cepheid variables)
10	Shapely	*Galaxies* (measurement of great distances)
11	Einstein	*Relativity* (gravity and cosmology)
12	Hubble	*The realm of the nebulae* (stars, galaxies, Hubble's law)
13	Lemaitre	*The primeval atom* (big bang cosmology)
14	Eddington	*The running down of the universe* (cosmology & thermodynamics)

UNIT	TEXT (TOPICS)
1-6	Galileo's *Dialogues concerning two new sciences*: • strength of materials (scaling laws, equilibrium, levers, torque, fracture, yield strength, anatomy of animals) • projectile motion (falling bodies, drag, buoyancy, pendular motion, harmony, music theory, sympathetic resonance, kinematics, artillery)
7-8	Pascal's *Treatise on the equilibrium of fluids and the weight of air* • hydrostatic pressure, Pascal's principle, specific gravity, buoyancy, siphons, meteorology
9-12	Newton's *Mathematical principles of natural philosophy* • mass, momentum, inertia, force, relative motion, absolute motion, conservation of momentum, center of gravity, mechanical advantage, power, circular motion, fictitious forces, scientific method, Kepler's laws, universal gravitation
13-15	Einstein's *Relativity* • length contraction, time dilation, velocity addition, relativistic energy and momentum, 4-D space-time

Scanning, converting and editing source texts. After having selected the texts, undergraduate research and editorial assistants obtained printed copies of the text. They then scanned the texts and the resulting pdf files were converted into ascii text using an optical character recognition (OCR) program. The ascii text was proofread for errors in OCR and then formatted using LaTeX, a typesetting program conducive to scientific and mathematical publications.

Development of supplementary materials. In Figs. 1-5 in the appendix to this report, I provide some selections from a sample chapter of the textbook. Here I describe the basic components of each chapter.

1. I begin each chapter with a pithy quote, gleaned from the source text, which is selected to arouse the student's interest in the text and to set the stage for a broader conversation.
2. Next, I provide a short introduction to the text selection. If this is the first source text by a particular author, historical and biographical comments are offered so as to provide an appropriate context for the reading. I also include one or two provocative questions to focus the student's attention while studying the text.
3. Next, the source text itself is included, along with the bibliographical information and appropriate footnotes.
4. After the source text comes a series of study questions. These can be employed by the classroom discussion leader or by the independent student. They have been designed to draw out key points in the text and to highlight the author's definitions, methods, analysis and conclusions. They do not include anachronistic concepts or methods, so they encourage the student to approach the text in the same sprit, as it were, as the author.
5. After the study questions are a set of homework exercises which are designed to test the student's understanding of the text and ability to apply key concepts in solving problems. The homework exercises differ from the study questions in that they occasionally require the student to employ mathematical methods beyond those included in the text itself. Students may, for example, be asked to search other texts or website resources.
6. After the homework exercises is a list of vocabulary words which have been extracted from the text. These serve two purposes: to enhance the student's reading comprehension and to prepare the student for standardized tests such as the GRE or LSAT. Selection of vocabulary lists from source texts was the topic the fourth project activity, described below under the heading "Development of computer code for vocabulary lists."
7. Finally, laboratory exercises are included where appropriate.

Development of computer code for vocabulary lists. The general problem of selecting a list of appropriate vocabulary words from a source text is one encountered by educators from grade school through post-secondary education. The typical method of assembling a vocabulary list involves reading the source text, picking out "good" words and putting these into a list. Unfortunately for the teacher, such a vocabulary list might change if different translations of the source text are employed from year to year, or if different paragraphs of the source text are omitted from year to year. Moreover, it is difficult to determine what constitute "good" vocabulary words: the longest words? most common words? rarest words? most foreign words?

We have contrived a method to turn the art of assembling vocabulary lists into a science. In particular, two students have developed computer code which facilitates the automatic selection of vocabulary lists from a given source text. The code, written in C++, makes use of the Google Ngrams database, which consists of millions of scanned source texts along with word frequency

data. The code works as follows. First, one of Google's Ngram databases is downloaded. Second, the database is compared to a dictionary to eliminate misspellings included in Google's data. Third, the a searchable source text, such as Blaise Pascal's *Treatise on the Weight of Air*, is read. An algorithm then compares words in the source text to word frequency data in the Ngram database. The algorithm can be manipulated to favor certain types of words: old words, new words, long words, rare words, etc. Here, for instance, is a set of twenty vocabulary words gleaned from Christiaan Huygens' *Treatise on Light* using a particular vocabulary selection algorithm.

1. Propound
2. Presuming
3. Assuredly
4. Ingeniously
5. Intersected
6. Manifestly
7. Diaphanous
8. Impugn
9. Imparts
10. Supposed
11. Suffices
12. Insinuate
13. Fraught
14. Excellently
15. Dissipate
16. Smallness
17. Evenness
18. Sensibly
19. Diminishes
20. Imaginable

At this stage in the project, Cody Morse (a returning sophomore) is taking over the project from Tim Kriewall (a returning senior). He plans to migrate to a PERL/mySQL platform from the working C++ platform. Once we have finished this, our eventual goal is to publish a dedicated website which makes our algorithm widely available. This website will allow educators to upload text files, adjust word priority parameters (old/new, common/rare, etc.) using virtual knobs or sliders, and generate tailored vocabulary lists for use in the classroom.

Appendix

Chapter *title* and pithy *quote* from text →

Introduction gives historical context & biographical notes →

Footnotes direct the student to related texts & concepts. →

Chapter 60

Relativistic energy and Minkowski space

> The non-mathematician is seized by a mysterious shuddering when he hears of "four-dimensional" things, by a feeling not unlike that awakened by thoughts of the occult.
>
> —Albert Einstein

Introduction

The theory of space and time that Einstein describes in his book *Relativity* is remarkably different than the one described by Newton in his *Principia*. On the one hand, Newton assumes absolute (observer independent) distance and time intervals between events; this necessitates a subjective (observer dependent) speed of light. On the other hand, Einstein assumes an absolute speed of light; this necessitates subjective distance and time intervals between events.

Indeed, the Lorentz transformations described in section XI, which relate the space-time coordinates of events in Einstein's theory, were constructed with precisely this end in mind: to preserve an observer-independent speed of light.[1]

[1] The Lorentz transformations can also be understood as four-dimensional coordinate transformations under which the space-time interval defined by Eq. 59.5 is invariant.

Stated in this way, Einstein's theory of space and time is arguably as "absolute" as Newton's; they only disagree on what is absolute.

Now, in the reading selections that conclude Part I of *Relativity*, Einstein explains that the theory of relativity also implies a certain equivalence of mass and energy. It is here that he introduces the reader to his famous formula, $E = mc^2$. What does this mean? For instance, are we to believe that a thrown baseball, by virtue of its kinetic energy, is more massive than a held one? Or that a teapot, when heated, becomes a bit heavier?

Reading

Einstein, A., *Relativity*, Great Minds, Prometheus Books, Amherst, NY, 1995. Part I. Sections XV-XVII.

XV.

General results of the theory

It is clear from our previous considerations that the (special) theory of relativity has grown out of electrodynamics and optics. In these fields it has not appreciably altered the predictions of theory, but it has considerably simplified the theoretical structure, *i.e.* the derivation of laws,

Fig. 1

and—what is incomparably more important—it has considerably reduced the number of independent hypotheses forming the basis of theory. The special theory of relativity has rendered the Maxwell-Lorentz theory so plausible, that the latter would have been generally accepted by physicists even if experiment had decided less unequivocally in its favour.

Classical mechanics required to be modified before it could come into line with the demands of the special theory of relativity. For the main part, however, this modification affects only the laws for rapid motions, in which the velocities of matter v are not very small as compared with the velocity of light. We have experience of such rapid motions only in the case of electrons and ions; for other motions the variations from the laws of classical mechanics are too small to make themselves evident in practice. We shall not consider the motion of stars until we come to speak of the general theory of relativity. In accordance with the theory of relativity the kinetic energy of a material point of mass m is no longer given by the well-known expression

$$m\frac{v^2}{2}, \tag{60.1}$$

but by the expression

$$\frac{mc^2}{\sqrt{1-v^2/c^2}}. \tag{60.2}$$

This expression approaches infinity as the velocity v approaches the velocity of light c. The velocity must therefore always remain less than c, however great may be the energies used to produce the acceleration. If we develop the expression for the kinetic energy in the form of a series, we obtain

$$mc^2 + m\frac{v^2}{2} + \frac{3}{8}m\frac{v^4}{c^2} + \cdots .$$

When v^2/c^2 is small compared with unity, the third of these terms is always small in comparison with the second, which last is alone considered in classical mechanics. The first term mc^2 does not contain the velocity, and requires no consideration if we are only dealing with the question as to how the energy of a point-mass depends on the velocity. We shall speak of its essential significance later.

The most important result of a general character to which the special theory of relativity has led is concerned with the conception of mass. Before the advent of relativity, physics recognised two conservation laws of fundamental importance, namely, the law of the conservation of energy and the law of the conservation of mass; these two fundamental laws appeared to be quite independent of each other. By means of the theory of relativity they have been united into one law. We shall now briefly consider how this unification came about, and what meaning is to be attached to it.

The principle of relativity requires that the law of the conservation of energy should hold not only with reference to a co-ordinate system K, but also with respect to every co-ordinate system K' which is in a state of uniform motion of translation relative to K, or, briefly, relative to every "Galileian" system of co-ordinates. In contrast to classical mechanics, the Lorentz transformation is the deciding factor in the transition from one such system to another.

By means of comparatively simple considerations we are led to draw the following conclusion from these premises, in conjunction with the fundamental equations of the electrodynamics of Maxwell: A body moving with the velocity v, which absorbs[2] an amount of energy E_0 in the form of radiation without suffering an alteration in velocity in the process, has, as a consequence, its energy increased by an amount

$$\frac{E_0}{\sqrt{1-v^2/c^2}}.$$

In consideration of the expression given above for the kinetic energy of the body, the required

[2] E_0 is the energy taken up, as judged from a co-ordinate system moving with the body.

Source text must fulfill two criteria. It must be *significant* and *appropriate*.

Fig. 2

cording to classical mechanics, time is absolute, *i.e.* it is independent of the position and the condition of motion of the system of co-ordinates. We see this expressed in the last equation of the Galileian transformation ($t' = t$).

The four-dimensional mode of consideration of the "world" is natural on the theory of relativity, since according to this theory time is robbed of its independence. This is shown by the fourth equation of the Lorentz transformation:

$$t' = \frac{t - vx/c^2}{\sqrt{1 - v^2/c^2}}.$$

Moreover, according to this equation the time difference $\Delta t'$ of two events with respect to K' does not in general vanish, even when the time difference Δt of the same events with reference to K vanishes. Pure "space-distance" of two events with respect to K results in "time-distance" of the same events with respect to K'. But the discovery of Minkowski, which was of importance for the formal development of the theory of relativity, does not lie here. It is to be found rather in the fact of his recognition that the four-dimensional space-time continuum of the theory of relativity, in its most essential formal properties, shows a pronounced relationship to the three-dimensional continuum of Euclidean geometrical space. In order to give due prominence to this relationship, however, we must replace the usual time co-ordinate t by an imaginary magnitude $\sqrt{-1} \cdot ct$ proportional to it. Under these conditions, the natural laws satisfying the demands of the (special) theory of relativity assume mathematical forms, in which the time co-ordinate plays exactly the same rôle as the three space co-ordinates. Formally, these four co-ordinates correspond exactly to the three space co-ordinates in Euclidean geometry. It must be clear even to the non-mathematician that, as a eral theory of relativity, of which the fundamental ideas are developed in the following pages, would perhaps have got no farther than its long clothes. Minkowski's work is doubtless difficult of access to anyone inexperienced in mathematics, but since it is not necessary to have a very exact grasp of this work in order to understand the fundamental ideas of either the special or the general theory of relativity, I shall leave it here at present, and revert to it only towards the end of Part II.

Study questions

QUESTION 60.1. Is mass a conserved quantity?

a.) How is the kinetic energy of a particle expressed in the theory of relativity? In what way is the relativistic expression similar to the classical expression?

b.) Prior to the advent of relativity theory, was mass considered to be a conserved quantity? How are inertial mass and energy related according to the theory of relativity?

c.) What bearing does the existence of a fundamental speed limit have upon the notion of action-at-a-distance?

QUESTION 60.2. Is the Maxwell-Lorentz theory of electromagnetism consistent with the theory of relativity?

a.) Does the motion of the earth around the sun affect the apparent position or color of the stars? And is this consistent with Maxwell's theory of electromagnetism?

b.) If the electron is negatively charged all over, then what holds its left half to its right half?

Study questions draw out key points in the text and highlight the author's definitions, methods, analysis and conclusions.

Fig. 3

Is Maxwell's theory able to account for the nature of the electron? Where, then, does Einstein seek a solution to this problem?

c.) How did Lorentz arrive at a correct law of motion for the magnetic deflection of high-speed electrons? How does Einstein's approach differ? Which is better?

QUESTION 60.3. Did the Michelson-Morley experiment verify the theory of relativity?

a.) How did Michelson and Morley attempt to measure the motion of the earth using terrestrial measurements?

b.) What would constitute a positive result of this experiment? What would a positive result imply? What would constitute a negative result, and what would this imply?

c.) What were the actual results of their experiments? How were the explanations of Lorentz and FitzGerald and of Einstein different? Which explanation is better?

d.) Is Einstein's theory inconsistent with the existence of æther?

QUESTION 60.4. What does Minkowski mean when he says that the world is a four-dimensional continuum?

a.) In what sense is space a three-dimensional continuum? How many numbers does it take to describe a particular event?

b.) Why are space and time coordinates treated differently in classical mechanics? And how is this expressed in the Galileian transformation equations?

c.) In what sense are space and time coordinates treated more symmetrically in the theory of relativity? Are they treated identically?

d.) Is the notion of four-dimensional space-time

Homework exercises

EXERCISE 60.1 (Nuclear fusion reaction). When a gas consisting of the hydrogen isotopes deuterium and tritium is raised to a sufficiently high temperature, the atomic nuclei have enough kinetic energy to overcome their mutual coulomb repulsion, fusing to form stable helium-4 isotopes. This nuclear reaction is given by

$$ {}^2_1H + {}^3_1H \longrightarrow {}^4_2He + {}^1_0n. $$

The superscripts here denote the approximate rest masses of the reactants and products; the more precise rest masses are, from left to right, 2.014, 3.016, 4.003 and 1.009 atomic mass units.

a.) Is rest mass conserved during this nuclear reaction? If not, how much is gained or lost?

b.) How much heat is evolved when one mole of deuterium fuses with one mole of tritium? From where does this heat arise?

c.) Compare the heat evolved during this fusion reaction to that evolved during the combustion of one mole of a conventional explosive, such as dynamite.

EXERCISE 60.2 (Relativistic energy). Shown in Tab. 60.1 are expressions for the mass, momentum and energy of a particle according to both classical (Newtonian) and relativistic (Einsteinian) mechanics.

	Classical	Relativistic
mass	$m = m_0$	$m = \gamma m_0$
momentum	$p = mv$	$p = mv$
rest energy	0	$E_0 = m_0c^2$
total energy	$E = \frac{1}{2}mv^2$	$E = mc^2$

Table 60.1

Homework exercises test students' understanding of the text and their ability to apply key concepts.

Exercises occasionally require students to employ mathematical methods beyond those included in the text itself.

Fig. 4

$E = p^2/2m$.

b.) Now combine the relativistic expressions for momentum and energy to demonstrate that the energy of a particle may be expressed as $E^2 = (pc)^2 + (m_0c^2)^2$.

c.) What is the rest energy of an electron? What is its total energy, E, when it is moving at $0.995c$? What is its kinetic energy at this speed? By how much do the classical and relativistic calculations of the speeding electron's kinetic energy disagree?

d.) According to quantum theory, the momentum of a particle may also be written as $p = h/\lambda$, where h is Planck's constant and λ is the particle's so-called *DeBroglie wavelength* of the particle. How does this allow one to express the kinetic energy of a particle having zero rest mass, such as a photon?

e.) Suppose a photon of blue light, having a wavelength of 400 nanometers, undergoes a completely elastic collision with an unknown stationary particle. As a result, the photon recoils straight backwards and its wavelength is doubled. What is the rest mass of the unknown particle?

EXERCISE 60.3 (Relativistic ice-skating). Suppose that you are standing on a frozen pond watching a boy and a girl ice skate. The two skaters, who are initially at rest with respect to the ice, suddenly push off against each other. The boy moves away with a velocity of 6 m/s relative to the ice. The rest masses of the boy and girl are 20 kg and 15 kg, respectively.

a.) First, ignoring relativistic effects, find the recoil velocity of the girl relative to the ice.

c.) What is the girl's speed relative to the boy? Does her speed relative to the boy exceed the speed of light?

d.) If the boy is wearing a watch that ticks once per second (according to him), what is the time between ticks of his watch, as measured by you, and by the girl?

Vocabulary

1. appreciable
2. plausible
3. unequivocal
4. ion
5. unity
6. advent
7. unification
8. premise
9. conjunction
10. electrodynamics
11. abberation
12. radial
13. hitherto
14. auxiliary
15. extraneous
16. cathode rays
17. allude
18. terrestrial
19. æther
20. occult
21. space-time
22. continuum
23. prominence
24. perforce

Vocabulary selections from the text enhance reading comprehension.

Fig. 5

23rd Annual Conference
Part Three

Posters

Degassing of FC-72 in Microgravity

Danielle Weiland[1], Kevin Crosby[1], Nancy Hall[2]

[1]Carthage College, Kenosha, WI, USA

[2]NASA Glenn Research Center, Cleveland, Ohio, USA

Abstract

The Carthage College Microgravity Team designed and built a system to degas FC-72 during microgravity conditions through the NASA SEED program. FC-72 is an electronic coolant with low boiling point and surface tension that would be an ideal coolant for use in a two-phase cooling system onboard spacecraft [3M, 2013]. The goal of the project was to remove the dissolved gases from liquid FC-72 to improve the efficiency of flow boiling in microgravity as part of the Flow Boiling and Condensation Experiment conducted jointly by NASA Glenn Research Center (GRC) and Purdue University. A radial membrane contactor was used to remove the gases from the liquid during microgravity. Data from the lab was compared with the parabolic flight data to determine the relative effectiveness of the radial membrane contactor in reduced gravity.

Introduction

In the work reported here, we demonstrate a method of de-gassing of the dielectric coolant FC-72 (perfluorohexane) using a radial membrane contactor (RMC). The method was tested in the reduced gravity environment of parabolic flight. The tests were conducted as part of NASA's Systems Engineering Education Discovery (SEED) program. A team of seven undergraduate students designed and built a flow-loop to measure and characterize the efficiency of the RMC in extracting dissolved oxygen from the liquid FC-72. Dissolved oxygen content as a function of flow rate and ambient conditions were measured and compared with 1-g laboratory testing. Data from the microgravity tests will be used to inform the design of the Flow Boiling and Condensation Experiment (FBCE) being developed at NASA-GRC [3M, 2013].

The FBCE scheduled for deployment on the International Space Station (ISS) in 2017 will provide the first data on heat transfer rates and condensation dynamics in reduced gravity. The FBCE will serve as a first step toward developing two-phase cooling systems for future spacecraft. A significant technical challenge of two phase heat exchange systems is the removal of dissolved gasses introduced into the coolant fluid during condensation. Dissolved gasses

The authors gratefully acknowledge the Wisconsin Space Grant Consortium for financial support and the Reduced Gravity Office at NASA Johnson Space Center for support of the Systems Engineering Educational Discovery (SEED) program. The authors also acknowledge the useful contributions made by the Carthage Microgravity Team student members who worked on this project include Daisy Bower, Amelia Gear, Eli Favela, Kevin Lubick, Steven Mathe, John Robinson, and Seth Schofield.

(primarily atmospheric oxygen) reduce the effective heat capacity of the fluid, making the cooling less efficient. Therefore, a method of degassing coolant in microgravity environments is needed before two-phase cooling systems can be practically implemented.

Background

The purpose of the current experiment is to test a method of degassing a next-generation coolant using a radial membrane contactor. We measure the rate of atmospheric oxygen removal in a saturated liquid coolant and compare these measurements to those obtained in ground testing. One candidate fluid for a two-phase cooling system aboard the ISS is a member of the perfluorohexane family. The commercial product FC-72 (manufactured by 3M) has been chosen as the perfluorohexane of choice for this experiment due to low boiling point, the fact that it is a liquid at STP, its high dielectric constant, as well as the absence of toxic effects in humans. In this experiment we test the ability of a Radial Membrane Contactor (RMC) to remove dissolved gas from FC-72 in a microgravity environment [3M, 2013] using parabolic flights provided by NASA.

The RMC exploits the principles of capillary action to remove dissolved gas from a liquid without removing or chemically modifying the liquid [Liqui-cel, 2013]. Unlike degassing techniques used in industry, which typically involve cycles of boiling the fluid followed by vacuum exposure, the present technique does not depend on gravity to function properly, making it an ideal candidate for working aboard the ISS. The RMC has three main parts – a vacuum port, a series of thin, radially-aligned glass tubes wrapped around the flow tubing and a thin membrane that acts as an interface between the liquid and the induced vacuum. This setup allows a small vacuum pump to pull dissolved gas out of the fluid flowing through the RMC. Figure 1 shows a diagram of the RMC.

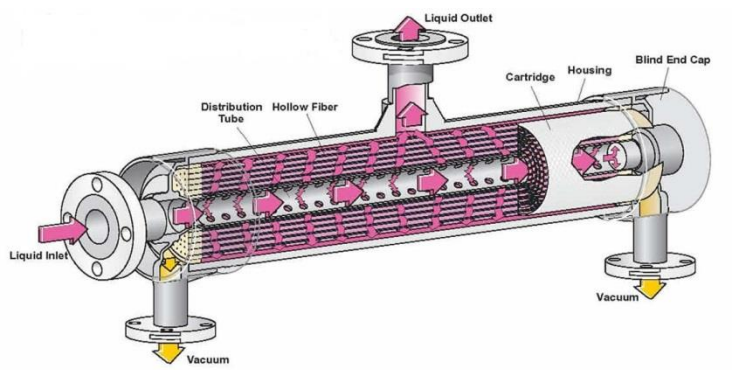

Figure 1: Diagram of the Radial Membrane Contactor [3M, 2013].

Properties of FC-72

Perflourohexane (FC-72) is a clear, colorless, odorless liquid with no known hazards. Relevant properties of FC-72 are listed in Table 1[3M, 2013].

Flammable Limit:	*Nonflammable*
Boiling Point:	*50-60 C*
Pour Point:	*-90 C*
Density:	*1.7 g/ml*
Vapor Density:	*~ 11.7 (at 20 C)*
Vapor Pressure:	*~ 232 mmHg (at 20 C)*
Specific Gravity:	*~ 1.7*
Evaporation Rate:	*> 1*
Viscosity:	*~ 0.42 centistoke (at 20 C)*

Table 1: Properties of FC-72

There are a few key properties that make FC-72 ideal for use in heat exchange systems. One such property is its low viscosity. Low viscosity fluids require comparably smaller pump pressure heads and therefore require less energy to circulate. Another property that makes FC-72 favorable for use in the present application is its high dielectric constant which will prevent any damage to electronics during a spill or leak. Also, there are no known hazards to humans in contrast to ammonia which is commonly used in two fluid, single phase cooling systems and is extremely toxic.

Heat Exchange Systems

Dissipation of environmental heat is a problem in large spacecraft. Under normal gravitational conditions, heat diffuses through the internal atmosphere of the spacecraft by convection until it can be dissipated externally. In the absence of gravity, natural convection does not occur and alternate methods of heat transfer must be used.

The current method of environmental cooling on the International Space Station is a two-fluid, single-phase system in which liquid water is circulated through Station to absorb heat, and then is brought into conductive contact with pipes containing anhydrous ammonia that dissipate this heat into space. The two-fluid, single-phase system on the ISS relies on sensible heat transfer (no phase change) and is less efficient than two-phase, single fluid heat transfer systems relying on latent heat exchange. Long-duration spaceflight will necessitate advancements in spacecraft heat dissipation and will likely rely on two-phase heat exchange systems.

In general, the use of a single-phase coolant loop, such as the one currently on the ISS, poses several problems that result in lowered cooling efficiencies. The fluid in contact with the external space environment (the ammonia) must have its contact time monitored and limited to prevent it from freezing. Finally, the use of ammonia poses health risks to crewmembers in the event of leaks.

An alternative, more efficient, approach is to use a liquid with a much lower boiling temperature in a two-phase cooling system. In two-phase systems, coolant has a low enough boiling temperature that when it absorbs heat from the station it will begin to boil. The vapors are then cycled outside the station, where they condense back into a liquid that can be cycled back into the station for reuse. The two phase system is, in general, more efficient than a single phase cooling system. However, during the boiling and condensation processes gas dissolves into the liquid. This process reduces the heat capacity and latent heat of the fluid, making the cooling less efficient. Therefore, a method of degassing coolant in microgravity environments is needed before two-phase cooling systems can be practically implemented.

Research Objectives

The central objective of the present study is to demonstrate the effectiveness of using a radial membrane contactor to degas a fluid in a zero-g environment. Radial membrane contactors have been used for many years in small laboratory experiments to remove dissolved gases from fluids. Extensive ground testing was performed to test the effectiveness of degassing both water and FC-72 in normal gravity conditions.

Another research objective is to demonstrate the radial membrane contactor's ability to bring fully oxygenated FC-72 down to its vapor pressure. If this is accomplished we know there are no dissolved gases present in the liquid and the efficiency of the FC-72 for cooling in microgravity would be maximized.

The zero-g data was obtained through participation in NASA's Systems Engineering Exploration Discovery (SEED) student microgravity parabolic flight program. We used the ground data as a reference to determine the effectiveness of the radial membrane contactor in microgravity conditions. The data collected on flight should closely represent the data from in lab testing.

Experimental Design

The experiment has multiple subsystems including the structural, electrical and hydraulic subsystems. The structural subsystem is comprised of all parts of the rig that house the electrical and hydraulic subsystems for safety. Figure 2 is a SolidWorks design showing the structural frame of the rig.

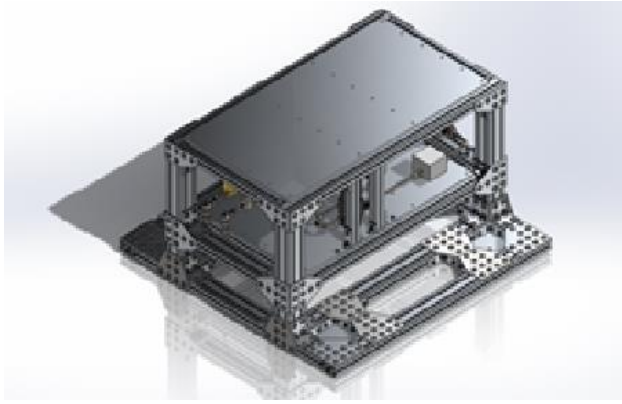

Figure 2: Structural Frame of Experiment (28.4in x 28.0in x 15.5in);
The experimental flow loop sits horizontally on the middle deck of the rig.

The structural frame of this rig is constructed from 6360 T6 aluminum extrusions, manufactured by TSLOTS, Inc. [TSLOTS, 2013]. These extrusions feature a slotted profile. These extrusions are fastened to each other using joint pieces machined from 6063 aluminum with zinc-plated A36 steel nuts and bolts. The extrusions have a spring locking feature, which creates a vibration-proof connection when tightened to the proper torque.

The electrical subsystem is comprised of all components that require power to run including the software used for data saving and analysis. The electrical subsystem is shown in Fig. 3. The design requires four primary sensors to record dynamic properties of the flow loop. These sensors measure temperature, pressure, flow rate and the concentration of dissolved O2 and are sampled by the analog to digital converter (ADC) at a rate of 1Hz. Additionally, the electrical subsystem includes programmable relays which control solenoid valves. The valves in turn allow the software to route the fluid through the membrane filter during microgravity periods on the parabolic flights.

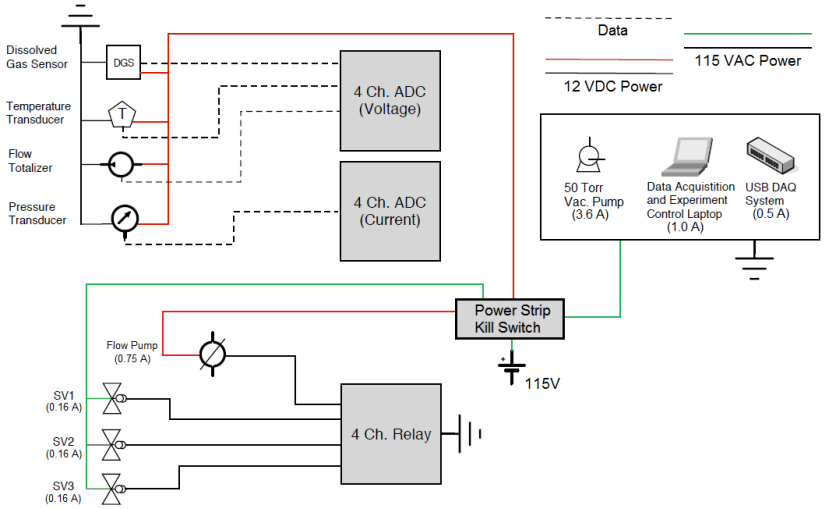

Figure 3: Electrical Subsystem

This experiment uses a tablet laptop equipped with a touch screen interface to allow for easy use in the microgravity environment of the aircraft. The laptop runs National Instruments LabVIEW software to control the data acquisition and fluid flow. A National Instruments four-channel USB chassis, item # NI-9174, is used to connect the relay module and DAQ modules to the computer via a USB cable [National Instruments, 2013].

The remaining subsystem constitutes the bulk of the experiment: the hydraulic subsystem. This includes all components that hold or transfer fluid. To test the effectiveness of the RMC at removing gas from FC-72 in microgravity conditions, the RMC is inserted into a flow loop designed to pump FC-72 through the RMC solely during the microgravity portions of flight. This flow loop is illustrated in Figure 4.

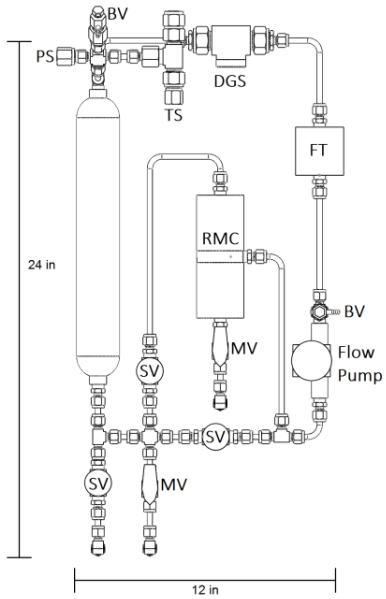

Figure 4: Flow loop with labeled components.
SV – Solenoid Valve; MV – Manual Valve; BV – Bleed Valve; FT – Flow Totalizer;
DGS – Dissolved Gas Sensor; TS – Temperature Sensor; PS – Pressure Sensor

The flow loop consists of the following components: the RMC, Flow Pump, Flow Totalizer, dissolved gas sensor, temperature probe, pressure transducer, a 500ml fluid reservoir, and assorted manual valves and solenoid valves to help control fluid flow. The FC-72 flows through all of the above components inside ¼ inch stainless steel tubing. Dissolved gasses in the FC-72 are extracted through the capillary tubes inside the RMC and removed via an oil-less vacuum pump. During flight, we have roughly 400ml of FC-72 in the flow loop.

Signals from the dissolved gas sensor, the temperature probe and the pressure transducer are acquired by a USB-based Data Acquisition (DAQ) module for data collection by a laptop. Additionally, the solenoid valves and the flow pump are controlled by relays driven by the DAQ module so that the laptop software can control the flow of the fluid through the flow loop [National Instruments, 2013].

During the first flight, the FC-72 is cycled through the RMC only during microgravity portions of the flight, and routed around the RMC during hypergravity. The FC-72 is cycled through the flow loop for the first 14 parabolas, and after data collection, will be bubbled for the 2g portion of parabola 15, and the entirety of parabola 16. The bubbling process is necessary to reintroduce oxygen into the FC-72. The fluid will then equilibrate for one parabola, circulating in a mode that bypasses the RMC, before the process begins again. During the second flight, the FC-72 is not reintroduced to oxygen and is degassed during all 30 zero-gravity portions of flight.

During the hypergravity portions of the flight, degassing of FC-72 ceases and the pressure and temperature of the gas in the flow loop are measured to obtain the dissolved gas content using the volume measurement obtained from the flow totalizer and ideal gas laws. Additionally, an in-line Dissolved Gas Sensor provides a secondary measurement of the partial pressure of dissolved gas in the FC-72.

Results

Figure 5 is a graph of the lab data when FC-72 was degassed for 35 minutes. The black line on the graph shows the measured pressure of the flow loop during the de-gassing and the red line is the percent of dissolved oxygen remaining in the FC-72. The blue dashed line is the vapor pressure of FC-72 – 26.9 kPa at STP.

The flow loop began at room temperature with 500ml of FC-72 in it and was cycled with a flow rate of 480ml/min.

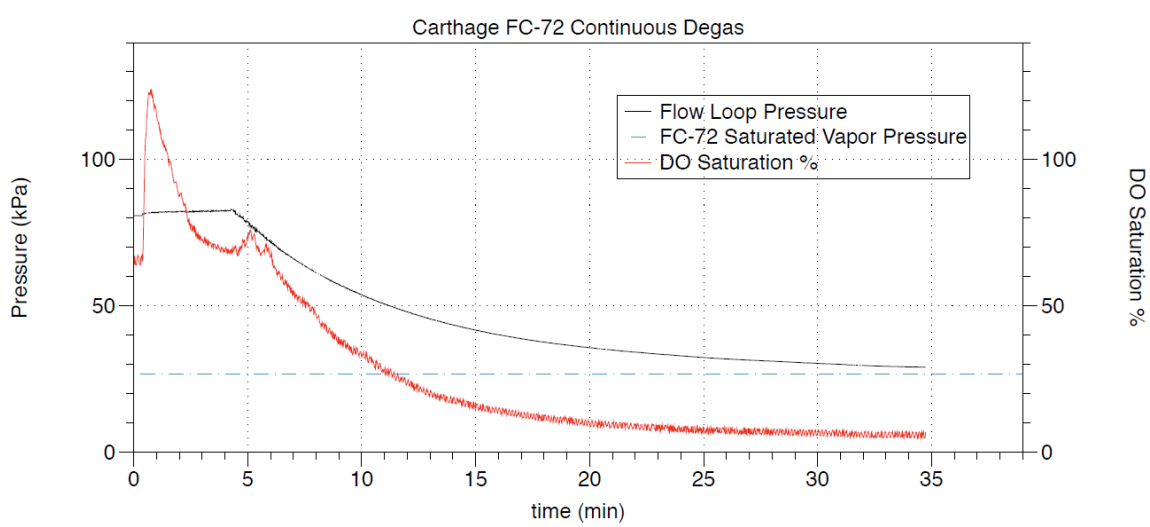

Figure 5: FC-72 Continuous Degas of FC-72 in 1-g (lab) conditions. Shown here are both pressure in the flow loop and Dissolved Oxygen (DO) saturation.

Figure 6 shows the pressure drop of the system during ground testing as well as comparison data for the first flight day. The flight data shows data retrieved during zero-gravity portions of the flight to compare with the continuous degas lab data.

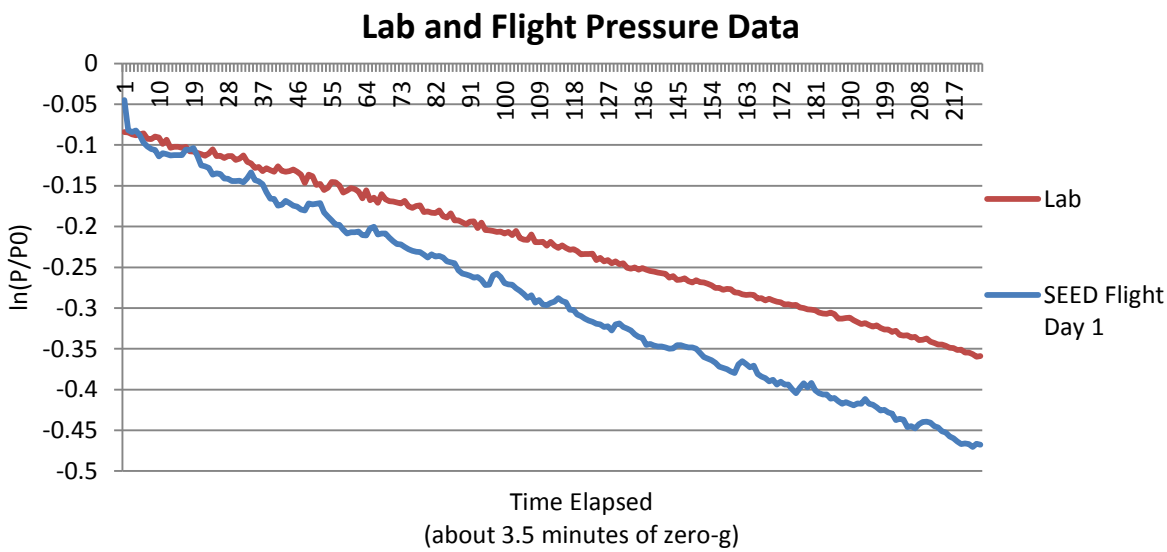

Figure 6: Lab and Flight Pressure Data for continuous degas (lab) and 0-g only (flight).

Discussion

The central objective of the study reported here was to determine the effectiveness of using a radial membrane contactor to degas a fluid in a zero-g environment with the results to be used to supplement the FBCE.

One goal of the study was the effort to degas the FC-72 down to its vapor pressure of 26.9 kPa. During the flight time available, the lowest pressure of the FC-72 achievable was 52 kPa. In 1-g lab testing the lowest pressure obtainable was 29.2 kPa and the amount of dissolved oxygen remaining was 5%.

It was shown that the RMC works in the lab but was incapable of bringing the FC-72 to its vapor pressure indicating that we were not able to remove all dissolved gases from the liquid. During the 35 minute in-lab degassing, data from our flow totalizer showed the flow rate decreasing. The reason for this may be that boiling of the FC-72 was occurring. The flow pump and totalizer only work with liquids and therefore would stop working with only gas in the system.

If we continued to try and degas the remaining liquid further, the pressure would begin to rise again instead of drop. A potential solution to this would be the use of more FC-72 in the system to slow the onset of boiling.

A possibility for why the degassing rate was lower in zero-g than in 1-g is that flow boiling onset occurs at higher gas pressure in microgravity and may contribute to decreased de-gassing efficiency. It was shown from this study that the radial membrane contactor does degas the FC-72 during microgravity conditions even though it is not as efficient as during normal gravity conditions.

References

[3M, 2013] 3M. *Flourinert FC-72*. (Material Safety Data Sheet). Retrieved from http://amsmaterials.com/products/Fluorinert-FC%252d72.html.

[Liqui-cel, 2013] Liqui-cel Membrana, Charlotte, South Carolina.

[National Instruments, 2013] National Instruments, Inc., Austin, TX.

[TSLOTS, 2013] TSlots/Futura Industries, Clearfield, Utah.

Single-Photon Detection using a Quantum-Dot-Gated Resonant RLC Circuit

Tyler Nickel, Yann Talhouarne, Andrew Prudhom, Richard Allenby, and Eric Gansen,[†]
Physics Department; University of Wisconsin-La Crosse, La Crosse, WI

Abstract: We report on a novel detection scheme that uses semiconductor quantum dots and electrical resonance to detect single photons of light. Here, a quantum-dot, optically gated field-effect transistor (QDOGFET) is used as the resistive element of a resonant RLC (resistor-inductor-capacitor) circuit. A photon is detected when it photocharges a quantum dot, thus modifying the resistance of the QDOGFET and altering the resonance condition of the surrounding circuit. Because the circuit functions as a bandpass filter, rejecting much of the electrical noise that can obscure weak photo-induced signals, the RLC detection scheme is sensitive enough to detect individual photons of light.

Introduction

The ability to detect single photons of light is fundamental to quantum information science and technology, is extremely useful for astronomical measurements, and may also lead to enhanced deep-space communication systems. In addition to being crucial measurement tools for experiments in quantum optics (Di Giuseppe *et al.*, 2003; *Waks et al.*, 2004; *Waks et al.*, 2006; Achilles *et al.*, 2006; Waks *et al.*, 2006), single-photon detectors (SPDs) are needed for quantum communication systems based on quantum-key distribution (Brassard *et al.*, 2000; Hiskett *et al.*, 2006) and form the basis for certain strategies for quantum computing (Knill *et al.*, 2001). In addition, arrays of SPDs are being developed to capture the faint images produced by telescopes (Romani *et al.*, 1999), and they may also find use in the receivers of advanced laser-based (so called 'lasercom') systems that can transmit information at high speeds over interplanetary distances (Boroson *et al.*, 2004; Mendenhall *et al.*, 2007; Hemmati *et al.*, 2007). For all of these applications, desired detector characteristics include high detection rates, low dark counts, high detection efficiency, low timing jitter, and photon-number resolving capability. In addition, SPDs should be compact, exhibit low power consumption, and be tolerant to changes in temperature and other environmental conditions.

In addition to detection mechanisms based on avalanche gain and low-temperature superconducting materials, another class of SPD that is being researched today makes use of semiconductor quantum dots (QDs). In one such device, referred to as a quantum dot, optically gated, field-effect transistor (QDOGFET) (Rowe *et al.*, 2006), a layer of self-assembled QDs is embedded in a specially designed high-electron mobility transistor (HEMT). As illustrated in Fig. 1(a), the structure consists of alternating layers of GaAs and AlGaAs with a single layer of InGaAs QDs. Si delta doping provides excess electrons to the conduction band of the structure that accumulate at the GaAs/AlGaAs interface forming a two-dimensional electron gas (2DEG). The device is fabricated by depositing electrical contacts, denoted as the source and drain, on the semiconductor structure; by etching a mesa between the contacts to channel the 2DEG; and by

[†] The authors would like to acknowledge M. A. Rowe, S. M. Etzel, S. W. Nam, and R. P. Mirin of the Quantum Electronics and Photonics Division of the National Institute of Standards and Technology (NIST) in Boulder, CO for their contributions to this work as well as the Wisconsin Space Grant Consortium for its financial support.

depositing a thin ribbon of platinum across the channel mesa. The platinum ribbon is used to gate the transistor and is thin enough (4 nm thick) to partially transmit light. The area where photons are detected is defined by the gated portion of the 2DEG channel. The detection area is typically about four square micrometers in size and contains approximately 2000 QDs.

The basic mechanism that makes QDOGFETs photosensitive is described in Figure 1(a). During operation, electrical current flows through the 2DEG channel while a negative bias is applied to the gate. The key to detecting photons with this structure is that the resistance of the 2DEG depends strongly on the electric field produced by the gate. A photon produces a response when it charges a QD by exciting an electron-hole pair in the GaAs absorption region. Due to the internal electric field, the hole is directed to the QDs, where it is trapped, while the electron joins the 2DEG. The electric field associated with the charged QD combines with the electric field produced by the gate modifying the total field 'seen' by the current. Consequently, the absorbed photon causes a small change in the transistor resistance, which has been traditionally read out by monitoring the current (Rowe *et al.*, 2006; Gansen *et al.*, 2007*a*; Gansen *et al.*, 2007*b*; Rowe *et al.*, 2008; Rowe *et al.*, 2010; Gansen *et al.*, 2013). The resistance change persists for as long at the hole is confined to the dot, and it is the *photoconductive gain* associated with this process that makes QDOGFETs extremely photosensitive.

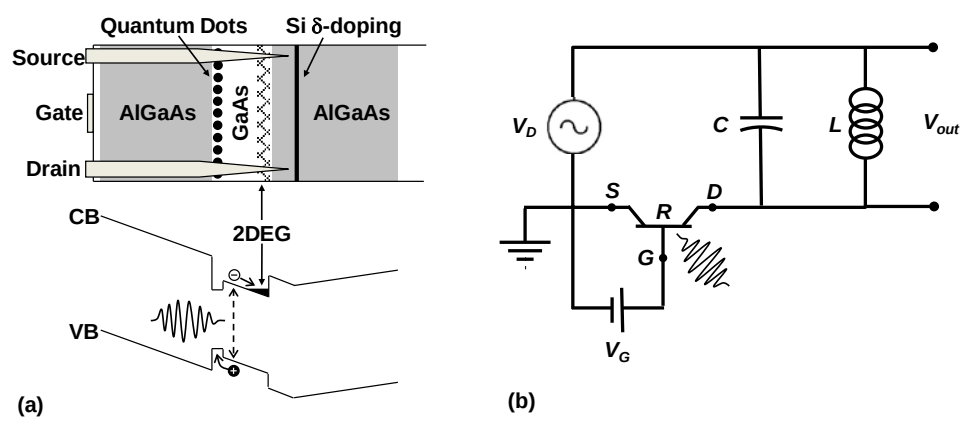

Figure 1. (a) Schematic diagram of the composition and band structure of the QDOGFET single-photon detector. CB and VB denote the conduction band and valence band, respectively, and 2DEG denotes the two-dimensional electron gas. (b) QD-gated resonant RLC detection circuitry that utilizes a QDOGFET as the resistive and photosensitive element. V_D and V_G denote the drive and gate voltages, respectively.

The photoresponse of QDOGFETs and similarly designed structures (Shields *et al.*, 2000; Shields *et al.*, 2001; Kardynal *et al.*, 2004; Kardynal *et al.*, 2006; Kardynal *et al.*, 2007) has been studied extensively at cryogenic temperatures (4 K – 77 K). They have been shown to exhibit photon-number-resolving capabilities (Gansen *et al.*, 2007*b*; Kardynal *et al.*, 2007; Rowe *et al.*, 2008), detection rates as high as 400 kHz (Kardynal *et al.*, 2004; Gansen *et al.*, 2013), and when properly designed, high internal quantum efficiency (Rowe *et al.*,

2006; Gansen *et al.*, 2007). However, while persistent photoconductivity lasting for hours has been demonstrated in transistors for temperatures as high as 150 K (Finley *et al.*, 1998), demonstrations of single-photon detection using QDOGFETs and similar structures have been limited to cryogenic temperatures (<77 K) due to electrical noise (Shields *et al.*, 2001; Gansen *et al.*, 2013). Electrical noise is the random fluctuation in current and voltage that is present in all electrical circuits. It is a common problem in detectors as it can obscure weak photo-induced signals. Electrical noise in two-dimensional electron systems has been studied extensively due to its impact on high-speed HEMTs (Kirtley *et al.*, 1988; Hofman *et al.*, 1990; Paransin *et al.*, 1990; Chen *et al.*, 2000), Hall bar structures (Müller *et al.*, 2006 and reference therein), and SPDs (Rowe *et al.*, 2010; Gansen *et al.*, 2013). Studies on QDOGFETs have shown that the power spectral density of the noise in such structures is typically $1/f$ in nature (i.e. inversely proportional to frequency) and increases with temperature (Rowe *et al.*, 2010; Gansen *et al.*, 2013).

Here, we report on a novel detection scheme that promises to reduce the impact of electrical noise in QD-based detectors. In this scheme, QDs are embedded in the resistive element of a resonant RLC (resistor/inductor/capacitor) circuit, as shown schematically in Fig. 1(b). A QDOGFET functions as the resistive element and the absorber for the detection system. When a photon is absorbed in the QDOGFET, it modifies the 2DEG resistance by charging a QD and subsequently modifies the resonant behavior of the circuit. The advantage the resonant detection circuitry has over traditional detection electronics is that the resonant nature of the circuit prohibits electrical noise at off-resonant frequencies from contaminating the responses produced by photons. In this way, the circuit functions as a bandpass filter, only allowing signals with frequencies near the resonant frequency to contribute the output signal, V_{out}. Consequently, the resonant detection circuitry is expected to provide enhanced sensitivity over traditional read out schemes that provide no such noise discrimination.

The sensitivity of the detection scheme is derived from the photoconductive gain provided by the persistent nature of the QDOGFET's response coupled with the resonant nature of the surrounding detection circuitry. Other forms of resonance have been shown to be sensitive mechanisms for detecting individual photons, as exemplified by QD resonant tunneling diodes (Blakesley *et al.*, 2005). In these devices, photocharged QDs are used to shift the energies of discrete levels required for resonant tunneling through a double-barrier junction. The resonance, in this case, is characteristic of the semiconductor structure itself and is not easily modeled. By contrast, the resonance conditions for RLC circuits are well understood and easily engineered.

In this work, we demonstrate the ability of a QD-gated resonant RLC circuit to detect single photons of light and discuss how it works. First, we describe the detection mechanism in detail by presenting the results of mathematical simulations and experimental measurements of the electrical characteristics of the circuitry. We then demonstrate the photosensitivity of the detection system by presenting the results of measurements where we illuminate the active area

of the QDOGFET with highly attenuated laser pulses. Finally, we characterize the performance of the system by performing statistical analysis of the optical data. We show that the device can detect single photons of light with a signal-to-noise ratio of 2.7:1 at an operating temperature of 6 K.

Detection System and Principles of Operation

As illustrated schematically in Fig. 1, the detection circuitry consists of a QDOGFET wired in series with the parallel combination of an inductor, *L*, and a capacitor, *C*. The circuit is driven with a sinusoidal bias voltage, V_D. The transistor contacts and 2DEG channel are the dominant resistive elements in the circuit and are represented in the schematic by total resistance, *R*. The conductivity of the QDOGFET channel is variable and controlled by the gate voltage, V_G.

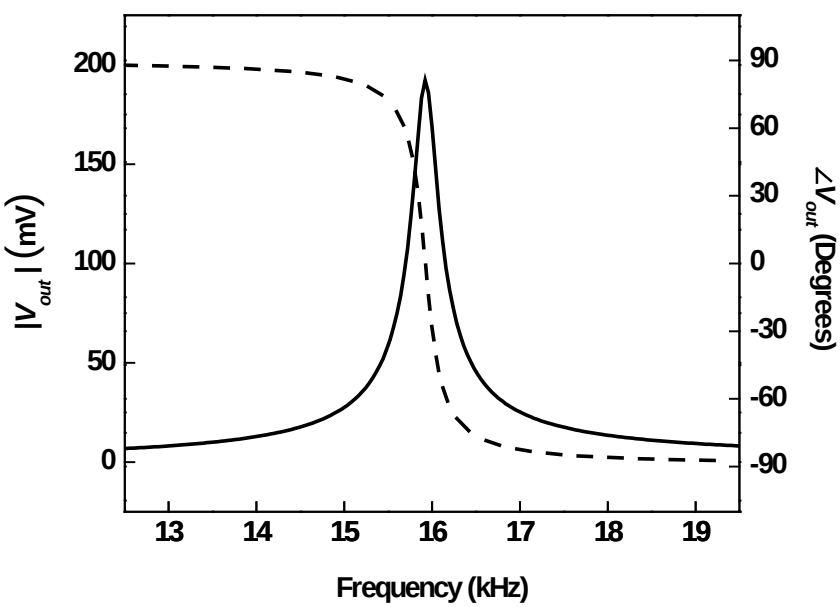

Figure 2. Mathematical simulation of the amplitude, $|V_{out}|$, and phase, $\angle V_{out}$, of the output signal as a function of the driving frequency for *L*=1 mH, *C*=100nF, *R*=30 kΩ, and 0.7 Ω parasitic resistance in the inductor and capacitor branches of the circuit. The drive voltage was taken to be 1 V_{pp}.

In Fig. 2 we show the results of simulations that demonstrate the resonant nature of the detection circuit. From basic circuit analysis, the characteristic parameters of the *ideal* circuit (which assumes no resistance in the inductor and capacitor branches) are easily determined and are given by: amplitude $|V_o| = |V_D|$; resonant frequency $f_o = (2\pi\sqrt{LC})^{-1}$; and bandwidth $\Delta f = (2\pi RC)^{-1}$. For a circuit containing components with values *L*=1 mH, *C*=100nF and *R*=30 kΩ, the ideal model yields $|V_o|$ = 1 V, f_o = 15.9 kHz and Δf = 53 Hz. However, parasitic resistance in the branches of the circuits will modify the resonant conditions. The simulation shown in Fig. 2 includes parasitic resistances of 0.7 Ω in both the capacitive and inductive branches of the circuit. Such resistance is reasonable for actual circuit components, and as we

will show, provides good agreement between simulation and experimental data. Parasitic resistance does not modify the resonant frequency of the circuit considerably, but it does reduce the magnitude and quality factor of the resonance. In the simulation, approximately 20% of the 1 V_{pp} (peak-to-peak voltage) drive voltage is passed by the circuit on resonance, and the bandwidth of the circuit is ~370 Hz (as defined by the full-width at the $\sqrt{2}^{-1}$ of the maximum points).

When a photogenerated hole is trapped in a QD, the charged dot screens the gate field changing the resistance of the transistor channel. The simulation shown in Fig. 3 illustrates the effect of the photo-induced change in *R* on the resonant peak. In this simulation it was assumed that a hole trapped in a QD changes the channel resistance of the QDOGFET by 2 Ω. The result indicates that the dominate effect of the resistance change is an increase in the magnitude of the resonance. Consequently, the largest photoresponse should be achieved when the circuit is driven at its resonant frequency.

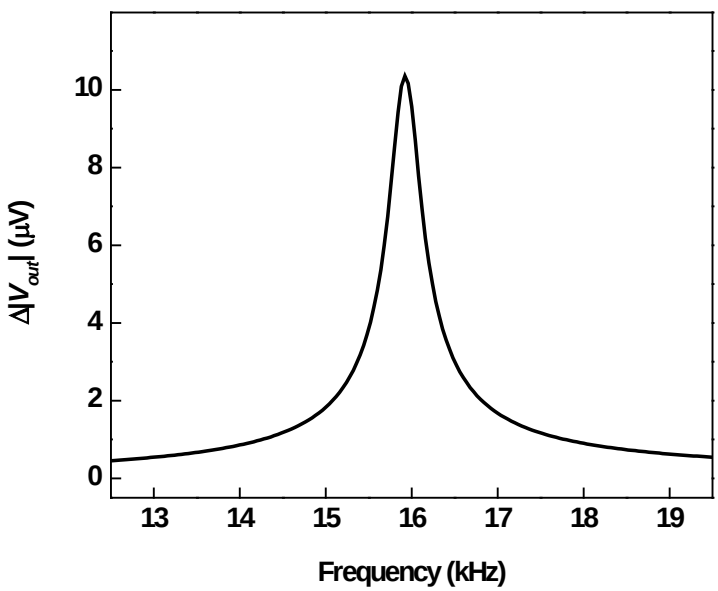

Figure 3. Mathematical simulation of the change in $|V_{out}|$ caused by reducing the QDOGFET channel resistance by 2 Ω. All other circuit parameters are the same as indicated in Fig. 2.

The simulations are to be compared with the experimental data shown in Fig. 4, which demonstrates the electrical characteristics of a QD-gated resonant RLC circuit. The structural details of the specific QDOGFET used in the circuit can be found in Rowe *et al.*, 2006 and Gansen *et al.*, 2007*a*. The circuit components (capacitor, inductor, and QDOGFET) were mounted on the cold stage of a liquid helium cryostat and cooled to 6 K. The inductor and capacitor used in the circuit exhibited room temperature values of L=1 mH and C=100nF; however, these values undoubtedly changed at the operating temperature. Fig. 4(a) shows the dependence of $|V_{out}|$ on the drive frequency for a drive voltage of 1 V_{pp} and for V_G = 0 V. The maximum output voltage is similar to that obtained in the

simulation (V_o = 200 mV_{pp}), while the experimental peak is broader (Δf = 715 Hz) and shifted to a higher central frequency (f_o = 22.4 kHz).

To maximize the photosensitivity of the detection system, it is important to bias the gate of the QDOGFET such that V_{out} is sensitive to changes in the gate field. In Fig. 4(b) we show how the magnitude of the resonance depends on the gate voltage. Optimal photoresponse is achieved for gate voltages where the slope of the curve is largest. It has been shown and substantiated with experiments (Rowe *et al.*, 2006; Gansen *et al.*, 2007*a*; Gansen *et al.*, 2007*b*; Rowe *et al.*, 2008; Rowe *et al.*, 2010; Gansen *et al.*, 2013) that the change in V_G caused by the trapping of N holes in the QD layer is given by

$$\Delta V_G = \frac{eW}{\varepsilon' A} N , \qquad [1]$$

where e is the elementary charge, W is the distance between the gate contact and the QD layer, ε' is the electric permittivity of the material, and A is the transistor active area. Consequently, the photo-induced change in the output signal is given by

$$\Delta |V_{out}| = M \frac{eW}{\varepsilon' A} N , \qquad [2]$$

where $M = dV_{out}/dV_G$ represents the slope of the curve shown in Fig. 4(b). Given the electrical properties of the circuit and the geometry and composition of the QDOGFET, each photon is expected to modulate the output voltage by $\Delta|V_{out}|$ = 10.5 μV_{pp} for V_G = -0.5 V.

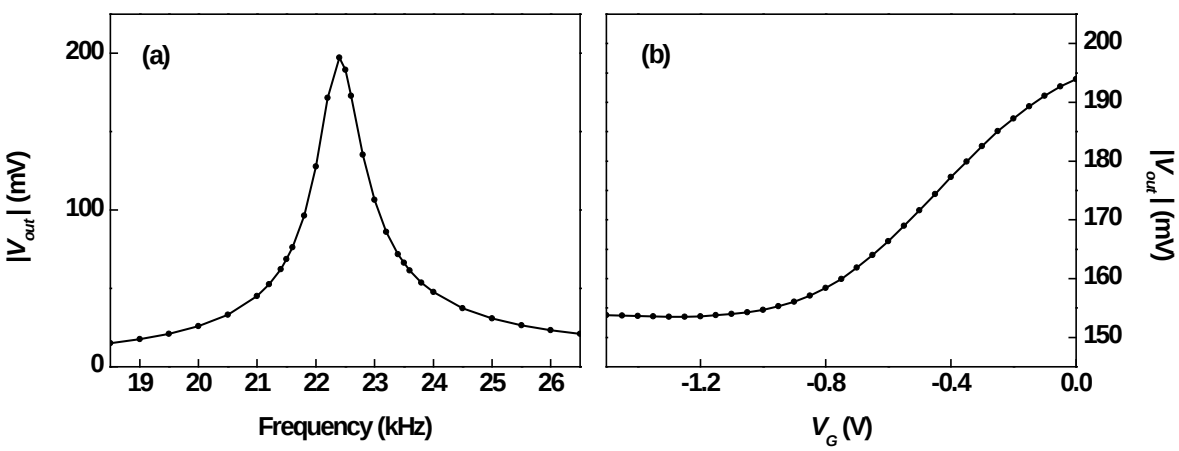

Figure 4. Experimental measurements of **(a)** $|V_{out}|$ as a function of the driving frequency for V_G = 0V and **(b)** $|V_{out}|$ as a function of V_G with the circuit driven at its resonance frequency. In both (a) and (b) the drive voltage was 1 V_{pp}.

Experimental Demonstration of Single-Photon Detection

A schematic of the measurement system used to test the photoresponse of the QD-gated resonant RLC circuit is shown in Fig. 5. The AC output voltage of the circuit was amplified by a preamplifier and then sent to a lock-in amplifier that was referenced to the drive frequency. The analog output signal from the lock-in amplifier was subsequently sent through a low-pass filter with a cut-off frequency of 1 kHz and converted to a digital signal for collection by a computer. Taking into account the voltage gain provided by the added detection electronics, the amplified signal captured by the computer is given by $V_c = G|V_{out}|$, where G = 667 is the total gain provided by the amplifiers. With this amplification in place, theory (Eq. [2]) predicts that each photon should produce a 7.0 mV change in V_c when the circuit is driven at resonance.

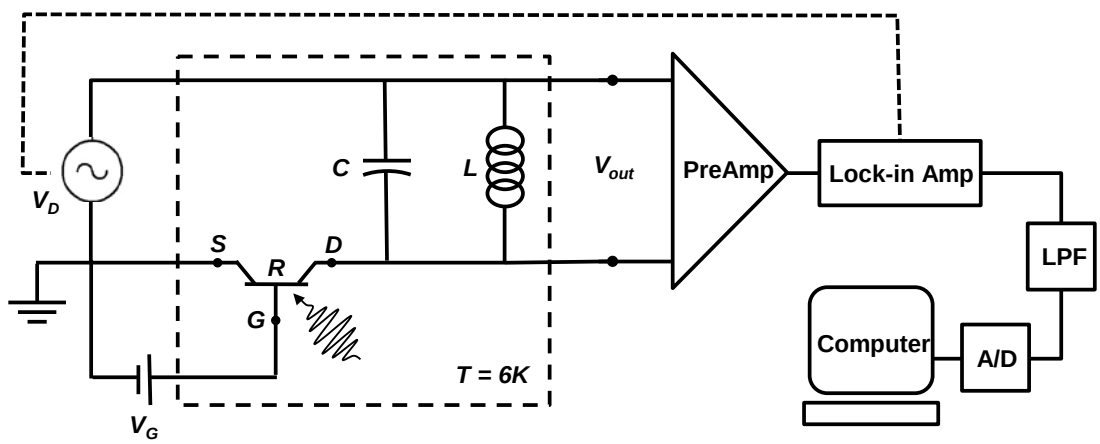

Figure 5. Schematic diagram of the electronics used to test the photosensitivity of the QD-gated resonant RLC detection circuitry. The total voltage gain of the preamplifier and lock-in amplifier combination was 667, and the cut-off frequency of the low-pass filter (LPF) was 1 kHz. A computer with an analog-to-digital (A/D) converter card was used to collect and store the amplified signals from the detection circuitry which was housed in a liquid helium cryostat (represented by dashed box).

The detection system was tested by illuminating the active area of the QDOGFET with a 1-Hz train of laser pulses from a diode laser that were properly tuned to be absorbed in the GaAs absorption layer of the transistor. In these measurements, the RLC circuit was cooled to 6 K, and the 300-ns-long laser pulses were attenuated such that on average less than one photon was detected per pulse. During illumination, a bias of -0.5 V was applied to the gate to maximize the photoresponse of the detection system; however, 500 ms after each pulse, the gate voltage was temporarily raised to +1.0 V for 1 ms to discharge the dots. Here, the electrical reset pulse flooded the QDs with conduction band electrons which recombined with trapped holes (Gansen *et al.*, 2007*a*; Rowe *et al.*, 2008).

In Fig. 6, we show the results of measurements where we illuminated the QDOGFET with 3000 laser pulses and monitored the magnitude of the system's response to each pulse of light. A

typical trace showing the system's response to a pulse of light arriving at t = 0.31 s is shown in Fig. 6(a). The response of the system is characterized by a persistent increase in the amplified output voltage where the rise time (~13 ms) of the signal is limited by the passband of the RLC circuit and the cut-off frequency of the low-pass filter.

A histogram of the 3000 responses is shown in Fig. 6(b). Here, we averaged the amplified output signal over 500-μs intervals leading up to and following a 30-ms window surrounding the arrival time of each pulse. We then subtracted the two averaged values to determine the magnitude of the response produced by each pulse. A histogram acquired without illumination is also shown for comparison. In the absence of photons, the histogram is characterized by a single Gaussian-shaped peak centered at zero volts. The width of the peak is representative of the electrical noise in the system. With illumination, the central Gaussian peak is reduced by comparison (indicating fewer occurrences of zero detected photons), and an additional shoulder is observed in the histogram comprised of non-zero photocounts.

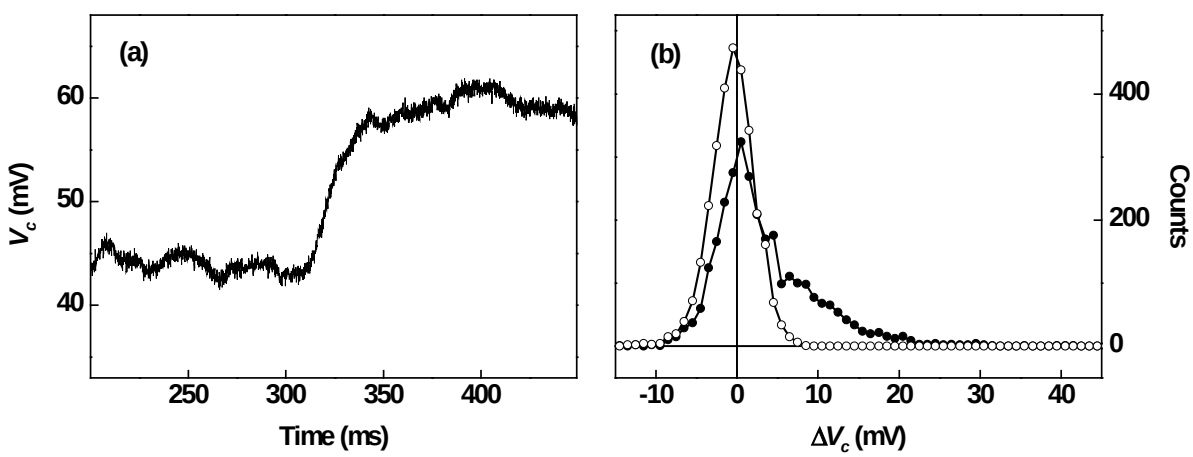

Figure 6. (a) Single-shot measurement of V_c responding to a laser pulse arriving at t = 0.31 ms. The detection circuit was driven at its resonant frequency ($f_D = f_o$ = 22.5 kHz) with a drive voltage of 1 V_{pp}. The gate bias was set at V_G = -0.5 V during the arrival of the light pulses. 500 ms after each pulse it was raised to V_G = 1 V for 1 ms to empty the QDs. (b) Histograms of binned signal changes, ΔV_c, with (solid circles) and without (open circles) illumination.

The mean number of photons detected per pulse, λ, and the average magnitude of the response per photon can be determined by conducting a statistical analysis of the histograms shown in Fig. 6(b). The probability that N photons are detected for any given light pulse from a *Poisson* source is given by $P(N) = (\lambda^N/N!)e^{-\lambda}$. The central Gaussian peak (associated with zero photons) in the histogram acquired with illumination has 69% as many counts as the Gaussian peak acquired without illumination. As a result, the mean number of photons detected per pulse is estimated from $P(0) = e^{-\lambda}$ to be λ = 0.38. It follows directly that $P(1)$ = 0.26 and $P(2)$ = 0.05. Consequently, most of the photocounts observed in the histogram with illumination are produced by single photons of light with fewer coming from higher numbers of photons. With

illumination, the average signal produced is 3.3 mV, which when divided by λ yields an average amplified response of ΔV_c = 8.7 mV per photon. This value agrees quite well with the amplified response predicted by theory. It is most likely an overestimate of the single-photon response caused by the absorption of photons in the gated portions of the channel mesa as the capture of photo-generated holes in QDs near but beyond the edges of the gate contact has been shown to contribute photo-induced signals in QDOGFETs (Gansen *et al.*, 2007*a*).

The single-photon sensitivity of the detection system is apparent by comparing the average response produced by individual photons to the random signal changes produced by electrical noise. The standard deviation of the histogram acquired without illumination is 3.3 mV, which is 37% the size of the average response produce by a single photon. As a result, most photoevents can be clearly distinguished from noise, which is the defining characteristic of a single-photon detector.

Conclusions

We have demonstrated the ability of a QD-gated resonant RLC circuit to detect single photons of light. We described the detection mechanism using mathematical simulations and experimental measurements of the circuit's electrical characteristics, and we tested the detection system by performing optical measurements. We found that the single-photon response of the system is consistent with that predicted by theory and is clearly distinguishable from the electrical noise produced in the circuitry. Future work will include optimizing the detection circuitry to improve the sensitivity of the system, demonstrating photon-number-discriminating detection by incorporating a number-resolving QDOGET into the circuit, and investigating the temperature and speed limitations of the system.

References

[1] Achilles, D., Silberhorn, C., and Walmsley, I. A., "Direct, loss-tolerant characterization of nonclassical photon statistics," *Phys. Rev. Lett.* 97, 43602 (2006).

[2] Blakesley, J. C., See, P., Shields, A. J., Kardynal, B. E., Atkinson, P., Farrer, I., and Ritchie, D. A., "Efficient single photon detection by quantum dot resonant tunneling diodes," *Phys. Rev. Lett.* 94, 67401 (2005).

[3] Boroson, D. M., Bondurant, R. S., and Scozzafava, J. J., "Overview of high rate deep space laser communications options," in *Free-Space Laser Communication Technologies XVI*, G. S. Mecherle, C. Y. Young, and J. S. Stryjewsjki, eds., *Proc. SPIE* 5338, 37-49 (2004).

[4] Brassard, G., Lütkenhaus, N., Mor, T., and Sanders, B. C., "Limitations on practical quantum cryptography," *Phys. Rev. Lett.* 85, 1330-1333 (2000).

[5] Chen, Y., VanVliet, C. M., Larkins, G. L., and Morkoç, H., "Generation-Recombination Noise in Nongated and Gated $Al_xGa_{1-x}As$/GaAs TEGFETs in the Range 1 Hz to 1 MHz," *IEEE Trans. Electron Devices* 47, 2045-2053 (2000).

[6] Di Giuseppe, G., Atatüre, M., Shaw, M. D., Sergienko, A. V., Saleh, B. E. A., Teich, M. C., Miller, A. J., Nam, S. W., and Martinis, J., "Direct observation of photon pairs at a single output of a beam-splitter interferometer," *Phys. Rev. A* 68, 63817 (2003).

[7] Finley, J. J., Skalitz, M., Arzberger, M., Zrenner, A., Böhm, G., and Abstreiter, G., "Electrical detection of optically induced charge storage in self-assembled InAs quantum dots," *Appl. Phys. Lett.* 73, 2618 (1998).

[8] (*a*) Gansen, E. J., Rowe, M. A., Greene, M. B., Rosenberg, D., Harvey, T. E., Su, M. Y., Hadfield, R. H., Nam, S. W., and Mirin, R. P., "Operational Analysis of a Quantum Dot Optically Gated Field-Effect Transistor as a Single-Photon Detector;" *IEEE. J. Sel. Topics Quantum Electron.* 13, 1-11 (2007).

[9] (*b*) Gansen, E. J., Rowe, M. A., Greene, M. B., Rosenberg, D., Harvey, T. E., Su, M. Y., Hadfield, R. H., Nam, S. W., and Mirin, R. P., "Photon-Number-Discriminating Detection using a Quantum-Dot, Optically Gated, Field-Effect Transistor," *Nature Photonics* 1, 585-588 (2007).

[10] Gansen, E. J., Rowe, M. A., Harrington, S. D., Nehls, J. M., Etzel, S. M., Nam, S. W., and Mirin, R. P., "Temperature Dependence of the Single-Photon Sensitivity of a Quantum Dot, Optically Gated, Field-Effect Transistor," *J. Appl. Phys.* 114, 093103 (2013).

[11] Hemmati, H., Biswas, A., and Boroson, D., "Prospects for Improvement of Interplanetary Laser Communication Data Rates by 30 dB," *Proc. IEEE* 95, 2082-2092 (2007).

[12] Hiskett, P. A., Rosenberg, D., Peterson, C. G., Hughes, R. J., Nam, S. W., Lita, A. E., Miller, A. J., and Nordholt, J. E., "Long-distance quantum key distribution in optical fibre," *New J. of Phys.* 8, 193 (2006).

[13] Hofman, F., Zijlstra, R. J. J., and Bettencourt de Freitas, J. M., "Voltage Noise in an $Al_xGa_{1-x}As$-GaAs Heterostructure," *J. Appl. Phys.* 67, 2482-2487 (1990).

[14] Kardynal, B. E., Hees, S. S., Shields, A. J., Nicoll, C., Farrer, I., and Ritchie, D. A., "Photon number resolving detector based on a quantum dot field effect transistor," *Appl. Phys. Lett.* 90, 181114 (2007).

[15] Kardynal, B. E., Shields, A. J., Beattie, N. S., Farrer, I., Cooper, K., and Ritchie, D. A., "Low-noise photon counting with a radio-frequency quantum-dot field-effect transistor," *Appl. Phys. Lett.* 84, 419-421 (2004).

[16] Kardynal, B. E., Shields, A. J., Farrer, I., Cooper, K., and Ritchie, D. A., "Single electron dynamics in a quantum dot field effect transistor," *Appl. Phys. Lett.* 89, 113503 (2006).

[17] Kirtley, J. R., Theis, T. N., Mooney, P. M., and Wright, S. L., "Noise Spectroscopy of Deep Level (DX) Centers in GaAs-$Al_xGa_{1-x}As$ Heterostructures," *J. Appl. Phys.* 63, 1541-1547 (1988).

[18] Knill, E., Laflamme, R., and Milburn, G. J., "A scheme for efficient quantum computation with linear optics," *Nature* 409, 46-52 (2001).

[19] Mendenhall, J. A., Candell, L. M., Hopman, P. J., Zogbi, G., Boroson, D. M., Caplan, D. O., Digenis, C. J., Hearn, D. R., and Shoup, R. C., "Design of an Optical Photon Counting Array Receiver System for Deep-Space Communications," *Proc. IEEE* 95, 2059-2069 (2007).

[20] Müller, J., Li, Y., von Molnár, S., Ohno, Y., and Ohno, H., "Single-Electron Switching in $Al_xGa_{1-x}As$/GaAs Hall Devices," *Phys. Rev. B* 74, 125310 (2006).

[21] Peransin, J. M., Vignaud, P., Rigaud, D., and Vandamme, L. K. J., "1/*f* Noise in MODFET's at Low Drain Bias," *IEEE Trans. Electron Devices* 37, 2250-2253 (1990).

[22] Romani, R. W., Miller, A. J., Cabrera, B., Figueroa-Feliciano, E., and Nam, S. W., "First Astronomical Application of a Cryogenic Transition Edge Sensor Spectrophotometer," *Astrophys. J.* 521, L153-L156 (1999).

[23] Rowe, M. A., Gansen, E. J., Greene, M. B., Hadfield, R. H., Harvey, T. E., Su, M. Y., Nam, S. W., and Mirin, R. P., "Single-photon detection using a quantum dot optically gated field-effect transistor with high internal quantum efficiency," *Appl. Phys. Lett.* 89, 253505 (2006).

[24] Rowe, M. A., Gansen, E. J., Greene, M. B., Rosenberg, D., Harvey, T. E., Su, M. Y., Hadfield, R. H., Nam, S. W., and Mirin, R. P., "Designing High Electron Mobility Transistor Heterostructures with Quantum Dots for Efficient, Number-Resolving Photon Detection," *J. Vac. Sci. Technol. B* 26, 1174-1177 (2008).

[25] Rowe, M. A., Salley, G. M., Gansen, E. J., Etzel, S. M., Nam, S. W., and Mirin, R. P., "Analysis of photoconductive gain as it applies to single-photon detection," *J. Appl. Phys.* 107, 63110 (2010).

[26] Shields, A. J., O'Sullivan, M. P., Farrer, I., Ritchie, D. A., Hogg, R. A., Leadbeater, M. L., Norman, C. E., and Pepper, M., "Detection of single photons using a field-effect transistor gated by a layer of quantum dots," *Appl. Phys. Lett.* 76, 3673-3675 (2000).

[27] Shields, A. J., O'Sullivan, M. P., Farrer, I., Ritchie, D. A., Leadbeater, M. L., Patel, N. K., Hogg, R. A., Norman, C. E., Curson, N. J., and Pepper, M., "Single photon detection with a quantum dot transistor," *Jpn. J. Appl. Phys.* 40, 2058-2064 (2001).

[28] Waks, E., Diamanti, E., Sanders, B. C., Bartlett, S. D., and Yamamoto, Y., "Direct observations of nonclassical photon statistics in parametric down-conversion," *Phys. Rev. Lett.* 92, 113602 (2004).

[29] Waks, E., Diamanti, E., and Yamamoto, Y., "Generation of photon number states," *New Journ. Phys.* 8, 4-8 (2006).

[30] Waks, E., Sanders, B. C., Diamanti, E., and Yamamoto, Y., "Highly nonclassical photon statistics in parametric down-conversion," *Phys. Rev. A* 73, 33814 (2006).

23rd Annual Conference
Part Four

Chemistry and Biosciences

Soft X-Ray EPMA analyses of nanophase lunar Fe-Si compounds

P. Gopon[1], J. Fournelle[1], J. Valley[1], W. Horn[2], P. Pinard[3], P. Sobol[1], M. Spicuzza[1], X. Llovet[4]

[1]Dept. of Geoscience, University of Wisconsin, Madison, Wisconsin USA
[2]ExxonMobil Research and Engineering Company, Annandale, New Jersey 08801 USA
[3]RWTH University, Aachen, Germany
[4]CCiTUB, University of Barcelona, Barcelona, Spain

Abstract
Conventional electron-probe microanalysis (EPMA) has an X-ray analytical spatial resolution on the order of 1-4 μm width/depth. Many of the naturally occurring Fe-Si compounds analyzed in this study are smaller than 1 μm in size, requiring the use of lower accelerating potentials and non-standard X-ray lines for analysis. The problems with the use of low energy X-ray lines (soft X-rays) of iron for quantitative analyses are discussed and a review is given of the alternative X-ray lines that may be used for iron at or below 5 keV (i.e., accelerating voltage that allows analysis of areas of interest smaller than 1 μm). Problems include the increased sensitivity to surface effects for soft X-rays, peak shifts (induced by chemical bonding, differential self-absorption, and/or buildup of carbon contamination), uncertainties in the mass attenuation coefficient (MAC) for X-ray lines near absorption edges, and issues with spectral resolution and count rates from the available Bragg diffractors. In addition to the results from the traditionally used Fe Lα line, alternative approaches, utilizing Fe Lβ, and Fe Ll-η lines, are discussed.

Introduction
Conventional electron probe microanalysis (EPMA) uses high electron beam energies (15-20 keV) to eject inner shell electrons, and measures the characteristic photon energy emitted when an outer shell electron transitions into a vacant inner shell electron state. This technique is able to nondestructively and accurately determine the chemical composition of materials to within ~1% accuracy. The volume that the incident electron beam excites is directly proportional to the voltage of the incident beam and the material composition. At 20 keV a general depth/width of the incident electron scatter (in common geologic materials) is on the order of 1-4 μm (figure 1). Conventional EPMA is therefore not suited for analyses of features under 2 μm width, because the electron beam would cause excitation of electrons in atoms that are outside of the feature of interest. It has long been recognized that to properly analyze samples under 5 μm, it becomes necessary to use low voltage electron beams. However, this has been difficult with traditional tungsten source electron probes. With the development of field emission source electron probes, it is now possible to focus low voltage beams to sizes required for nanoscale features. Doing so introduces many complications such as changes in X-ray peak position/shape, surface contamination, and limited understanding of the mass absorption coefficients for low energy (soft) X-rays (Pouchou, 1996).

A recent study (Llovet et al., 2012) showed the difficulties of using L lines for quantitative EPMA. Some of the causes of these problems include changes in peak position/shape of the X-ray lines, increased sensitivity to surface contamination, and errors in accuracy of the tabulated

This research project was funded by the Wisconsin Space Grant Consortium. Additional support was provided by an ExxonMobil research grant. I would like to acknowledge Silvia Richter at RWTH Aachen, Michel Outrequin of CAMECA France, and Bill Horn of ExxonMobil Research and Engineering Corporation for the generous use of their electron microprobe facilities, without them this work would not have been possible.

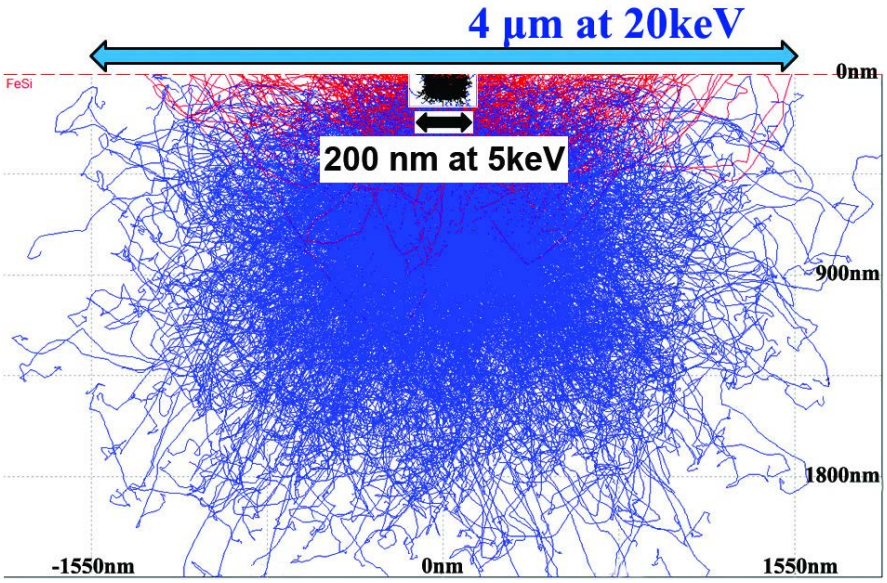

Figure 1: Monte Carlo simulation of the interaction volumes of a 5 keV (black) and 20 keV (blue) incident electron beam in FeSi. (using the CASINO software; Drouin et al, 2007)

mass attenuation coefficients (MACs) for low energy X-rays. The $L\alpha_{1,2}$ lines of the first-row transition metals are particularly problematic for quantitative analysis due to their proximity to their respective L_3 absorption edges. The $L\alpha$ transitions is between the M_5 and L_3 orbital (figure 2). The M_5 orbital in unfilled in the transition metals and is involved in bonding. This causes the $L\alpha$ transition to change energy depending on the bonding environment. Since even a small change of the X-ray line energy near absorption edges, changes the MAC by a large amount, this leads to large problems for quantitative analysis (figure 3).

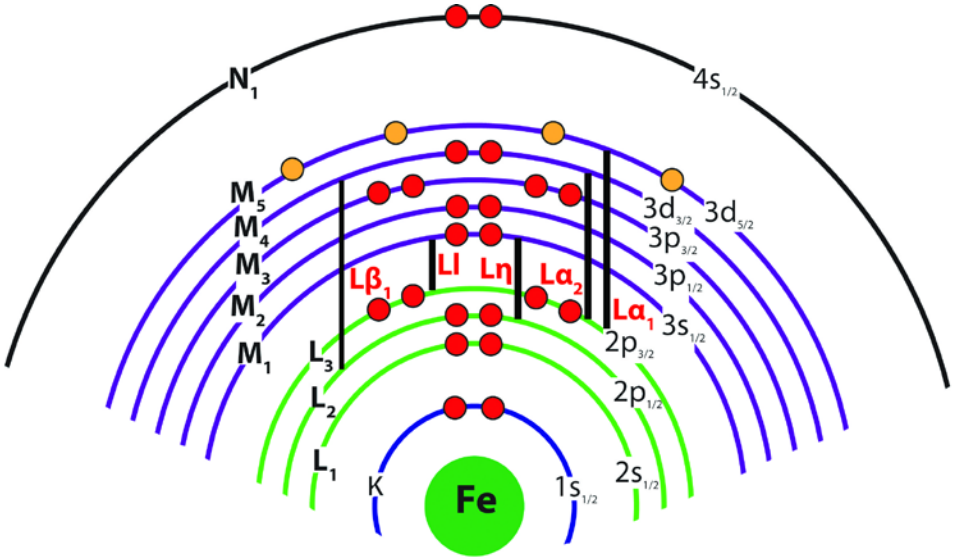

Figure 2: Schematic diagram of Fe electron cloud showing the major X-ray lines in Siegbahn and IUPAC notation, as well as the five transitions Fe $L\alpha_1$ $L\alpha_2$, $L\beta$, Ll, Ln.

Objectives

This study's goal is to measure the chemistry of sub-micron iron-silicides found in lunar regolith believed to be associated with impact structures. These iron-silicides are of particular importance because of the extreme reducing conditions required for their formation. Analyses of lunar iron silicides has been attempted in the past by Anand, et al, 2004. However, analyses

were only done on the a small number of Fe-Si grains that were large enough for conventional analysis, due to the difficulty of analyses of sub-micron grains.

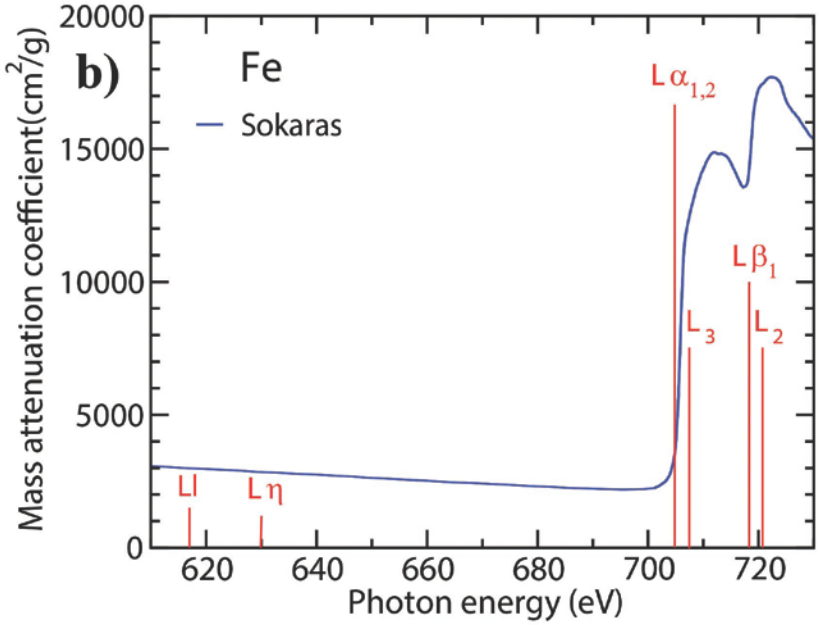

Figure 3: Experimental MAC's (taken from Sokaras et al., 2010) at the energies around the Fe Lα, Lβ, Ll and Lη lines, overlain with the corresponding tabulated line energies, and L_3 and L_2 absorption edges (values taken from Deslattes et al., 2003)

The motivation for the current study was an attempt at a proper EPMA analysis on sub-micron lunar Fe-Si compounds reported by Spicuzza et al. (2011) in Apollo 16 lunar regolith grains A6-8 (figure 4) and A6-7. These are hypothesized to have formed in the reducing environment of the moon after micro-meteorite impacts (Annad et al., 2004). They are significant because of the extreme reducing conditions required for formation. While native iron is fairly common in lunar dust, native silicon and iron-silicides have been rarely found. This is due to the order of magnitude lower reducing conditions needed to reduce to native silicon, as compared to native iron. However, their small size (< 1 µm) precludes quantitative measurements using conventional EPMA.

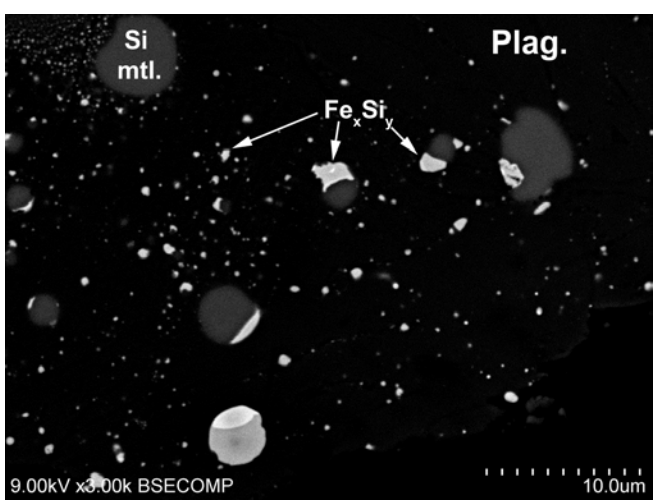

Figure 4: BSE image of plagioclase grain A6-8 from Apollo 16 regolith showing nano-phase Fe-Si compounds (bright phases), in a plagioclase matrix, the medium bright phases are silicon metal.

Background

These Fe-Si compounds are rarely found on Earth, the most notable example is in fulgarite deposit studied by Essene and Fisher (1986), but they do appear to be important in extraterrestrial bodies where highly reduced environments need for their formation are more common. Extra-terrestrial iron silicides have been described in samples collected from the comet Wild-2 (Rietmeijer, et al 2008), in iron-rich meteorites, and lunar impact environments. Such lunar impact iron-silicides were identified by Spicuzza et al. (2011) in a shocked plagioclase grain (grain A 6-8) from Apollo 16 lunar regolith sample 61501,22. However, due to the small size of the iron silicides (0.1-2 µm) chemical analyses if the Fe-Si compounds was not possible with conventional EPMA (15 keV). When soft X-ray EPMA (5 keV) was attempted on these lunar Fe-Si compounds, highly erroneous analyses were produced, both by standards-based EDS on an SEM and WDS on an electron microprobe.

Interest in Fe L lines is nothing new in EPMA. Early interest focused upon changes in peak shape and position between Fe metal and Fe oxides (Fischer, 1965). Anderson (1967) in a review of soft X-ray EPMA, included a study of the use of three Fe L lines: Fe-Lα, Fe-Lβ, and Fe-Ll. He used pure Fe and Fe_3O_4 standards to quantify the Fe in two Fe oxides, FeS_2 and Fe_3C, and noted major problems. O'Nions and Smith (1971) evaluated Fe Lα - Lβ spectra of a variety of minerals with different oxidation states in the hope of using EPMA to easily determine Fe^{3+}/Fe^{2+} ratios. The results were not encouraging. All of these studies refer to the issue of carbon contamination and of surface artifacts having a deleterious role. They have ranged from describing the detailed electron structure of iron compounds, to being able to determine the ferrous to ferric iron ratio in minerals of interest to geologists.

Methods

Analyses were first conducted at the Eugene Cameron Electron Microprobe Laboratory (UW Madison) using a CAMECA SX-51 electron microprobe (W filament source, operated at 5 keV) and Probe for EPMA software (Donovan et al., 2012). Initial data obtained on the Fe-Si reference materials (mounted in epoxy and coated with an ~200 Å carbon coating) using the Fe Lα and Si Kα lines returned ~120 wt.% totals. In each case the Fe wt.% was anomalously ~20 wt.% high). In all cases we used the same high purity metals as standards (99.99 % Fe, and 99.9 % Si). The metal standards were mounted in each Fe-Si block. To validate the high wt.% totals, a sample mount with the Fe-Si reference materials was sent to the University of Barcelona to be analyzed there on a CAMECA SX-50. Also, the reference materials, as well as the lunar grain, were analyzed on the prototype CAMECA SX-5 FE, located in Fitchburg, Wisconsin, at the time. Similar erroneous results were obtained on all machines.

Our approach was to obtain several synthetic Fe-silicides with well determined compositions, then study the possible factors involved in the inaccurate Fe compositional determinations, initially focusing on (1) chemical peak shifts, (2) comparing usage of the 3 possible crystal diffractors: TAP, PC0, PC1 (count rates versus spectral resolution), and (3) MACs.

The Fe-Si samples had to be large enough to be analyzed with a tungsten source. Some were supplied by a colleague (Heikinheimo, E., Aalto University, Espoo, Finland). Others were synthesized in the UW-Madison Departments of Material Science and Chemistry. Fe:Si ratios in the synthetic samples were chosen to ensure that the full range of compositions in the Fe-Si

system were covered. Samples were first weighed as a powder, using reagent grade material, then pressed into pellets. The pellets were then transferred to an arc-melter, where the samples were arc-melted three times. The entire procedure (weighing, pressing, and arc melting) was carried out in an argon-filled glove-box to minimize oxidation.

Multiple samples of each phase were synthesized. The samples were annealed at either 900°C or 1125°C for a month at a time until each sample was deemed fully homogenous (figure 5). After each month of annealing one of the samples from each phase was quenched, cut in half, and checked with high contrast backscattered electron imaging (on a Hitachi S3400-N scanning electron microscope) to verify phase homogeneity. The reference materials were then analyzed with the UW Madison CAMECA SX-51 at 15 keV to determine the composition of the reference materials, as there is some solid solution in some of the phase fields.

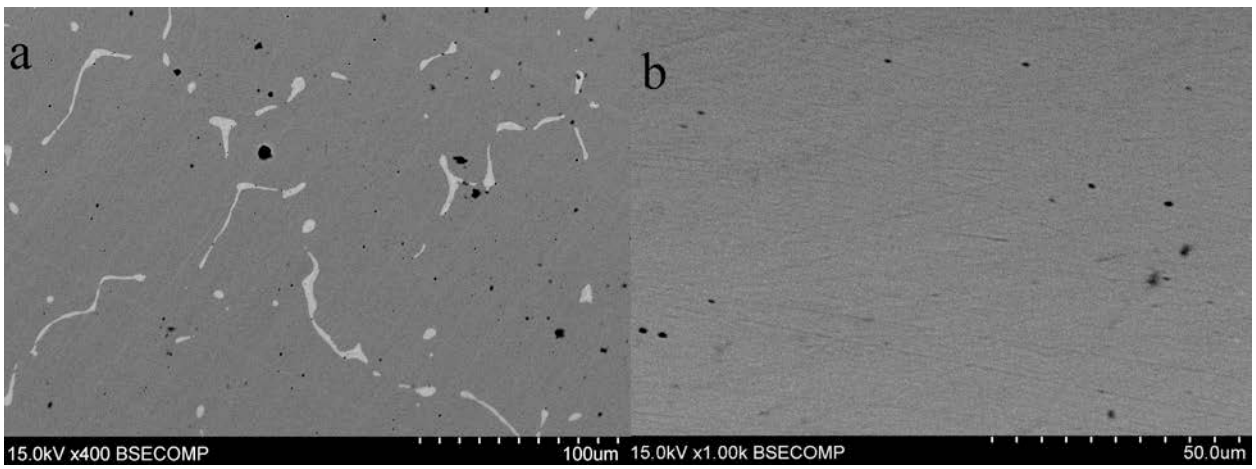

Figure 5: BSE images of FeSi after 1 week (a) and 4 weeks (b) annealing at 1100°C.

The Fe-Si reference materials mounted in electrically conductive indium (so as the samples could remain uncoated) were then quantitatively analyzed using 5 keV/100 nA using both the Fe Lα and Lβ lines. By analyzing an uncoated sample at 100 nA with short count times (20 seconds on peak/ 10 seconds on the background) we avoided most of the time dependent effects of the carbon buildup. Alternatively a time dependent intensity (TDI) correction, such as that used in the Probe for EPMA software (Donovan et al., 2012) could be used; however it was not needed in the case of our analyses because of the care taken to avoid carbon coated samples. The iron wt.% was closer to the nominal composition, but still high (Table 1).

Fialin et al. (1998) suggested the use of Ll and Lη lines, as alternatives to the normally used Lα and Lβ lines. As none of the commercially available electron probe software allows for the use of Ll-η lines for quantitative analysis, an alternative method was used to test the feasibility of the Fe Ll line for quantitative EPMA. The raw counts were obtained on the UW Madison CAMECA-SX 51, using the Probe for EPMA software, and “mispeaking” the Fe Lα line on the Ll line. The K-ratios obtained were then run through the Pouchou and Pichoir (PAP) model (Pouchou and Pichoir, 1984) matrix corrections in "Son of Desktop Spectrum Analyzer" (DTSA II) (Ritchie, 2009). The quantification tool in DTSA II does not allow for use of Ll lines; however, in the newest version of the software (Gemini), a command window is available for implementing a desired code. Phillippe Pinard at RTWH Aachen (Germany), wrote a script for

DTSA II that allowed the quantification of Ll lines. This code was then used to determine the compositions of our Fe-Si compounds, with the K-ratios determined in Probe for EPMA.

After the groundwork to develop the technique to analyze sub-micron phases, we were able to analyze lunar Fe-Si using a JEOL 8530 FE at the RWTH University Aaachen and another JEOL 8530 FE at ExxonMobil Research and Engineering Corporation. Care was taken to reduce the carbon contamination on the sample prior to analysis, because we were interested in the carbon concentration in the Fe-Si blebs.

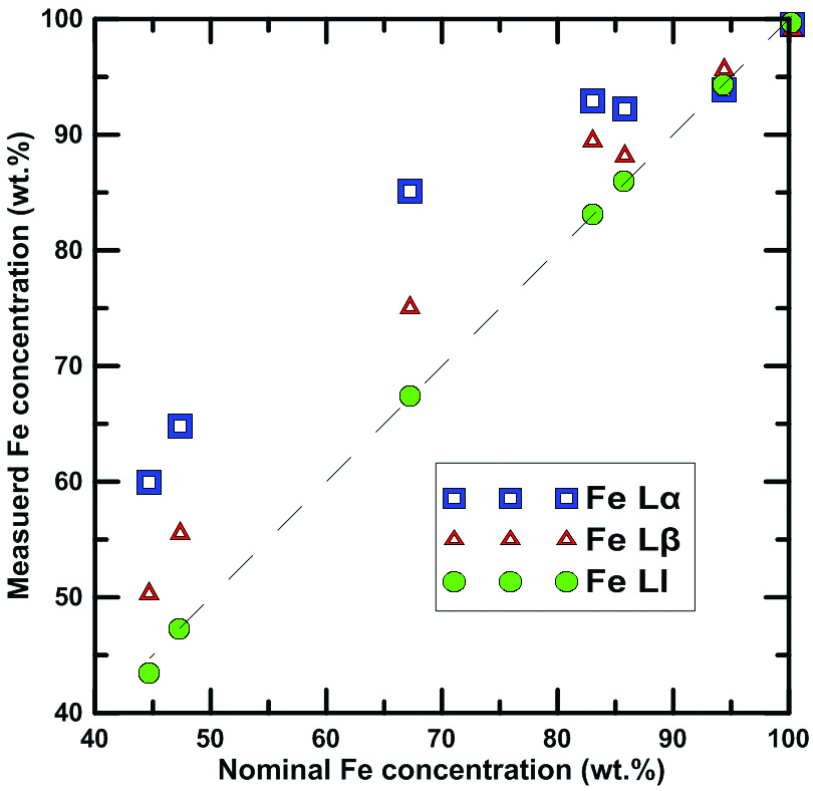

Figure 6: Measured at low voltage versus nominal (as measured at 15 keV with Fe Kα; dashed line) Fe concentrations obtained on the various Fe-Si reference materials, in the epoxy mount coated with platinum. Fe Lα and Lβ were acquired and quantified in Probe for EPMA, using the full PAP matrix correction. Fe Ll was acquired in Probe for EPMA, but quantified in DTSA II using the PAP model.

Results

Table 1 shows the results of using the Fe Lα, Lβ, and Ll lines, as well as different MACs, for the analysis of Fe-Si compounds, at 5 keV. The data with the greatest deviation from the nominal composition is that acquired with the Fe Lα line. The Fe Lβ line gives Fe wt.% closer to nominal, but still off by over 10 wt.% for Fe30Si70. The Si wt.% obtained at 5 keV are systematically higher than those obatined at 15 keV by a factor ranging from 1.03-1.05, except for the Fe90Si10 alloy. This discrepancy is probably due to measurement difficulty combined with a change in the matrix correction with the incorrect Fe concentration. The effect of using different MACs is noticeable (~ 2 wt% difference in Fe counts), but is not enough to correct for the large errors in Fe numbers using the Fe Lα and Lβ lines. Using the Fe Ll line (L_3-M_1 transition), in conjunction with the DTSA II, for quantitative analysis gives compositions closer to the nominal values, even whilst using pure metals as standards.

At %	Wt %	Wt%15keV		Lα			Lβ			Ll		
			MAC	**Fe wt%**	**Si wt%**	**Total wt%**	**Fe wt%**	**Si wt%**	**Total wt%**	**Fe wt%**	**Si wt%**	**Total wt%**
Fe90 Si10	Fe94.71 Si5.20	Fe95.13 Si5.23	Henke	94.22	4.95	99.17	X	X	X	X	X	X
			Heinr.	94.21	4.95	99.16	95.50	5.04	100.53	94.37	4.99	99.36
			Chant.	94.26	4.95	99.21	95.89	5.04	100.92	94.33	4.95	99.28
			Sokar.	93.87	4.95	98.82	95.64	5.04	100.68	X	X	X
			Gopon	93.86	4.95	98.81	94.80	5.04	99.84	X	X	X
Fe75 Si25	Fe85.64 Si14.36	Fe85.08 Si13.34	Henke	93.16	13.85	107.02	X	X	X	X	X	X
			Heinr.	93.16	13.85	107.01	87.76	14.26	102.02	86.14	13.99	100.13
			Chant.	93.27	13.85	107.13	88.81	14.26	103.07	86.01	13.87	99.88
			Sokar.	92.28	13.85	106.13	88.15	14.26	102.42	X	X	X
			Gopon	92.27	13.85	106.12	85.84	14.26	100.11	X	X	X
Fe70 Si30	Fe82.27 Si17.73	Fe82.97 Si16.34	Henke	93.97	17.03	111.01	X	X	X	X	X	X
			Heinr.	93.97	17.03	111.00	88.94	18.22	107.16	83.25	17.21	100.46
			Chant.	94.11	17.03	111.14	90.26	18.22	108.48	83.11	17.07	100.18
			Sokar.	92.92	17.04	109.96	89.44	18.22	107.66	X	X	X
			Gopon	92.91	17.04	109.95	86.53	18.22	104.75	X	X	X
Fe50 Si50	Fe66.54 Si33.46	Fe67.23 Si31.21	Henke	86.80	32.99	119.79	X	X	X	X	X	X
			Heinr.	86.79	32.99	119.78	74.25	34.40	108.65	67.57	33.45	101.02
			Chant.	87.01	32.99	120.00	76.45	34.39	110.85	67.37	33.22	100.59
			Sokar.	85.11	33.01	118.12	75.08	34.40	109.48	X	X	X
			Gopon	85.09	33.01	118.10	70.09	34.42	104.51	X	X	X
Fe33 Si67	Fe49.82 Si50.18	Fe47.35 Si50.17	Henke	66.88	52.51	119.39	X	X	X	X	X	X
			Heinr.	66.86	52.51	119.38	54.47	53.93	108.41	47.41	53.31	100.72
			Chant.	67.13	52.51	119.64	57.23	53.90	111.13	47.23	53.06	100.29
			Sokar.	64.85	52.56	117.41	55.53	53.92	109.44	X	X	X
			Gopon	64.83	52.56	117.39	49.25	54.00	103.25	X	X	X
Fe30 Si70	Fe46.01 Si53.99	Fe44.67 Si53.66	Henke	61.96	55.96	117.92	X	X	X	X	X	X
			Heinr.	61.94	55.96	117.90	47.86	56.57	104.43	43.62	56.78	100.40
			Chant.	62.21	55.96	118.17	50.54	56.53	107.06	43.45	56.54	99.99
			Sokar.	59.94	56.02	115.96	50.36	57.25	107.60	X	X	X
			Gopon	59.53	56.02	115.55	42.79	56.65	99.44	X	X	X

Table 1: Comparison of Fe Lα, Lβ, and Ll and the effect of different MACs for quantitative EPMA at 5 keV. Fe Lα and Lβ were acquired and quantified in Probe for EPMA, using the full PAP matrix correction. Fe Ll was acquired in Probe for EPMA, but quantified in DTSA II using the full PAP matrix correction. The Ll data only shows results for Heinrich and Chantler because DTSA II only allows for use of those two MAC tables. At the top of each composition(black background) is both the nominal composition of the phase (left), and the composition as measured at 15 keV (right) using the Fe Kα line with the LIF crystal, the PAP matrix correction, and the Chantler MACs. All data was acquired on a platinum coated block of our Fe-Si standards, with the exception of the 15 keV data which was acquired in the same block when it had a carbon coating.

Figure 6 graphically shows the improvement in the measurements, using the various Fe L lines. One possible explanation for the better results obtained by using the Fe Ll line is that this line is the furthest L line away from the L_3 absorption edge (figure 3), and unlike the Lβ line, it has a relatively low MAC, and should not be affected by near-edge absorption effects. Moreover, the L_3-M_1 transition involves electron orbitals other than the 3d which are not involved in chemical bonding (figure 2), thus keeping an "atomic-like" character.

The Fe Ll X-ray lines do not yield high count rates (relative to those of Fe Lα/Lβ). Low count rates mean that either more current or longer counting times (or both) must be used to get statistically significant data. Longer counting times and higher currents lead to larger surface effects being produced over the course of the analysis. This may lead to changing counts on the various samples. Given that the Fe Lη (L_2-M_1 transition) has virtually the same character as that of the Ll line, their combination should not be critical. Even though the Fe Ll line has the lowest count rates out of the three possibilities being investigated (Lα, Lβ, and Ll lines), it appears to be the best X-ray line for quantitative EPMA at low voltage. Fialin et al (1998) however, already made the prescient suggestion related to the transition metals, that "Despite their low intensities, the 'atomic' Ll -η peaks (3s-2p transition) are more convenient [than Lα-β] for those applications to [EPMA] practice."

Figure 7 shows the results of our EPMA data acquired on the JEOL 8350 FE. We found appreciable carbon concentrated in the Fe-Si blebs. Due to concern over contamination we do not know exactly how much carbon is present in the Fe-Si, but the X-ray maps of carbon clearly show that the carbon is concentrated in the Fe-Si. While iron metal is common on the moon as a product of micro-meteorite impacts, the conditions for silicon metals and iron-silicides to occur are an order of magnitude more reducing. The presence of carbon would explain how such a highly reduced phase could have formed on the moon. A carbonaceous impactor is a likely scenario as to how the carbon ended up in the Fe-Si blebs. The meteorite would have impacted the lunar surface and locally vaporized the lunar surface. The vacuum of the lunar environment would have reduced the vapor cloud to a large degree, but the presence of carbon in the vapor would have scavenged the remaining oxygen and allowed for the extreme reducing conditions required to form the iron-silicides.

Conclusions

Currently one of the factors holding back full application of the low voltage, high spatial resolution EPMA (e.g. field emission EPMA) is the "energy barrier" raised by usage of the traditional X-ray analytical lines, e.g. Fe Kα. We have demonstrate that non-traditional lines such as Fe Ll-η can provide significant improvements in EPMA of iron silicides at low voltages. Additionally, fully quantitative EPMA using standards with un-normalized totals must be utilized as the analytical total is a critical tool for quality control of micro-analytical results. Using this new technique for analysis of sub-micron phases we were able to quantitatively measure the Fe-Si blebs and determine that they contained an appreciable amount of carbon. This finding provides new interesting insight into lunar geology.

Table 2: Results of quantitative analysis on Fe-Si blebs in lunar grain A6-8. Note the carbon measurements in blebs 1-5 are compromised because of contamination.

Bleb #	Fe	Si	Ni	Al	C	P	S	Total
1	47.10	27.68	5.91	0.63	17.81	0.14		99.26
2	30.28	40.44	3.77	1.63	23.37	0.11		99.59
3	35.97	43.31	4.45	0.69	17.63	0.13		102.18
4	41.44	48.98	2.80	0.61	4.70	0.20	0.05	98.78
5a	26.77	50.30	6.83	1.02	9.53	2.22	0.13	96.81
5b	0.00	91.19	0.03	0.88	15.08	0.74	0.04	107.96
6	0.00	97.48	0.00	0.16	2.90	0.88	0.00	101.41
7	0.00	97.25	0.09	0.16	4.30	1.20	0.04	103.03
8	37.04	50.87	3.58	2.39	4.47	1.27	0.06	99.68
9	32.57	49.24	12.50	1.14	3.17	0.48	0.02	99.12
10	34.10	51.89	8.38	0.83	2.87	0.70	0.07	98.85
11	0.00	94.33	0.18	0.29	19.42	1.22	0.03	115.46
12a	0.00	101.38	0.10	0.29	4.21	0.97	0.04	106.99
12b	35.68	53.09	4.43	0.32	7.50	3.55	0.02	104.59
13a	39.79	55.38	4.53	0.73	4.64	0.83	0.01	105.91
13b	0.00	95.75	0.11	0.86	15.19	0.69	0.04	112.64
14a	39.89	54.09	3.93	0.92	5.83	0.41	0.03	105.10
14b	37.65	54.06	3.60	0.80	7.30	0.12	0.03	103.55
15	25.52	50.23	27.76	1.18	5.84	1.38	0.09	111.99
16	14.86	50.61	23.98	1.55	4.19	0.69	1.93	97.81
17	25.22	50.95	9.97	2.57	4.75	1.60	0.11	95.17

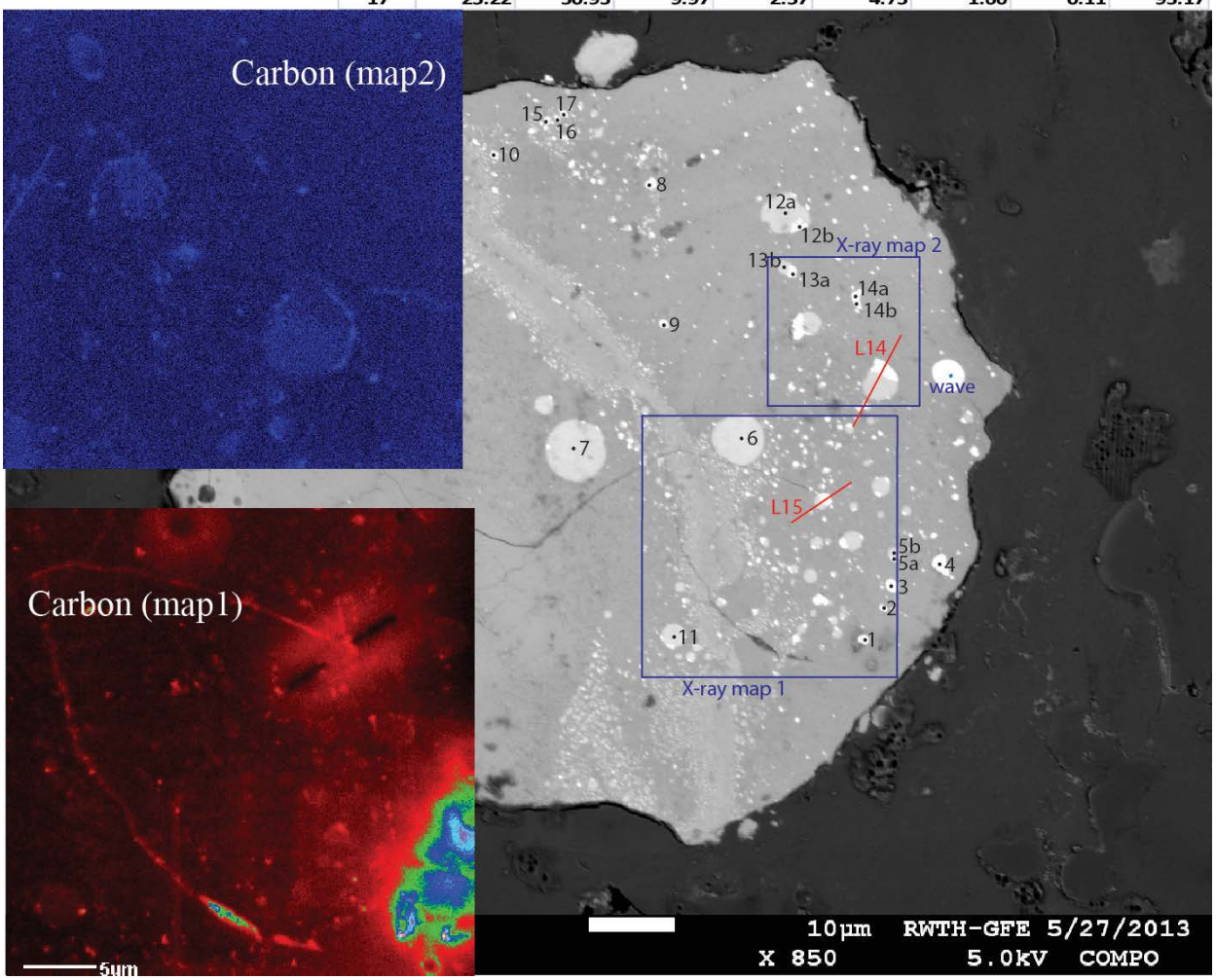

Figure 7: BSE image of lunar grain A6-8 showing location of quantitative analyses as well as locations of X-ray maps, with the carbon maps for each shown on the left.

References

ANDERSON, C. A. (1967). The quality of x-ray microanalysis in the ultra-soft x-ray region. *Bri. J. Appl. Phys.* **18**, 1033–1043.

ANAND, M., TAYLOR, L. A., NAZAROV, M. A., SHU, J., MAO, H.K., & HEMLEY, R. J. (2004). Space weathering on airless planetary bodies: clues from the lunar mineral hapkeite. *Proc. Natl. Acad. Sci. U. S. A.* **101**, 6847–51.

ARMSTRONG, J. (2011). Low voltage and low overvoltage X-ray nanoanalysis with field emission electron microprobes and SEMs: Problems in quantitation for first-row transition elements. 2011 AGU Fall Meeting, San Francisco, CA.

CASTAING, R. (1951). Application of electron probes to local chemical and crystallographic analysis. Thesis, University of Paris 1951 Publication *O.N.E.R.A No*. **55** (1952).

CHANTLER, C. T., OLSEN, K., DRAGOSET, R.A., CHANG, J., KISHORE, A.R., KOTOCHIGOVA, S.A., ZUCKER, D.S. (2005). X-ray form factor, attenuation, and scattering tables. Retrieved from www.nist.gov/pml/data/ffast/index.cfm.

DONOVAN, J.J., KREMSER, D., FOURNELLE, J., & GOEMANN, K. (2012), *Probe for EPMA: Users Guide and Reference.* 438 pp. *Available online as pdf at ProbeSoftware.com.*

DROUIN, D., COUTURE, A. R., JOLY, D., TASTET, X., AIMEZ, V. & GAUVIN, R. (2007). CASINO V2.42: a fast and easy-to-use modeling tool for scanning electron microscopy and microanalysis users. *Scanning* **29**, 92–101.

ESSENE, E. J. & FISHER, D. C. (1986). Lightning strike fusion: extreme reduction and metal-silicate liquid immiscibility. *Science (New York, N.Y.)* **234**, 189–93.

FIALIN, M., WAGNER, C., REMOND, G. (1998). X-ray emission valence band spectrometry: application to cu and fe L-series. In *EMAS **98***, 129–140.

FISCHER, D. W. & BAUN, W. L. (1967). Self-absorption effects in the soft X-Ray Mα and Mβ emission spectra of the rare earth elements. *J. Appl. Phys.* **38**, 4830–4836.

GOPON, P., FOURNELLE, J., LLOVET, X. (2012). Soft X-ray EPMA of submicron phase lunar Fe-Si compounds**:** *Microsc. Microanal.***18** (Suppl 2) 1728-1729.

GOPON, P., SOBOL, P.E. (2012). Non-sequential spectral acquisitions to remove time or dose dependent effects. *Unpublished report.*

HEINRICH, K.F.J., (1987). Mass attenuation coefficients for electron microprobe microanalysis. in *Proc. 11th ICXOM*, 67-119.

HEINRICH, K. F. J. (1964). X-ray absorption uncertainty. In McKinley T.D., ed., *The electron microprobe*, 296–377. New York: John Wiley & Sons.

HENKE, B.L., LEE, P., TANAKA, T.J., SHIMABUKRO, R.L., FIJIKAWA, B.K. (1982) *Atomic Data Nucl. Data Tables* **27**, 1.

HENKE, B. L., WHITE, R. & LUNDBERG, B. (1957). Semi-empirical determination of mass absorption coefficients for the 5 to 50 angstrom X-Ray region. *J. Appl. Phys.* **28**, 98.

LLOVET, X., HEIKINHEIMO, E., NÚÑEZ, A., MERLET, C., ALMAGRO, J., RICHTER, S., FOURNELLE, J. & VAN HOEK, C. (2012). An inter-laboratory comparison of EPMA analysis of alloy steel at low voltage. In *IOP Conf. Ser.: Mater. Sci. Eng*. **32**. 1-14.

MACKENZIE, A.P. (1993). Recent progress in electron-probe microanalysis. *Rep. Prog. Phys.* **56**, 557–604.

O'NIONS, R.K., SMITH, D.G.W. (1971) Investigation the $L_{II, III}$ emission spectra of Fe by electron microprobe: Part 2. The Fe $L_{II, III}$ spectra of Fe and Fe-Ti oxides, *Am. Mineral.*, **56**, 1452-1455.

POUCHOU, J. L. (1996). Use of soft X-rays in microanalysis. *Mikrochim. Acta (Suppl.)* **12**, 39–60.

POUCHOU, J. L., PICHOIR, F., & BOIVIN, D. (1990). XPP procedure applied to quantitative EDS x-ray analysis in the SEM," in *Microbeam Analysis* (San Francisco, San Francisco), pp. 120–126.

POUCHOU, J. L., PICHOIR, F., (1984). A New Model for Quantitative X-Ray Microanalysis. I.--Application to the Analysis of Homogeneous Samples. *Rech. Aerosp.*, (3), 167-192.

RIETMEIJER, F., NAKAMURA, T., TSUCHIYAMA, A., UESUGI, K., NAKANO, T. & LEROUX, H. (2008). Origin and formation of iron silicide phases in the aerogel of the Stardust mission. *Meteoritics and Planet. Sci.* **1/2**, 121–134.

RITCHIE, N.W.M. (2009). Spectrum simulation in DTSA-II. *Microsc. Microanal.* **15,** 454-468.

SOKARAS, D., KOCHUR, A., MÜLLER, M., KOLBE, M., BECKHOFF, B., MANTLER, M., ZARKADAS, C., ANDRIANIS, M., LAGOYANNIS, A. & KARYDAS, A. (2011). Cascade L-shell soft-x-ray emission as incident x-ray photons are tuned across the 1s ionization threshold. *Phys. Rev. A* **83**, 1–12.

SPICUZZA, M. J., VALLEY, J. V., FOURNELLE, J., HUBERTY, J. M. & TREIMAN, A. (2011). Native silicon and Fe-silicides from the Apollo 16 lunar regolith: Extreme reduction, metal-silicate immiscibility, and shock melting. In *42nd Lunar and Planet. Sci. Conf. (2011)* **97**, 16–17.

Coacervates as Prebiotic Reactors

Vera Kolb

Department of Chemistry

University of Wisconsin-Parkside, Kenosha, WI 53141-2000

Abstract

In this work we summarize the important findings about coacervates as prebiotic reactors. We have found out that it is possible to run a chemical reaction in a coacervate, which fulfills the early predictions by Oparin that coacervates may have been the original prebiotic reactors. We have prepared two types of coacervates and have found that Passerini reaction in water occurs in both of them.

Introduction and Objectives

Coacervates are important for astrobiology. Specifically, they would be of interest based on the Goal #3, Objectives 3.4, on the "Origins of cellularity and protobiological systems", from the NASA's Astrobiology Road Map (http://astrobiology.arc.nasa.gov/roadmap/g3.html) (Des Marais et al., 2008). Coacervates are aqueous colloidal systems. They are initially composed of droplets, which eventually equilibrate to form two layers. These are the colloid-rich layer, so-called coacervate, and the colloid-poor layer, known as the equilibrium liquid or supernatant. The two layers, both of which are aqueous, are immiscible (Coacervate, 2011; Creating Coacervates, Flammer web site; Menger and Sykes, 1998).

Prebiotic importance of coacervates was proposed by Oparin in 1924. The typical macromolecular components of Oparin's coacervates were polypeptides and polysaccharides (Evreinova et al, 1973, 1974, 1975, 1977; Gladilin et al, 1978; Oparin, 1967, 1968, 1969; Oparin and Gladilin, 1980; Walde et al., 1994). The coacervates droplets made from these materials give appearance of amoeba-like objects, which change shape, form "vacuoles", release "vacuole contents", flow, merge, divide and show other life-like properties. It should be pointed out that in those early days DNA has not been discovered and that the origin of life was thought to be protein based. Among the most studied features of coacervates is their ability to grow and to mimic self-reproduction, by splitting into the "daughter cells (Creating Coacervates, Flammer web site; Evreinova et al, 1973, 1974, 1975, 1977; Gladilin et al, 1978; Oparin, 1967, 1968, 1969; Oparin and Gladilin, 1980; Walde et al., 1994). According to Oparin, various organic reactions could occur inside coacervates. The coacervates which are able to utilize the organic materials from the environment more efficiently than others would survive better. Thus, a primitive selection could occur which would favor such coacervates. The coacervate systems have been studied also more recently (Burgess 1990; Burgess et al., 1991; Burgess and Singh 1993; Dubin et al., 2008; Liberatore et

al., 2009; Menger 2002, 2011; Menger et al., 2000; Menger and Sykes, 1998; McClements et al., 2009; Rabiskova et al., 1994; Singh and Burgess, 1989; Stuart et al, 1998; Wang et al, 1999, 2000), but not in the prebiotic context.

Results

Our preliminary results were published (Kolb et al., 2012). We give here a summary of our published results and add new findings which we have not published yet.

We have prepared two types of coacervates. The first type was Oparin's and the second one was based on AOT, a surfactant. Oparin's coacervate was prepared by the experimental procedures by Flammer (Creating Coacervates, Flammer web site) and the AOT coacervate by the preparation published by Menger and Sykes (Menger and Sykes, 1998). We show below the structure of the AOT in Fig. 1.

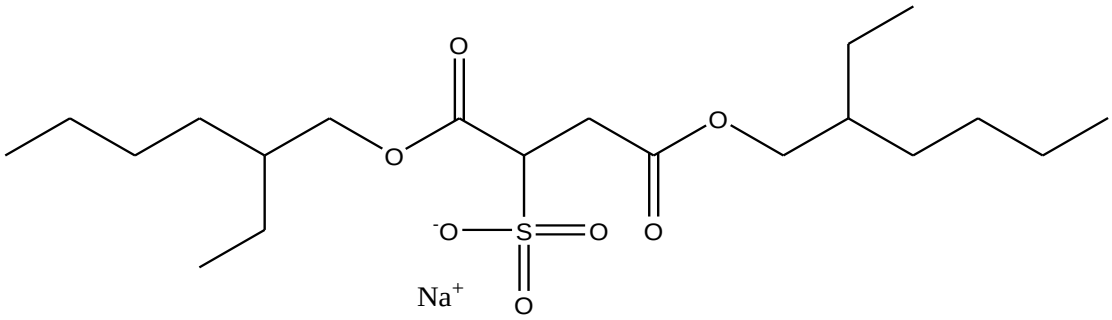

Figure 1. Structure of AOT, Dioctyl sodium sulfosuccinate

The reason why we sought a coacervate different than Oparin's is because polysaccharides which were used in the Oparin's coacervates cannot be prepared prebiotically. In contrast, AOT molecule has all the functional groups and required chemical bonds that have ample precedent in the prebiotic world.

We have chosen Passerini multicomponent reaction (Hooper and DeBoef, 2009) to test the proposal that coacervates could be used as prebiotic reactors. The reasons for this choice are multiple. Firstly, all the components in the Passerini reaction are prebiotically feasible compounds. The same is the case for the product. Secondly, the reactants, although not water soluble, do react in water and they give a single product. Finally, the Passerini reaction has been studied extensively for its pharmaceutical applications. Thus, we could devote our time to running the reaction in coacervates, rather than having to study the reaction nuts and bolts from the beginning. The reaction scheme for the Passerini reaction is shown below, in Fig. 2.

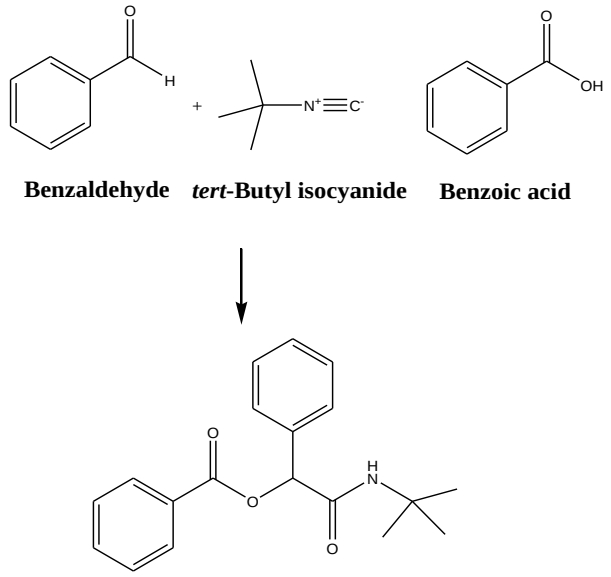

Figure 2. The aqueous Passerini reaction which was used in this study.

The reaction product is a white solid. It was isolated from the coacervate layer, and was washed, dried and analyzed. It is a pure product, which had melting point and IR (Infra-red spectrum) the same as those described in the literature.

The details and procedures of our work are described in our recent publication (Kolb et al., 2012).

Our new and so far unpublished results are concerned with the kinetics of Passerini reaction in the coacervate layer as compared to the equilibrium layer. The research question was if the Passerini reaction will be faster or slower in the coacervate as compared to the equilibrium liquid and pure water. We have obtained preliminary results and the study is in progress. First, we had to slow down the Passerini reaction, since it was too fast already in water, outside the coacervate or equilibrium layer, for us to measure even the relative rates accurately. Addition of additives, such as methanol and salts did slow down the Passerini reaction sufficiently for the measurements to become more reliable. We have added these additives into the Passerini reaction mixture before we transferred it to the coacervate or equilibrium layer. We have prepared coacervates with the same amounts of methanol and salt to match those added to the Passerini reaction mixture. We have improved on the quality of the measurements. We still need to address the fact that AOT and salt are found in the coacervate and equilibrium layer in different concentrations. This is due to the nature of the coacervate preparation. The difference in these concentrations is also expected to be reflected in the rate of the Passerini reaction. We need to measure these differences accurately and set up controls for them in respect to the Passerini reaction. The

preliminary work is described in the Undergraduate Senior Thesis by Armando Ramirez, from UW-Parkside, who has worked in our research group for two semesters.

Acknowledgments

Wisconsin Space Grant Consortium has sponsored this work. UW-Parkside has supported Armando Ramirez via URAP (Undergraduate Research Apprenticeship Program) for two semesters. Both sponsors are gratefully acknowledged.

References

Burgess, D. J., "Practical Analysis of Complex Coacervate Systems", J. Colloid and Interface Sci., *140*, 227-238 (1990).

Burgess, D. J., Kwok, K. K., and Megremis, P. T., "Characterization of Albumin-Aacacia Complex Coacervation", J. Pharm. Pharmacol., *43*, 232-236 (1991).

Burgess, D. J., and Singh, O. N., "Spontaneous Formation of Small Sized Albumin/acacia Coacervate Particles", J. Pharm. Pharmacol., *45*, 586-591 (1993).

"Coacervate", Wikipedia, en.wikipedia.org/wiki/Coacervate, last modified on November 21, 2011.

"Creating Coacervates", adapted by L. Flammer, www.indiana.edu/~ensiweb/lessons/coac.lab.pdf

Des Marais, D. J.; Nuth III, J. A.; Alamandola, L. J.; Boss, A. P.; Farmer, J. D.; Hoehler, T. M.; Jakosky, B. M.; Meadows, V. C.; Pohorille, A.; Runnegar, B.; Spormann, A. M. The NASA Astrobiology Roadmap. Astrobiology, *8*, 715-730 (2008). See also: http://astrobiology.arc.nasa.gov/roadmap/g3.html

Dubin, P. L., Li, Y., and Jaeger, W., "Mesophase Separation in Polyelectrolyte-Mixed Micelle Coacervates", Langmuir, *24*, 4544-4549 (2008).

Evreinova, T. N., Mamontova, T. W., Karnauhov, V. N., Stephanov, S. B., and Hrust, U. R., "Coacervate Systems and Origins of Life", Origins of Life, *5*, 201-205 (1974).

Evreinova, T. N., Mel'nikova, E. V., Allakhverdov, B. L., and Karnaukhov, V. N., "Coexistence of Coacervate Systems with Different Chemical Composiiton", Zhurnal Evolyutsionnoi Biokhimii i Fiziologii, *13*, 330-335 (1977).

Evreinova, T. N., Mel'nikova, E. V., Pogorelov, A. G., and Allakhverdov, B. L. "Stabilization and Coexistence of Coacervate Systems of Different Chemical Composition", Doklady Akademii Nauk SSSR, *224*, 239-241 (1975).

Evreinova, T. N., Stefanov, S. B., and Marmontova, T. V., "Structure of Coacervate Drops in an Electron Microscope", Doklady Akademii Nauk SSSR, *208*, 243-244 (1973).

Gladilin, K. L., Orlovsky, A. F., Kirpotin, D. B., and Oparin, A. I., "Coacervate Drops as a Model for Precellular Structures", Origins of Life, Proc. ISSOL Meet. 2nd, 357-362 (1978).

Hooper, M. H., and DeBoef, B., "A Green Multicomponent Reaction for the Organic Chemistry Laboratory, The Aqueous Passerini Reaction", J. Chem. Ed., *86*, 1077-1079 (2009).

Kolb, V. M., Swanson, M., and Menger, F. M., "Coacervates and their Prebiotic Potential", in "Instruments, Methods, and Missions for Astrobiology XV", R. B. Hoover, G. V. Levin, and A. Y. Rozanov, Eds., Proc. of SPIE, Vol. 8521, pp. 85210E pp.1-8 (2012).

Liberatore, M. W., Wyatt, N. B., Henry, M., Dubin, P. L., and Foun, E., "Shear-Induced Phase Separation in Polyelectrolyte/Mixed Micelle Coacervates", Langmuir, *25*, 13376-13383 (2009).

Menger, F. M., "Remembrances of Self-Assemblies Past", Langmuir, *27*, 5176-5183 (2011).

Menger, F. M., "Supramolecular Chemistry and Self-Assembly", PNAS, *99 (8)*, 4818-4822 (2002).

Menger, F. M., and Sykes, B. M., "Anatomy of a Coacervate", Langmuir, *14*, 4131-4137 (1998).

Menger, F. M., Peresypkin, A. V., Caran, K. L., and Apkarian, R. P., "A Sponge Morphology in an Elementary Coacervate", Langmuir, *16*, 9113-9116 (2000).

McClements, D. J., Decker, E. A., Park, Y., and Weiss, J., "Structural Design Principles for Delivery of Bioactive Components in Nutraceuticals and Functional Foods", Critical Rev. in Food Sci. and Nutrition, *49*, 577-606 (2009).

Oparin, A. I., "The Origins of Life", Reprinted from Bernal, J. D., "Origins of Life", London: Weidenfeld & Nicolson, 1967, pp. 199-234, in "Origins of Life: the central concepts", Deamer, D. W., and Fleishaker, G. R., Eds., Jones and Bartlett Publ., Boston, MA, 1994, pp. 31-71.

Oparin, A. I., "Chemistry and the Origin of Life", RIC Reviews, *2*, 1-12 (1969), Published on 01 January 1969 on http://pubs.rsc.org/doi:10.1039/RR9690200001

Oparin, A. I., "Genesis and Evolutionary Development of Life", Academic Press, New York, 1968, pp. 101-126.

Oparin, A. I., and Gladilin, K. L., "Evolution of Self-Assembly of Probionts", BioSystems, *12*, 133-145 (1980).

Rabiskova, M., Song, J., Opawale, F. O., and Burgess, D. J., "The Influence of Surface Properties on Uptake of Oil into Complex Coacervate Microcapsules", J. Pharm. Pharmacol., *46*, 631-635 (1994).

Singh, O. N., and Burgess, D. J., "Characterization of Albumin-Alginic Acid Complex Coacervation", J. Pharm. Pharmacol., *41*, 670-673 (1989).

Stuart, M. A. C., Besseling, N. A. M., and Fokking, R. G., "Formation of Micelles with Complex Coacervate Cores", Langmuir, *14*, 6846-6849 (1998).

Walde, P, Goto, A., Monnard, P-A., Wessicken, M., and Luisi, P. L., "Oparin's Reactions Revisited: Enzymatic Synthesis of Poly(adenylic acid) in Micelles and Self-Reproducing Vesicles, J. Amer. Chem. Soc., *116*, 7541-7547 (1994).

Wang, Y., Kimura, K., Dubin, P. L., and Jaeger, W., "Polyelectrolyte-Micelle Coacervation: Effects of Micelle Surface Charge Density, Polymer Molecular Weight, and Polymer/Surfactant Ratio", Macromolecules, *33*, 3324-3331 (2000).

Wang, Y., Kimura, K., Huang, Q., Dubin, P. L., and Jaeger, W., "Effect of Salt on Polyelectrolyte-Micelle Coacervation", Macromolecules, *32*, 7128-7134 (1999).

23rd Annual Conference
Part Five

Team Projects

2013 Payload Team Report

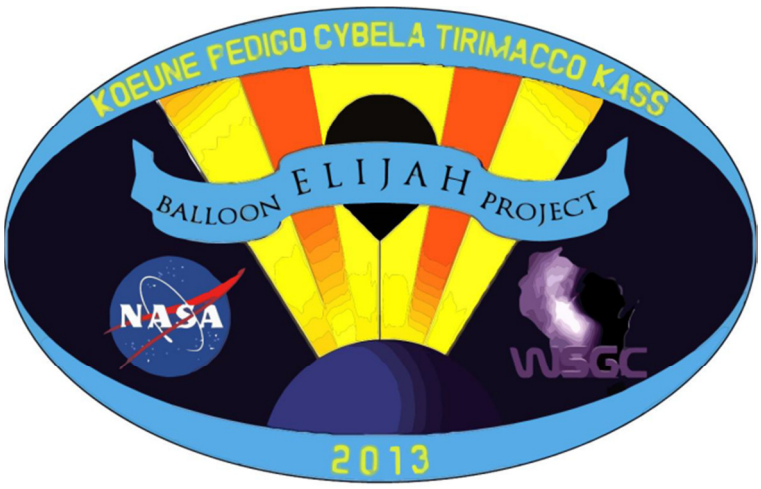

2013 Elijah High Altitude Balloon Payload Team

Trent Cybela, Daniel Kass, Amber Koeune, Nathaniel Pedigo, and Alana Tirimacco

Faculty Advisor: Dr. William Farrow

Wisconsin Space Grant Consortium

August 16, 2013

Executive Summary

Over the past ten weeks, the payload team for the Elijah High Altitude Balloon Project has researched, designed, and constructed a scientific payload that would fly to the edges of space and gather data advancing the team's knowledge of Earth sciences, aerospace sciences, and aerospace engineering. The payload packages consisted of a sensor suite, telemetry system, Geiger counter, and camera. The telemetry system was able to provide a live data feed that interacted with existing networks to record data acting as a proof of the concept that a similar system would be viable and even suggested for future teams. The sensor suite was designed to gather data that would provide tracking data and finalize the battery experiment. While the tracking sensors were unsuccessful the thermistors and voltmeter reported data that confirmed that the various electronic components onboard were kept within their operating temperatures and gave data on the battery performance inflight. The Geiger counter data that was gathered was not able to be directly correlated with an altitude, it was able to be correlated with time, and as all data points received were on the ascent of the balloon it is possible to state that there was a positive correlation between radiation levels and altitude. The camera system that was included in the payload was able to record the entirety of the two flights and provided imagery from the edge of space. A large amount of the project was also devoted to the development of a rugged and reusable capsule; this task was accomplished by the creation of a layered capsule wall that insulated the capsule and gained increased rigidity due to the geometry of the capsule and an internal rib cage that supported plates for the electronics.

Table of Contents

List of Figures and Tables

Introduction

The 2013 Elijah High Altitude Balloon Project Payload Team was composed of five engineering students of varying disciplines; as such, the team was interested in creating a well-designed capsule and program that would resolve existing problems and act as a stepping stone for future teams. Previous team's reports were examined and the problems from their designs were determined; the two main problems found were a weak capsule design resulting in payload failures and a lack of redundant data recording systems

To address the total capsule failures the capsule design became a prominent focus of the team as past teams frequently had issues with the capsule cracking or failing entirely. Research performed also indicated that the capsules of previous teams may not have been well enough insulated to protect the on-board electronics from freezing, which prompted the team to include insulation into the designs of the capsule.

The team also attempted to create a redundant data collection system that would not require the recovery of an intact payload to gather data, as half of the previous teams had been unable to gather or recover any data. A telemetry system should be included in the payload that would allow the team to transmit data from the payload to ground via HAM radio.

Other portions of the payload included a camera system, a sensor suite, and a Geiger counter; these components were included to satisfy the current team's inquiries. It was decided that a camera should be included in the payload to record images of the payload, balloon, and Earth during the flight; this is a traditional package that all previous teams have included, however it was to be modified to pan during flight. It was decided that another package should consist of a series of sensors that would be useful for determining the efficacy of the thermal insulation and the tracking of the payload; this package would communicate to with the ham radio and its data would be broadcasted periodically. A Geiger counter was also to be included as a package to gather data about the relationship between altitude and radiation levels in counts per minute.

Ground Tests

Several experiments were performed prior to the balloon launch to choose between the many options for various components of the payload. These tests were based upon preliminary research and were designed to target the differences between products.

Battery Tests

Overview

The battery experiment was designed to help future high altitude balloons teams with their design process. This experiment was designed to show how sub-zero temperatures and low

pressures will affect lithium-ion batteries. Preliminary ground experiments were performed in order to decide which batteries would be ideal for the final experiment. The purpose of the tests was to see if battery voltage would be affected by the decreased temperature and pressure experienced inflight; the voltage must be maintained above certain levels in order to power the microcontrollers and sensors on board.

Dry ice was used to simulate the sub-zero conditions the batteries would experience during flight, and a vacuum bell jar was used to simulate the decreased pressure. Energizer lithium AA and Samsung Aviator cell phone batteries were to be used for the tests. AA batteries were chosen because they have been used in past balloon flights and have a high current to weight ratio. Since most previous teams have used alkaline AA batteries, it was decided that the team would test how lithium batteries would work in the extreme conditions. The Samsung Aviator battery was chosen because it was the only smart phone battery that could be removed and charged using a team member's smartphone and had a relatively high amount of power. Both batteries chosen were lithium-ion batteries because of their known properties, including high battery life, low weight, and ability to produce heat. Different brands of batteries were not tested and compared due to the time and budget constraints of the project. After preliminary experiments were conducted, the Samsung Aviator cell phone batteries were eliminated from further testing because they did not produce enough current to power the Arduino.

A digital reading of the surface temperature for the batteries was taken during the middle of the dry ice experiment and at the end of the experiment. The way the batteries reacted to the temperature and pressure changes provided information on how the batteries might perform inflight. The data was recorded on the Arduino during the experiments and extracted from the Arduino when the experiment had completed.

During the balloon flight, the voltage was recorded and graphed to track the battery voltage throughout the trip.

Procedure

The first set of batteries underwent the test in room temperature and pressure to provide a control data set. The second set was tested in a vacuum bell jar which provided a decreased pressure. The final set was tested in a cooler along with dry ice. A set of batteries consisted five Energizer AA lithium-ion batteries connected in series.

For each of the three sets of batteries, the same procedure was used. The only changes were the environment the test took place in. The set of batteries was used to power the Arduino board, with a voltage divider circuit connected to monitor the voltage of the battery set throughout the test. The Arduino requires between six and twelve volts for operation, so five AA batteries were arranged in series to meet this constraint. Due to the limited amount of storage on the Arduino,

the program was set to record data for eight hours and take a voltage reading every 30 seconds. After the program had been uploaded to the board, the Arduino setup was left to run for eight hours. For the vacuum bell jar test, the same setup, with fresh batteries, was placed in a vacuum bell jar. The next day, the test was replicated using dry ice and fresh batteries. The setup was placed in a cooler with dry ice, recording data in the sub-zero temperatures.

During flight, the battery experiment was again replicated, to yield data about battery performance when both temperature and pressure are decreased simultaneously. The voltage was monitored using the same code as the ground experiments. Five lithium AA batteries were used to power all of the electronics except for the GoPro camera and the handheld radio, both of which had self-contained batteries.

Working with the Arduino

The Arduino was used to take readings and store data, which would later be extracted for analysis. A voltage divider was created to divide the battery voltage to a value below five volts which is the maximum voltage the Arduino can handle as an input reading. The voltage dividing method takes advantage of circuit properties as the voltage was divided between two resistors, as shown in the figure below.

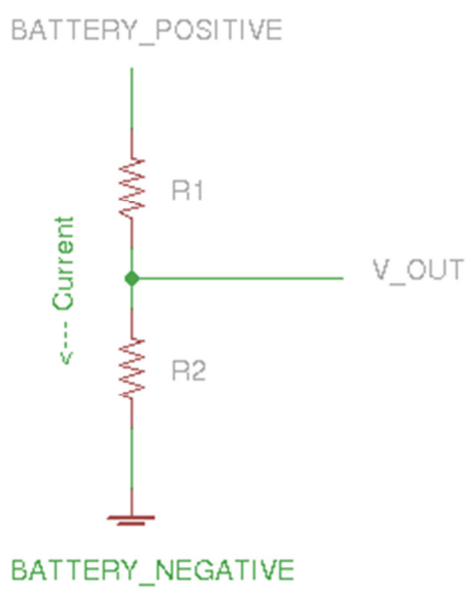

Figure 1: The Voltage Divider Circuit.

The formula used to determine how much voltage is divided between each resistor is:

$$V_{R_2} = R_1 R_2 + R_2 V_{in}$$

V_{R_2} is the voltage dropped across R_2 or the amount of voltage that the R_2 resistor divides. R_2 and

R_1 are resistors in Ohms and V_{in} is the battery voltage. The amount of voltage across R_2 is determined by the value of the ratio of R_1 and R_2 combined. If the resistors were the same value then the voltage drop on R_2 will be equal to R_1. As the battery voltage varies, the output voltage will vary proportionately, and this is the property of the voltage divider that was used to safely read the voltage on the batteries.

Results

The below graphs were generated from the data gathered in the various battery tests performed for the project.

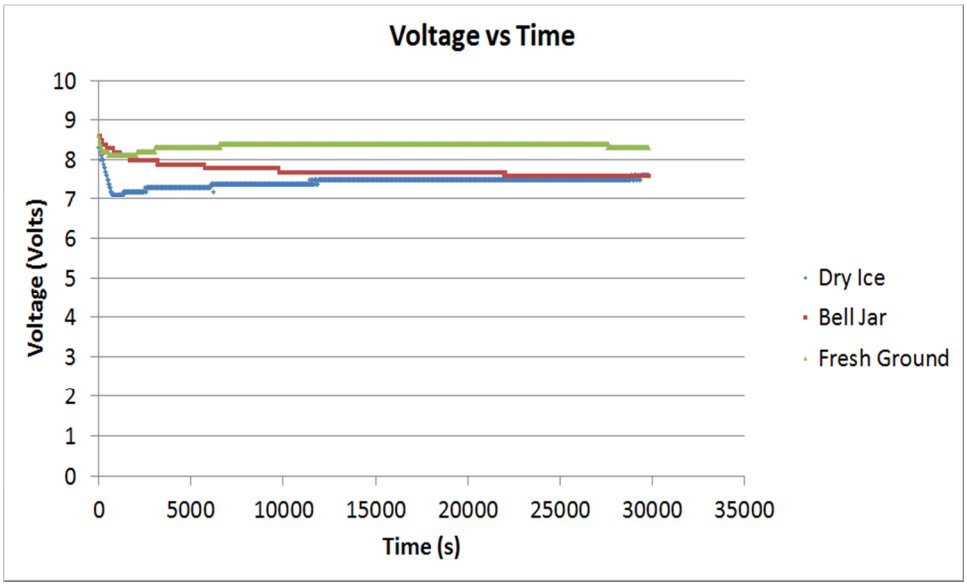

Figure 2: Voltage vs. Time Graphs for all Ground Tests.

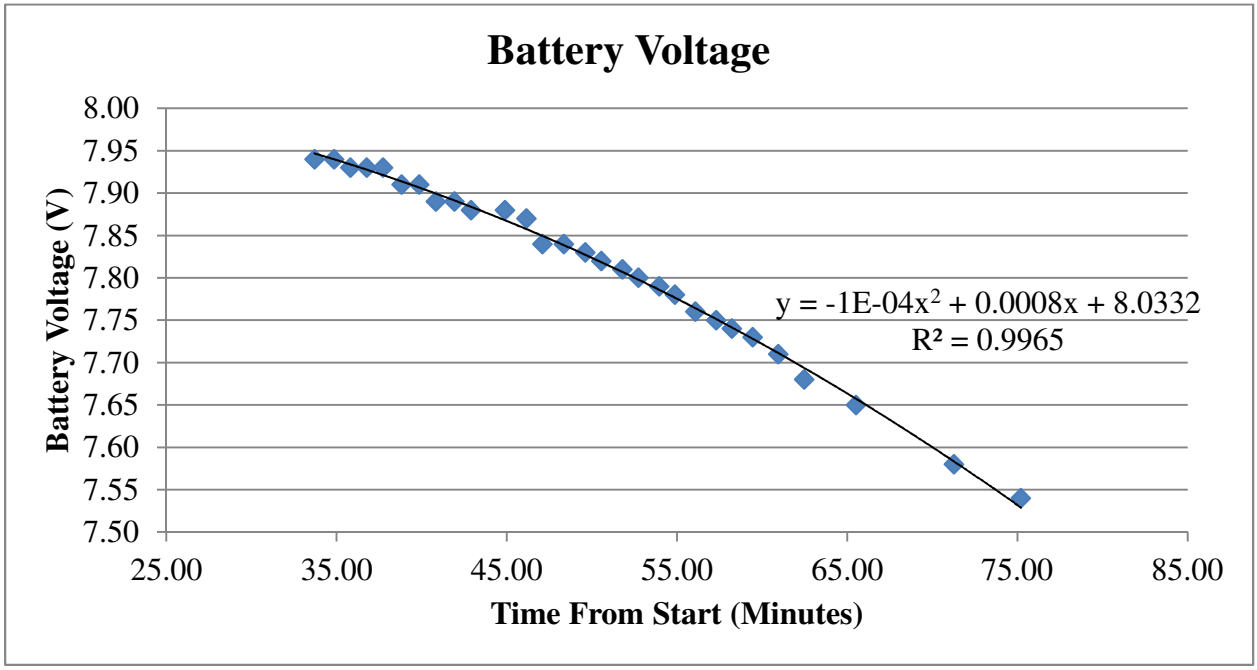

Figure 3: Battery Voltage vs. Time. The above graph shows how the battery voltage decreased during the duration of the flight. The voltage changes are modeled by a second-degree polynomial function.

Conclusion

The battery voltage was also monitored in flight. All data from the experiment and balloon flight will be documented in such a way that it will be beneficial to future teams who are looking for a way to power their payloads. The room temperature and pressure test was the control for this experiment. The data and results from the vacuum bell jar and dry ice experiments will be later compared to the control once testing is completed.

Composite Material Tests

Overview

It was decided that composite materials were to be used in the construction of the capsule body, so it was decided that several varieties of composite materials would be tested and assessed to determine the proper material for this application. Because composite cloths come in many arrangements of weight and weaving patterns, deciding on one type proved to be difficult. Twelve different types of composite materials (including two types of carbon fiber) were tested to determining what the exterior of the capsule would be laminated in. The materials were judged against one another to determine which cloth material would be strong enough, yet still lightweight enough to be used in application. The samples were provided courtesy of the Milwaukee School of Engineering, but upon selection of a particular material more stock would have to be ordered for the project.

Procedure

Mounting surfaces needed to be created for each sample. For this, 6x6" squares of extruded polystyrene (EPS) foam were cut. The EPS was chosen as substrate because it is same material which would make up the capsule body core. The twelve squares of EPS were each marked with a letter for recording purposes. With swatches of fiber cloth cut, EZ-Lam brand 30 minute cure epoxy was used to apply the material to the foam squares. For this procedure the team also made use of paintbrushes, shop towels, drop cloth, latex and nitrile gloves, safety glasses, mixing cups, acetone, and a slop bucket. Once the panels were saturated with epoxy, the samples were left to fully cure and dry overnight.

Once curing had completed, the team proceeded to investigate the finished samples. Data was recorded giving information such as texture, weight, the ease and feasibility of sanding, hardness, and thickness.

Another important factor was how difficult it was to "lay-up" the swatches onto the foam squares when applying epoxy. This was an important factor to the team as the team would need to apply the chosen composite material without the use of specialty machinery.

Conclusion

No hardness or impact testing was performed on the test samples, though tests that explored these properties may be useful to future teams. Ultimately, a four ounce (medium weight) plain weave fiberglass cloth was chosen. Although not the hardest of the test samples, its ease of application combined with low weight would provide more benefit than the heavier but stronger samples. More information regarding fiberglass materials can be found under the capsule design section.

Camera Tests

After the GoPro Hero 3 Silver Edition was chosen as the camera that would be flown on the capsule it remained to decide what settings should be used. In order to make this decision it was decided that recording time tests would be performed for each of the settings considered: 960p (960 progressive) without Protune activated, 960p with Protune activated, 1080p without Protune activated, and 1080p with Protune activated. Viewing sample videos recorded prior to testing allowed us to eliminate the 960p without Protune activated which yielded an almost incomprehensible video. Each setting configuration recorded 30 frames per second, the lowest frame rate supported by the GoPro Hero 3 series of cameras. Each test was initiated with an empty 64 GB class 10 micro SD card and a full charge on the battery. The camera would then be turned on and recording would be started immediately, the camera would then be left to run until it turned itself off due to lack of battery life or memory space. After the camera turned off the memory card would be removed from the camera and the length of the video to be recorded. Ten tests were to be performed in each setting configuration after which an average and

uncertainty in the average were determined for each setting configuration. The below table indicates the major results of the experiments; a full table can be found in Appendix 1.

GoPro Hero 3 Silver Edition Camera Recording Time Testing

Trial	Recording Time at 960p With Protune	Recording Time at 1080p Without Protune	Recording Time at 1080p With Protune
Average (hours)	3.6291	4.0382	3.7375
Uncertainty (hours)	0.0248	0.0397	0.0174

Table 1: Results of the Ground Testing of the GoPro Hero 3

Capsule Design

The capsule design – including body shape, material, and selected fasteners – was based on the fulfillment of both primary and secondary mission objectives which were decided by the team as important goals for creating a well-engineered capsule.

Objectives

The objectives set by the team could be divided into primary objectives that involved the utility of the payload itself and secondary objectives that would increase the ease of use of the payload. Primary objectives included: the launch and recover the capsule safely, with minimal damage to both the vessel and it's payload; and the use of HAM radio to successfully send/receive telemetry data from the capsule, and by doing so monitor the capsule's status in real-time. Secondary objectives included: successfully communicate with all payload sensors simultaneously; use LED indicator lights to confirm payload functionality; record payload data locally by use of microprocessor and SD card storage device; and to fly secondary payload of commemorative coins for dispersal to team members and other persons of interest.

Combining both the team's objectives for the capsule with constraints assigned in section 101 of FAA regulations, work on the design could begin. As part of the primary condition of launching and returning the capsule safely, an area of major importance was the determination of how much impact force the capsule would have to endure both during flight and landing. Given that the capsule would need to return to earth in an airworthy condition, it was decided that the strength of the capsule body would need to be great enough to support an unaided fall from apogee – meaning a fall without parachutes. An algebraic simplification was used to approximate terminal velocity:

$$v_t = \sqrt{\frac{2mg}{\rho A C_d}}$$

Values considered for this calculation included mass, gravity, fluid density, surface area of capsule, and the relating coefficient of drag. Using this methodology, terminal velocity was

found to be approximately 37 miles per hour. Using the same methodology, maximum velocity for a parachute-aided fall was found to be 12 mph. The impulse-momentum equations then gave an approximation for max impact force:

$$m_1 v_1 + \int_0^t F dt = m_2 v_2$$

Assuming an impact time less than a tenth of one second (t0.1sec) max impact force was estimated at 102 lbs. It was clear from these approximations that if the team was to protect both the capsule and payload under the most drastic conditions, new avenues of design, materials selection, and fabrication would have to be explored.

Early Concepts

Choosing a strong geometric shape was a key factor for the development a payload capsule which would be able to effectively withstand and absorb the stresses predicted to occur during flight and landing. Taking inspiration from various sources, a spherical capsule was initially decided upon for its ability to more effectively distribute compressive forces relative to designs which included edges, and therefore more stress risers. The added benefit to a sphere is its ability to function well as a pressure vessel. Early discussions also included the possibility of creating a hermetic vessel – a capsule which could cope with the extremely low external pressures while containing a ground atmosphere within. The justification behind such a design was the added insulation benefits of retaining air within the capsule body. By doing so the team believed that the decrease of internal temperature could be reduced, thereby protecting the power supply from voltage drops due to low temperatures (which were expected to reach -50º C). This “stretch goal” was dropped however, so that focus could be put on more immediate project objectives.

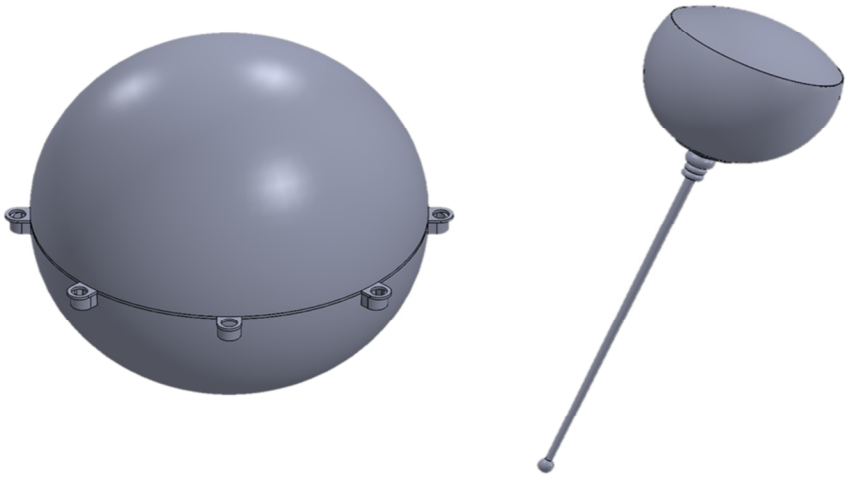

Figure 4: Early Capsule Design Concepts

After several revisions a final design was set on which we believed would be conducive to the accomplishment of the specified objectives. The final design was composed of a hemispherical body with a convex lid to increase the volume of the capsule.

Capsule Sections

The capsule body can be divided into exterior, core, and interior layers. The core, or base material, consisted of extruded polystyrene (EPS) foam. This pink, rigid foam was purchased in thick, 4x8 foot sheets, and though many methods for shaping this foam exist it was decided that a "build up" method for construction was most suitable. By this method of construction, multiple sections of the board would be cut using a CNC (computer numerical control) router. Once the sections were cut to size they would be stacked and bonded together to create the full shape. The EPS proved to be an excellent core material, given its low thermal conductivity, high strength to weight ratio, availability, and its machinability. A prototype, scaled-down version of the core was built first as a proof of concept for the design. Access to the CNC router was gained later through a partnership with the Milwaukee Makerspace. With the help of Makerspace we were able to cut the foam to an amazing level of accuracy.

Unlike earlier iterations, the final body profile was not a full sphere. Reasoning behind this was the lack of necessity for so much internal volume. Also from a practical standpoint, having a full sphere of electronics - with components residing both in the top and bottom hemispheres of the capsule - would have been very difficult to pack together and assemble on launch day. The bowl approach was much easier to handle, and a convex lid was added to give a slightly larger amount of headroom for any of the taller electronics or related wiring. The mating surface between body

and lid was beveled in order to ensure a snug, no-slip, and well centered fit between these two components.

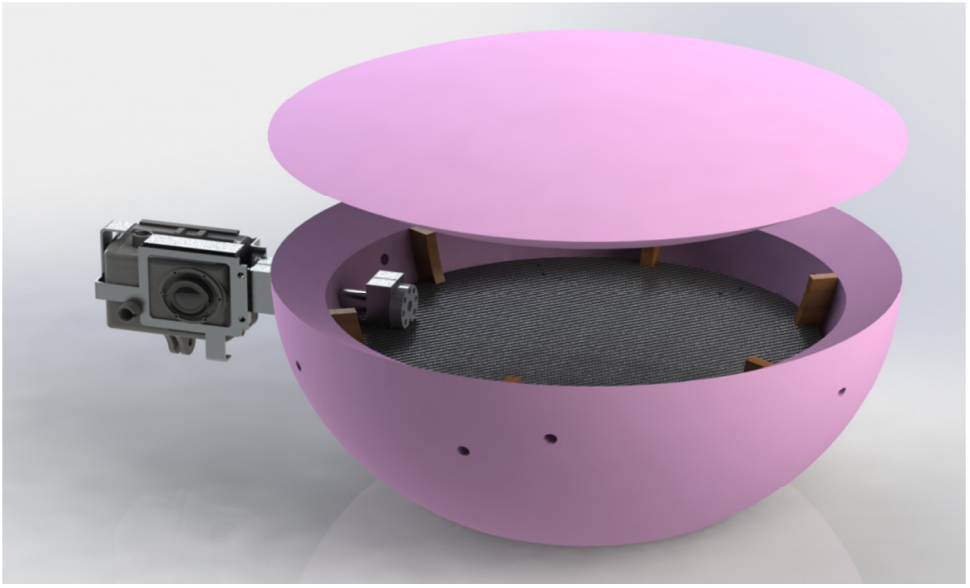

Figure 5: Capsule Design

As stated previously, the foam core touted a high strength to weight ratio, and because it's initial purpose was intended for home insulation it was believed that it would serve well as a non-conductive thermal barrier (R value approximately 5) between the sensitive electronics and the harsh -50^{0}F environment outside the capsule. Despite these benefits however, the team felt that more could be done to make the body impact resistant. This was due mainly to conversations with past Elijah team members, who found that EPS alone was impressionable and could crack easier than expected. Adding an additional layer of rigid strength was deemed necessary, and for this purpose composite materials were explored for use as an exterior layer.

A combination of 4oz S-2 unidirectional plain weave fiberglass and epoxy resin was used to laminate the exterior surface of the foam capsule. After a series of testing involving 12 different samples of fiberglass material - each with its own weave and weight characteristics - the 4oz fiber was decided upon for its ability to provide appropriate hardness and scratch resistance to the exterior while adding very minimal weight to the capsule. Heavier weaved fibers were effective as well, but were also more difficult to lay up over the curved capsule body. A layer of reflective Mylar and foil tape was added to surround the fiberglass hull. This wrapping was used for the purpose of retaining heat inside the capsule, which otherwise would have been leaked gradually to the surrounding atmosphere in the form of infrared radiation.

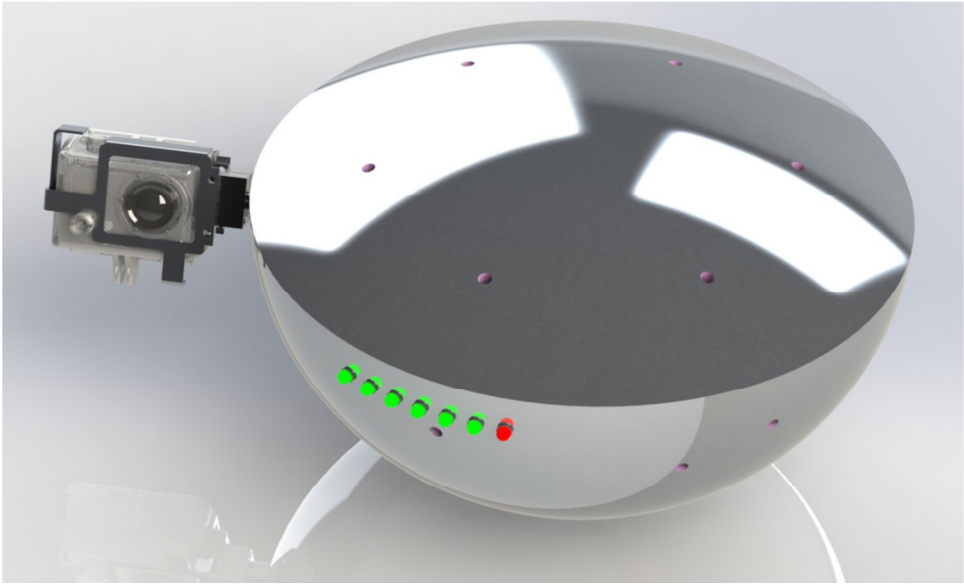

Figure 6: Capsule Rendering Shown with Aluminized Mylar Layer

A very important design consideration made was the method of mounting the microcontroller, radio, and other peripheral components to the interior of the capsule. Initial designs called for either heavy threaded studs to suspend mounting platforms within the body, or alternatively to machine ledges into the foam itself to provide a seat for those same platforms to rest. Either for reasons relating to weight restrictions or to concerns regarding the robustness of the design, an alternative method of mounting was developed to provide two stable mounting platforms supported by a hemispherical "ribcage-like" framework. In the final design, the actual electronic components were mounted to circular plates of rigid fiberglass FR4 board (similar to G10 board). These circular plates were cut using a similar CNC machine to that used for the EPS foam core. The disks were not cut as perfect circles, but instead included holes for threading screws as well as carefully placed slots which would allow the disks to conform around the six-rib array. The array - which would support the payload - in combination with Thinsulate fabric comprised the inner layer of the capsule. Basswood which was used for the 6 vertical ribs, was chosen because of its high strength-to-weight ratio. While balsa wood performs better in this category, higher porosity and lower machinability of the material was a serious concern. The rings which bound together the rib array were Baltic birch plywood. Because these rings created the ledge onto which the electronics plates (avionics plates, or AV-plates) would be mounted, a less compressible/higher strength wood was needed which could more readily accept fastening hardware.

Figure 7: Ribcage Design

The nine components which comprised the finished ribcage were cut by use of a 60 Watt CNC laser. The cutter provided a precision which our team would not have been able to replicate by use of hand tools. The assembly was completed using a combination of wood glue and epoxy adhesives, and the wood was then further treated with a sealant to prevent moisture from entering the material. By use of additional epoxy and steel u-pins, the frame was then lowered and anchored into the interior of the capsule. The telemetry radio and power supply were attached to the lower AV plate, while the remaining components attached to the top. Though the radio was the largest of our airborne components, and therefore not the best candidate for the smaller of the two compartments, it was believed that by placing it low we would ensure that the center of gravity would remain below the midline of the capsule. This would be an important consideration in the event of a parachute failure, where the capsule would impact the ground in a free fall condition.

Electronics were fastened to the AV plates by use of machine screws, washers, nylon standoffs, zip ties, and nuts. T-nuts were pressed into the birch wood seating rings to receive the machine screws from the AV plates. Out-holes were drilled through the capsule walls and lid to provide exits for externally mounted components (including the camera, temperature, and altitude sensors) as well as the Dacron cord which attaches to the rest of the flight train.

In past years many teams have experienced failures related to capsule detachment from the rest of the flight train. To avoid capsule separation, six Dacron (polyester) leader cords were used in the connection to the launch train. Each of these six cords were routed through all three sections of the capsule: internal, external, and core. If the cords were to “zipper” through one or more of the capsule segments, the redundancy in the cord routing would ensure the best possibility of retaining a solid connection between those two components. Another creative feature was the

design of brass, tubular fittings through which the Dacron is routed. These flared metal components give the cord a smooth surface to ride against when leaving the capsule body, thereby eliminating much of the worry associated with fatigue failure of the cord. A combination of high strength swivels and quick-links (ranging from 150-1500 lb. test) were used to connect all six leaders to the upper portions of the launch train.

Materials

Research was done to determine the best materials available to insulate and protect the payload during flight. The below listed materials were chosen by balancing cost and availability with beneficial materials properties and ease of fabrication.

Woven fiberglass is a material consisting of weaved and interlocking strands of glass (GFK glass fiber) reinforced by an epoxy resin. The resin acts as both an adhesive for whatever surface the fiberglass is laminated to, as well as a binder for the glass fibers. Fiberglass is a popular solution for many applications where having a high strength to low weight ratio is critical, such as aerospace engineering pursuits. Common uses for fiberglass include glider aircraft, boats, piping, and body/shell structure for various high stress applications.

Aluminized Mylar, the material used in space blankets, was used to reflect back radiated heat from inside the capsule to prevent radiated heat from escaping. The Aluminized Mylar was very flexible and easily punctured and therefore required support to be an effective component of the capsule, so it was bonded to the exterior of the fiberglass shell.

In order to further address the temperature concerns of the capsule air trapping insulators were also used, these insulators were extruded polystyrene foam and Thinsulate. Air pockets are essential to the function of these insulators since they both prevent warm air from escaping the capsule. The R value is a measure of thermal resistance, the higher the R value the greater the material resists the flow of heat from one side of the material to the other. Thermal conductivity is a measure of how well a material conducts heat. If a material has a low thermal conductivity then it does not easily allow for heat to travel from one side to the other and in turn creating a better insulator.

Polystyrene, also known as extruded polystyrene (EPS), is a commonly used insulation foam that works by trapping air inside small pockets formed during its manufacturing process. EPS is a rigid, yet easily breakable housing insulation foam, which can typically be purchased as large board/panels from a hardware or home improvement store. EPS has been used many times in the past for ballooning capsules because it is relatively easy cut and form. Further, because it is lightweight, has low thermal conductivity, and is rigid, it is a very cost effective “all in one” solution for capsule construction - provided the capsule is not required to endure high stresses during flight.

Thinsulate is a relatively new product developed by 3M. It is an extremely lightweight insulation fabric commonly used in winter jackets, hats, and gloves. This fabric is known for its ability to breathe, thus in order to prevent the air from leaving the microfibers, a layer of material will be placed on each side of the fabric. Fabric from a t-shirt was used as the inside layer and polystyrene on the outer side layer attached to the Thinsulate. Thinsulate has a high R value and low thermal conductivity and worked very well for our purposes. It added very little weight to the capsule and was easy to cut and sew into gores. 3M 79 spray foam worked well as an adhesive between the Thinsulate and polystyrene.

Packages

Packages are those components of the scientific payload that were not structural and were used to gather, process, or transmit data; the packages included the Arduino Mega 2560 (which process and controlled various sensors and systems), the telemetry system, the Geiger counter, the sensor suite and the camera. The full code that controlled the sensors and electronics can be viewed in Appendix 2.

Telemetry

Purpose

One of the objectives the team had for the launch was to receive a live data feed from all of the sensors aboard the payload. To achieve this objective, one of our team members needed to obtain an amateur radio operator's license (HAM license) to allow the use of the frequency band necessary for this type of data transfer. Dan Kass was able to pass the test and receive this license, KC9ZGW.

System Components

The next step was to determine how the data would actually be sent. With the help of another HAM Radio Operator, it was determined that the use of the Automatic Packet Reporting System (APRS) should be used on the frequency 144.390 MHz. 144.390 MHz is the standard ARPS frequency, meaning that on this frequency there are many repeaters. More repeaters will increase the likelihood of keeping a strong signal at great distances. One other advantage of using the standard APRS frequency was the digipeter which is similar to a repeater but instead of rebroadcasting the single it uploads it to the internet for access anywhere in the world. This was how data was eventually acquired for our second launch.

The radio that chosen for the balloon was the Kenwood TH-D7A which was chosen because the WSGC already owned two and that it included a built in Terminal Node Controller (TNC). The TNC is needed to convert text into tones that the radio can transmit

System Communications

The communication done between the radio and the Arduino was done using Serial Communication. The Arduino mimicked the commands that can be sent from a personal computer that can control the radio. By doing it that way the communications was relatively simple. The Arduino would perform a Serial print with the command and parameterize the information as the text. An example of the code is:

```
Serial.print("BT This is an Arduino on the radio");
```

The "BT" is the command for the radio that stands for Beacon Text and the text "This is an Arduino on the radio" is the text that the radio will broadcast at an interval of time that is set with other command.

There was originally going to be a radio on the ground connected to a laptop to receive the data packets coming in, but due to time constraints there was no time to create an interface to display the information nicely so it was determined to use the digipeters and the internet to collect the data from the balloon. The information was accessed from http://aprs.fi; a Packet of information looked like this:

```
2013-08-08, 11:34:23, CDT:KC9ZGW-7>GPS,qAR,N9QIP:
2021969,35.05,20.77,7.94,2.00,0.00,0.00,0.00000,0.00000,0.00,0.00,0
```

Everything after the colon was the information the Arduino sent, which is the data from the sensors in a pre-set order.

Results

The receiving radio in the chase car was plagued with slight issues at the connection points between the antenna and radio, and radio and computer; information was recovered from a website that receives and reports information sent over the APRS frequencies. With the collection of data from the radio we proved that information can be sent from an Arduino in the High Altitude Balloon and received on the ground before the balloon lands.

Geiger Counter

Purpose

A Geiger counter was included as one of the sensors to be included in the payload to observe the galactic cosmic rays (GCR) and solar radiation that are constantly bombarding the Earth. The Geiger counter would measure the amount of radiation in counts per minute, from which a dosage equivalency can be estimated and the effects that being exposed to those levels of radiation can be generalized. To most accurately fulfill this purpose the Geiger-Muller is to be mounted so that it receives no shielding form the capsule.

Information Concerning Radiation

Two main types of radiation are constantly bombarding the Earth: galactic cosmic rays and solar rays. Both of these types of radiation are highly variable; constantly changing and interacting with the upper atmosphere. The solar radiation levels are relatively stable compared to GCR and can be predicted with a fair degree of accuracy while the GCR is entirely unpredictable. Most of the solar radiation is gamma rays however alpha and beta radiation are also constantly being thrown off of the sun while GCR is mostly alpha and beta rays with some gamma rays also being present. The Earth's magnetosphere tends to deflect most of the alpha and beta radiation towards the poles, as both alpha and beta rays are charged particles, creating the borealis. The gamma radiation can pass through the magnetosphere and interact with the atmosphere more extensively, often penetrating the atmosphere until the atmosphere becomes dense enough to dissipate the radiation. The interaction of the incoming radiation and the atmosphere produces secondary radiation, typically in the form of positrons, muons, pi mesons (pions), alpha rays, and beta rays. The positrons, muons, and pions are typically very reactive and have very little penetrating power, consequently these types of radiation interact with the atmosphere and can generate different types of radiation, i.e. alpha and beta rays.

Justification of Geiger Counter

Interfacing with Arduino

Many options exist for a digital Geiger counter however relatively few of these are open source, meaning that we would be able to access codes for them, and only two of these were compatible with an Arduino board. The Geiger counter manufactured by Sparkfun Electronics was able to be integrated into the main capsule system as it could, by use of the serial peripheral interface (SPI), communicate with and be controlled by the Arduino that would be controlling all sensors in flight. The Geiger counter manufactured by Libellium also could communicate with an Arduino board via the SPI but this board was encumbered by a large amount of features that detracted from its usefulness for recording data, chief amongst these was a LCD display board.

Geiger – Muller Tube Specifications

The Geiger counter chosen included a more sensitive tube than was offered by other manufacturers, meaning that it would detect more of the radiation incident upon the tube. The original intent of the Geiger counter was to observe the radiation levels of the upper atmosphere where most of the radiation is in the form of alpha, beta, and gamma rays. For this reason it was important to use Geiger-Muller tube that could measure each of these forms of radiation, and the only Geiger counter that featured such a tube and was Arduino compatible was the one manufactured by Sparkfun Electronics, the one manufactured by Libellium only measured gamma and beta rays.

Expected Results

The GCR and solar radiation levels are expected to rise significantly with altitude as the radiation will not have had as much of a chance to interact with the air. The secondary radiation levels are likely to peak at approximately 45,000 ft. as this is the altitude at which the atmosphere is sufficiently thick enough to interact heavily with incoming radiation, while not yet being thick enough to dissipate most of the energy. As a consequence of the design changes that necessitated that the window of the Geiger-Muller tube not be exposed to the open air it is likely that most of the secondary radiation will be blocked by the capsule and so not be read by the Geiger counter. Because all alpha and most of the beta particles will be blocked by the capsule it is likely that low levels of radiation will be read until approximately 45,000 ft. after which the radiation levels should rise significantly and have a positive correlation with altitude.

Results

The first flight provided no data on the radiation levels at any altitude while the second flight provided data from only a portion of the flight. The second flight data did indicate that the radiation increased with altitude as all data points recorded were taken prior to the balloon reaching its apogee and increased exponentially with time as indicated in the figure below.

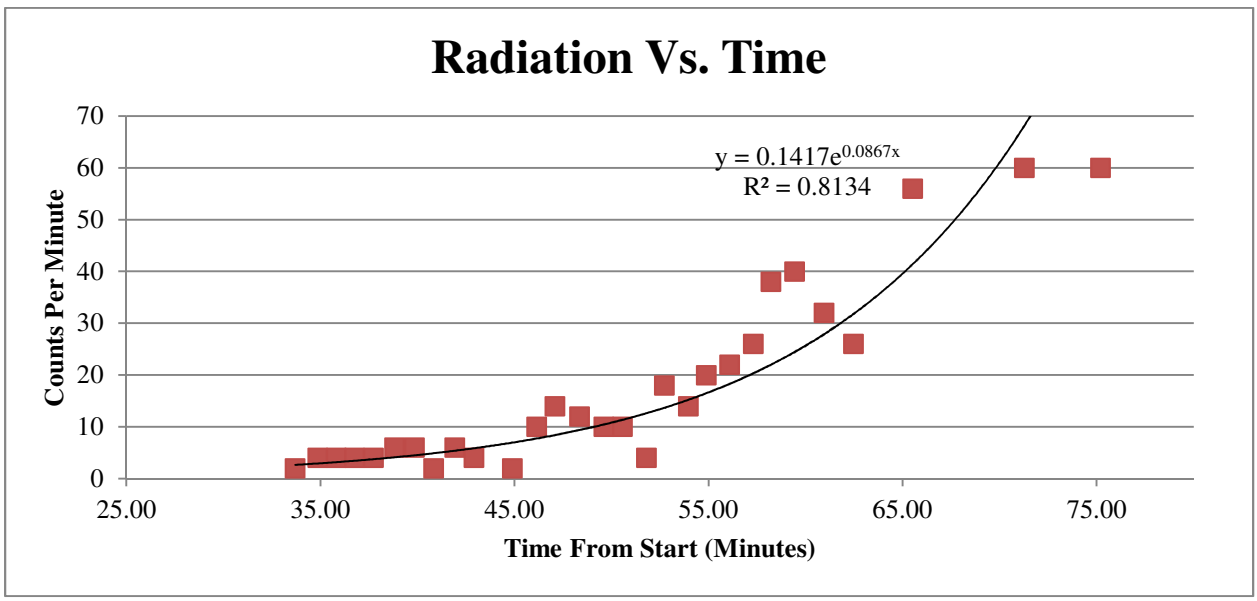

Figure 8: Gamma Radiation Vs. Time

The exponential line in the figure above is the best fit line for a plot of the radiation versus the time inflight generated by Microsoft Excel. The R^2 value reported indicates that there is a fairly strong correlation between the radiation levels and time inflight; as the times that the radiation levels were reported the balloon was still on its ascent to its apogee this also indicates that there is a correlation between the radiation levels and altitude.

Sensor Suite

Altimeter

Purpose

An Altimeter was included in the sensor suite to give a more accurate figure for the altitude of the balloon as GPS systems tend to have poor accuracy in altitude calculations. This information would be used as a reference point for other data gathered so that the data could be correlated with altitude.

Altitude Calculations

The altimeter used both a temperature sensor and a barometric sensor to calculate the altitude, by use of known relationships between temperature and pressure in the atmosphere. The sensor used had been tested to be accurate to an altitude of 120,000 ft. and was thus well suited for the purposes of the team.

Results

The altimeter was not used successfully, likely due to a wiring issue, and no data was recorded during the flight. As no data was recorded inflight it was not possible to fulfill the purposes of the altimeter, however approximations could be made using the altitudes reported by the primary and secondary tracking payloads.

Thermistor

Purpose

Thermistors were included in the sensor suite because this would allow for the evaluation of the efficacy of the insulation that was used in the construction of the capsule. The thermistors also allowed for the team to determine whether or not other sensors and electronics were working properly as most of the electronics were rated to -40° C while others are rated to -20° C. The thermistors were also to be used to verify the altitudes reported by the altimeter, which would also report the temperature and pressure that it used to calculate the altitude this would be useful as inaccurate temperature readings in the altimeter would result in inaccurate altitude data.

Placement

One thermistor was placed on the outside of the payload to record the external temperature as the payload flew. The other thermistor was placed inside of the capsule to record the internal temperature of the capsule. From these two data sets it was possible to evaluate the efficacy of the insulation of the capsule.

Process

Thermistors use the resistance of a piece of metal to determine the ambient temperature of its surroundings. The resistance of the metal varies as the temperature changes, as the metal

expands; the resistance of the thermistor is recorded and the temperature then calculated from this information relatively simply.

Results

Both thermistors worked well in flight, reporting temperatures that were within the temperature range anticipated during the flight, with a minimum external temperature of -50° C. The data gathered by the thermistors also indicated that the insulation included in the capsule was highly effective as at an external temperature of -50° C the internal temperature was 4.5^{o} C; the temperature gap between internal and external temperatures was evident at all points in the recorded data, with the external temperature decreasing at a greater rate than the internal temperatures as indicated by the figure below.

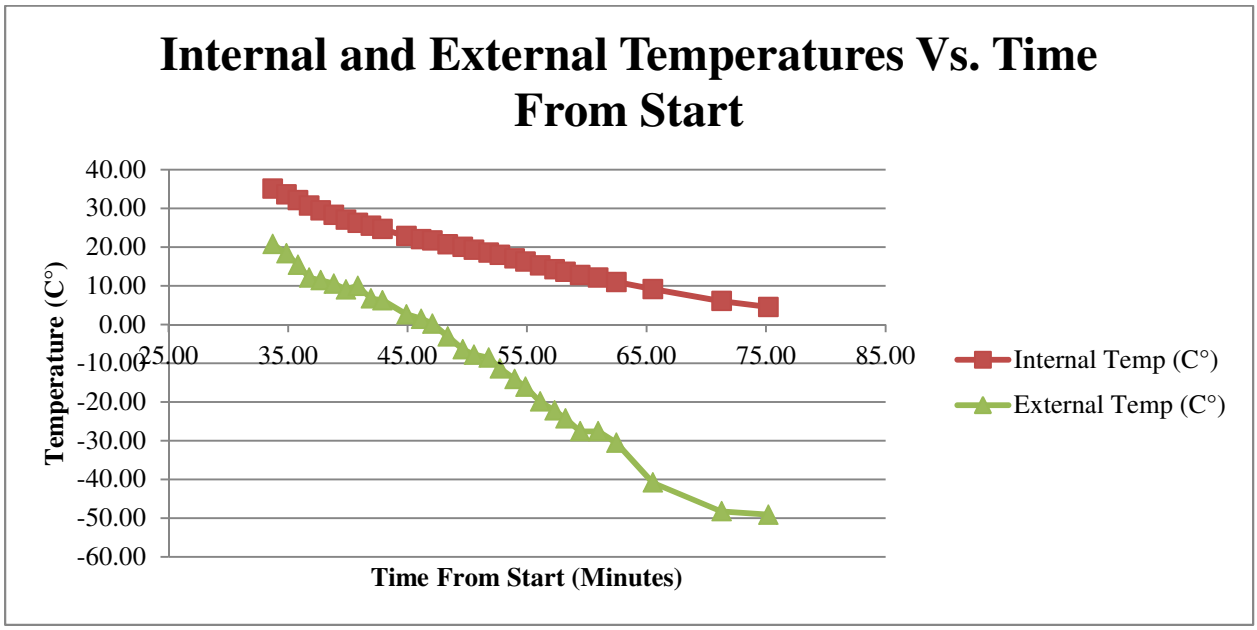

Figure 9: Graph Depicting the Effectiveness of the Capsule Insulation

Global Positioning System

Purpose

A GPS or Global Positioning System device was chosen to go into the payload to get information on latitude, longitude, altitude, speed, and the number of satellites it was connected to. This GPS was a further redundancy on the tracking systems for the payload train and was intended to give an alternate method of accessing the GPS location of the payload inflight.

Accuracy

The GPS was fairly accurate for latitude and longitude readings but was fairly inn accurate in altitude readings which necessitated the use of an altimeter to gain altitude data.

Results

Unfortunately while testing the device it stopped working the manufacture thought that the device had burnt out, and this was too close to launch day to get a replacement in so the device was not flown. Latitude, Longitude, and Altitude, however inaccurate, data was however collected by both the main and secondary tracking payloads that the launch team was responsible for.

Camera

The team decided that one of the items to be included was some form of camera to record imagery of the Earth during the flight; this portion payload was later expanded to incorporate a mount for the camera that would pan the camera in flight, reducing the number of shots that will contain essentially the same view.

Camera Selection

An initial decision was made to focus our camera searches on action cameras (action cams) which are by necessity of purpose rugged, lightweight cameras that are typically small in size.

Camera Selected

The camera that was selected is a GoPro Hero 3 Silver Edition, this action cam is renowned for its durability, and is easily modified to better suit our specific needs. We will be using the camera with the Battery BacPac which essentially doubles the battery life of the camera and the water proof housing with Battery BacPac back door, an expansion of the GoPro water proof housing that allows for the use of the Battery BacPac.

Justification

The camera selection process was done by the research of a myriad of action cam and action camera manufactures. It was found that a vast majority of the action cams available had poor image quality and battery life, leaving relatively few possibilities to pursue more closely. Of the remaining cameras, the forerunners of which were the GoPro Hero 3 line of action cams and the JVC GC-XA1 ADIXXION, all of which could be modified to increase battery life to the desired level, approximately three hours. The JVC ADIXXION and the White and Silver editions of the GoPro Hero 3 action cams were comparable in price while the Black Edition of the GoPro Hero 3 was considerably above this price range. The GoPro Hero 3 line of action cams have an optional auxiliary battery which doubles the battery life of the camera in almost all modes and attaches securely to the back of the camera. The JVC ADIXXION action cam had no options for extending battery life; however it could be modified to charge inflight and was fairly shock resistant. Due to the ease with which the action cams could be modified we decided to pursue the GoPro Hero 3 line of action cams, comparing the different editions looking for a balance of battery life, image quality, and price. The White Edition was fairly basic and did not include high quality software, so its image quality was often poor. The Black Edition was overwrought

with features such as a Wi-Fi remote that drastically reduced battery life and would be unusable for our purposes. The Silver Edition included better software that significantly increases the image quality of the camera; and while this camera too had many superfluous features, they could be suppressed to increase the battery life of the camera.

Camera Settings

Settings Selected

The GoPro Hero 3 Silver Edition was flown in the 1080p wide frame mode with Protune turned on, which allowed for high definition (HD) recording with minimal compression artifacts and an acceptable battery life.

Protune

Protune is a proprietary software package manufactured by GoPro for its action cams that reduces the number and frequency of compression artifacts by altering the algorithm by which the images are saved. The software that is standard on the GoPro Hero 3 line of action cams is not fast enough to process and compress HD footage at 30+ frames per second which leads to large compression artifacts in the video and ghosting, when images are placed in the wrong frame.

Ground Test Results

Ground testing indicated that all modes tested had a battery life that would last the expected three hours of flight. The recording life of the GoPro Hero 3 Silver Edition in all tested settings was adequate for the payloads flight, which was anticipated to be no longer than 3 hours. With the matter of recording time being a non-issue the setting selection process became an issue of image quality, and as 1080p with Protune activated clearly had the best image quality this was the setting configuration chosen for the flight.

Camera Mount

It was decided by the team that the camera should be mounted on a device that would allow for camera to be panned in flight, thus reducing the amount of time that the camera would capture essentially the same image.

Mount Selected

Two main options were presented to the team for the purposes of achieving the camera panning: the use of a simple mechanical device or a servo motor system. The simple mechanical suggested was a Scotch Yoke mechanism which changes rotational motion into alternating linear motion. This mechanism would then be attached to a bar extending from the GoPro housing, using the alternating linear motion to rotate the camera. The use of a servo motor to pan the camera would involve the programming of a servo motor to rotate the camera a certain number of degrees at set intervals.

The servo motor method of panning the camera involved fewer exposed moving parts and could be completed without the need to manufacture many custom parts or the calibration of motors. The servo motor mount would also be more flexible in terms of placement within the capsule, not requiring near perfect alignment like the Scotch Yoke mechanism. The servo motor mount consisted of three main portions: the servo motor, the arm assembly, and the camera holster.

Servo Motor

Servo Motor Selected – The servo selected for the mount is the Hitec HS-765HB Sail Arm, a servo motor intended for use on small remote controlled sail boats that allowed for 140° of rotation and was relatively light. This servo motor weighs 3.6 ounces, which is lighter than other servo motors considered, and did not rotate an excessive amount, some servo motors considered rotated 1260°.

Controlling the Servo Motor – The servo motor was controlled by the Arduino board that also communicated with the sensors and radio in the payload. The program written that controlled the sensors, radio, and servo motor used rotated the servo motor five degrees approximately once a minute, using the sensors and radio to control the timing of the program. The full program can be found in Appendix 2.

Results – On the first flight the servo motor appears to have been ineffectual, due to the program not running as anticipated, however, while the program was running the servo portion of the program ran smoothly. Additionally the reason that the servo mount was included on the payload, to change the view from the camera, was shown to be un-based as the capsule was constantly in motion, swaying and rotating, preventing the camera from capturing the similar images for more than a few frames, approximately a tenth of a second.

Arm Assembly

Components – The arm of the mount assembly was constructed using pre-fabricated parts and intended to allow the camera to be outside of the capsule while the servo could remain inside of the capsule. The am assembly consisted of a hub horn, two bore clamps, a tube, and a 90° quad hub mount; all of these components were made of 6061 aluminum. The hub horn attached directly to the servo motor; attached to this was one of the bore clamps, next was the tube, then another bore clamp, and finally the 90° quad hub mount.

Results – The assembly described above was successful as it allowed the servo motor to remain inside of the capsule and the camera to be rotated outside of the capsule. This assembly was also very strong, surviving the impact of the capsule as it returned to ground and despite the teams' best efforts could not be pulled apart without unscrewing the bore clamps.

Camera Holster

Design – The camera holster was designed to fit around and firmly grip the waterproof housing of the GoPro camera, while being flexible enough to remove the GoPro and housing, and remaining fairly light weight. The mount also had to be designed to be compatible with the 90° quad hub mount. The design process began by taking the dimensions of the GoPro housing and recording the placement of the tapped holes on the 90° quad hub mount. Next an initial mockup of the holster was created in SolidWorks that conveyed the general concepts to be explored for the holster design. Further iterations were created that reflected necessary revisions and strengthened the design until the mount seemed as though it would be reasonably strong. The model was then converted into a flat pattern for fabrication using SolidWorks sheet metal tools. A model of the arm assembly and the camera holster can be viewed in the figure below.

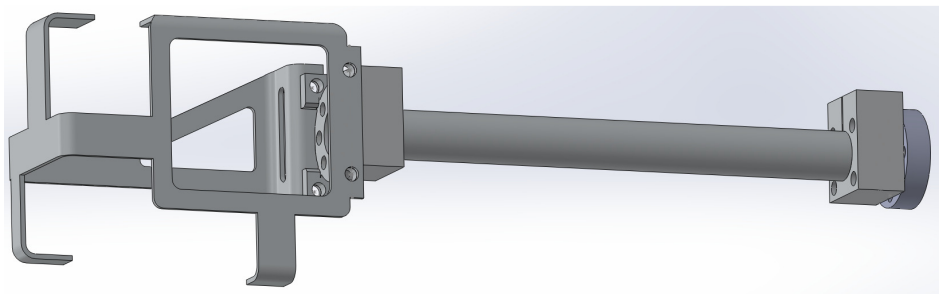

Figure 10: Camera Holster on Arm Assembly

Fabrication – A piece of sheet aluminum was cut by a computer numerical control (CNC) router using the flat pattern to control the milling of the metal. After the sheet metal had been cut to shape it had to be bent and formed to create the holster. The first bend made was a hard bend that would allow the holster to attach to the 90o quad hub mount. All other bends were made using the housing as a form and pressing the sheet metal into shape, the tabs were further bent using jewelry pliers to give a firmer fit.

Results – The camera holster fit the housing exceptionally well, requiring a great amount of force to be applied to the holster to either insert or remove the housing from servo motor mount. Additionally, while the holster was not designed to do so, the sheet metal acted as a spring and pressed in on the housing; this resulted in a firmer grip on the housing than was anticipated.

Conclusions

Throughout the duration of this project, the team achieved their goals of flying a successful payload and learning more about science and engineering in the process. The capsule performed well, sustaining no visible damage on either of the two flights, and the methods used to fabricate the capsule body while not readily available at the Milwaukee School of Engineering would be available to future teams if needed through the Milwaukee Makerspace. The telemetry system created performed well on the second flight but was somewhat temperamental; nevertheless this

system could be expanded upon by future teams increasing the utility system. The Geiger counter gathered evidence that supported the hypothesis that the radiation levels would increase with altitude, but was unable to determine an exact correlation. The sensor suite performed in part, the GPS and altimeter did not report data, and provided information that was used to complete the battery tests and confirm that the electronics onboard were kept within their operating temperature ranges.

Acknowledgements

The 2013 Elijah High Altitude Balloon Internship Payload Team would like to extend a special thanks to the following organizations and individuals:

The Wisconsin Space Grant Consortium
The Milwaukee School of Engineering
Dr. Matthew Panhans
Professor Jeff Korn
Vivian Mickelson
Jim Yauch
Roger Hajny
Richard Phillips
Valery Meyer
Jeananne Bargholz
Gary Bargholz
Marcus Reed Jr.
Jeff Hanson
Matt Neesley
Steve Pilone
Annya Ertel

Appendix 1: Camera Testing Table of Results

GoPro Camera Testing With 64 GB Micro SD Card			
Trial	Recording Time at 960p With Protune	Recording Time at 1080p Without Protune	Recording Time at 1080p With Protune
1	12975	14796	13517
2	13388	13555	13603
3	13330	14905	13462
4	13274	14641	13067
5	13002	14645	13434
6	13222	13904	13779
7	13125	14993	13296
8	12457	14629	13635
9	12772	14613	13358
10	13102	14693	13398
Average (s)	13064.7	14537.4	13454.9
Sample Standard Deviation (s)	281.944	451.726	197.793
Uncertainty (s)	89.2	142.8	62.5
Average (converted to minutes)	217.745	242.290	224.248
Uncertainty (converted to minutes)	1.486	2.381	1.042
Average (converted to hours)	3.62908	4.03817	3.73747
Uncertainty (converted to hours)	0.02477	0.03968	0.01737

Appendix 2: Full Code Used for Flights

```
/*************************************************************
 * Filename: payload.ino
 * Date: 8/7/2013
 * Author: Dan Kass (kassd@msoe.edu)
 *      2013 WSGC High Altitude Balloon Payload Team
 * Version: 1.6
 * Micro-controller: Arduino Mega
 * Provides: This is the main code that will run on the
 *    Arduino Mega during flight
 *************************************************************/

/**************************
 *********Includes*********
 **************************/

#include <Wire.h>          //I2C Library (Altimeter)
#include <TinyGPS.h>       //GPS Library
#include <Radio.h>         //Radio Library
#include <GeigerCounter.h> //Geiger Counter Library
#include <Servo.h>         //Servo Library
#include <SD.h>            //SD Card Library
#include <math.h>          //Math Library for Thermistors
#include <stdlib.h>        //Stard Library

/**************************
 ********Variables*********
 **************************/
 //LED Pin Locations
 int LED1 = 44; //Thermister LED  gray
 int LED2 = 45; //Geiger Counter  blue
 int LED3 = 46; //Altimeter  green
 int LED4 = 47; //GPS  brown
 int LED5 = 48; //Servo  purple
 int LED6 = 49; //SD Card  white
 int LED7 = A15; //Power LED

 int delayLED = 350; //The delay between delay Flashes

 double externTemp; //external temperature
 double interntemp; //internal temperature
 int externTherm = 0; //Location of Pin
 int interntherm = 1; //Location of Pin

 int geiger = 13; //Location of pin
 int cpm; //counts per minute
 GeigerCounter geigerCounter(geiger);

 Servo camera; //creates servo object
 int camMax = 160; //max degree of Servo
 int camMin = 20; //min degree of Servo
 int cameraLocation = camMin; //start of the servo
 int camDirection = 1; // 1 is up 0 is down
 int servo = 7; //Location of Pin

 const int SENSORADDRESS = 0x60; // address specific to the MPL3115A1 used in I2C
```

```
Radio radio;  //creates radio object

TinyGPS gps; //creates the GPS Object

//Variables from the GPS
float latitude = 0;
float longitude = 0;
float gpsAlt = 0;
float gpsSpeed = 0;
int gpsSatellites = 0;

//Voltage Divider Variables
int val = 0;
float pinVoltage = 0;
float batteryVoltage = 0;
float ratio = .423;

File data; //used for SD Card
int slaveSelect = 53; //must be set to output for SD card to work

//Set up Code
void setup(){
//Start up code initialize devices.

        //LED Initialization
        //Must write low so that are off to start
        pinMode(LED1, OUTPUT);
        digitalWrite(LED1, LOW);
        pinMode(LED2, OUTPUT);
        digitalWrite(LED2, LOW);
        pinMode(LED3, OUTPUT);
        digitalWrite(LED3, LOW);
        pinMode(LED4, OUTPUT);
        digitalWrite(LED4, LOW);
        pinMode(LED5, OUTPUT);
        digitalWrite(LED5, LOW);
        pinMode(LED6, OUTPUT);
        digitalWrite(LED6, LOW);
        pinMode(LED7, OUTPUT);
        digitalWrite(LED7, LOW);

        //Start up lights run across to the power light
        digitalWrite(LED1, HIGH);
        delay(delayLED);
        digitalWrite(LED1, LOW);
        delay(delayLED);
        digitalWrite(LED2, HIGH);
        delay(delayLED);
        digitalWrite(LED2, LOW);
        delay(delayLED);
        digitalWrite(LED3, HIGH);
        delay(delayLED);
        digitalWrite(LED3, LOW);
        delay(delayLED);
        digitalWrite(LED4, HIGH);
        delay(delayLED);
        digitalWrite(LED4, LOW);
        delay(delayLED);
```

```
digitalWrite(LED5, HIGH);
delay(delayLED);
digitalWrite(LED5, LOW);
delay(delayLED);
digitalWrite(LED6, HIGH);
delay(delayLED);
digitalWrite(LED6, LOW);
delay(delayLED);
digitalWrite(LED7, HIGH); //want to keep the power LED on

//Serial
Serial.begin(9600);
//GPS Serial Setup
Serial1.begin(9600);

radio.mycall("KC9ZGW-7");

//setup I2C
Wire.begin();
if(IIC_Read(0x0C) == 196){ //checks who_am_i bit for basic I2C handshake test
        digitalWrite(LED3, HIGH);
}
else {
        digitalWrite(LED3, LOW);
}
//These are the sensor configuration values used in the sample code
//they work so don't want to mess with it.

// CTRL_REG1 (0x26): enable sensor, oversampling, altimeter mode
IIC_Write(0x26, 0xB9);
// CTRL_REG4 (0x29): Data ready interrupt enabled
IIC_Write(0x29, 0x80);
// PT_DATA_CFG (0x13): enable both pressure and temp event flags
IIC_Write(0x13, 0x07);
// This configuration option calibrates the sensor according to
// the sea level pressure for the measurement location
// BAR_IN_MSB (0x14):
IIC_Write(0x14, 0xC6);
// BAR_IN_LSB (0x15):
IIC_Write(0x15, 0x5B);

//SD Card Setup
pinMode(slaveSelect, OUTPUT);
if(SD.begin()) {
        digitalWrite(LED6, HIGH); //turn on LED SD Card initialized
}

data = SD.open("datalog.csv", FILE_WRITE);
if(data) {
        //writing the header to the csv file, column titles
        data.println("Time From Start, Internal Temperature, External Temperature, Battery Voltage, Counts
Per Minute, Altitude, Altimeter Temperature, Latitude, Longitude, GPS Altitude, Speed, Satellites");
        data.close(); //close the file
}
else {
        digitalWrite(LED6, LOW); //There was an error opening the file turn off the LED
}

//Servo
```

```
	//to get it to move camera.write(20 through 160)
	camera.attach(servo);
	camera.write(cameraLocation);
	if(camera.attached()) {
		digitalWrite(LED5, HIGH);
	}


	//Radio set up beacon and location time
	radio.beaconText("WSGC High Alt Balloon. DataOrder: Time, Intern Temp, Extern Temp, Bat Volt, Counts Per
Minute, Alt, Alt Temp, Lat, Long, GPS Alt, Speed, Sats");
	radio.beacon(300); //beacons every 300 seconds (5 minutes)
	radio.location(60); //location sends out every 60 seconds

}


//Main running loop
void loop(){

	//get the Internal and External Temperatures;
	externTemp = getTemp(analogRead(externTherm));
	internTemp = getTemp(analogRead(internTherm));

	//The best way to check to see  if they are working properly is
	//to check their values against them self
	//might have to be changed for launch
	if((externTemp < internTemp + 2) && (externTemp > internTemp - 2))
	{
		digitalWrite(LED1, HIGH);
	}
	else
	{
		digitalWrite(LED1, LOW);
	}

	//getting GPS Data
	bool newData = false;
	// For one second we parse GPS data and report some key values
	for (unsigned long start = millis(); millis() - start < 1000;)
	{
		while (Serial1.available())
		{
			char c = Serial1.read();
			// Serial.write(c); // uncomment this line if you want to see the GPS data flowing
			if (gps.encode(c)){ // Did a new valid sentence come in?
				newData = true;
			}
		}
	}

	if (newData)
	{
		digitalWrite(LED4, HIGH);
		unsigned long age;
		gps.f_get_position(&latitude, &longitude, &age);
		gpsSatellites = gps.satellites();
		gpsSpeed = gps.f_speed_mph();
		gpsAlt = gps.f_altitude();
```

```
}
else
{
        digitalWrite(LED4, LOW);
}

//getting Altimeter data

// This function reads the altitude and temperature registers, then
// concatenates the data together, and prints in values of
// meters for altitude and degrees C for temperature.

// variables for the calculations
int m_altitude, m_temp, c_altitude;
// these must be floats since there is a fractional calculation
float l_altitude, l_temp;
float altitude, temperature;

// read registers 0x01 through 0x05
m_altitude = IIC_Read(0x01);
c_altitude = IIC_Read(0x02);
// the least significant bytes l_altitude and l_temp are 4-bit,
// fractional values, so you must cast the calculation in (float),
// shift the value over 4 spots to the right and divide by 16 (since
// there are 16 values in 4-bits).
l_altitude = (float)(IIC_Read(0x03)>>4)/16.0;
m_temp = IIC_Read(0x04); //temp, degrees
l_temp = (float)(IIC_Read(0x05)>>4)/16.0; //temp, fraction of a degree

// here is where we calculate the altitude and temperature
altitude = (float)((m_altitude << 8)|c_altitude) + l_altitude;
temperature = (float)(m_temp + l_temp);

long time = millis() + 2000; //current time plus 2 seconds
// wait here for new data
while(check_new() == false)
{
        //had some problems with data retrial if problem with altimeter so put
        //a break if takes longer than 2 seconds
        if(millis() > time){
        digitalWrite(LED3, LOW);
        break;
        }
}

//move the servo
if(camDirection == 1) {
        //if direction is up add 5 degrees
        cameraLocation += 5;
}
else {
        //other wise subtract 5 degrees
        cameraLocation -= 5;
}

if(cameraLocation == camMax) {
        //when location is max set label to go down
        camDirection = 0;
}
```

```
if(cameraLocation == camMin) {
        //when location is min set label to go up
        camDirection = 1;
}
camera.write(cameraLocation);

//getting Geiger Counter data
cpm = geigerCounter.read(30); //going to get a 30 second sample
//That is background radiation so if it is reading that we want the light on
if((cpm > 1) && (cpm < 30)) {
        digitalWrite(LED2, HIGH);
}
else {
        //otherwise we want it off
        digitalWrite(LED2, LOW);
}
//Battery Monitor
val = analogRead(batMonPin);
pinVoltage = val * 0.00488; //calculate the voltage on the a/d pin

batteryVoltage = pinVoltage / ratio; //used with voltage divider

//create data string

//need to convert all of the floats/doubles to strings
//dtostrf(value, width, precision, output);
char temp[10];//temporary string

//gets the time from start
dtostrf(millis(),1,0,temp);
String information = String(temp) + ",";

dtostrf(internTemp,1,2,temp);
information = information + String(temp) + ",";

dtostrf(externTemp,1,2,temp);
information = information + String(temp) + ",";

dtostrf(batteryVoltage,1,2,temp);
information = information + String(temp) + ",";

dtostrf(cpm,1,2,temp);
information = information + String(temp) + ",";

dtostrf(altitude,1,2,temp);
information = information + String(temp) + ",";

dtostrf(temperature,1,2,temp);
information = information + String(temp) + ",";

dtostrf(latitude,1,5,temp);
information = information + String(temp) + ",";

dtostrf(longitude,1,5,temp);
information = information + String(temp) + ",";

dtostrf(gpsAlt,1,2,temp);
information = information + String(temp) + ",";
```

```
	dtostrf(gpsSpeed,1,2,temp);
	information = information + String(temp) + ",";

	dtostrf(gpsSatellites,1,0,temp);
	information = information + String(temp);

	//send data string over radio
	radio.locationText(information);

	//save data to SD card
	data = SD.open("datalog.csv", FILE_WRITE);
	if(data) {
		//writing the header to the csv file, column titles
		data.println(information);
		data.close(); //close the file
	}
	else {
		digitalWrite(LED6, LOW); //There was an error opening the file turn off the LED
	}

	delay(10000); //just wait 10 seconds don't need to go to fast
}


/***************************
 ********Functions*********
 ***************************/

/************************************
 * Function: getTemp
 * Author: Mark McComb, hacktronics LLC
 * Parameters: Raw ADC Value from the
 *    Arduino
 * Returns: Temperature in C
 * Provides: The temperature reading
 *    from the thermistor
 ************************************/
double getTemp(int RawADC) {
	double Temp;
	// See http://en.wikipedia.org/wiki/Thermistor for explanation of formula
	Temp = log(((10240000/RawADC) - 10000));
	Temp = 1 / (0.001129148 + (0.000234125 * Temp) + (0.0000000876741 * Temp * Temp * Temp));
	Temp = Temp - 273.15;		// Convert Kelvin to Celsius
	return Temp;
}

/************************************
 * Function: IIC_read
 * Author: SparkFun Electronics, A.Weiss, 7/17/2012
 * Parameters: register Address
 * Returns: byte of data
 * Provides: The I2C read functionality
 *    for the altimeter
 ************************************/
byte IIC_Read(byte regAddr)
{
	// This function reads one byte over IIC
	Wire.beginTransmission(SENSORADDRESS);
	Wire.write(regAddr);  // Address of CTRL_REG1
```

```
	Wire.endTransmission(false); // Send data to I2C dev with option
	//  for a repeated start. THIS IS
	//  NECESSARY and not supported before
	//  Arduino V1.0.1!!!!!!!!!
	Wire.requestFrom(SENSORADDRESS, 1); // Request the data...
	return Wire.read();
}

/***********************************
 * Function: IIC_Write
 * Author: SparkFun Electronics, A.Weiss, 7/17/2012
 * Parameters: register Address, and value
 * Returns: none
 * Provides: The I2C write functionality
 *    for the altimeter
 ************************************/
void IIC_Write(byte regAddr, byte value)
{
	// This function writes one byte over IIC
	Wire.beginTransmission(SENSORADDRESS);
	Wire.write(regAddr);
	Wire.write(value);
	Wire.endTransmission(true);
}

/***********************************
 * Function: check_new
 * Author: SparkFun Electronics, A.Weiss, 7/17/2012
 * Parameters: none
 * Returns: boolean true if there new data
 * Provides: The test for new date
 *    for the altimeter
 ************************************/
boolean check_new()
{
	// This function check to see if there is new data.
	// You can call this function and it will return TRUE if there is
	// new data and FALSE if there is no new data.

	// If INT_SOURCE (0x12) register's DRDY flag is enabled, return
	if(IIC_Read(0x12) == 0x80) // check INT_SOURCE register on
	// new data ready (SRC_DRDY)
	{
		return true;
	}
	else return false;
}
```

Team Whoosh Generator
2013 WSGC Collegiate Rocket Competition

Kirsti Pajunen, Eric Johnson, Chris Larson, Victoria Falcon, James Ihrcke

Department of Mechanical Engineering, Milwaukee School of Engineering

Abstract
The objective of the 2013 Wisconsin Space Grant Consortium Collegiate Rocket competition was to design, build, and launch a single-stage high powered rocket that must reach a target altitude of 3000 feet and deploy a parachute(s) electronically for a successful recovery. Upon recovery, the rocket must be determined to be in a flyable condition to be considered a successful launch. Teams receive a launch score based on their combination of reaching the desired altitude and on whether or not the rocket was recovered in a flyable condition.

At the kick-off meeting, Team Whoosh Generator was informed they would be using a Cesaroni I540 motor and a 4.0-in airframe diameter. An RRC2 mini altimeter (from last year's rocket) and an ALTS25 altimeter given to the team at this year's altimeter conference were selected to complete the apogee requirements. Upon reaching apogee (estimated around 3080 feet) a drogue chute deployed under which the rocket descended until it reached an altitude of 500 feet. A second chute then deployed such that a slow decent speed was obtained for landing. A Transolve Beep-X Sonic Locator was activated before launch and was used to aid in recovery of the rocket.

Included in this report are design details considered, anticipated performance, photos of the construction process, and flight results.

Team Whoosh Generator thanks the Wisconsin Space Grant Consortium (WSGC) for the funding to make this project possible.

1.0 Rocket Design and Construction

The following subsections will detail the airframe design, nosecone and fin design, rocket stability, electronics bays, pressure relief considerations, and recovery method.

1.1 Airframe design. It was decided to build the rocket from the selection of individual components and not the use of a kit. This seemed most logical because of the many design restrictions (weight, length, diameter, and motor restrictions) and the necessity to reach an altitude between 2500 and 3500 feet. The following sections describe how the airframe of the rocket was designed using these parameters.

Several of the team's members attended the WSGC Altimeter Conference on December 1, 2012. At this conference, the team constructed an electronics bay, built to fit a 4.0-inch outer diameter body tube. Since it was not desired to build an alternate diameter electronics bay, it was decided to design a rocket with a 4.0-inch outer diameter body tube to fit the electronics bay constructed at the altimeter conference. With this parameter set, fewer independent variables remained, making the subsequent rocket design easier.

The body tubes could be selected from several different kinds of materials, including cardboard, fiberglass, and PVC. Cardboard was selected as the body tube material for the rocket because of its simplicity, strength, price, and ease of cutting and drilling. Cardboard has proven to work well from previous years' rockets.

The body tube lengths were heavily dependent on the design restriction of a maximum total rocket length of 72 inches. OpenRocket, a free rocket design software program, was the primary software used to design much of the rocket. OpenRocket was used to calculate optimum body tube lengths. It was found that the lower body tube (to house the motor mount and drogue parachute) would have a length of 25 inches. The upper body tube (to house the main parachute) would have a length of 20 inches. These lengths help to bring the rocket to an apogee of approximately 3000 feet, with favorable centers of gravity and pressure. The total length of the rocket is 55 inches, which is below the 72 inch maximum restriction.

1.2 Nose cone. The nose cone was decided to be a durable plastic 4 inch diameter Madcow Rocketry cone. It is a short ogive cone, 9.5 inches in length. This was chosen because a short, ogive cone has a low coefficient of drag allowing the rocket to achieve a higher apogee. An eyebolt was attached to the bottom of the cone to allow for a stronger point of attachment for the recovery harness.

1.3 Fins. The fins are the main component that determines the location for the center of pressure on a rocket and therefore the stability of the rocket. The design of the fins was determined by placing different shapes and sizes of fins in open rocket until a stable ratio between the center of gravity and center of pressure was obtained. It was determined to use 4 fins spaced evenly around the rocket.

The fins chosen were A-05 G-10 fiberglass fins from public missiles shown in Figure 1. The fins were attached to the rocket using through the wall construction with epoxy filets on each contact surface shown in Figure 2.

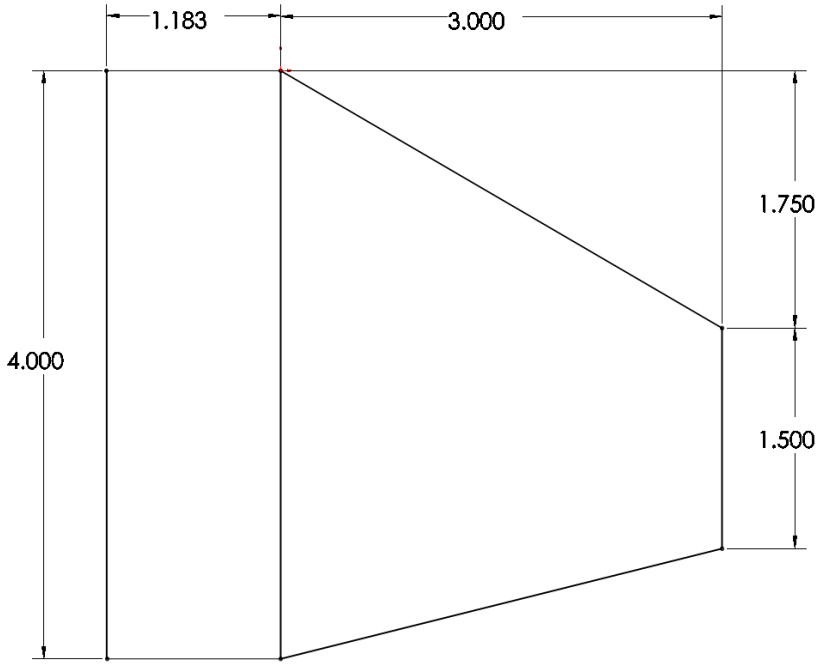

Figure 1: Fin construction with dimensions

Figure 2: Assembled fins

1.4 Rocket stability. The relationship between the center of pressure (CP) and center of gravity (CG) is one of the most important relationships in high-powered rocketry. The center of pressure is defined as the point at which aerodynamic forces on the rocket are centered. The center of gravity is the location at which the whole weight of the rocket can be considered to act as a single force. The ratio between the locations relative to the rocket diameter can be used to predict the stability of the rocket during flight. Generally, the center of gravity must be at least one (but not more than two) body tube diameters in front of the center of pressure.

The center of pressure and center of gravity were determined for this design using the OpenRocket software. The results were then compared against the results using Barrowman's Theory, and the two agreed acceptably.

The following assumptions were made during the derivation of Barrowman's theory for predicting the center of pressure (Barrowman, 2013):

1) The flow over the rocket is potential flow.
2) The point of the nose is sharp.
3) Fins are thin flat plates.
4) The angle of attack is near zero.
5) The flow is steady and subsonic.
6) The rocket is a rigid body.
7) The rocket is axially symmetric.

The rocket design presented in this paper did violate some of these assumptions, particularly assumptions 2, 6, and 7. However, the theory was still applied with the understanding that minor uncertainties will be present as a result.

Table 1 shows the locations of the CP and CG and the caliber stability at ignition and at burnout according to the OpenRocket simulation.

Table 1: Locations of CP and CG (In Inches from Nose Cone Tip)

	CP	**CG**	**Stability (Caliber)**
Ignition	38.5	32.6	1.47
Motor Burnout	38.5	31.2	1.83

From this analysis, it can be concluded that the rocket will be stable during the entire ascent portion of the flight.

1.5 Electronics bay. The electronics bay was made from a Giant Leap Rocketry avionics bay kit provided to the team at the WSGC Altimeter Conference. It is 8 inches long and has an outer diameter of 3.9 inches allowing it to fit perfectly into a 4 inch diameter airframe. A small piece of airframe, measuring 1.5 inches in length, was cut from a body tube and epoxied in the center of the electronics bay to turn the bay into a coupler. Two barometric altimeters were used in the electronics bay a RRC2 mini used in previous years and an ALTS25 given to the team at the Altimeter Conference. These altimeters will be used to deploy the drogue and main parachutes as

well as record the altitude of the rocket. The electronics bay also holds the Raven III (WSGC flight data recorder) along with a Transolve BeepX sonic locator which is a location device that puts out a 105 decibel tone allowing location and recovery of the rocket to be easier. A GPS was going to be used but due to space in the electronics bay the sonic locator was chosen. Two key switches were placed 180 degrees apart on the electronics bay to allow easy arming of devices on the launch pad. One key switch is for turning on the WSGC flight data recorder and the other is for arming both altimeters. The sonic locator is activated by a pushbutton on the device. Terminal blocks were placed at either end of the bay to allow easier attachment of black powder charges on launch day. The assembled electronics bay is shown in Figure 3.

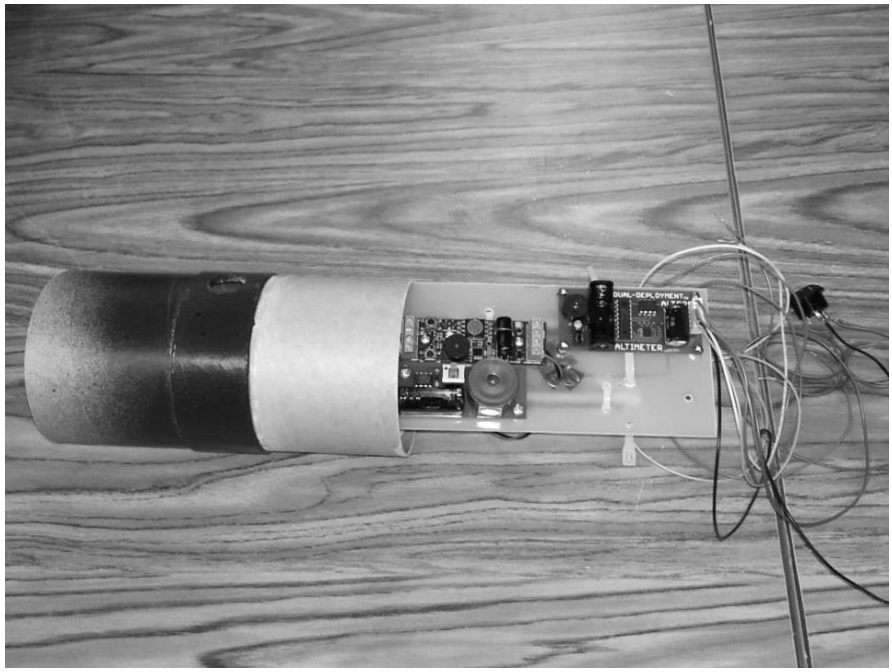

Figure 3: Electronics bay assembly

1.6 Pressure relief. The two barometric altimeters used to deploy the drogue and main parachutes require static pressure port holes. The static port holes are required for pressure equalization between the air inside the bay and the outside air during flight. The parachutes could be deployed too early or too late if the static port holes are not the correct size. The general rule for port hole sizing is to use a ¼ inch diameter hole (or equivalent area if multiple holes are used) for every 100 cubic inches of volume in the bay. It is also recommended to use at least three holes spaced evenly around the body tube to help negate the effects of crosswinds. The RRC2 mini user manual recommends the use of the following equations for port hole sizing.

The volume of the bay:

$$Volume(in^3) = Bay\ Radius(in)\ x\ Bay\ Radius(in)\ x\ Bay\ Length(in)\ x\ \pi \tag{1}$$

The diameter of a single port hole:

$$Single\ Port\ Hole\ Diameter = 2\sqrt{\frac{Volume}{6397.71}} \tag{2}$$

The area of a single port hole:

$$Single\ Vent\ Area = \left(\frac{Single\,Vent\ Diameter}{2}\right)^2 x\,\pi \tag{3}$$

The diameter of multiple port holes:

$$Multiple\ Port\ Hole\ Diameter = 2\sqrt{\frac{Single\,Vent\ Area}{(\#\,of\ \ Holes)(\pi)}} \tag{4}$$

The radius of the electronics bay is 3.9 inches and the length of the bay is 8 inches. This yields a volume of 95.57 cubic inches. The diameter of a single port hole is equal to 0.24 inches with an area of 0.047 square inches. Three holes were used on the electronics bay each with a diameter of 0.141 inches spaced 120 degrees apart.

One quarter inch holes were also drilled into the upper and lower body sections of the rocket. During the rocket's ascent the atmospheric pressure surrounding the rocket decreases. If these holes are not present the higher pressure inside the rocket could cause the rocket to separate and deploy its parachutes early.

1.7 Recovery. The rocket used a dual deployment system. This means the rocket deploys a small drogue parachute at apogee and then a main parachute at a lower altitude to minimize the drift of the rocket allowing easier retrieval of the rocket. A 24 inch drogue chute that deploys at apogee and a 44 inch main SkyAngle Classic parachute that deploys at 600 feet were used. The rocket has a descent rate of 16 feet per second once the main cute has opened. Two altimeters were used for redundancy to ensure the parachutes deploy. The parachutes are shown in Figure 4.

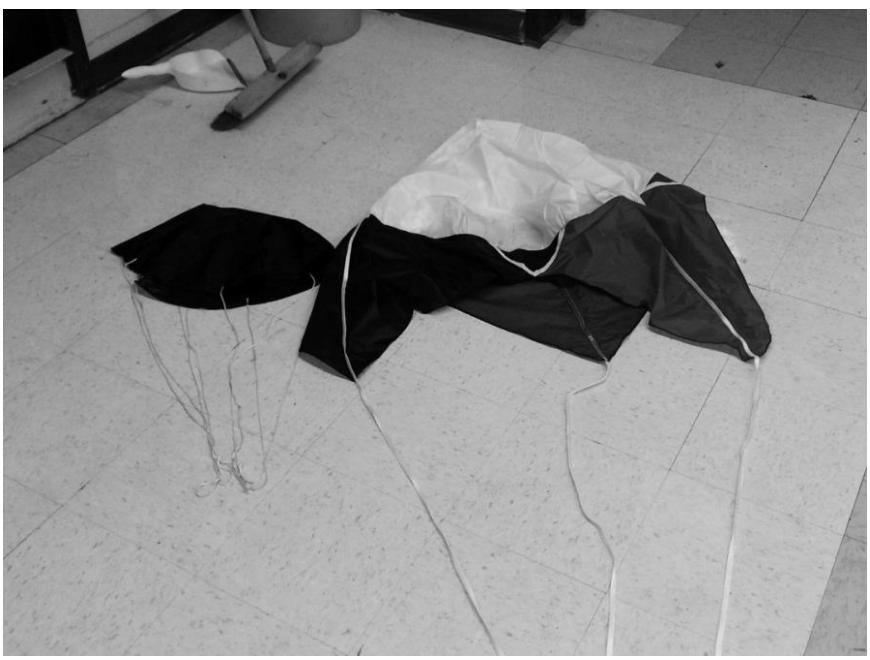

Figure 4: Drogue and main parachutes

2.0 Anticipated Performance

The anticipated performance of the rocket was simulated using two programs: MATLAB and OpenRocket. The results of both simulations were compared to estimate the performance of the rocket on launch day. The following sections detail these simulations.

2.1 MATLAB Simulation. The primary assumptions made were that the rocket would be launched vertically and that the rocket would follow a vertical flight path. Additionally, standard temperature and pressure were assumed to determine air density, which was also assumed to be constant throughout the range of flight.

A MATLAB simulation for the rocket flight performance was then developed using numerical methods. The main function used is from previous years of rocket competitions, but the simulation program itself was developed by the Team Lead this year. The function developed was designed to perform the following:

1) Load thrust data obtained from ThrustCurve.org.
2) Interpolate thrust curve for more discrete steps.
3) Calculate change in mass resulting from burnt propellant.
4) Calculate velocity from the combined impulse from drag, gravity, and thrust.
5) Calculate altitude and acceleration from velocity.

The rocket simulation function operates in the following way.
The velocity of the rocket was determined from the previous momentum plus the impulse. This relationship is shown in Eq. 5:

$$m_i v_i + F_i \Delta t = m_{i+1} v_{i+1} \tag{5}$$

Where F_i is the net force acting on the rocket and Δt is the time step between calculations. The net force acting on the rocket during accent is expressed in Eq. 6:

$$\begin{aligned} F_{net} &= F_{grav} + F_{drag} + F_{thrust} \\ &= m_i g + \frac{1}{2}\rho v_i^2 C_d A + T_i \end{aligned} \tag{6}$$

Where:

ρ is the density of air

C_d is the coefficient of drag

A is the frontal cross sectional area of the rocket

T_i is force from the motor

Substituting Eq. 6 into Eq. 5 and solving for v_{i+1} yields:

$$v_{i+1} = \frac{1}{m_{i+1}}\left[v_i m_i + \frac{1}{\Delta t}\left(T_i - m_i g - k v_i^2 \right) \right] \tag{7}$$

Where:

$$k = \frac{1}{2} C_d A$$

Acceleration was calculated using Newton's second law which is expressed in Eq. 8:

$$a_i = \frac{F_i}{m_i} \tag{8}$$

The trapezoidal method for approximating the area under a curve was used to calculate the altitude of the rocket during the flight.

The simulation calculated the altitude, velocity, and acceleration versus time for the flight until apogee, based on the assumptions as stated in the Assumptions and Limitations section. The drag coefficient for the MATLAB simulation was found in OpenRocket. The drag coefficient used was 0.43.

2.2 OpenRocket. OpenRocket is a free, open source, software similar to RockSim. It is capable of calculating acceleration, velocity, and position data while accounting for variables including: elevation, wind speed, and the effects of individual components on performance such as: surface roughness and leading edge fin radii on drag and stability. Also included in the program is the ability to construct full to-scale schematics of the rocket design. From this schematic the CP and CG can also be approximated.

OpenRocket was the main source used in designing the rocket. The rocket was modeled entirely in the program, providing a way to design and calculate proper lengths of body tubes, optimal fin and nosecone designs, rocket weights, acceptable locations of the CP and CG, and drag coefficients. This was an extremely powerful tool, and it has already been mentioned in several previous sections.

2.3 Flight Predictions. The peak altitude, acceleration and velocity for both simulation methods are shown in **Error! Reference source not found.**.

Table 2: Maximum Flight Predictions		
	OpenRocket	**MATLAB**
Altitude (ft)	3082	3011
Velocity (ft/s)	566	562
Acceleration(ft/s^2)	574	575

3.0 Results

Simulations were run to design and estimate flight performance of the rocket. The two programs that were used were OpenRocket and MATLAB code written by the team. Actual flight data was recorded using a Raven 3 flight data recorder provided by WSGC. The flight of the rocket matched well with the estimates of both simulations. A comparison between predicted and measured results is shown in **Error! Reference source not found.**3.

Table 3: Flight Performance Comparisons		
	Apogee (ft)	**Maximum Acceleration (ft/s^2)**
MATLAB	3011	575
OpenRocket	3082	574
Actual	3061	680
	Percent Error From Actual (%)	
MATLAB	2	15
OpenRocket	1	15

Predicted and actual altitude and acceleration data are shown in Figure 5 and Figure 6, respectively.

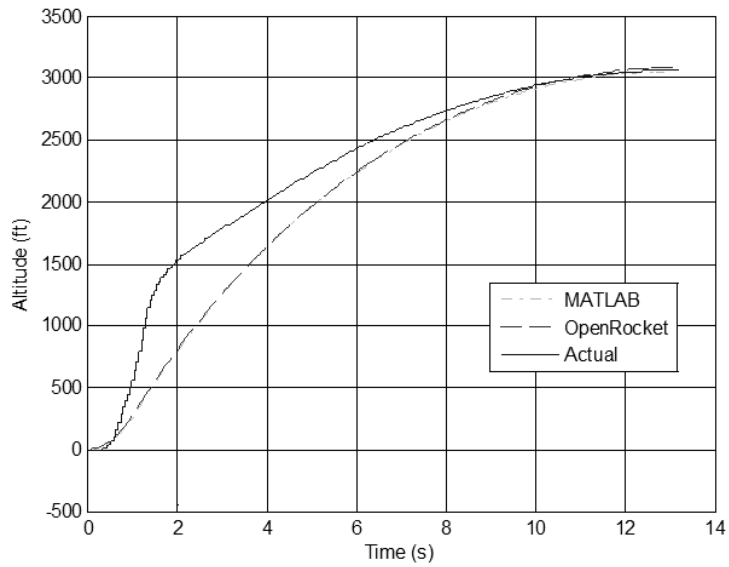

Figure 5: Comparison between predicted and actual

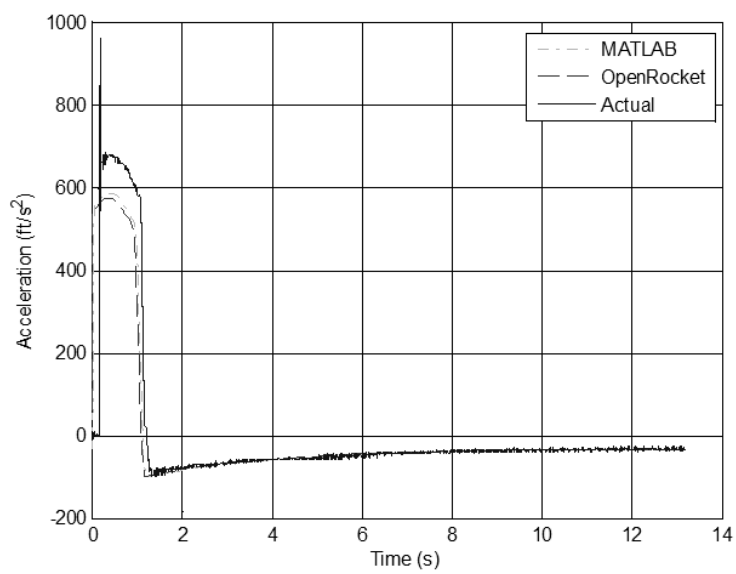

altitude

Figure 6: Comparison between predicted and actual acceleration

The rocket overshot the desired altitude of 3,000 feet by 61 feet. This was fairly good because MATLAB predicted an apogee of 3,011 feet and OpenRocket predicted 3,082 feet. Since the actual apogee was in between these two predicted values (with percent errors of 1 or 2%), the simulations were good representations of the actual flight. For future flights, choosing a weight (reducing it) that places the MATLAB prediction under 3,000 feet and the OpenRocket simulation slightly above 3,000 feet would likely put the actual apogee very close to 3,000 feet.

The maximum acceleration of the rocket was quite higher than predicted. The actual maximum acceleration was 680 ft/s^2, with predicted accelerations of around 575 ft/s^2. This is a percent error of 15%. While this is not an extremely large percent error, it is significant. This discrepancy in acceleration can be accounted for in many ways. The most significant contributor to this discrepancy is likely the weather conditions on launch day. The air was probably less dense than normal, with a temperature around 46 degrees Fahrenheit. It was also very windy and cloudy, contributing to turbulent flow occurring sooner on the rocket than it normally would. The faster jump to turbulent flow reduced pressure drag on the rocket, allowing for a higher acceleration. The rocket surface also probably was smoother than indicated in OpenRocket, allowing for decreased drag as well. Another significant contributor to the rocket seeing a high acceleration could be the motor performing differently than predicted. The motor could have had more propellant than originally stated in the motor specifications, producing greater thrust and, therefore, greater acceleration.

4.0 Conclusion

The rocket was successfully recovered in a flyable condition in compliance with the competition rules. The software utilized for this design predicted the altitude of the rocket to an exceptional margin given the uncertainties present in the launch and design. The acceleration of the rocket was higher than predicted, possibly due to the motor burning differently than expected. Lessons learned through this design will be incorporated into future competitions by returning team members.

5.0 References

Barrowman, James. "The Theoretical Prediction of the Center of Pressure." (1966). Apogee Rockets. Web. 13 Apr. 2013. <http://www.apogeerockets.com/downloads/PDFs/barrowman_report.pdf>.

Team Jarts Rocket Design

Brett Foster, Joe Hintz, Eric Logisz, Cameron Schulz

Milwaukee School of Engineering

Executive Summary

The objective of the 2013 Wisconsin Space Grant Consortium collegiate rocket competition was to construct a rocket to achieve an apogee of 3,000 feet and recover the rocket safely in flyable condition

The rocket was designed to reach an apogee of 3000 feet. The main feature of the rocket includes passively controlling the drag to control the altitude reached. This is done by initial design of the airframe and fins. The other feature is deploying a drogue parachute on the ascent of the rocket in order to stop the rocket at 3000 feet. The rocket was designed to achieve an apogee greater than 3000 feet so that the deployment of a drogue parachute can stop the rocket at 3000 feet. Fiberglass tubing makes up the rocket due to its high strength and durability. Extra support was designed into the rocket to ensure that zippering does not occur. The rocket design included resulting in stable rocket based on the center of pressure and center of gravity.

The recovery system of the rocket involves a dual deployment system. A drogue parachute is to be deployed at 2900 feet to stop the rocket at 3000 feet and control the rockets descent until the main parachute is deployed. The main parachute is then deployed at 700 feet and controls the rocket descent until landing on the ground. There is also a second set of ejection charges that will deploy the drogue parachute at apogee and the main parachute at 500 feet if the main charges do not deploy them. These ejection charges are fired by the MARSA4 and PerfectFlite StratoLogger altimeters. There is also a motor ejection charge backup based on a time delay to ensure the deployment of a parachute.

Analysis of the predicted flight was done in both OpenRocket and MATLAB. OpenRocket predicted an apogee of 3074 feet and MATLAB predicted an apogee of 3092 feet without simulating the deployment of the drogue parachute. A predicted flight including the deployment of the drogue parachute resulted in an apogee of 2990 feet.

A variety of testing was done to confirm the design and function of the rocket. This testing includes ground testing for the deployment of the parachutes, altimeter testing for the confirmation of the programming and function and two test launches. During the first test launch, the parachutes were deployed at maximum acceleration. No damage occurred on the rocket confirming the structural design of the rocket. The second test launch resulted in a successful flight reaching an apogee of 3272 feet. The drogue parachute did not deploy during this launch. This allowed for a more accurate coefficient of drag to be calculated. This then lead to more accurate predictions of the achieved apogee with the deployment of the drogue parachute. Figure 1 shows the rocket on a component by component basis.

Figure 1: Rocket Components (OpenRocket Model)

Objective and Constraints

Scope. The objective of this project is to design a one-stage, high powered rocket that has an apogee of 3000 feet. The rocket must be recovered in flyable condition safely. The desired flight is shown in Figure 2.

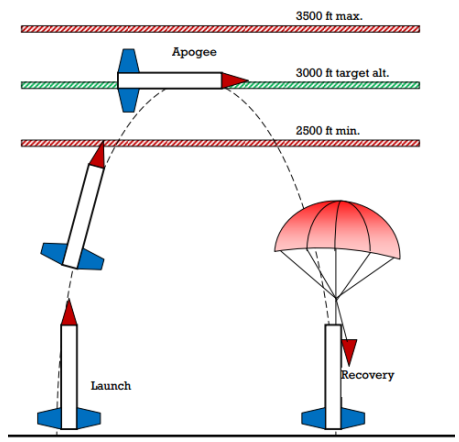

Figure 2: Desired Rocket Flight

Source:
http://www.uwgb.edu/wsgc/collegiate_rocket_launch/2013/RocketCompetition13Handbook.pdf
(4/3/2013)

Application. The Wisconsin Space Grant Consortium (WSGC) collegiate rocket competition allows students to apply engineering skills learned in class directly to a project. This results in a great experience in the aerospace field. WSGC intends to further the education and experience of students in order to benefit the future in Space and Aerospace science, design and technology in Wisconsin. This allows students to develop their skills for the future. High powered rocketry involves a lot of concepts learned in an engineering education. Concepts such as aerodynamics, statics, dynamics, numerical analysis, etc. can be applied.

Design Requirements. The following are design parameters for the 2013 WSGC Collegiate Rocket Competition:

- Altitude of at least 2500 feet but not to exceed 3500 feet reached
- Rocket recovered safely and in flyable condition
- Electronics used to deploy a parachute for your recovery system as well as have an engine based backup deployment
- Structural components and materials obtained from a reputable high powered rocket vendor or provide engineering analysis supporting their suitability
- Cesaroni I540 used as the motor
- Raven III altimeter carried on board as the competition altimeter
- Maximum body tube diameter of 4 inches
- Maximum overall length in launch configuration of 72 inches
- Maximum weight in launch configuration less motor of 7.5 pounds

Design

Summary of Design. A simple design for the rocket was chosen to eliminate as many unneeded risks as possible. The idea that many things can go wrong with a rocket was considered and therefore the design was chosen such that it added as little more risks. The drag force of the rocket was the main component used to control the apogee of the rocket. This is done both passively and actively. The rocket was designed such that the simulation of apogee is just over 3000 feet. Also, the design actively controls the altitude by releasing a parachute on the way up near 2900 feet the stop the rocket at 3000 feet.

Airframe Design. The overall length of the rocket is 67.75 inches with a body tube diameter of 3.129 inches. These overall dimensions determined by many factors. Factors that include the space inside the rocket for parachutes, electronics, shock cord and more, the resulting center of gravity and center of pressure of the rocket which determines stability and the approximate altitude the rocket will reach. The length, weight, and diameter of the rocket also meet the constraints given. The rocket also has three clipped delta fiberglass fins evenly spaced around the bottom of the rocket's airframe. The shape of the fin was chosen based on where the desired location for the center of pressure of the rocket should occur. The three fins are sufficient to maintain a stable flight with a center of pressure lower than the center of gravity. Not needing a fourth fin reduces the drag of the rocket. The fins are through the wall fins for sufficient strength and are attached to the motor mount tube that is secured by several centering rings spaced along the tube.

The rocket will be comprised of 5 sections. These sections include the nose cone, the upper tube, a coupler, the lower tube with a coupler attached, and an engine mount section. The rocket will break at the nose cone and right above the engine mount. The rest of the sections will be secured by pem nuts and screws. These sections are shown in Figure 3.

Figure 3: Rocket Components (OpenRocket Model)

Fiberglass tubing with a diameter of 3.129 inches makes up the main airframe of the rocket. Fiberglass was chosen due to its high strength as well as its low weight. Fiberglass also provides durability that other common rocket materials do not provide. With the plan of launching multiple times before the competition day, durability of the rocket is an important factor.

Along with the strength of fiberglass, extra design was done to reduce the chance of zippering. Zippering of the body tube becomes a big factor especially when launching a parachute on the ascent of the rocket flight. Besides the strength of the material, the rocket was designed with extra strength right above the engine mount where the drogue parachute will exit on the ascent of the rocket flight. A centering ring was added right above the engine mount in order to increase the surface area that the shock cord will rip down on. This will reduce the shearing force exerted by the impulse of the shock cord after the drogue parachute is released. An axial support tube was added to support this centering ring as it will only be attached to the engine mount tube and not the outer wall. A picture of this section is shown in Figure 4. In addition, the length of the shock cord is 15 feet in order to reduce the impulse force exerted.

Figure 4: Zipperless Design Feature

Recovery System. In order to recover the rocket safely and in flyable condition, a dual deployment system will be used. The components used in the system include a 48 inch main parachute, a 24 inch drogue parachute, 30 feet of 1500 pound test Kevlar cord, lettuce and nylon shear pins. The 24 inch drogue parachute shrouds can be pulled tighter to decrease the drag force. The Kevlar cord was chosen due to its low weight but high strength properties as well as its fire resistance. Lettuce will not allow the parachutes to burn when the ejection charges are blown. Nylon shear pins will be used to attach the nose cone to the upper section tube and the engine mount section to the coupler attached to the lower section tube. These

nylon shear pins will shear when an ejection charge is blown, causing the rocket to separate at the desired locations. Figure 5 shows the two parachutes and Kevlar cord.

Figure 5: Parachutes and Shock Cord

The recovery system begins after the engine burnout occurs as well as the rocket coasting until 2900 feet. At 2900 feet an ejection charge will blow from an altimeter based trigger, deploying the drogue parachute from the break point right above the engine mount where extra support exists. The drogue is attached to 15 feet of 1500 pound test Kevlar cord. This drogue parachute acts as a break parachute in order to stop the rocket at 3000 feet. The rocket will then have a rapid, controlled descent under the control of the drogue parachute until 700 feet. At 700 feet above the ground, the main parachute will be deployed via another ejection charge from the same altimeter based trigger. The main parachute will exit the rocket from the upper section tube when the nose cone is blown off. A controlled descent will then occur until the rocket lands on the ground safely.

With the risk of parachutes not deploying, a second set of charges will be present, which are triggered from a separate altimeter. The first charge will be set to trigger at apogee in case the drogue parachute does not deploy on the way up at 2900 feet. The second charge will trigger at 500 feet in case the main parachute does not deploy at 700 feet during the rocket's descent. As well as having redundancy with two altimeters, a motor ejection charge based on a time delay will be used. This will ensure that a parachute will come out regardless of the functioning of the electronics. The built in redundancy as well as the backup motor ejection charge will ensure safe recovery of the rocket, resulting in a rocket returning in flyable condition.

Electronics Bay. The coupler section joining the upper and lower sections of the rocket is where the electronics are housed. The section consists of an 11.75 inch long coupling tube with a 2.5 inch fiberglass thrust ring epoxied around the coupling tube. This section is displayed in Figure 6.

Figure 6: Electronics Bay

Each end of the electronics bay is capped with a bulkhead that has a U-bolt mounted on it as well as a bridge. The shock cord is attached to each of the U-bolts to connect the whole rocket. The bridges are used to connect the wires from the altimeters to the ejection charges. This is shown in Figure 7.

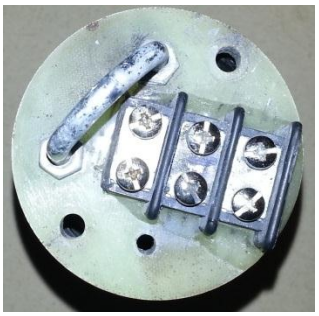

Figure 7: Bulkhead for Electronics Bay

Threaded rods are run through the whole length of the electronics bay to secure the bulkheads as well as provide a way to mount the altimeters. The altimeters are mounted on plywood sleds with standoffs and screws. These sleds also have metal tubing epoxied to them so that they can be slid onto the threaded rods in the electronics bay. For ease of assembly and access, two sleds were made to slide in from either end of the bay and meet in the middle. There are spacers in between these sleds such that key switches can be mounted. Three key switches are mounted to the outside of the electronics bay that will allow one to turn on each altimeter separately while the rocket is on the launch rail. This system ensures the altimeters are securely mounted as well as allows for ease of assembly and disassembly.

The primary altimeter used for this rocket is the MARSA4, a programmable parachute deployment system. This altimeter allows for 4 separate channels to trigger ejection charges. Some other features include field programmability, data analysis and diagnosis. The combination of these features allow for the descent of the rocket to be controlled as described in the recovery system section. The capability to launch the drogue parachute on the ascent is an important feature for the rocket's performance. The programmability of the altimeter along with the post flight data analysis ensures the most successful flight. The MARSA4 is shown in Figure 8.

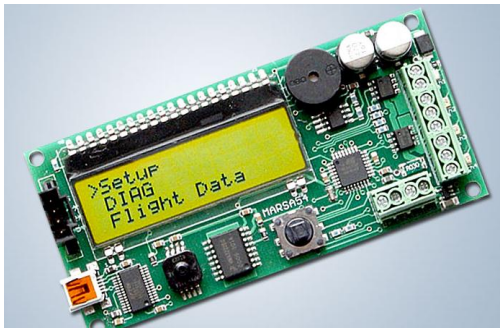

Figure 8: MARSA54 Parachute Deployment System
Source: http://www.rocketryplanet.com/content/view/3541/29/#axzz1KVksSdHZ (4/3/2013)

The second altimeter on board the rocket is the PerfectFlite StratoLogger Altimeter. This altimeter is capable of deploying the drogue parachute at apogee and the main parachute at an altitude ranging from 100 feet to 9,999 feet in 1 foot increments. This satisfies the conditions that this secondary altimeter needs to perform. This altimeter records the data from flights and will output altitude and velocity plots. Although this altimeter has lower accuracy than the MARSA4, it fulfills the requirements to serve as a redundant altimeter. The StratoLogger is shown in Figure 9.

Figure 9: PerfectFlite StratoLogger

Source: http://www.perfectflite.com/sl100.html (4/3/2013)

Along with the two altimeters described above, a Raven III will be housed in the electronics bay. This altimeter will serve as the competition altimeter to record flight data. It will have the official data for the altitude of the rocket. This altimeter is housed in the same bay as the other electronics to ensure accurate, consistent data.

Center of Pressure & Center of Gravity

OpenRocket was used to determine the locations of the center of pressure and center of gravity. This program allows one to perform a component by component design with custom overrides for materials, weights, dimensions, etc… The properties of the purchased materials can then be updated into the model. The program also allows for ease of design for stability. As each component is added or changed the location of the center of pressure and center of gravity is updated. This analysis ensures that a stable rocket will be designed. The resulting calculations for the locations of the center of gravity and the center of pressure are shown in Figure 10. The center of pressure must be located more than 1 airframe diameters below the

center of gravity to make the rocket stable. The design of the rocket resulted in a stability margin of 2.03. This margin is a little over stable. The result of this is not an optimal performance by the rocket in windy conditions. This would lead to a lower maximum altitude. Since the stability of the rocket flight is an important factor, this design is suitable. With the over design of the rocket reaching greater than 3000 feet, there is a factor built in for the rocket not reaching maximum altitude if the conditions are very windy.

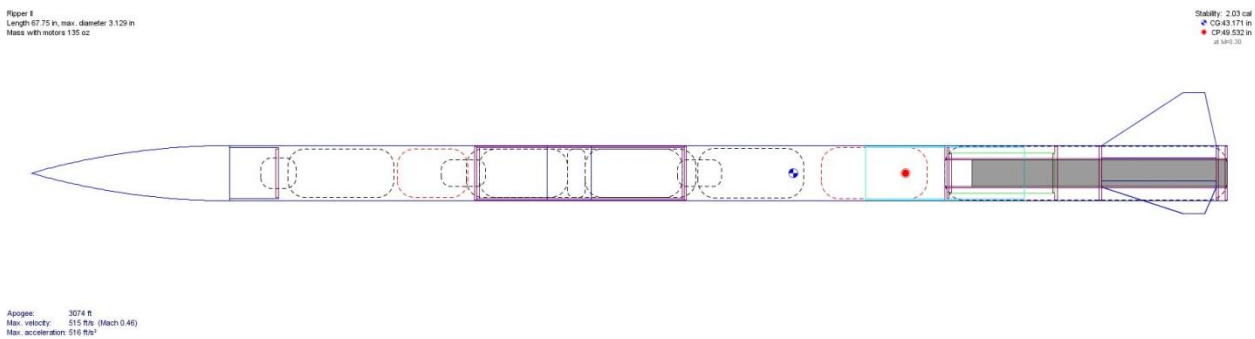

Figure 10: OpenRocket Construction Analysis

CP_{Rocket} =49.5” from top of rocket
CG_{Rocket} = 43.2” from top of rocket **with motor**
CG_{Rocket} = 40.0” from top of rocket **after burnout**
Stability Ratio = 2.03

Analysis of Anticipated Performance

Overview. Two methods of simulation were used in order to predict the performance of the rocket. These include the utilization of OpenRocket and MATLAB. OpenRocket was used for analysis earlier regarding the center of pressure and center of gravity as well as apogee predictions. OpenRocket can take into account wind forces, lift forces, drag forces, and much more. On the other hand, the MATLAB code written has more assumptions, but can be manipulated more. In MATLAB, there is more control over determining specific velocities at altitudes. Also, a simulation of the stopping distance after the drogue parachute is deployed is possible.

OpenRocket. Table 1 includes the predicted altitude and acceleration in ideal conditions.

Table 1: OpenRocket Anticipated Performance

Maximum Altitude	3074 ft
Maximum Acceleration	516 ft/s^2

The above anticipated performance was performed under ideal conditions, or no wind conditions. This will not be the case on the day of the launch, so analysis on wind effect on altitude was conducted. Anticipated performance of the rocket was done at wind speeds of 5 mph to 20 mph at 5 mph increments. Figure 11 illustrates the results of this analysis.

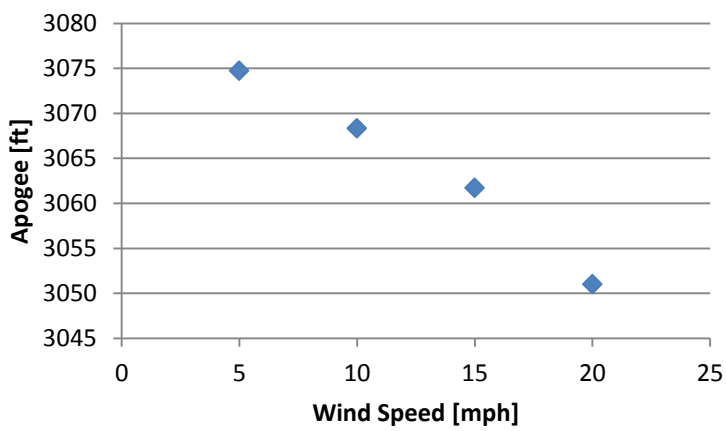

Figure 11: Effect of Wind Speed on Altitude

As illustrated above, even with extreme wind conditions of 20 mph, the predicted altitude of the rocket will still reach over 3000 feet.

MATLAB. The rocket flight consists of two segments:

i. During the 1st segment, the rocket is propelled upward by a variable thrust force opposing gravity and drag forces for a short time after which time the rocket fuel is exhausted and
ii. In the 2nd segment, the rocket continues to ascend with no thrust while slowing down due to gravity and drag until it reaches an apex in altitude.

With the experimental data of a thrust curve and known properties of a rocket, the rocket's flight can be modeled with aerodynamic drag while accounting for dependent thrust and variable change in mass of the rocket.

Assumptions. To model the rocket's flight to apogee taking into account every parameter would not be practical. Therefore, some assumptions were made. The following are the assumptions made when modeling the rocket flight.

i. Thrust Burn- Although thrust is not being assumed to be constant, it is being assumed that the thrust has a constant even burn.
ii. Gravity – Gravity is assumed to be a constant of 9.81 m/s^2. The change in gravity is so small, it will be considered negligible.
iii. Wind – It is assumed that there was minimal transverse wind, meaning that it will not be accounted for in the model.
iv. Vertical Flight – In order to simplify the model to fit our needs, it will be assumed that the flight of the rocket was strictly vertical.
v. Drag Force – When modeling this numerically, the following assumption will be made for the drag force.

Aerodynamic drag

$$F_D = \frac{1}{2}\rho C_D A V^2$$

where ρ is the density of air, C_D is the drag coefficient, A is the rocket cross-sectional area and V is the velocity of the rocket.

vi. Density-The density of air was assumed to be constant throughout the entire portion of the flight.

ρ_a=0.00238 slug/ft^3

Mathematical Model.

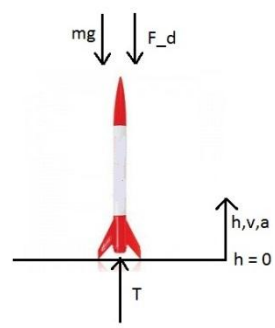

Figure 12: Free Body Diagram (thrust phase)

The conservation principle governing this free body diagram (thrust phase) is the following:

$$\sum F_{Vert} = \frac{d}{dt}(mv)$$

where the initial conditions are the following:

$$v(t=0) = 0\, ft/s$$
$$h(t=0) = 0\, ft$$

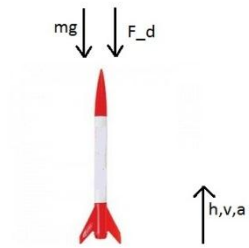

Figure 13: Free Body Diagram (after thrust phase)

The conservation principle governing this free body diagram (after thrust phase) is the following:

$$\sum F_{Vert} = \frac{d}{dt}(mv)$$

where the initial conditions are taken from the end of the thrust phase.

Numerical Model. Linear interpolation was used to extract data points of the thrust of the motor to take in account the variation. (http://www.thrustcurve.org/simfilesearch.jsp?id=1398)

The thrust curve determined by interpolating the given data was numerically integrated using the Trapezoidal Method as shown below.

$$\int T(t) = \left(\frac{T_i + T_{i+1}}{2}\right)dt$$

The percentage of the thrust burned off compared to the total impulse was calculated as shown below. (The integral of the thrust curve was cumulatively added while numerically integrating)

$$m_{fuel} = m_{fuel\_total} - m_{fuel\_total}\left(\frac{T_{cumulative}}{I}\right)$$

where I is the net impulse.

The mass during the thrust phase was calculated by the following expression.

$$m = m_{rocket} + m_{fuel}$$

After the thrust and mass were determined for each time step, fourth order Runge-Kutta numerical integration was used to calculate the velocity history. The acceleration expression used is from the conservation principle applied when determining the governing differential equation. The following describes the general form of fourth order Runge-Kutta numerical integration.

The four following slopes are determined first.

$$\varphi_1 = \varphi_i$$
$$\varphi_2 = \varphi(t_i + \frac{\Delta t}{2}, y_i + \varphi_1 \frac{\Delta t}{2})$$
$$\varphi_3 = \varphi(t_i + \frac{\Delta t}{2}, y_i + \varphi_2 \frac{\Delta t}{2})$$
$$\varphi_4 = \varphi(t_i + \Delta t, y_i + \varphi_3 \Delta t)$$

After the four slopes are calculated, the following relationship is used.

$$y_{i+1} = y_i + \frac{1}{6}(\varphi_1 + 2\varphi_2 + 2\varphi_3 + \varphi_4)\Delta t$$

The following algorithm was used to calculate the velocity history.

$$\varphi_1 = \frac{T_i}{m_i} - g - \frac{F_{D_i}}{m_i}$$
$$v^*_{i+1/2} = v_i + \varphi_1 \frac{\Delta t}{2}$$
$$\varphi_2 = \frac{T_{i+1/2}}{m_{i+1/2}} - g - \frac{F_{D_i+1/2}}{m_{i+1/2}}$$
$$v^{**}_{i+1/2} = v_i + \varphi_2 \frac{\Delta t}{2}$$
$$\varphi_3 = \frac{T_{i+1/2}}{m_{i+1/2}} - g - \frac{F_{D_i+1/2}}{m_{i+1/2}}$$
$$v^{***}_{i+1} = v_i + \varphi_3 \Delta t$$
$$\varphi_4 = \frac{T_{i+1}}{m_{i+1}} - g - \frac{F_{D_i+1}}{m_{i+1}}$$
$$v_{i+1} = v_i + \frac{1}{6}(\varphi_1 + 2\varphi_2 + 2\varphi_3 + \varphi_4)\Delta t$$

An Euler algorithm was used to solve for the altitude history.

The following is the basic form of the Euler algorithm.

$$x_{i+1} = x_i + \frac{dx}{dt}(i) * \Delta t$$

It is also known that:

$$h_{i+1} = h_i + v_i * \Delta t$$

The above algorithm is used during the thrust phase of the flight. Once the motor burns out, the algorithm remains the same except that the thrust term is taken out.

Predicted Velocity History.

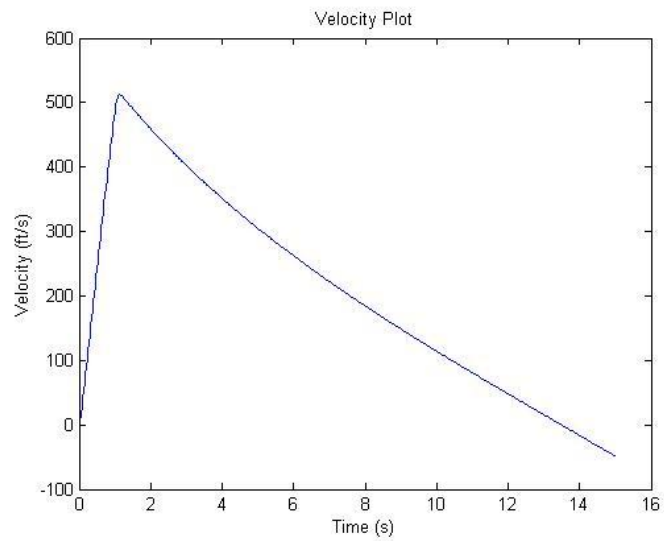

Figure 14: Velocity History Plot of the Rocket Produced by MATLAB

The maximum velocity during the flight is 513 ft/s. Note that the velocity after about 13 seconds (apogee) does not reflect the actual predicted velocity of the rocket.

Predicted Acceleration History.

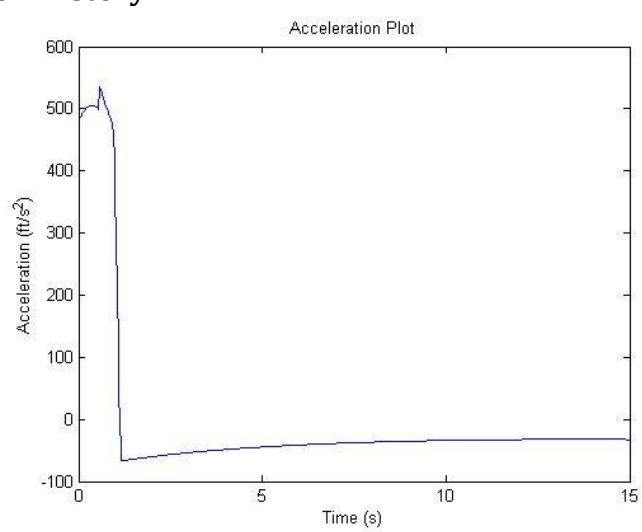

Figure 15: Acceleration History Plot of the Rocket Produced by MATLAB

It is anticipated that acceleration is initially positive since thrust is applied. The acceleration decreases during this phase because the drag force is increasing. Acceleration is negative after thrust ends because the rocket is slowing down. It should be noted that the maximum acceleration achieved in the flight is 537 ft/s^2.

Summary of Flight Performance.

Maximum Acceleration	**537** $\boldsymbol{ft/s^2}$
Maximum Altitude	**3092** $\boldsymbol{feet}$
Time to Apogee	**13** $\boldsymbol{seconds}$

Table 2: Pre-Flight Analysis Predictions of Results

Although the maximum altitude is predicted to be 3092 feet, the rocket will be stopped at 3000 feet due to a drogue chute. Therefore the time to apogee will also be less.

The analysis does not take into account launching a drogue parachute on the way up. Since there were test flights completed, more accurate data was used to predict the stopping distance. This analysis can be found in the testing section under stopping distance.

Testing

Ground Testing. A test was performed to size the ejection charges. The rocket was packed as it would when ready for launch, except the ejection charges were wired to an electronic trigger. Both the upper section and lower section were tested such that the size of the ejection charges would shear the shear pins and the parachutes would come out. This test was performed and the parachutes were deployed successfully on the ground.

Altimeter Testing. A test was performed in order to ensure the programming and function of the altimeter. This test was done on the MARSA4, the primary altimeter. The test was based on barometric pressure only. The altimeter was placed inside a plastic jar, where the wires to the e matches were wired through the jar and then epoxied to seal the hole created. A lid for the jar was constructed with fittings through the middle such that a tube can be attached to the outer fitting. A hand vacuum pump was then attached with a tube to this fitting. The pressure change caused by the vacuum pump will simulate a change in altitude by the barometric sensor reading the pressure. Through published tables, it was determined that a 3 or 4 in Hg change in pressure, would simulate the rocket reaching an altitude of 3000 feet (http://www.sablesys.com/baro-altitude.html). The jar is able to change the pressure by 5 or 6 in Hg. A picture of the setup is in Figure 17.

Figure 17: Altimeter Test Setup

To conduct the test, the altimeter was armed in the same way that it would be on the launch rail in the rocket. Then the pressure was changed via the hand vacuum pump to simulate a flight. The e matches fired when they were programmed to fire. Watching the test and looking at the data recorded on the computer confirmed that our altimeter was programmed correctly and functioning correctly.

Test Launches. Two test launches were performed in order to test the simulations and the overall function of all the components of the rocket. This will also allow for changes to be made before the competition launch day.

Test Launch #1 The first test launch had an error with the altimeter causing the parachutes to deploy immediately. After diagnosis of the altimeter, low voltage occurred on the altimeter causing it to fire the ejection charges. This occurred at maximum acceleration during the initial thrust phase. The rocket reached an altitude of around 700 feet and then descended down under the control of both parachutes. After retrieving the rocket safely, no damage occurred and the rocket returned in flyable condition. This verified the structural design of the vehicle. It confirmed that the additional support and choice of fiberglass prevented zippering. This then confirms that deploying a parachute on the way up will not cause zippering of the body tube.

Test Launch #2 The second test launch was a successful flight in regards to the competition parameters. The rocket achieved an apogee of 3272 feet and was recovered safely in flyable condition. This meets the window of apogee occurring between 2500 feet and 3500 feet. During the flight, the drogue parachute never deployed due to catching on the wing nut and screw of the rail button. Although this feature did not function properly, this allowed for recorded data of just the flight of the rocket. Without the drogue deploying, this altitude can now be compared to the simulated models. From this data, a more accurate coefficient of drag can be backed out. Even though there is still error in the simulated model, this will allow for more accurate calculations of stopping distances when the drogue is deployed correctly.

Stopping Distance Analysis

In order to model the stopping of the rocket once the drogue parachute is deployed, the following free body diagram was considered.

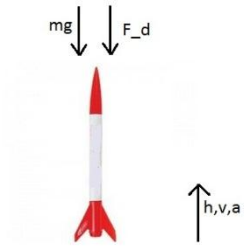

Figure 18: Free Body Diagram (Drogue Deployed)

The same forces are applicable as during the coasting phase of the rocket except that the coefficient of drag now includes the parachute. The parachute has a large cross sectional area and a larger drag coefficient, increasing the drag forces significantly. A coefficient of drag of 1.2 was used. The cross sectional are was calculated based on the size of the parachute. This was done for several different sizes of parachutes. Based on this data, the 24 inch drogue parachute has the capability to stop the rocket by 3000 feet when firing the parachute at 2900 feet. The parachute size could also be altered by tightening the shroud lines. A tenth of a second delay was added for the delay to fire the ejection charge based on the altimeter. Figure 19 shows an altitude history plot with the inclusion of the deployment of the 24 inch drogue parachute.

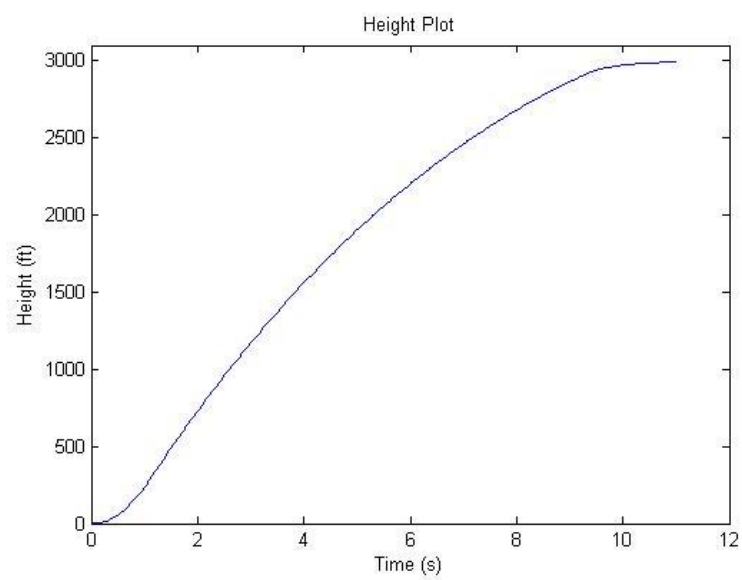

Figure 19: Altitude History with Drogue Deployment

The final altitude with the drogue deployment in the simulation is 2990 feet.

Conclusion

"The Ripper II" was designed with minimal additional features that can cause problems. Due to this simplicity, the main control of altitude is by passively controlling drag via the design of the airframe and fins of the rocket. The altitude is also controlled by actively controlling the drag. This is done by deploying a parachute on the ascent of the flight to stop the rocket at 3000 feet. Analysis simulating the flight of the rocket was conducted as well as the simulation of the stopping distance of the rocket after the drogue parachute is deployed. The simulated apogee of the rocket occurs at 2990 feet. This satisfies the parameters of the competition and is very close to the objective. The recovery system that includes dual deployment with redundancy along with a backup motor ejection charge will ensure the rocket returns safely in flyable condition. Along with testing in the form of stationary tests and test launches, the design of the rocket will lead to a successful flight with an apogee nearing 3000 feet.

Acknowledgement

Team Jarts' thanks Wisconsin Space Grant Consortium (WSGC) for their contributions to make this project possible.

23rd Annual Conference
Part Six

Engineering

Reliability Analysis of Light Emitting Diode Technologies for Cabin Lighting in Manned Space Flight Applications

Todd H. Treichel[1]
Orbital Technologies Corporation, Madison, Wisconsin 53717

Light emitting diode (LED) technology is used by the commercial markets to replace traditional fluorescent and incandescent lighting technologies for consumers to take advantage of energy savings. Advantages of transitioning to LED technologies in spacecraft are reduced mass, reduced occupied volume, reduced power, improved color control, longer operating life, and lower cost associated with power consumption and disposal. Components and subsystems that make up the Environmental Control and Life Support System (ECLSS) require continued performance and operation. A system failure cannot be tolerated for it is extremely difficult to repair and expensive to replace. Therefore, the vehicular LED module must function when launched and continue to function throughout the respective product life-cycle (days, month, or years depending on mission). This analysis evaluates three different LED package types for reliability performance using Electrical, Electronic, and Electro-mechanicals (EEE) parts testing techniques. The goal of the study was to investigate the suitability of commercial off the shelf (COTS) LED technologies in accordance with a probable EEE parts management plan.

Nomenclature

C^O	=	degrees Celsius
COTS	=	commercial off the shelf
DOD	=	department of defense
ECLSS	=	environmental control and life support system
EEE	=	electrical electronic and electro-mechanical
FSC	=	federal stock class
G	=	acceleration force due to gravity
HI-REL	=	high reliability
Hz	=	hertz
ISS	=	international space station
LED	=	light emitting diode
LEO	=	low earth orbit
LUX	=	lumens per meter squared
MIL	=	military
NSPAR	=	non-standard part application request
QML	=	qualified manufacturers list
QPL	=	qualified parts list
RH	=	relative humidity
SSP	=	space station program
rmsG	=	root-mean square acceleration
UV	=	ultraviolet
VDC	=	voltage from direct current
µmol	=	micromole
WSGC	=	wisconsin space grant consortium

[1] Systems Engineer, Space Center, 1212 Fourier Drive, Madison, Wisconsin, USA

I. Introduction

AEROSPACE and military applications are those where continued performance and operation -on-demand is critical, equipment downtime cannot be tolerated, end-use environments may be uncommonly harsh, and the equipment must function when required (Hersman & Fowler, 2009). Technology in the electronics industry changes rapidly and engineers within the aerospace industry do not always have access to new technology due to high-reliability (HI-REL) requirements established in DOD and NASA procurement standards. Engineers designing for commercial products can experiment with new technologies with little or no restrictions in design component selection. Military and aerospace engineers are required to manage product designs by making component selections from DOD and NASA approved part lists, where specific components have been tested extensively and heritage field data is cataloged for quality and reliability performance. New electronic technologies are being developed and by the time these technologies become available on a DOD quality parts list (QPL) or quality manufacturer's list (QML), the technology may have been replaced or improved in the commercial markets, thus making it difficult for aerospace engineers to select state-of-the-art design components without extensive testing. This analysis investigates the suitability of selecting white LED components from three leading manufacturers currently supplying commercial markets.

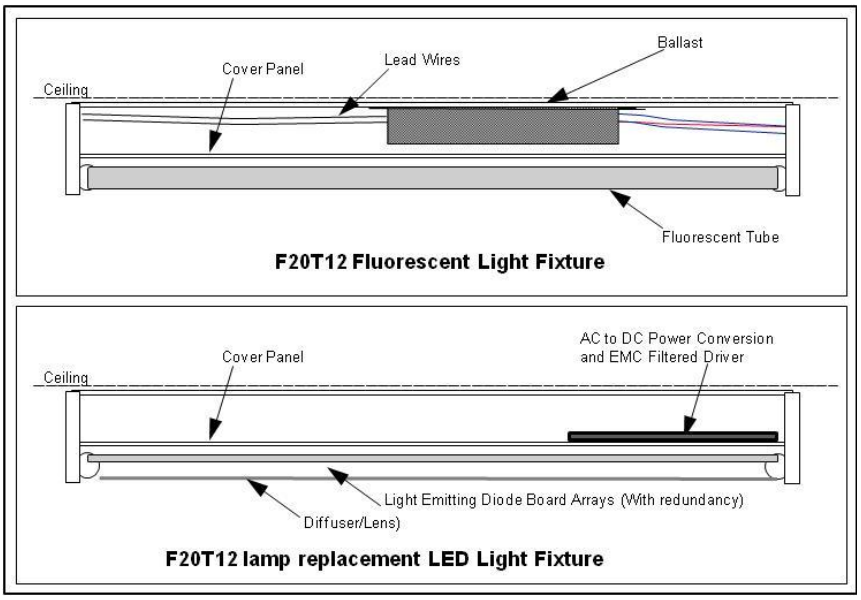

Figure 1. Schematic of fluorescent light replaced with LED technology.

II. Light Emitting Diodes

Light emitting diodes are semiconductors that convert electrical energy into light energy. The color of the emitted light is designed into a specific semiconductor material composition for each component where individual LEDs may be selected for mixing of colors to obtain a desired color of light output. Light emitting diodes are classified into ultraviolet, visible, and infrared wavelengths depending on the technological application (Lenk & Lenk, 2011).

Development of high-power LED technology involves challenges for design engineers in that LED lighting devices are subject to high temperatures that must be properly managed. Increased junction temperatures of the LED chip, causes stress on associated material and may cause earlier than expected light output degradation which will lead to an operational failure. Lenk and Lenk (2011) described two primary methods for producing high intensity white-light using LED technology: (1) one is to use individual LEDs that emit the three primary colors of red, green, and blue, and mix the three colors to produce white light, and (2) is to use a phosphor material to convert monochromatic light from a blue or ultraviolet (UV) LED to broad-spectrum white light. The latter of these two primary methods are applicable to the investigation

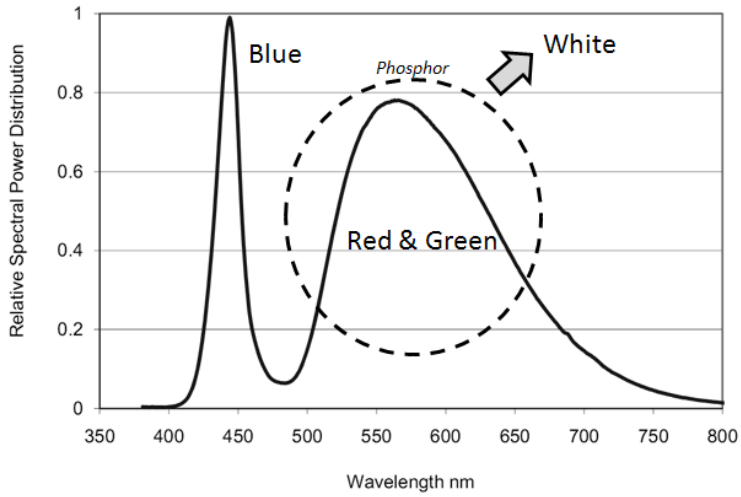

Figure 2. Broad-spectrum white light color distribution model.

discussed herein.

Light emitting diode technology can provide the military and space community with advantages when compared to the current use of incandescent light sources including: (a.) lower power consumption, (b) improved reliability by use of redundancy, (c) improved ruggedness for harsh environments, (d) lighter weight, (e) smaller size, (f) improved control over color and brightness and, (g) faster switching. Figure 1 illustrates the differences between a fluorescent light fixture, commonly used in military applications such as US Navy vessels, and the smaller, and lighter weight LED technology which may be retrofitted into an existing fluorescent light fixture.

III. Purpose of Investigation

Advantages, similar to those previously mentioned, have been noted by Brainard, Coyle, Ayers, Kemp, Warfied, Maida, Bowen, Bernecker, Lockley, & Hanifin (2012). The International Space Station (ISS) contains fluorescent light technologies for illuminating the astronauts' research and living environments NASA engineers have built a case for replacing fluorescent lighting with LED technology due to advantages such as: (a) lower heat generation, (b) lower power consumption, (c) less weight, (d) greater resistance to damage, (e) less toxic material, (f) elimination of fluorescent tube disposal, and (g) improved reliability. The fluorescent lamp technology on ISS is aging and there is an acceleration of failures which require replacement, due to a deficiency of NASA flight qualified fluorescent units, LED technologies provides an opportunity for retrofitting the ISS with lighting that has improved efficiency, no mercury, and improved reliability (Brainard et al., 2012). Little is known about which commercially available LED components are the most robust in accordance with aerospace requirements. This information will prove useful for future commercial space applications which may include both vehicles and habitable structures.

Flexible Path Space Missions

In September of 2009 the 156 page *Augustine report* was published, by the US Government Printing Office, documenting a new space exploration concept called *flexible path*. Flexible path is a concept that involves human space flight vehicles and missions travelling beyond low-Earth-orbit (LEO) and unlike past space missions managed by NASA, development of space vehicles, rocket engines, and instrumentation will be the responsibility of commercial companies with NASA oversight (Szajnfarber, Coles, Sondecker, Wicht, & Weigel, 2011). Commercial aerospace companies are to be utilized, in lieu of NASA resources, in an effort to save costs and add flexibility with choices in technology and mission objectives. Flexible path missions require commercial crew launches to LEO, followed by further technology developments for exploration to destinations farther away from Earth, such as asteroids, the Lunar surface, and Mars (Szajnfarber et. al, 2011).

Literature contained in the Augustine report provides a baseline for this analysis. Research and analysis of LED technology is justified with the intent of meeting human space flight goals by conducting development and mission operations with improved efficiency and lower cost. Flexible path missions will involve risk, management of lifecycle cost, and development of reliable equipment capable of reliable on-demand-operation over the course of the entire mission.

Aerospace Technology Readiness

Hersman and Fowler (2009) emphasized that electronics on spacecraft must be able to withstand the space environment to assure mission success and meet design criteria that is more robust than equivalent commercial products available for terrestrial applications. Engineers working in the aerospace and military industries, order relatively low quantities of space qualified electrical components, often at irregular intervals, with long lead times, and high dollar costs for specialized manufacturing. Light emitting diodes remain an unproven technology in the aerospace industry, where commercial manufacturers are the only source for procurement and require research for space flight suitability. Engineers are required to reference NASA or DOD approved parts lists and select parts based on flight heritage and proven reliability. Approved components are termed *high reliability* (HI-REL) and are listed by Federal Stock Class (FSC) numbers on lists called quality parts list (QPL) and quality manufacturer's list (QML), managed by the US Defense Logistics Agency (DLA). No FSC number exists for LED component technologies. These parts lists are updated periodically and inclusion of new technology is slow due to lack of historical flight or reliability data.

Advancements in technologies are made in the commercial sector where state-of-the-art component technologies are not accessible to aerospace engineers when designing space flight hardware. Selection of commercial parts to be considered grade level three (see Table 1) because proof-of-concept and reliability test data are not available for reference, thus rendering these new technologies unavailable for immediate use. The only

alternative is to select a commercial off the shelf (COTS) component and perform *electrical, electronic, and electromechanical* (EEE) qualification testing to provide evidence that selected components are capable of meeting specified mission requirements.

Selecting grade level three parts is the least desirable option for engineer component selection and a literature review of NASA parts management documents yielded that there are no specified test paths for qualifying LED technology for space flight. Grade level three parts are classified as the highest risk selection. Table 1 illustrates criteria of grade level classifications assigned to component reliability. Parts not EEE listed are to be evaluated for space flight heritage, similarity, and existing test data for the purpose of classifying parts to desired grade level.

Table 1. Key requirements for project initiation and management

Grade Level	Mission Selection Criteria
1	Components selected for mission application requiring the highest reliability and lowest level of risk. Typical mission durations are five years or longer.
2	Components selected for low to moderate risk. Selection is to be balanced by cost constrains and mission objectives. Reliability and performance data specific to desired mission may not be available and some testing may be required. Typical mission durations are one to five years.
3	Components selected for mission represent inherently high risk unknown risk due to lack of formalized reliability assessment, screening, and qualification. Available data does not address flight history and construction materials, manufacturing, and design processes are in continuous change, which is unreliable due to lack of consistency and process repeatability. Level three components are the least desirable for use where typical mission durations are less than one to two years.

IV. EEE Test Plan

Components used for flight design and construction are evaluated for HI-REL heritage and suitability. Documents such as SSP 30312 *Electrical, Electronic and Electromechanical (EEE) and Mechanical Parts Management and Implementation Plan for Space Station* and NASA-EEE-INST-002 *Instructions for EEE Parts Selection, Screening, Qualification, and Derating* are typically referenced for managing qualification and up-screening techniques for evaluation of COTS parts usage in flight system designs.

When approved within the non-standard part application request (NSPAR) document, screening tests may be employed with the intent to remove nonconforming parts (parts with random defects that are likely to result in early failures, known as infant mortality) from an otherwise acceptable lot and thus increase confidence in the reliability. A technology review board holds authority over NSPAR approval where certain part requirements may not be sufficient, depending on the specific device construction, mission life and reliability goals of the project. For the purpose of this analysis no NSPAR documents were involved and for the promotion of science and not LED companies, product brand names have been omitted from the three selected LED manufacturers selected for investigation. Figure 3 illustrates graphical representations for the three different LED package types, purchased from industry leading manufacturers, for the purpose of this EEE evaluation.

Environmental tests are applied to accelerate the aging rate of a product by elevating and/or cycling the product temperature. The process may be amplified by introducing other environmental factors such as vibration and shock etc. Regardless of the technique employed, the purpose of environmental testing is twofold:

1) To weed out the early life failures. The intent is to detect non-conformances before the product is shipped to the customer. By doing this, the customer should experience a low failure rate characterized by the useful product life.

2) To provide a feedback mechanism, whereby test failures are analyzed and appropriate design and process changes are implemented prior to continuous manufacturing of a released design.

SSP 30312, NASA-EEE-INST-002, and similar EEE parts management plans typically reference a FSC number for an appropriate qualification and screening test path. Federal stock class number 5961 references diodes, where this researcher determined that an LED package is not applicable to the composition of a two-terminal part designed to direct circuit current flow in one direction. An LED provides a semiconductor based light source, a review of Figure 3 reveals design construction containing a miniaturized electronic circuit bonded to a substrate containing a cavity, semiconductor material layer, wire bonds, and epoxy encapsulation. For this reason this researcher chose FSC 5962 for hybrid microcircuits as the most applicable FSC reference for EEE testing. Lenk and Lenk (2011) supported this view by stressing the fact that some LED packages contain bond wires that connect the dies to leads for the purpose of putting current through the circuit where a single device contains multiple bond wires used in parallel to accommodate relatively high currents.

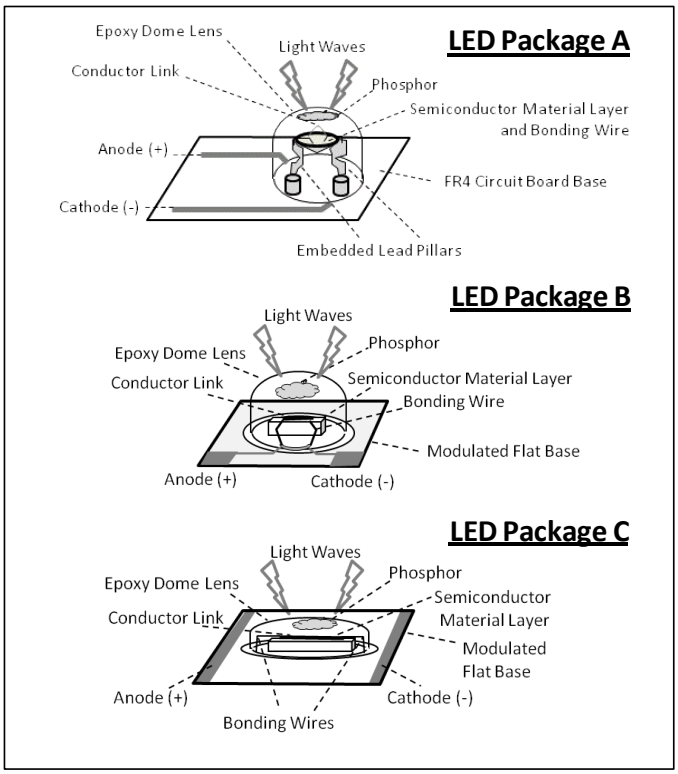

Figure 3. Representation of different LED packages under test.

Referencing MIL-PRF-38534 *General Specification for Hybrid Microcircuits* Table 2 was constructed and summarizes the implemented test plan. Environmental tests were selected by choosing those conditions deemed suitable for qualification and for the purpose of investigation potential failure modes. For example, MIL-PRF-38534 stated that constant acceleration or mechanical shock could be administered and in this analysis both tests were performed.

Table 2. Test plan.

Subgroup	Test	MIL-STD-883		Quantity (Accept Number)
		Method	Condition	
1	Electrical Verification	-	-	5 (0)
	External Visual Inspection	2009	Examined at 1.5X to 10X magnification.	
	Temperature Cycling	1010	Cond. C: 20 Cycles	
	Constant Acceleration	2001	Cond. A: 5000 g's, Y axis	
	Mechanical Shock	2002	Cond. B: 1500 g's	
	Random Vibration	2026	Cond. F: 20.0 GRMS	
	Sinusoidal Vibration	2005	Cond. A: 20 g's	
	Moisture Resistance	1004	24 Hours	
	Barometric Pressure	1001	Cond. G: 2.4 x 10^{-6} mm Mercury	
	End Point Electrical	-	-	
2	Electrical Verification	-	-	22 (0)
	Steady State Life Test	1005	Cond. B: 1000 hours, 125°C	
	End Point Electrical	-	-	

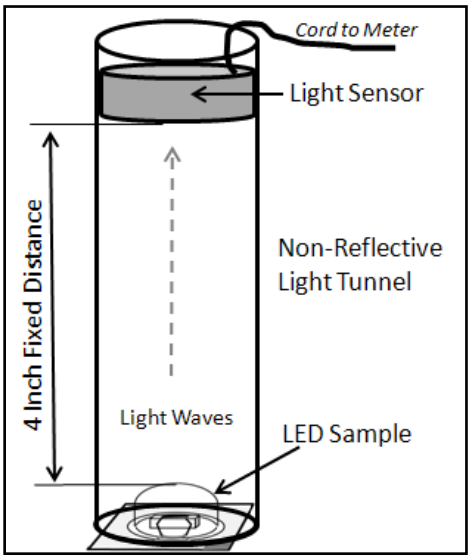

Figure 4. Light output measurement configuration.

Light output data were recorded throughout the investigation using a calibrated light meter (see Figure 4) where measurements were collected by placing the meter over the respective LED sample. The LED sample was powered in accordance with voltage and current specifications and data recorded in micromoles/m^2sec (µmol). A mole is a unit of measurement used in chemistry to express the amount of a chemical substance and in the case of an LED photon flux tensity is what is being detected by the meter.

V. Environmental Testing

A. Temperature Cycling

The purpose of temperature cycling is to determine the resistance of a part to extreme high and low temperatures, and to the effect of alternate exposures to such extremes. The LED samples were placed onto a temperature cycling chamber and tested to MIL-STD-883, method 1010, condition C. This test method exposed the samples to twenty (20) cycles of temperature extremes. The low temperature extreme was –65°C and the high temperature extreme was +150°C. Figure 5 illustrates what constitutes one cycle where samples dwelled for fifteen minutes at each extreme with transfer rates of > 10°C per minute between extremes. Upon completion the LED devices were electrically tested in search of device failures and a visual examination was conducted in search of mechanical damage. No failures were found.

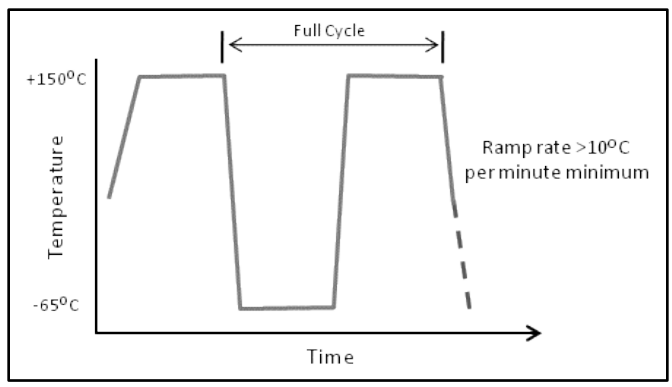

Figure 5. Temperature cycling profile.

B. Constant Acceleration

The purpose of constant acceleration testing is to determine the effects on the types of structural and mechanical weaknesses not necessarily detected in vibration tests. It may be used as a high stress test to determine the mechanical limits of the package, internal metallization, and lead system, die or substrate attachment, wire bond attachment, and other elements of the device.

Samples were placed into a centrifuge and subjected to constant acceleration per, MIL-STD 883, method 2001, Y_1 axis only, for one (1) minute at five-thousand (5000) *g*'s. Figure 11 provides a schematic outlining the positioning of each LED device in the Y_1 direction. Upon completion the LED devices were electrically tested in search of device failures and a visual examination was conducted in search of mechanical damage. No failures were found.

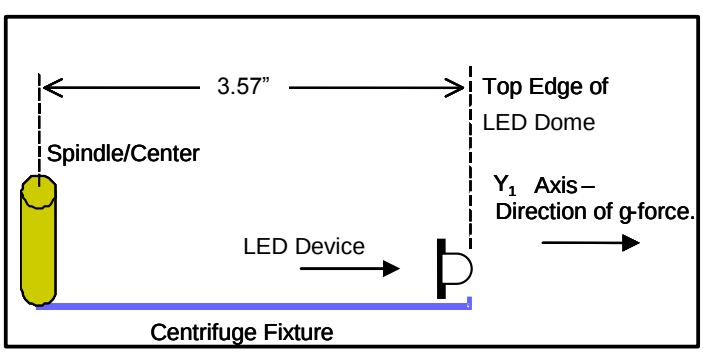

Figure 6. Constant acceleration centrifuge configuration.

C. Mechanical Shock

The purpose of mechanical shock is to determine the suitability of the devices for use in electronic equipment which may be subjected to moderately severe shocks as a result of suddenly applied forces or abrupt changes in motion produced by rough handling, transportation, or field operation. Shocks of this type may disturb operating characteristics or cause damage similar to that resulting from excessive vibration.

Samples were mounted in a fixture and

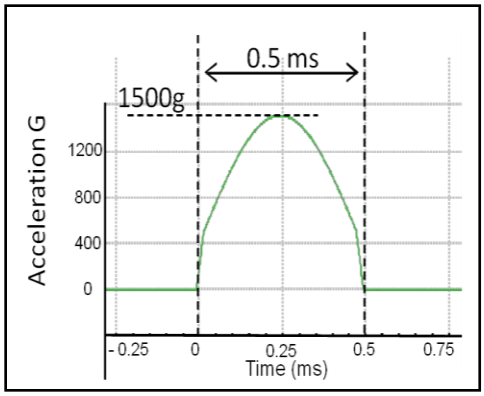

Figure 7. Shock half sine pulse.

placed onto a Mechanical Shock machine and shock tested to MIL-STD-883, method 2002, condition **A**. Figure 7 illustrates the one-thousand five-hundred (1,500) G shock profile executed on each of six (6) mutually perpendicular axes. Positive and negative pulses were tested by applying five (5) shocks for each axes respectively. Upon completion the LED devices were electrically tested in search of device failures and a visual examination was conducted in search of mechanical damage. No failures were found.

D. Random Vibration

The purpose of random vibration testing is to determine the ability of the device to withstand the dynamic stress exerted by random vibration applied between upper and lower frequency limits (20 – 2000 hertz (Hz) using the power spectral density) to simulate the vibration experienced in various field environments. Random vibration is characteristic of modern field environments produced by manned-launch vehicles, unmanned cargo vehicles, missiles, high-thrust jets and rocket engines.

The LED samples were placed on a vibration shaker table and tested in accordance with MIL-STD-883, method 2026, condition F. Figure 8 illustrates the 20.0 GRMS random profile that was performed on each of three (3) mutually perpendicular axes for fifteen (15) minutes each. Upon completion LED devices were electrically tested in search of device failures and a visual examination was conducted in search of mechanical damage. No failures were found.

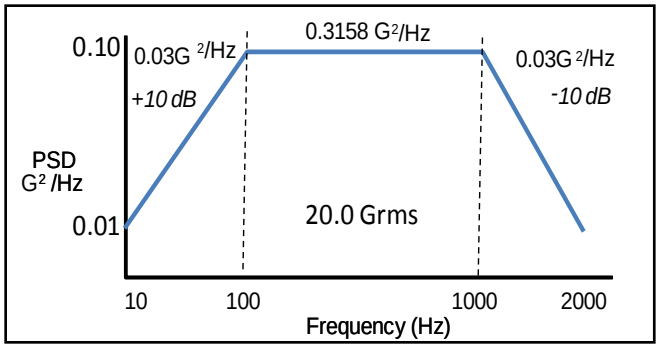

Figure 8. Random vibration profile.

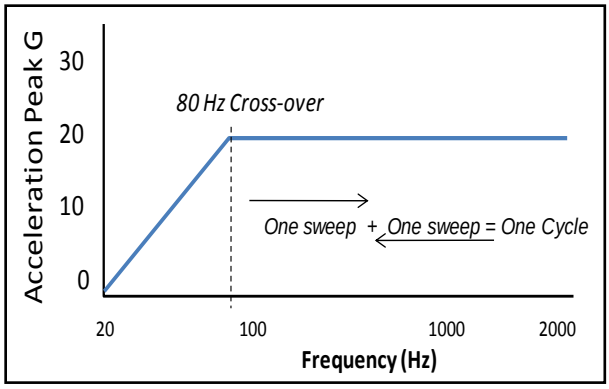

Figure 9. Sinusoidal vibration profile.

E. Sinusoidal Vibration

The purpose of sine vibration test is to determine the effect of high-frequency vibration on component parts in the frequency range of 10 – 2000 Hz, as may be encountered in manned-launch vehicles, unmanned cargo vehicles, aircraft, missiles, and tanks. This test does not strike random frequency vibrations, but sweeps across the frequency spectrum as prescribed in search of resonant frequencies that cause damage.

The LED device was mounted to the same shaker table used for random vibration testing and tested in accordance with MIL-STD-883, method 2005, condition A. Figure 9 illustrates the sinusoidal vibration profile executed on each of three (3) mutually perpendicular axes. A total of six (6) cycles were administered at twenty (20) G's. Upon completion LED devices were electrically tested in search of device failures and a visual examination was conducted in search of mechanical damage. No failures were found.

F. Moisture Resistance

A moisture resistance test is performed for the purpose of evaluating, in an accelerated manner, the resistance of component parts and constituent materials to the deteriorative effects of high-humidity and heat conditions. Most material degradation results directly or indirectly from absorption of moisture vapor and films by vulnerable insulating materials, and from surface wetting of metals and insulation. These phenomena produce many types of deterioration, including corrosion of metals, constituents of materials, and detrimental changes in electrical

properties. This test differs from the steady-state humidity test and derives its added effectiveness in its use of temperature cycling, which provides alternate periods of condensation and drying essential to the development of the corrosion processes and produces a *breathing* action of moisture into partially sealed enclosures. Increased effectiveness is also obtained by use of a higher temperature, which intensifies the effects of humidity. This test included a low-temperature sub-cycle that served as an accelerant to reveal otherwise indiscernible evidences of deterioration caused by freezing moisture, which tends to widen cracks and fissures.

The LED samples were placed into a humidity test chamber and subjected to twenty-four (24) hours of humidity cycling in accordance with the profile illustrated in Table 3. Upon completion the LED device were electrically tested in search of device failures and a visual examination was conducted in search of mechanical damage. No failures were found.

Table 3. Humidity cycling test profile per MIL-STD-883, test method 1004.

STEP	TEMPERATURE (In deg C)	HUMIDTIY (In % RH)	TIME (In hours)
1	125	NA	24
2	25 to 65	0.0 to 95	2.5
3	65	95	3.0
4	65 to 25	95	2.5
5	25 to 65	95	2.5
6	65	95	3.0
7	65 to 25	95	2.5
8	25	95	1
9	25 to -10	95 to 0.0	1
10	-10	0.0	3
11	-10 to 25	0.0 to 95	1
12	25	95	2

G. Barometric Pressure Altitude Test

The purpose of vacuum testing is to determine the suitability of component parts and subassemblies for flight-worthiness in avionics applications or exposure to space vacuum. Differential pressure is used to simulate exposure to varying altitudes and seek information about adverse effects and unwanted failure modes. Devices were place into a vacuum chamber (see Figure 10) and tested in accordance with MIL-STD-883, method 1001, condition G. The LED samples were powered in compliance with operating specifications and subjected to an atmospheric pressure of (760 Torr). Within ten (10) minutes the test environment transitioned to a vacuum environment of $\leq 10^{-6}$ Torr for a total duration of one (1) hour. The LED device continued to successfully operate during the entire test duration. Upon removal from the vacuum vessel, a visual examination was conducted in search of mechanical damage. No failures were found.

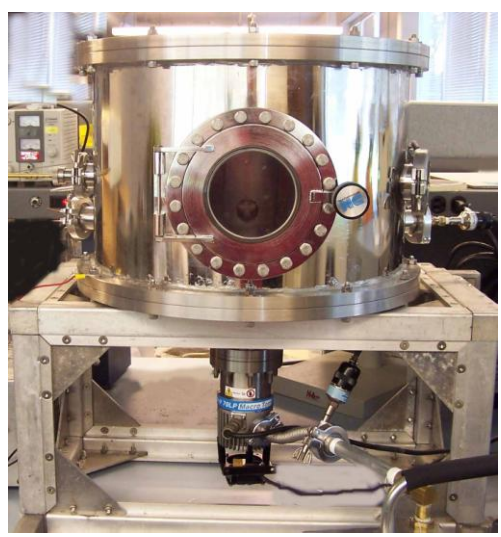

Figure 10. Space altitude vacuum chamber.

H. Steady State Life Test

The purpose of powered life testing is to screen for and eliminate marginal devices, those with inherent defects or defects resulting from manufacturing weaknesses, which cause time and stress dependent failures. The theory behind this activity is to verify performance capability and eliminate infant mortality (early life cycle failures) with the intent of stressing electronics in an accelerated manner, which will reveal time and stress dependent failure modes. Steady state life testing is a test technique considered to be longer than a typical burn-in with the intent of seeking information about qualification

and acceptance for space flight usage. Samples were placed into an environmental test chamber and exposed to +125°C for 1000 hours of powered operation in accordance with MIL-STD-883, method 1005, Condition B (forward bias). The +125°C test environment is also the same temperature required for *Class S* (space) rated components when qualifying to a QML. It should be noted that 22 LED samples were selected for powered life testing, separate from those exposed to the environmental tests (from the same production lot) previously discussed herein, and powered at 24 VDC with specified nominal current applied in accordance with manufacturers' operating specifications. At the conclusion of the 41.6 days of steady state life testing, LED samples remained powered while the temperature chamber environment was changed from +125°C down to +24°C for the purpose of collecting post-test light output data at the same temperature the initial data were collected. A visual examination was conducted in search of mechanical damage and confirmation was made that all LED samples remained operable with no notable failures found.

VI. Performance Analysis

A. Mechanical and Visual Inspection

Upon completion of all subgroup 1 testing, LED device were mechanically inspected in accordance with dimensional requirements specified in the respective design specification using a microscope (10 – 60 power) with no observed failures resulting from environmental testing previously illustrated in Table 2.

B. Electrical Test

Subgroup 1 and subgroup 2 sample sets were all tested using a calibrated light meter. All LED samples were powered at 24 VDC with specified nominal current applied in accordance with manufacturers' operating specifications. Table 4 illustrates initial light output data and the end point light output data for the purpose of comparison. Likewise, Table 5 illustrates initial and the end point light output data for subgroup 2 samples resulting from steady state life testing.

Table 4. Subgroup 1 data from environmental stress testing.

	Package A	Package B	Package C
Initial Light Output Average (µmol/m^{2}sec)	23.50	24.75	15.40
Post Testing Light Output Average (µmol/m^{2}sec)	23.60	24.62	15.43
Difference	-0.10	0.13	-0.03
Percent Change	-0.43%	0.54%	-0.22%

Table 5. Subgroup 2 data from steady state life test.

	Package A	Package B	Package C
Initial Light Output Average (µmol/m^{2}sec)	23.82	24.13	15.71
Post Testing Light Output Average (µmol/m^{2}sec)	19.78	20.73	14.08
Difference	4.04	3.41	1.62
Percent Change	16.97%	14.12%	10.34%

VII. Conclusion

Quality can be defined as conformance to specification and reliability can be defined as quality over time. O'Connor and Kleyner (2012) defined a reliability failure as termination of the ability for a product to perform the required function according to design specifications. Lenk and Lenk (2011) described two measures for reliability when conducting experimentation using LED technologies: (a) operational hours to failure, and (b) the point where an LED no longer provides sufficient light output. This particular analysis resulted in neither of these measures producing a significant failure.

Typical life studies involving electronics record number of hours until breakage or failure where this particular analysis yielded no failures for the subgroup 1 testing and yielded negligible changes in subgroup 2 steady state life samples. The percentage of light output loss observed in subgroup 2 are insignificant where Lenk and Lenk (2011)

stressed that LED components do not necessarily fail by burning out but become dimmer over time. Therefore, an LED component should be considered an end-of-life failure when it reaches 70% of the initial light output. A review of Table 5 supported this researcher's conclusion that there were no observed failures from either subgroup 1 or subgroup 2 testing. For the purpose of selecting commercially available LED components for *warm white light* space applications, selected samples have provided objective evidence that these components may be selected as part of an EEE management plan with high probability that these types of technology are capable a sustaining a wide variety of harsh operating environments and are suitable for space flight and other applications requiring ruggedized design features.

Light emitting diodes are to be considered an integral part of future spacecraft design and must be evaluated for reliability as part of the environmental control and life support system (Jiank, Rodngues, Bell, Kortenkamp, & Capristan, 2011). Jiank et al. (2011) stated that future space craft architecture must include design provisions for longer duration missions where supplies for food, water, air, and life essentials significantly increase spacecraft support costs, hence making LED technologies a viable consideration for off-setting high costs with lower volume, less energy consumption, and longer reliability.

Figure 11. Paul Wedel – UW LaCrosse.

VIII. Acknowledgement

The author would like to thank the Wisconsin Space Grant Consortium for their support of this academic partnership and recognize the University of Wisconsin –LaCrosse and physics major Paul Wedel (see Figure 11) who was instrumental in configuring the LED test vehicle discussed herein.

References

Brainard, G. C., Coyle, W., Ayers, M., Kemp, J., Warfied, B., Maida, J., Bowen, C., Bernecker, C., Lockley, S. W., & Hanifin, J. P. (2012, April). Solid-state lighting for the international space station: tests of visual performance and melatonin regulation. *Acta Astronautica*. doi:10.1016/j.actaastro.2012.04.019

Hersman, C. & Fowler, K. (2009, October). Best practices in spacecraft development. *Mission Critical and Safety Critical Systems. 1* (3), 269-460. doi:10.1016/B978-0-7506-8567-2.00005-6

Jiank, H., Rodngues, L. F., Bell, S., Kortenkamp, D., & Capristan, F. (2011, April). Prediction of reliability for environmental control and life support systems. *Journal of Spacecraft and Rockets, 48* (2), 336 – 345. doi:10.2514/1.44792

Lenk, R., & Lenk, C. (2011), *Practical lighting design with leds*. Hoboken, NJ: John Wiley and Sons, Inc.

MIL-PRF-38534 (13 September 2010). *General specification for hybrid microcircuits* (Revision H), FSC: 5962 United States Department of Defense, USA.

MIL-STD-883 (26 February 2010). *Test method standard for microcircuits* (Revision H), FSC: 5962 United States Department of Defense, USA.

Szajnfarber, A., Coles, T. M., Sondecker, G. R., Wicht, A. C., & Weigel, A. L. (2011, August). Moon first versus flexiblepath exploration strategies: considering international contributions. *Space Policy, 27* (3), 131-145. doi:10.1016/j.spacepol.2011.05.003

New Capabilities and Discovered Interconnectivities for a Curriculum-Integrated Multicourse Model Rocketry Project

Matthew J. Traum[1], Vincent C. Prantil, William C. Farrow, Hope L. Weiss

Mechanical Engineering Department, Milwaukee School Of Engineering, Milwaukee, WI

Abstract

To provide students a more coherent and cohesive view of the mechanical engineering curriculum, we created and are delivering a multicourse curriculum-integrated engineering project that permeates and unifies five required classes within our undergraduate curriculum: 1) Freshman Design, 2) Dynamics, 3) Numerical Analysis, 4) Fluid Mechanics, and 5) Thermodynamics. Students enrolled in these Rocket Project (RP) classes design, build, flight test, and analyze model rockets through hands-on exercises. These activities challenge students to work on different aspects of the same rocket project across all four years of their degree program.

Critical to the seamless collection and presentation of data and experimental/numerical techniques across five courses was the development of new laboratory, field, and simulation capabilities driven by our goal: to measure all unknown variables needed for rocket performance analysis and modeling in-house without reliance on external data. These needed capabilities included: 1) collecting acceleration and barometric altitude data from a model rocket flight, 2) simulating via computer rocket trajectories for comparison to actual measured altitudes, 3) evaluating rocket performance by numerical methods to validate modeling assumptions, 4) determining rocket drag coefficient as a function of Reynolds number for velocities relevant to a launch, and 5) measuring rocket motor thrust as a function of time as well as the energy density of the fuel used. As these capabilities were developed, additional course interconnectivities and opportunities for data sharing were discovered and exploited to further enrich the course experience for students.

Introduction

We are delivering to undergraduate mechanical engineering (ME) students at the Milwaukee School of Engineering (MSOE) multicourse curriculum-integrated aerospace engineering projects. The projects challenge students to work on different aspects of the same rocket project across all four years of their degree program. Students design, build, flight test, and analyze model rockets through hands-on projects that unify different ME classes by permeating five unique areas within our undergraduate curriculum: 1) Freshman Design, 2) Dynamics, 3) Numerical Analysis, 4) Fluid Mechanics, and 5) Thermodynamics. These classes will hereafter be referred to as Rocket Project (RP) classes. The educational benefits of this program for student participants are described elsewhere [1].

[1]The lead author gratefully acknowledges the Wisconsin Space Grant Consortium 2012-2013 Higher Education Incentives Award Program for the financial support it provided to make this project possible.

To deliver this new hands-on content for RP classes, we developed new experimental and computer simulation capabilities at MSOE, which are described in this paper. Critically, we found that the RP courses were highly interdependent. In other words, as shown in Figure 1, a successful outcome in one class typically depended on the availability of information resulting from the activities of one or more other RP classes. The co-investigators' common passion for aerospace engineering offered a unifying thread and a natural collaborative opportunity that enabled needed data to be collected and presented seamlessly to students in five different required ME courses across all four program years.

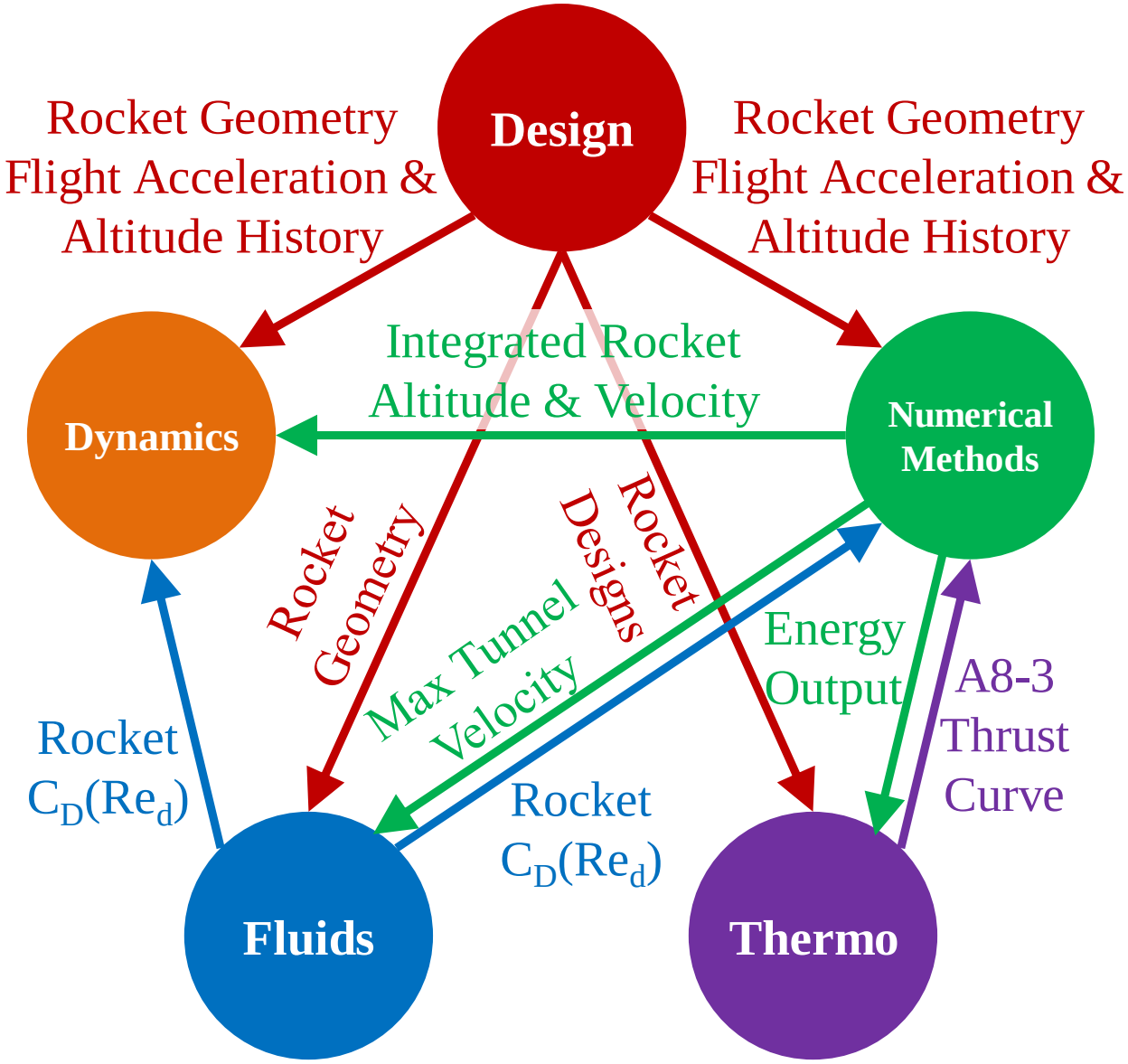

Figure 1: Interconnectivity map showing data, modeling, and analysis sharing across the five RP classes in this program. Since the classes were highly interdependent, successful outcomes in one class required availability of information resulting from one or more other RP classes.

METHODS

We describe new capabilities developed in each RP class arising from cross-course data and information sharing. Courses are listed in the progression order they appear in the ME curriculum, which also corresponds to the most likely order in which students would encounter each sub-project: 1) Freshman Design, 2) Dynamics, 3) Numerical Analysis, 4) Fluid Mechanics, and 5) Thermodynamics.

FRESHMAN DESIGN

First in the sequence is the Freshman Design course, which develops students' basic solid modeling skills and teaches stages of the formal engineering design process. For their rocket project, students in this class were asked to satisfy the following identified need:

"A model rocket company needs a payload module that can carry a specific altimeter with embedded accelerometer on a model rocket in a way that will allow the altimeter to record the rocket's altitude as it flies skyward."

Constraints placed on the problem solution were that the design:

- Must not alter the altimeter/accelerometer in any way;
- Must be capable of sensing the altitude;
- Must allow the altimeter/accelerometer to be easily removed and reinstalled;
- Must allow the altimeter/accelerometer battery to be easily removed and replaced;
- Must allow for the activation of the altimeter/accelerometer, reset of the mode button. and confirmation of mode by viewing the mode LED;
- Must allow the flight data to be downloaded without having to remove the altimeter/accelerometer from the payload module;
- Must be sized so that all parts of the payload module fit within a 3.5 x 3.5 x 7 inch volume (total rapid prototype volume available for each team); and
- Must be safe for a typical college student to operate.

After being assigned to project teams, students were supplied with a project kit that included the model rocket parts, the altimeter/accelerometer, and the basic tools needed to measure and assemble the rocket and payload. As part of their preparation for solving this design problem, teams had to reverse engineer the model rocket parts, digitize each part into a virtual solid model, and then assemble the parts into a virtual solid model of the entire rocket. Students' completed payload designs were fabricated using a solid laser sintering process in MSOE's Rapid Prototype Center (Figure 2). On the last weekend of the quarter in which the course is taught, each team launched their designs to collect acceleration and barometric altitude data from real flights; example data are shown in Figure 3.

At MSOE, the capabilities to 1) reverse engineer and digitize rocket solid models, 2) fabricate payload-carrying nosecones via rapid prototyping, and 3) to launch data-acquiring payloads on hobby-scale rockets all predate the multi-course rocket project. Previously, students in Freshman Design flew customized hobby-scale rockets with digital camera payloads in their nosecones that snapped downward-looking images at the vehicle's apogee [2].The new accelerometer/altimeter

flight capability was the cornerstone of expanding rocketry use into many classes because the acceleration and altitude data collected were useful for numerical simulation, modeling, and validating analysis of other experiments (drag and trust measurement). The importance of this capability and the Freshman Design class is clear in Figure 1, which shows how information from this class is fed into the other four classes within the program.

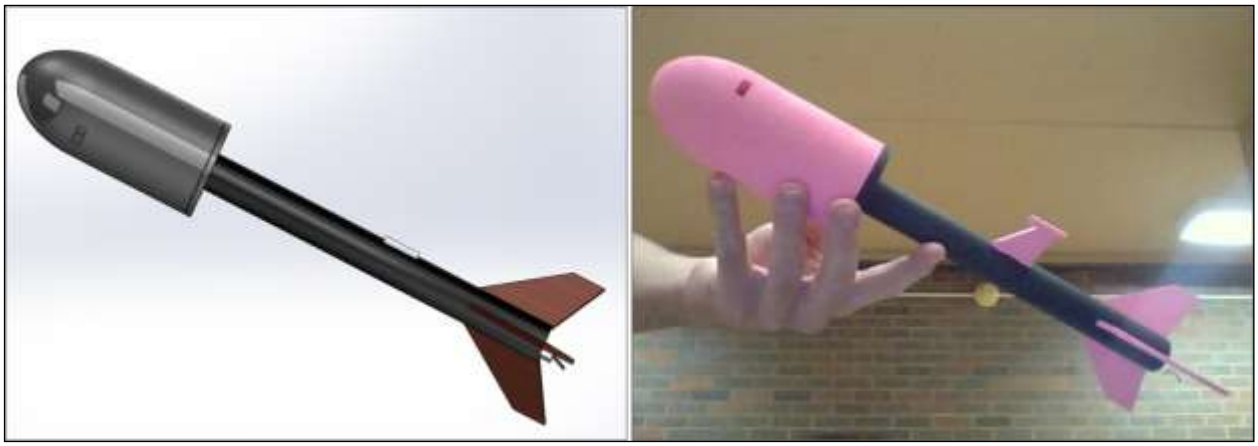

Figure 2: A mid-range sample of rocket payload module design to accommodate an altimeter. Designs in both virtual solid model (left) and physical model (right) forms are presented.

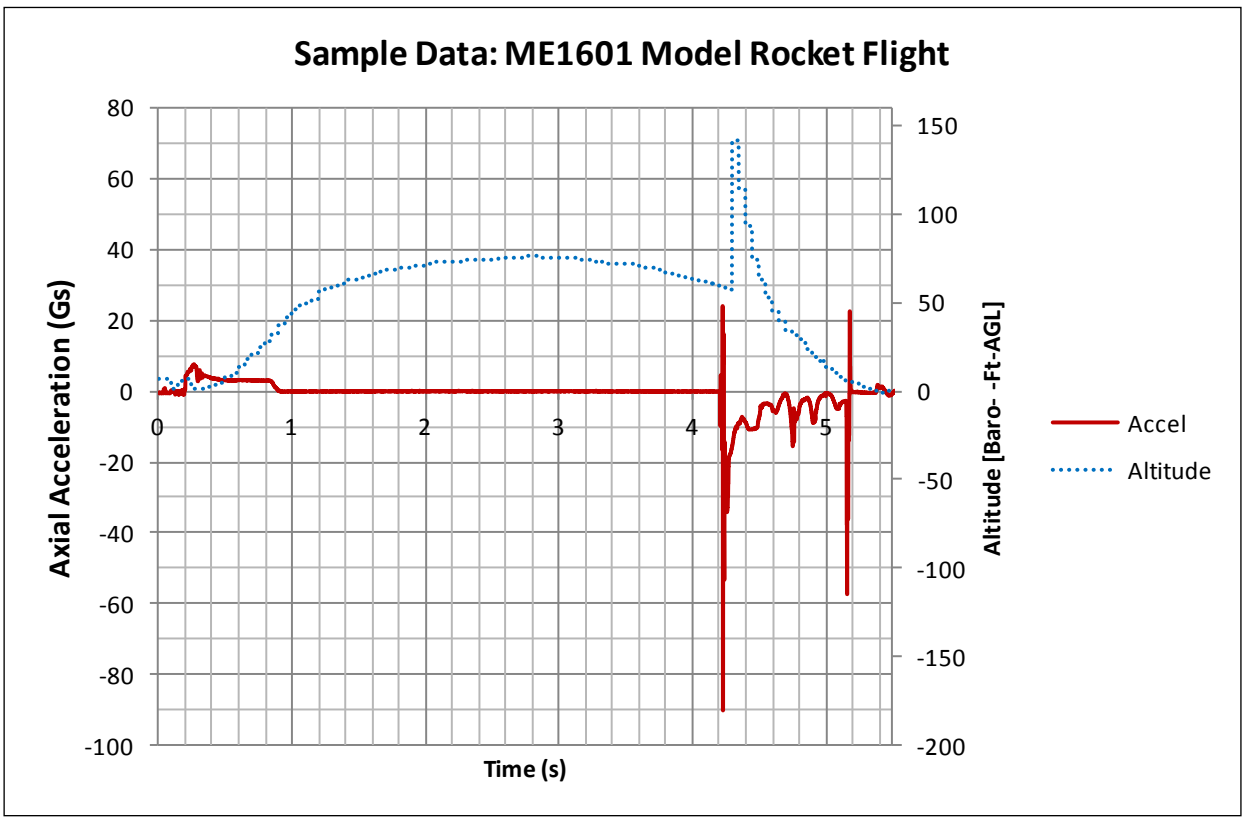

Figure 3: Sample flight data from a successful Freshman Design rocket launch with superimposed rocket altitude and acceleration.

DYNAMICS

The second class in the multi-course RP sequence is sophomore-level Dynamics. This course incorporates computer laboratory sessions that apply use of numerical simulation and approximation in dealing with particle kinematics and kinetics concepts. With respect to the rocket project, students revisit their long-held modeling assumption from lower-division physics that air resistance can be neglected in particle trajectory calculations. Numerical modeling is performed that requires calculation of work due to non-conservative forces, primarily friction, and inclusion of velocity-dependent acceleration relations in curvilinear coordinate systems inherent in rocket flights from oblique launches. An idealized version of the drag model is emphasized with a frictional component added to the rocket acceleration wherein:

$$a_{DRAG} = \frac{1}{2}\rho A C_D v^2(-\hat{e}_t) \tag{1}$$

where ρ is air density, A is maximum rocket cross sectional area, C_D is the drag coefficient, and v is rocket velocity. In this equation, the direction of frictional acceleration, $\hat{e}_t$, always directly opposes the velocity of the rocket. Trajectory modeling must account for both this frictional acceleration as well as the gravitational acceleration, which is assumed to remain constant and be directed toward the Earth at all times.

To tie the rocket performance modeling work in Dynamics back to the actual rockets built and launched in Freshman Design, the cross-sectional area of student-designed nosecones, A, and the measured mass of student-designed rockets (complete with altimeter/accelerometer and battery payload) are used for calculations in Dynamics. Rocket drag coefficient, C_D, which is measured via a wind tunnel experiment in Fluid Mechanics later in the multi-course RP sequence (described below) is also given.

In the past, these rocket trajectory simulations were performed independently from real data. However, the newly developed RP course capability for Dynamics is our ability to compare simulated rocket trajectories to actual measured altitude using the altimeter/accelerometer data collected from actual flights in Freshman Design. Experimental velocity and altitude time histories obtained by analyzing in-flight acceleration data are determined in the subsequent Numerical Analysis course. From these experimentally-measured flight data can be gleaned the critical output predictions useful for model/experiment comparison in Dynamics: maximum range, maximum altitude, and flight time.

NUMERICAL ANALYSIS

Third in the multi-course RP sequence is junior-level Numerical Analysis class. This class devotes substantial time to model construction: simplifying physical assumptions, validation of numerical simulation results, and model iteration. By revisiting physical assumptions inherent in the models developed earlier in Dynamics, the rocket trajectory is simulated using techniques that are much more sophisticated. The following modeling processes are carried out:

1. Double numerical integration of in-flight acceleration data [obtained from the Freshman Design course] to obtain experimental velocity and altitude time histories [which are used for calculations in the Dynamics class] as well as flight trajectories for oblique launches;
2. Calculation of work performed by aerodynamic drag forces [which is used in the Thermodynamics course];
3. Direct comparison of model/flight simulation velocity, altitude, and trajectory with three velocity-dependent drag model assumptions;
4. Determination of model prediction sensitivity to:
   a. Impulse delivered assuming a square pulse thrust profile, or
   b. Impulse delivered using experimental test data from a typical A8-3 Estes rocket motor [obtained from the Thermodynamics course]; and
5. Determination of model prediction sensitivity to assumptions regarding rocket payload weight including:
   a. Assuming constant rocket weight, or
   b. Accounting for mass fuel burn

As a baseline, constant rocket mass and constant step input (square pulse) thrust are assumed for the rocket. Using Newton's second law, the governing differential equation is

$$m\frac{dv}{dt} = T - W - F_D(v) \tag{2}$$

Where m is the constant mass of the rocket, v is the velocity of the rocket, T is a constant thrust delivered over a specified amount of time, W is the weight of the rocket, and $F_D(v)$ is the drag force on the rocket given as a function of velocity. Three drag models are evaluated: 1) No drag $F_D(v) = 0$; 2) Linear drag $F_D(v) = bv$ where b is a linear coefficient of drag [which is instructor-provided, but based on limited theory with no experimental data]; and 3) Aerodynamic drag $F_D(v) = 1/2\rho C_D A v^2$ where ρ is the density of air, C_D is the drag coefficient [measured by wind tunnel testing in the Fluid Mechanics course] and corroboration with literature-published values [3], and A is the cross-sectional area of the rocket (as built in Freshman Design). The velocity of the rocket is updated employing the simplest explicit time integration of Eqn. 2

$$v_{i+1} = v_i + \frac{1}{m}\left(T - W - F_D(v_i)\right) \tag{3}$$

using Euler's forward method (here i indicates the time step). Mass of the rocket as a function of time is estimated using experimental thrust data (collected in the Thermodynamics course) assuming a constant fuel burn rate [4]. The governing equation now becomes

$$m(t)\frac{dv}{dt} = T(t) - W(t) - F_D(v). \tag{4}$$

Again, Euler's forward method is used to update the velocity

$$v_{i+1} = v_i + \frac{1}{m_i}\left(T_i - W_i - F_D\left(v_i\right)\right). \tag{5}$$

The height achieved by the rocket is determined numerically using Euler's forward method. As before, the in-flight acceleration data are integrated using the trapezoidal rule once to obtain the velocity and twice to obtain the height.

Prior to being incorporated as a RP course, the above Numerical Analysis exercise was conducted using rocket acceleration data created by the instructor. We now have the capability to perform flight simulations by working from real experimental flight data. The experimental rocket velocity is plotted in Figure 5, along with the velocities found using the linear drag model and the aerodynamic drag model with constant mass and with variable mass. We also have the capability to compare simulated rocket altitude time histories with experimental altimeter data. Figure 6 shows the rocket height from the experimental flight compared to predicted model heights using constant and variable mass along with the linear drag and aerodynamic drag models.

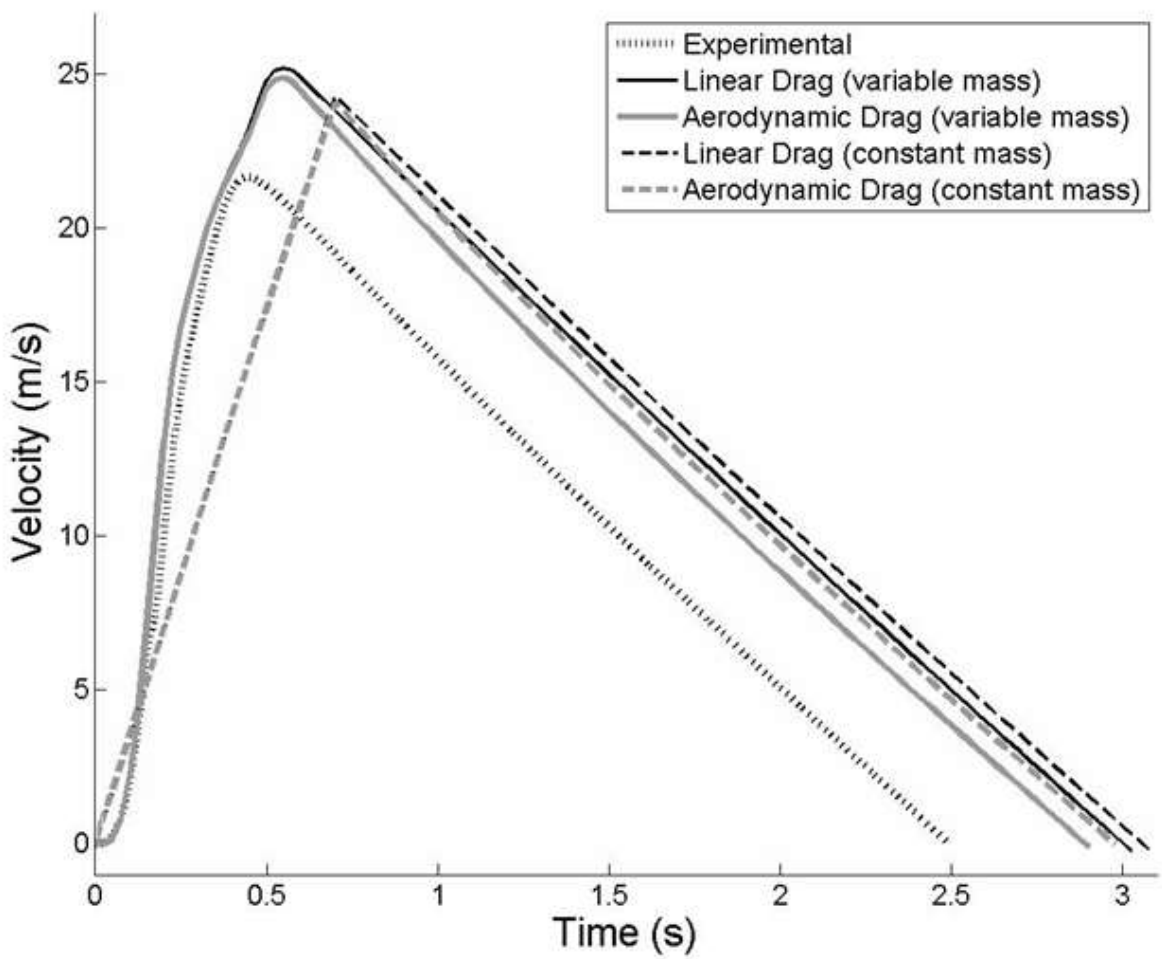

Figure 5: Rocket velocity as a function of time from the experimental flight compared against velocity history predicted by the model using constant and variable mass. The linear drag and aerodynamic drag models are shown.

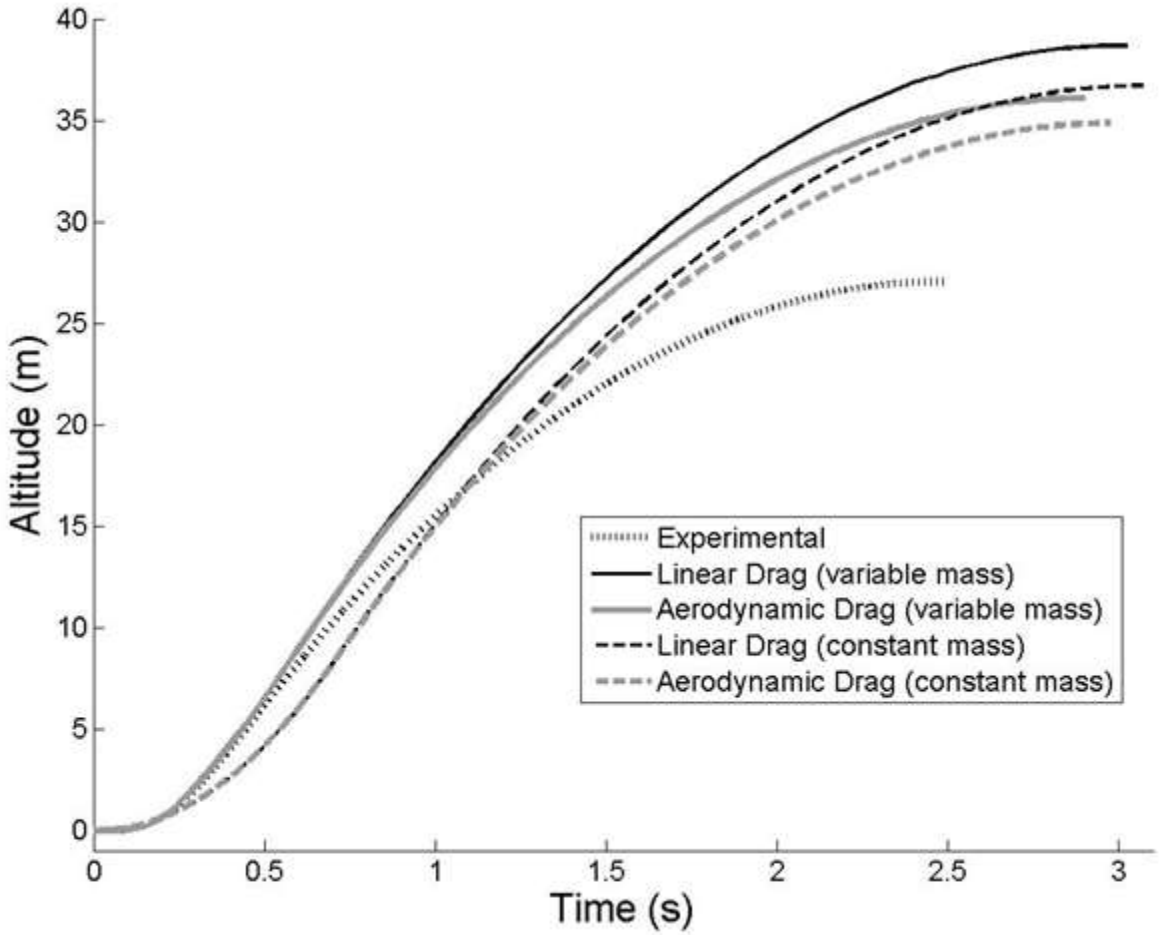

Figure 6: Rocket altitude from experimental flight data compared against altitude predicted from simulation using constant and variable mass. The linear drag and aerodynamic drag models are shown.

FLUID MECHANICS

The fourth class in the multi-course RP sequence is junior-level Fluid Mechanics for which a wind tunnel experiment was devised. Rocket drag was measured as a function of tunnel velocity, and the dimensionless variant (drag coefficient as a function of Reynolds Number) was also determined. The ability to make these measurements was a new capability developed for the rocket project to address the need to know rocket drag coefficients for the simulations performed in Dynamics and Modeling and Numerical Analysis.

As shown in Figure 7, the model rocket was initially hung in the tunnel's working section with the turbine off using two very thin threads positioned around the rocket's center of gravity. The rocket's mass was measured in advance of the experiment. A tripod-mounted digital camera captured the location of the rocket relative to a T-square, which indicated the reference vertical. A laser beam was directed at 45° from horizontal to calibrate the image against unintended angle offsets between the camera and the working section.

The wind tunnel was then turned on, and its velocity was measured using a pitot-static probe. Drag induced in the horizontal direction caused the rocket model to swing backward and assume a new equilibrium orientation. The new angle between the suspending rocket threads and horizontal was photographed for later measurement using digital image analysis software. The resulting drag coefficient was determined using Eqn. 6,

$$D = \frac{mg}{\cos\Theta} \tag{6}$$

where m is the rocket mass, g is the gravitational acceleration, and θ is the angle between the suspension threads and horizontal. Reliable data were taken at tunnel speeds as high as 32.9 m/s, which is faster than ~25 m/s achieved by the rocket, as determined from experimental flight data (see Figure 5).

A plot of drag force versus tunnel velocity was produced from these measurements. The data where then non-dimensionalized using rocket geometric and air fluid dynamic parameters to create a plot of drag coefficient versus Reynolds number, as shown in Figure 8. Apparent in Figure 8 is the drop in drag coefficient with increasing Reynolds number (i.e. tunnel velocity).

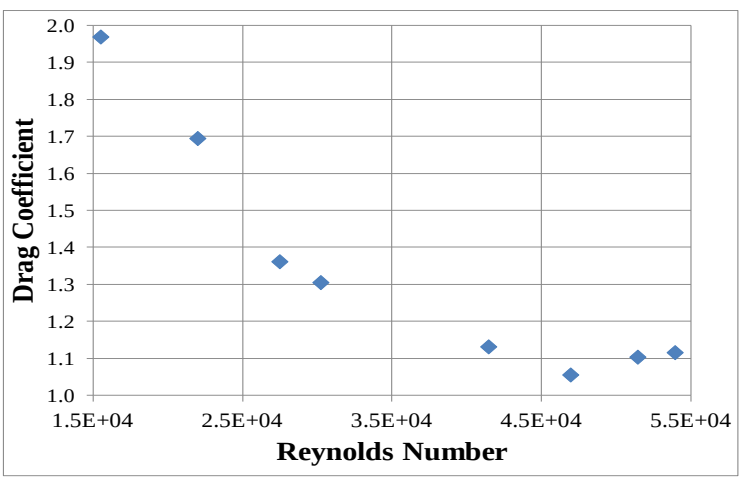

Figure 8: Rocket model drag coefficient as a function of Reynolds number measured in the Fluid Mechanics component of the rocket project. As with drag coefficient over a simple shape, like a sphere, drag coefficient is a strong function of Reynolds number for laminar flow, but this dependence disappears as flow transitions to turbulent.

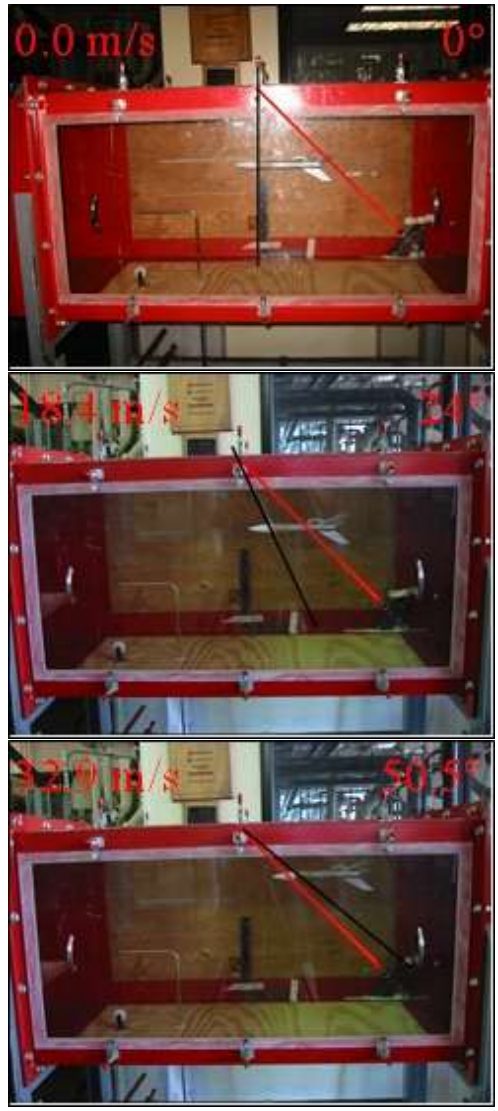

Figure 7: Model rocket drag coefficient as a function of velocity is experimentally measured in a wind tunnel. By suspending models about their center of mass by two threads. Wind tunnel velocity is increased and the resulting angle between the horizontal and the thread (black lines) is photographed for measurement. A laser beam projected 45° from horizontal (red lines) corrects for any systematic error in angle between the tunnel working section and tripod-mounted camera.

Above Reynolds number of about 40,000 the drag coefficient seems to lose its functional dependence on Reynolds number. Qualitatively, this behavior is consistent with external flow over three-dimensional objects in that increasing Reynolds number generally decreases drag coefficient until the flow transitions to the fully turbulent regime where Reynolds number no longer has an effect on drag coefficient.

THERMODYNAMICS

The fifth multi-course RP class in the sequence is senior-level Thermodynamics. Here, an experimental thrust measurement apparatus was constructed that can accommodate model rocket motors in the 13.0 mm, 18.0 mm, and 24.0 mm diameter size classes. Thus, any hobby-scale solid rocket motor from the 1/4A up to E total impulse classes can be tested. This capability was newly developed at MSOE for the multi-course rocket project to provide experimental motor thrust curves for the Numerical Analysis course.

Figure 9: An Estes A8-3 model rocket engine is tested on the motor thrust apparatus.

The motor is securely mounted in a vertical orientation atop a compression load cell and ignited so exhaust is vented through a hood out of the test cell (Figure 9). A data acquisition system collects thrust data at 0.002-second intervals and a low-pass-filter, implemented in the data collection software, eliminates high frequency vibration artifacts to produce a smooth thrust-versus-time curve.

To validate the thrust measurement apparatus, thrust curves were compared against curves published by the manufacturer based on data acquired through testing by the National Association of Rocketry (NAR), as shown in Figure 10. A useful repository of hobby rocket motor thrust curve data is archived on-line at www.thrustcurve.org [5].

For the specific Estes A8-3 motor shown tested in Figure 9, the experimental thrust apparatus under-measures manufacturer-stated maximum thrust by 5.3%, under-measures total impulse by 8.2%, under-measures burn time by 0.152 seconds, and under-measurers average thrust by 2.7%. However, uncertainty in experimental data was not quantified, and these data represent a single engine test. As pointed out by Haw [6], repeated tests generating enough data to enable statistical analysis would provide the most accurate global representation of motor performance.

In addition to obtaining motor thrust curves, experimental data were also used to estimate the energy density of black powder rocket motor fuel. The difference between pre-fire and post-fire motor masses gives an estimate of the mass of black powder consumed. So, if total motor output energy during launch is measured, the motor's energy density can be calculated. Most hobby motors include delay and recovery charges, which do not contribute to the measured output thrust but do contribute to the pre-fire/post-fire mass difference. To reduce the resulting error in

determining rocket fuel energy density, booster motors without delay charges (A8-0 motors) were used for these measurements, leaving only the recovery charge as a small unaccounted mass in the overall energy balance.

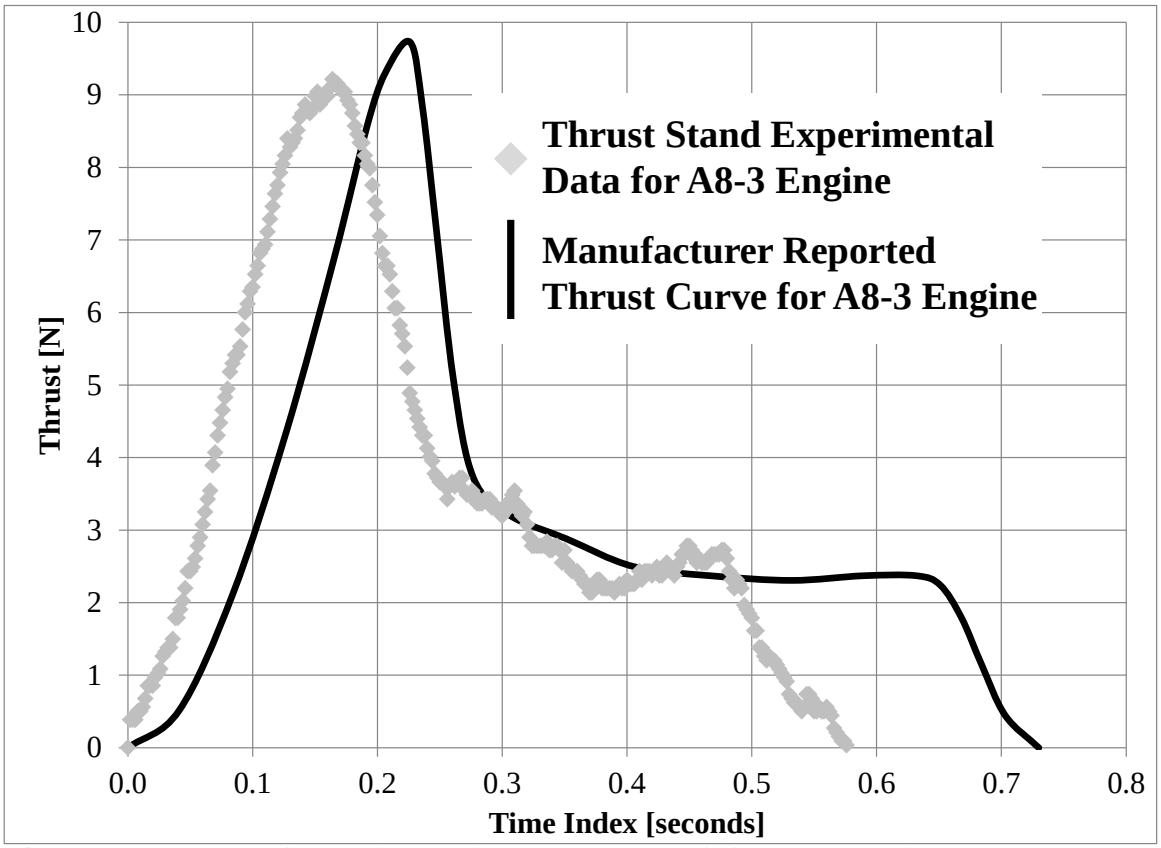

Figure 10: Comparison of manufacturer reported thrust curve for an Estes A8-3 model rocket engine versus experimental data collected using the motor thrust apparatus.

The resulting energy output is then validated in two ways. First, in the Numerical Analysis course, the energy output during a rocket launch is evaluated by combining dissipation from drag with the potential energy achieved at rocket apogee. This result directly benchmarks the product of motor energy density and mass consumed during static motor tests. Second Thermodynamics combustion analysis techniques are applied to black powder solid rocket motor fuel (charcoal and sulfur fuel combined with potassium nitrate oxidizer) to determine the specific energy released during the combustion process given formation enthalpies of the reactants and products:

$$8C + 3S + 10KNO_3 \rightarrow 2K_2CO_3 + 3K_2SO_4 + 6CO_2 + 5N_2 \tag{7}$$

Specific energy, e, obtained from this combustion analysis can then be compared against the energy released during experimental tests as represented by the thrust curve.

$$e = \frac{1/2(m_{f,i} - m_{f,f})}{m_{f,i}} v_e^2 \tag{8}$$

where $m_{f,i}$ and $m_{f,f}$ are respectively initial and final fuel mass and v_e is nozzle exit velocity. This velocity can be determined exactly via the following equation [7]:

$$v_e = \frac{\int_o^t F(t)dt}{\int_0^t \dot{m}(t)dt} \tag{9}$$

The numerator is calculated numerically as the area under the experimentally-measured thrust-versus-time curve. However, the function for instantaneous expulsion of mass, which appears in the denominator, cannot be determined from available experimental data as the rocket motor mass change cannot be separately measured from thrust data. Thus, the mass expulsion rate is assumed to be linear, $\dot{m}(t) \approx (m_{f,i} - m_{f,f})/\Delta t$, which is a reasonable engineering assumption for solid rocket motor grain that presents a constant area combustion front.

CONCLUSIONS

The authors collaborated across conventional ME Department division boundaries to create and deliver a multicourse curriculum-integrated rocket project that permeates and unifies five different classes within the ME undergraduate curriculum: 1) Freshman Design, 2) Dynamics, 3) Numerical Analysis, 4) Fluid Mechanics, and 5) Thermodynamics.

Seamless collection and presentation of data and experimental/numerical techniques across five courses was facilitated by the creation of new laboratory, field, and simulation capabilities at MSOE driven by our goal: to measure all unknown variables needed for rocket performance analysis and modeling in-house without reliance on external data. These needed capabilities included: 1) collecting acceleration and barometric altitude data from a model rocket flight, 2) simulating via computer rocket trajectories for comparison to actual measured altitudes, 3) evaluating rocket performance by numerical methods to validate modeling assumptions, 4) determining rocket drag coefficient as a function of Reynolds number for velocities relevant to a launch, and 5) measuring rocket motor thrust as a function of time as well as the energy density of the fuel used. As these capabilities were developed, additional course interconnectivities and opportunities for data sharing were discovered and exploited to further enrich the course experience for students.

BIBLIOGRAPHY

[1] M. J. Traum, V. Prantil, W. Farrow, H. Weis, “Interconnecting the Mechanical Engineering Curriculum Through An Integrated Multicourse Model Rocketry Project,” *Proceedings of the 120th American Society for Engineering Education (ASEE) Conference and Exposition*, Atlanta, GA, June 23-26, 2013.

[2] W. C. Farrow, “Freshman Engineering Video-Rocket Design Project,” *Proceedings of the 19th Annual Wisconsin Space Conference*, Milwaukee, WI, August 13-14, 2009.

[3] S. Niskanen, “Development of an Open Source Model Rocket Simulation Software”, M.S. Thesis, Engineering Physics, Information and Natural Sciences, Helsinki University, May 20, 2009.

[4] K. Penn, W. V. Slaton, “Measuring Model Rocket Engine Thrust Curves,” *The Physics Teacher*, Vol. 48, Issue 9, 2010, pp. 591.

[5] J. Coker, “Thrustcurve.org — Rocket Motor Performance Data On-Line,” Web Site URL: http://www.thrustcurve.org/ (last accessed 4/6/3013).

[6] M. Haw, “A8-3 Model Rocket Impulse Measurement,” The University of British Colombia cIRcle open access digital repository, Web Site URL: http://hdl.handle.net/2429/7905.

[7] G. P. Sutton, O. Biblarz, **Rocket Propulsion Elements, 8th Edition**, Chapter 2, John Wily & Sons, Hoboken, NJ, 2010, pp. 26-45.

Dynamic Dynamometry to Characterize Disk Turbines for Space-Based Power

Zhiyuan Yang, Hope L. Weiss, Matthew J. Traum[1]

Mechanical Engineering Department, Milwaukee School Of Engineering, Milwaukee, WI

Abstract

Rankine cycles will someday be the power plants of choice for manned space missions, providing excellent thermodynamic efficiency and high power density. The Rankine cycle's hallmark is a working fluid that changes phase between liquid and vapor. However, the working fluid must remain in the vapor phase as it passes through the turbine to avoid damaging this component. The need to tightly regulate the working fluid phase through the turbine imposes limits on the power produced and the overall efficiency of the cycle, especially given limitations on power plant volume and mass necessarily imposed by housing it in an interplanetary spacecraft.

These limitations could be relaxed if a turbine were incorporated into the Rankine power cycle that was robust and fully operational while processing two-phase flows. Disk turbines have the potential for continuous operation regardless of the thermodynamic quality of working fluid running through them. However, due to high rotational velocity and low torque output by disk turbines, their performance is difficult to evaluate using conventional techniques for aero-derived turbines.

To assess disk turbines as candidates for space-based power generation, we describe a method to accurately measure and predict turbine mechanical power output using the rational inertia of the turbine's spinning components and friction in its bearings as the load. The turbine's time response to Dirac load inputs, as well as its no-load responses to compressed air input over a range of pressures, are measured. This technique, called dynamic dynamometry, produces turbine power-versus-angular-velocity curves, useful for quantitative performance analysis.

Introduction

Working microgravity Rankine cycle technology is identified by NASA as an essential element for future manned space missions to provide high-power density and superior thermodynamic efficiency[i] compared to existing space-based energy generation methods.[ii] Given the extensive experience NASA has developed to handle fluids, especially low-temperature fluids, in microgravity, a space-based Rankine cycle could be implemented today using existing technology.[iii] The hallmark of the Rankine cycle is a working fluid that changes phase between liquid and vapor. However, the working fluid must remain in the vapor phase as it passes through

[1]The corresponding author gratefully acknowledges the Wisconsin Space Grant Consortium 2012-2013 Higher Education Incentives Award Program for the financial support it provided to make this project possible. All authors gratefully acknowledge EASENET, Inc. for project financial and in-kind support. This paper's undergraduate lead author is a member of the Milwaukee Undergraduate Researcher Incubator (MURI) at MSOE, an organization which fast-tracks undergraduates into meaningful early research experiences.

the turbine to avoid damage. This necessity imposes limits on the power produced and the overall efficiency of the cycle.

Better performance could be obtained if a non-conventional turbine were incorporated into the Rankine power cycle that operated reliably and robustly while processing two-phase flows. Disk turbines have the potential for continuous operation without damage when functioning with a working fluid of fractional thermodynamic quality.[iv] Disk turbines (also called boundary layer turbines or Tesla turbines) differ from conventional aero-derived turbines. Instead of gas impinging on aerodynamic blade surfaces to produce lift and spin the shaft, disk turbines rely on viscous shear between the working fluid and flat disks to provide motive torque. As a result, disk turbines typically operate at much higher rotational rates with lower torque than their aero-derived counterparts,[v] which makes their performance difficult to evaluate using conventional techniques for aero-derived turbines. [vi]

Experimental evaluation of engines and turbo-machinery typically requires a dynamometer to measure power curves – power output as a function of rotational rate for a series of loads. Due to the high-rotation-rate and low torque output by disk turbines, no commercially-available dynamometers are suitable. Instead, we use a technique called dynamic dynamometry, which uses the rotational inertia of the turbine spindle and the friction in the bearings as the load. No separate dynamometer is needed to extract power curves. This technique has already been used successfully by researchers to characterize tiny disk turbines,[vii] and its application as a classroom demonstration to teach mechanical engineering concepts has also been described.[viii]

This paper explains how the dynamic dynamometry technique can be applied to measure the rotational inertia and extract power curves for a disk turbine. This technique provides the foundation for future characterization and analysis of disk turbines for space-based power generation.

Theory and Experiments

All described experiments were carried out using a small pre-built disk turbine made available by an industry partner (Figure 1). The complete apparatus consisted of an optical tachometer located to enable continuous measurement of the turbine shaft rotation rate and a video recording device (an iPhone). The video-recorded tachometer readout provided time histories of the turbine shaft angular velocity during experimental events, which was the fundamental data stream analyzed to extract turbine performance metrics.

Figure 1: Optical tachometer and stopwatch positioned in the same video shot to enable video capture of turbine spindle experimental rotational velocity time histories for data analysis.

To reduce data to useful form, free frame-by-frame video viewing software was utilized (VLC Media Player[ix]). The approximate data sampling rate was determined by placing a stopwatch in the video recorder's field of view and counting the number of frames shot over some characteristic

duration. Each frame therefore showed the tachometer reading at a sampling interval equal to the frame rate of the video capture device used. An example of the entire set-up is shown in Figure 1.

Turbine Rotational Inertia Determination

The turbine was anchored about 2.5 meters above ground. One end of a long sewing thread was secured to the turbine spindle, and the other end was attached to a free weight of known mass resting at the elevation of the turbine. The thread was wrapped around the turbine shaft without doubling up on itself. With video capture of tachometer data enabled, the weight was knocked to the floor, spinning the turbine shaft with an instantaneous input of force provided by gravity acting on the weight's mass.

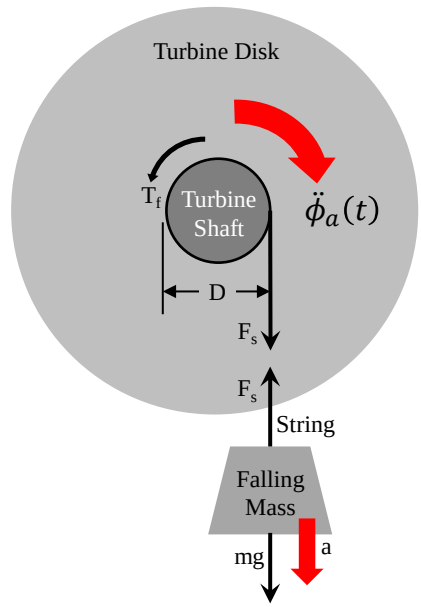

Figure 2: Free body diagram for weight-string-turbine system showing acceleration directions, forces, and torques acting on components.

In general, turbine spindle angular acceleration under inlet gas pressure, $\ddot{\Theta}_a(t)$, under a falling mass, $\ddot{\phi}_a(t)$, or deceleration due to bearing friction, $\ddot{\Theta}_d(t)$, are approximated via the time derivative of collected experimental angular turbine data,

$$\ddot{\Theta}(t) = \frac{\Delta\dot{\Theta}(t)}{\Delta t} \qquad \text{(Eq. 1)}$$

where $\dot{\Theta}(t)$ is the spindle angular velocity, and t is a time interval of measurement. Applying Newton's Second Law through a torque balance on the free body diagram in Figure 2, the difference between the torque imposed on the turbine shaft by the string, $F_s(D/2)$, and the frictional torque from the bearings, T_f, upon which the turbine spindle is mounted is given by

$$F_s\left(\frac{D}{2}\right) - T_f(t) = I \cdot \ddot{\phi}_a(t) \qquad \text{(Eq. 2)}$$

where I is the rotational inertia of the turbine spindle, F_s is the force of the sting arising from the weight of the fixed mass, m, and D is the diameter of the spindle around which the thread is wound. Finally, by applying a dynamic force balance to the falling mass alone (see Figure 2), the following expression results,

$$m \cdot \ddot{\phi}_a(t) \cdot \left(\frac{D}{2}\right) = m \cdot g - F_s \qquad \text{(Eq. 3a)}$$

where g is the local gravitational acceleration. This expression can be solved for F_s:

$$F_s = m \cdot g - m \cdot \ddot{\phi}_a(t) \cdot \left(\frac{D}{2}\right) \qquad \text{(Eq. 3b)}$$

To obtain an experimental function for T_f, the friction torque from the bearings, the unloaded turbine was spun up to its maximum operational rotational velocity using compressed air. When

the turbine reached a steady state rate of rotation, the input gas was instantaneously shut off, and the rotational velocity of the turbine with respect to time was logged while the turbine spun down under friction primarily imposed by the bearings. A torque balance on the decelerating turbine spindle alone yields

$$-T_f(t) = I \cdot \ddot{\Theta}_d(t) \qquad \text{(Eq. 4)}$$

where $\ddot{\Theta}_d(t)$ is determined from Equation 1. Substituting Eq. 4 into Eq. 2 and rearranging gives

$$I = \frac{F_s\left(\frac{D}{2}\right)}{\ddot{\phi}_a(t) - \ddot{\Theta}_d(t)} \qquad \text{(Eq. 5)}$$

and plugging the F_s expression of Equation 3b into Equation 5 results in an expression to determine I values exclusively from experimentally-measured inputs,

$$I = \frac{\left[mg - m\ddot{\phi}_a(t)\frac{D}{2}\right]\left(\frac{D}{2}\right)}{\ddot{\phi}_a(t) - \ddot{\Theta}_d(t)} \qquad \text{(Eq. 6)}$$

Now, to determine the value for I, the numerical values of the functions $\ddot{\phi}_a(t)$ and $\ddot{\Theta}_d(t)$ were found at each time step: t_1, t_2, … t_n. These values were plugged into Equation 6, which produced n-1 values for I where n is the total number of data points. The reported value for I is the average of all the discrete I values for each time step while the uncertainty in I is approximated as twice the standard deviation of all the data.

Turbine Power Curves

Turbine power output as a function of rotational velocity, the so-called turbine power curve, can be extracted experimentally by dynamic dynamometry. The turbine was run at 90 psi input pressure. Pressure upstream of the turbine was held constant using a regulator.

Video capture of tachometer data was initiated with the turbine at rest. The turbine gas inlet was instantaneously opened, and the turbine was allowed to spin up until its rotational velocity reached steady state (we describe later how 'steady state' is formally defined).

The following derivation leads to a turbine power curve expression. The turbine's moment of inertia, I, is already known from the above-described analysis. The turbine's power output, P_{out}, is

$$P_{out} = T_s \cdot \dot{\Theta}_a(t) = I \cdot \frac{d\dot{\Theta}_a(t)}{\mathrm{d}t} \cdot \dot{\Theta}_a(t) \qquad \text{(Eq. 7)}$$

since the output shaft torque, T_s, is

$$T_s = I \cdot \frac{\mathrm{d}\dot{\Theta}_a(t)}{\mathrm{d}t} \qquad \text{(Eq. 8)}$$

To find an equation for P_{out}, a functional form is needed for $\dot{\Theta}_a(t)$. This function can be determined by inspection. An example of a raw $\dot{\Theta}_a(t)$ data set is given in Figure 3, and it is

apparent from the non-zero initial slope that the function for $\dot{\Theta}_a(t)$ is a first order response (an asymptotic exponential) of the form

$$\dot{\Theta}_a(t) = \dot{\Theta}_{max} \cdot \left(1 - e^{-\frac{t}{\tau}}\right) \qquad \text{(Eq. 9)}$$

where $\dot{\Theta}_{max}$ is the maximum turbine rotational velocity achieved at steady-state, and τ is a time constant characteristic of the system.

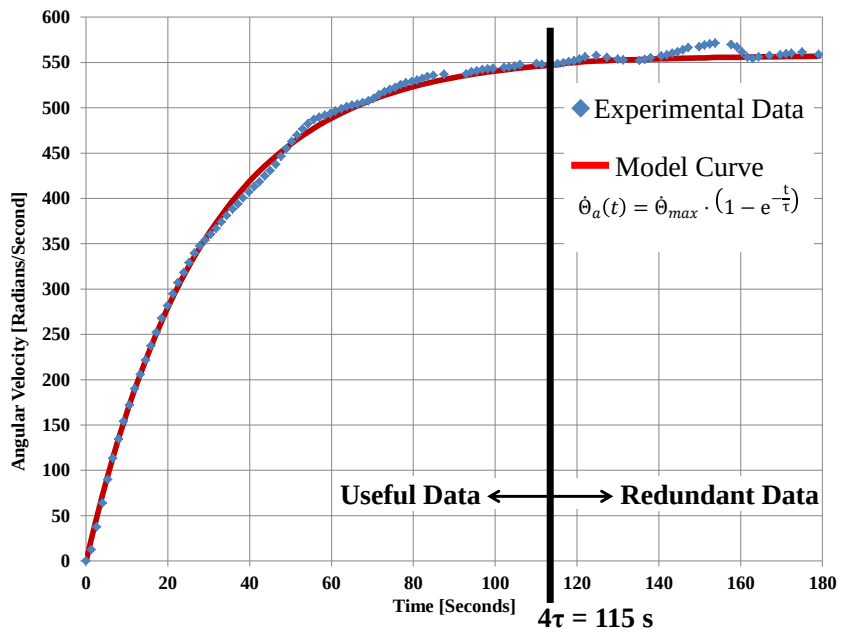

Figure 3: Rotational velocity versus time for a disk turbine spun up from rest at constant input gas pressure. The experimental data (blue diamonds) follow an asymptotic exponential, Equation 9, (red curve) where the system time constant, τ, must be selected to provide the best data/model fit. Data collected after time = 4τ are redundant and can be eliminated from the analysis.

To fit Equation 9 to the experimental data and obtain a useful function for $\dot{\Theta}_a(t)$, the time constant, τ, is treated as a variable parameter that is adjusted to achieve the best equation/experiment match. The fitting technique we used was minimization of the Standard Error of the Estimate (SEE). SEE is the sum of all the absolute differences between model and experiment at each discrete time step. As shown in Figure 3, exceptional experiment/model fit between real data and Equation 9 occurs when τ is correctly selected to minimize SEE.

Identifying the correct value for τ enables useful data reduction by approximating the time at which turbine steady state rotation rate was achieved. All data collected after this time can be discarded as redundant. We used 4τ as the number of time constants required for the system to reach steady state. This decision is justified via the following analysis. At time = 0, $\dot{\Theta}_a(0) = 0$. For a functional form of $\dot{\Theta}_a(t) = \dot{\Theta}_{max}\left(1 - e^{-\frac{t}{\tau}}\right)$, at time = 4τ, $\dot{\Theta}_a(4\tau) = \dot{\Theta}_{max}\left(1 - e^{-\frac{4\tau}{\tau}}\right) \approx 0.982 \cdot \dot{\Theta}_{max}$. At time $\rightarrow \infty$, $\dot{\Theta}_a(\infty) \rightarrow \dot{\Theta}_{max}$. Therefore, the percent error of $\dot{\Theta}_a(4\tau)$ at time = 4τ relative to $\dot{\Theta}_{max}$ at time $\rightarrow \infty$ is given by the following calculation:

$$\% = \frac{\dot{\Theta}_{max} - \dot{\Theta}_a(4\tau)}{\dot{\Theta}_{max}} = \frac{\dot{\Theta}_{max} - (98.2\%)\dot{\Theta}_{max}}{\dot{\Theta}_{max}} \approx 1.8\% \qquad \text{(Eq. 10)}$$

In other words, the percent error of $\dot{\Theta}_a(4\tau)$ relative to $\dot{\Theta}_{max}$ is less than 2%, which we deem to be an acceptable engineering approximation in characterizing this system. If additional error

reduction is desired, data can be retained for a duration of nτ where n is an arbitrary number selected based on the level of precision needed for calculations.

Given the experimentally determined functional form of $\dot{\Theta}_a(t)$ in Equation 9, the turbine output power, P_{out}, can be expressed by carrying out the derivative implied in Equation 7

$$P_{out} = I \cdot \frac{d\dot{\Theta}_a(t)}{dt} \cdot \dot{\Theta}_a(t) = I \frac{d\left[\dot{\Theta}_{max}\left(1-e^{-\frac{t}{\tau}}\right)\right]}{dt} \dot{\Theta}_a(t) = \frac{I}{\tau} \cdot \dot{\Theta}_a(t) \cdot \dot{\Theta}_{max} \cdot e^{-\frac{t}{\tau}} \qquad \text{(Eq. 11)}$$

which reduces through the following algebraic manipulations to a second-order polynomial equation.

$$P_{out} = \frac{I}{\tau} \cdot \dot{\Theta}_a(t) \cdot \left[\dot{\Theta}_{max} - \dot{\Theta}_{max} + \dot{\Theta}_{max} \cdot e^{-\frac{t}{\tau}}\right] \qquad \text{(Eq. 12a)}$$

$$P_{out} = \frac{I}{\tau} \cdot \dot{\Theta}_a(t) \cdot \left[\dot{\Theta}_{max} - \dot{\Theta}_{max} \cdot \left(1 - e^{-\frac{t}{\tau}}\right)\right] \qquad \text{(Eq. 12b)}$$

$$P_{out} = \frac{I}{\tau} \cdot \dot{\Theta}_a(t) \cdot \left[\dot{\Theta}_{max} - \dot{\Theta}_a(t)\right] \qquad \text{(Eq. 12c)}$$

$$P_{out} = \frac{I}{\tau} \cdot \left[\dot{\Theta}_{max} \cdot \dot{\Theta}_a(t) - \dot{\Theta}_a(t)^2\right] \qquad \text{(Eq. 12d)}$$

For any compressed air input pressure, experimental values for τ and $\dot{\Theta}_{max}$ are determined using techniques described above.

Discussion

To evalaute how well the empirical power curve model of Equation 12d matches the turbine's actual performance turbine power data are directly extracted via dynamic dynamomtry by using an approximate differential form of Equation 7

$$P_{out} \approx I \cdot \frac{\Delta\dot{\Theta}_a(t)}{\Delta t} \cdot \dot{\Theta}_a(t). \qquad \text{(Eq. 13)}$$

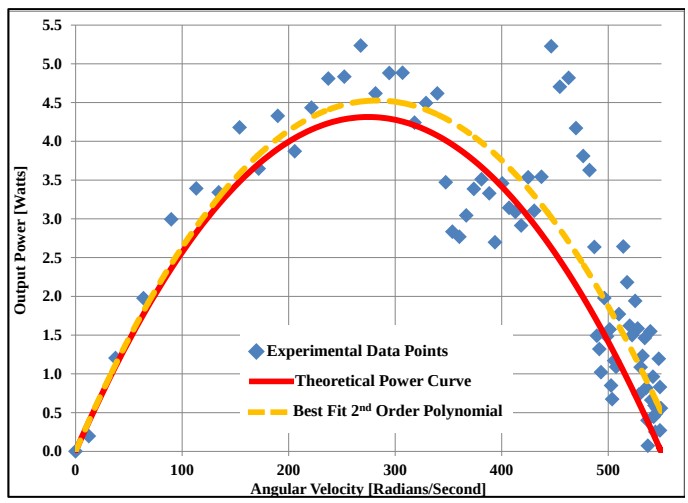

Figure 4: Example theoretical versus experimental turbine power curves obtained from dynamic dynamometry. The theoretical model slightly under-predicts peak power and the rotational velocity to achieve it compared to a polynomial fitted to experimental data.

Here, the differential rotational velocity measured during turbine spin-up at each time step substitutes for the pure derivative allowing the turbine power output at each rotational velocity to be quantified. For 90 psi input pressure, the resulting comparision between the empirical power curve model of Equation 12d and the discrete turbine power veruses rotational velocity represented by Eqauation 13 is shown in Figure 4.

Of paramount importance to power system designers is the turbine's peak power and the rotational velocity the turbine must run at to achieve this maximum performance point. For the theoretical power curve, the maximum power point is found by setting the derivative of the function to zero,

$$\frac{dP_{out}}{d\dot{\Theta}_a(t)} = \frac{I}{\tau} \cdot \left[\dot{\Theta}_{max} - 2\dot{\Theta}_a(t)\right] = 0 \qquad \text{(Eq. 14a)}$$

$$\dot{\Theta}_{a,maxpower} = \frac{\dot{\Theta}_{max}}{2} \qquad \text{(Eq. 14b)}$$

and maximum power is therefore

$$P_{out,maxpower} = \frac{I}{\tau} \cdot \left[\dot{\Theta}_{max} \cdot \frac{\dot{\Theta}_{max}}{2} - \left(\frac{\dot{\Theta}_{max}}{2}\right)^2\right] \qquad \text{(Eq. 15a)}$$

$$P_{out,maxpower} = \frac{I}{\tau} \cdot \left[\frac{\left(\dot{\Theta}_{max}\right)^2}{4}\right] \qquad \text{(Eq. 15b)}$$

For the example case of 90 psi input pressure, $\dot{\Theta}_{max} = 549.55\, rad/sec$. This measured result gives $\dot{\Theta}_{a,maxpower} = 274.76\, rad/sec$ for Eq. 14b yielding $P_{out,maxpower} = 4.32\, watts$ from Eq. 15b for the theoretical power curve. By comparison, the curve fitted to the empirical data gives $\dot{\Theta}_{a,maxpower} = 283.12\, rad/sec$ yielding $P_{out,maxpower} = 4.52\, watts$. In other words, the theory under-predicts $\dot{\Theta}_{a,maxpower}$ by only 2.95% resulting in an underproduction of $P_{out,maxpower}$ by only 4.70%. The predicative power of the theoretical model to pinpoint the turbine's maximum power point to better than 5% is an excellent and surprising result for such a simple analysis technique.

In addition to comparing the maximum power indicated by the theoretical curve of Eq. 12d to the best-fit curve for all data, another metric to evaluate the predictive capacity of Eq. 12d is comparison to the actual maximum power directly measured via dynamic dynamometry. From experimental data, $P_{out,maxpower} = 5.23\, watts$ at $\dot{\Theta}_{a,maxpower} = 267.70\, rad/sec$. Thus, Eq. 15b under-predicts maximum power by 17.5% and over-predicts the rotational velocity of the maximum power point by 2.58%. However, since direct measurement of maximum power and maximum power point are based on discretely sampled data, it is possible that closer theory/experimental agreement could be achieved if the data were sampled at a higher rate.

Conclusions

For Rankine power cycles, the need to tightly regulate working fluid phase through the turbine limits the power produced and overall cycle efficiency. While Rankine cycles will someday dominate spacecraft power generation for manned space missions, limitations on power plant efficiency and power imposed by need for single-phase through-turbine flow will hinder adoption of this technology to power in interplanetary spacecraft. Disk turbines have the

potential for continuous operation while processing two-phase (vapor-liquid) working fluid and are therefore a desirable technology to anchor space-based Rankine power cycles.

We describe a method called dynamic dynamometry to accurately measure and predict turbine mechanical power output using the rational inertia of the turbine's spinning components and friction in its bearings as the load. Using turbine spin-up, steady-state, and spin-down data captured via an optical tachometer, we present a method to indirectly determine the turbine's rotational inertia and predict its power curve. Comparing the resulting theoretical maximum power and rotational velocity for this point against a best fit curve for all experimental data yields excellent agreement. For the representative case of 90 psi turbine inlet pressure the maximum power is under-predicted by only 4.70% while the rotational velocity needed to operate at this point is under-predicted by only 2.95%. We conclude that the derived theoretical model is a reasonable tool to analyze and predict the actual performance of disk turbines. This tool will be used for future experimental and theoretical evaluations of disk turbines for space-based power generation using Rankine cycles.

---

[i] R. T. Lahey, V. Dhir, "Research in Support of the Use of Rankine Cycle Energy Conversion Systems for Space Power and Propulsion," Report NASA/CR-2004-213142, 2004.

[ii] T. Caillat, A. Borshchevsky, J. Fleurial, J. Snyder, "Space Technology and Applications International Forum," Editor: El-Genk, M. S., American Institute of Physics, 2000.

[iii] J. E. McKeathen, R. F. Reidy, S. K. S. Boetcher, M. J. Traum, "A Cryogenic Rankine Cycle for Space Power Generation," AIAA Paper Number 2009-4247, *Proceedings of the 41st AIAA Thermophysics Conference*, San Antonio, TX, June 22 - 25, 2009.

[iv] W. Rice, "Tesla Turbomachinery," In E. Logan & R. Roy (Eds.), Handbook of Turbomachinery, Marcel Dekker, New York:, 2003, pp. 861–874.

[v] T. A. Emran, "Tesla Turbine Torque Modeling for Construction of a Dynamometer and Turbine," Masters Thesis, University of North Texas, 2011.

[vi] T. A. Emran, R. C. Alexander, C. T. Stallings, M. A. DeMay, M. J. Traum, "Method to Accurately Estimate Tesla Turbine Stall Torque for Dynamometer or Generator Load Selection," *ASME Early Career Technical Journal*, Volume 10, pp. 158-164, 2010 [URL: http://districts.asme.org/DistrictF/ECTC/2010ECTC.htm].

[vii] V. G. Krishnan, Z. Iqbal, M. M. Maharbiz, "A micro Tesla turbine for power generation from low pressure heads and evaporation driven flows," *Proceedings of the 16th International Solid-State Sensors, Actuators and Microsystems Conference*, Beijing, China, June 5-9, 2011, pp. 1851-1854.

[viii] Z. Yang, H. Weiss, M. J. Traum, "Gas Turbine Dynamic Dynamometry: A New Energy Engineering Laboratory Module," *Proceedings of the 2013 ASEE North Midwest Section Conference*, Fargo, North Dakota, Oct. 17-18, 2013.

[ix] VCL Media Player, http://www.vlcapp.com/vlc-features/frame-by-frame-video-player/ , accessed 7/30/2012.

Nitrogen Phase Separation During Free Fall to Inform Design of Future Microgravity Cryogenic Rankine Power Cycles

Roberto J. Fernandez, Matthew J. Traum[1]

Mechanical Engineering Department, Milwaukee School Of Engineering, Milwaukee, WI

Introduction

On Earth, potential solutions for our sustainable, enduring, high-density power needs are plentiful. However, in space no practical solutions currently exist to support long-term manned interplanetary missions. These missions require power sources possessing three critical attributes: high power density, longevity, and continuous operation independent of direct sunlight. Many existing space power technologies have two, but not all three of these critical elements.

The two Voyager spacecraft use radioisotope thermoelectric generators (RTGs), which are extremely robust and long-lived with 50-year operational lives. Of the three essential attributes for interplanetary manned space missions, RTG's possess two: longevity and operation independent of sunlight. However, their energy density is low. Newly produced RTG's generate about 120 watts of electrical power and weigh about 45 kg, yielding an energy density of about 2.67 W/kg.[i] This low power density is far too small to support manned space missions.

Advanced fuel cells were used to power NASA's Orbiter. Of the three essential attributes for interplanetary manned space missions, fuel cells possess high energy density and can operate independent of sunlight. However, they do not possess longevity because their consumables are used up rapidly. The Orbiter's fuel cells were small in physical size and mass, able to produce 12 peak kilowatts, and they boasted energy density exceeding 529 W/kg.[ii] Nonetheless, these cells required routine maintenance and used consumable supplies of oxygen and hydrogen. Orbiters typically contained 3 fuel cells each with an operating life of 2000 hours. Each fuel cell consumed on average 1.8 kg of oxygen and 0.27 kg of hydrogen per hour.[iii] About 11,000 kg of oxygen and 1600 kg of hydrogen needed to be carried by the Orbiter for full operation of all three fuel cells. Use of fuel cells over the prolonged periods required for manned interplanetary missions would require massive fuel storage systems which are not feasible.

The Photovoltaic Cells (PVCs) making up the solar arrays of the International Space Station are the current answer to sustained power generation for manned space missions. Of the three essential attributes for interplanetary manned space missions, PVCs possess relatively high energy density as well as longevity. However, they require sunlight to operate. Sunlight intensity falls off as the square of the distance from the source. Thus, PVCs will produce significantly less power as interplanetary spacecraft travel away from the sun. For example, the semi-major radius of Earth's orbit versus Mar's orbit is

[1]The corresponding author gratefully acknowledges the Wisconsin Space Grant Consortium 2012-2013 Higher Education Incentives Award Program for making this project possible. Funding was also provided by the Texas Space Grant Consortium 2010-2011 New Investigator Award Program. Both authors acknowledge Cameron R. Schulz for his helpful consultation on the payload free fall model. This paper's undergraduate lead author is a member of the Milwaukee Undergraduate Researcher Incubator (MURI) at MSOE, an organization which fast-tracks undergraduates into meaningful early research experiences.

about 74,800,000 km versus 114,000,000 km respectively, meaning a PVC on a spacecraft orbiting Mars could produce only about 43% of the power it could while orbiting Earth. The other shortcoming of PVCs is need for large collector surface area. Due to their size, large arrays are expensive to launch into space. Hence power per unit area is the chief comparison metric to evaluate these systems. The solar array network on the International Space Station is 4047 square meters and produces 90 peak kilowatts of power,[iv] which equates to about 22.2 W/m^2.

Realizing that all conventional space power generation technologies lack at least one essential attribute for manned interplanetary missions, NASA identified Rankine cycle power plants as an essential element for future manned space missions. If operated from a nuclear heat source, these power cycles could provide high energy density, longevity, and continuous operation independent of direct sunlight.[v] In fact, recent advances in micro-fabrication technology suggest Rankine cycles could be produced with predicted power densities of 12,000 W/kg.[vi] The Rankine cycle is the same thermodynamic power cycle used in conventional terrestrial coal-fired power plants for electricity generation.

Background

One promising avenue for space-based power generation for manned interplanetary missions is the cryogenic Rankine power cycle. This power cycle is used on Earth by utilities within the Liquid Natural Gas (LNG) industry to recover energy otherwise lost via LNG vaporization to supply natural gas to end users.[vii] Given NASA's vast experience handling cryogenic fluids in space, nearly all the technologies to implement a space-based Rankine power cycle already exist.[viii] The largest element by area of a space-based Rankine power cycle would be the condenser, which could be integrated into the outer surface of a spacecraft to radiate entropy to space. This configuration, if fired by a nuclear reactor, would boast a much larger power to unit area ratio than PVCs, and would represent a viable solution to the need for high-density power generation in space for manned interplanetary missions.[ix]

Theory

The hallmark of the Rankine cycle is two-phase (liquid/vapor) working fluid. As it flows through the cycle, the working fluid is vaporized in the evaporator, expanded through the turbine, condensed in the condenser, and then pumped back into the evaporator. Critical to implementing a space-based Rankine cycle is handling microgravity phase separation in the condenser. Working fluid that has liquefied can be pumped back to the evaporator, but any remaining vapor must be separated and re-condensed before it can be pumped. On Earth, Rankine cycle liquid/vapor separation occurs naturally via gravity-induced buoyancy; with gravity absent in space, this separation mechanism will not work. Thus, to implement any space-based Rankine power cycle, a need exists to perfect microgravity phase separation.

Cryogenic fluid microgravity phase separation research with porous barriers has been conducted.[x] Both NASA and the U.S. military have perfected cryogenic fluid management techniques, including phase separation, for space flight functions including life support, fuel management, and supply transfer.[xi],[xii] Previous microgravity cryogenic fluid phase separators utilized thermo-mechanical effect, a super-fluid property of helium II, to phase separate fluid across a porous plug.[xiii,xiv,xv] Certain porous plugs were also found to be efficient microgravity phase separators for helium I, which is not a superfluid.[xvi] Thus, phase separation of other cryogenic fluids, such as liquid nitrogen, can be achieved by applying findings demonstrated for helium I.

A porous plug will be used as the phase separator within the cryogenic Rankine cycle condenser. The porous plug will have capillaries on the order of a few micrometers in diameter inlayed within it that serve as passages for the fluid. The plug shall also have a thickness equal to 4% of the diameter of the condenser. The thickness of the plug is an important variable because as the fluid travels through the barrier it will encounter viscous and capillary forces that retard motion, and it is desirable to minimize these energy loss mechanisms. The thicker the plug, the larger these retarding forces become making the pumping process more difficult and therefore less efficient.[viii] A diagram of the force interactions across the barrier is given in Figure 1.

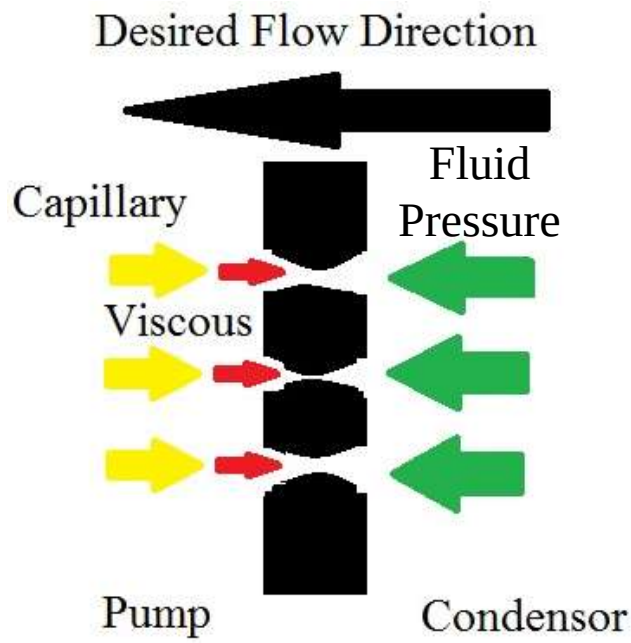

Figure 1: Depiction of the various dominant pressures and forces acting on microgravity capillary flow within a porous plug that is phase-separating a mixed liquid/vapor working fluid.

While cryogenic fluid phase separation using a porous plug is a proven concept, practical and efficient implementation of this idea within a space-based power plant is dependent upon optimizing many underlying variables: nitrogen thermal-fluidic properties such as contact angle, density, surface tension, and viscosity; as well as porous plug properties like material selection, void fraction, capillary size, interior surface roughness, and tortuosity. While some of these properties can be measured directly, many cannot. Moreover the effects of interactions between properties are complex and poorly understood. Therefore, we opt to proceed toward choosing the best porous barrier for cryogenic fluid microgravity phase separation via an empirical Design Of Experiments (DOE) approach.

Proposed Experiment

The experiment will rely upon a method of simulating microgravity shown in Figure 2. The phase separation efficacy of different porous plugs will be tested by launching a sounding rocket one mile (about 1609 meters) high. At apogee, the rocket will separate into two pieces: the rocket shell itself and a smaller payload pod containing the experimental apparatus. Experimental measurements will be taken in the payload pod, which will be designed to minimize drag, throughout its descent. While an object is accelerating during free fall, its contents are subjected to microgravity; the instant the falling object reaches terminal velocity, gravitational forces are balanced by drag forces and microgravity conditions cease in its interior. Therefore, the experiment will end once the rocket has attained terminal velocity.

To approximate how long the free-fall period will last, the kinematic equation for one-dimensional motion of an object falling under gravity is to be utilized. These equations are applied assuming gravitational acceleration, g, is independent of altitude; velocity of the pod at rocket apogee is zero; and that there is no drag on the payload pod:

$$y(t) = y_o - \frac{1}{2}gt^2 \quad \text{(Eq. 1)}$$

$$v(t) = -gt \quad \text{(Eq. 2)}$$

where *y(t)* and *v(t)* are the pod altitude and velocity as a function of time, t, and y_o is the rocket apogee altitude. The assumptions used, particularly ignoring drag, oversimplify the model, but they still provide a reasonable order-of-magnitude estimate of the time available to complete experimental measurements. Critically, this time is on the order of seconds, which is a reasonable duration during which thermodynamic measurements such as temperature and pressure can be taken.

The payload pod will be designed so its parachutes deploy 150 meters above the ground, allowing it to slow to a safe impact velocity for successful recovery. Under the stated modeling assumptions, the payload pod will fall for about 17.25 seconds traveling over 1459 meters and reaching a velocity of over 169 m/s at the time of chute deployment.

The total number of possible flights will be limited by cost, time, and the repeated successful launch and recovery of both the rocket and its payload. Therefore an empirical Design Of Experiments (DOE) approach will be used to minimize the number of flights needed to obtain information about how various porous plug parameters impact microgravity phase separation. For each test, the thermodynamic state of the nitrogen will be fixed by ensuring two independent intensive thermodynamic variables (temperature and specific volume) are identically reproduced each time. Porous plugs will be selected that exhibit four levels each of three different important independent variables: material selection, void fraction, and internal capillary size. To run every test in this experiment matrix would require $4^3 = 64$ unique flights. However, using an orthogonal array following Taguchi's method for experiment reduction, only 16 launches will be needed to fully explore the experimental space. The results from these tests will be used to select the best combination of porous plug parameters for use in microgravity cryogenic Rankine power cycles to enable nitrogen liquid/vapor phase separation in the condenser.

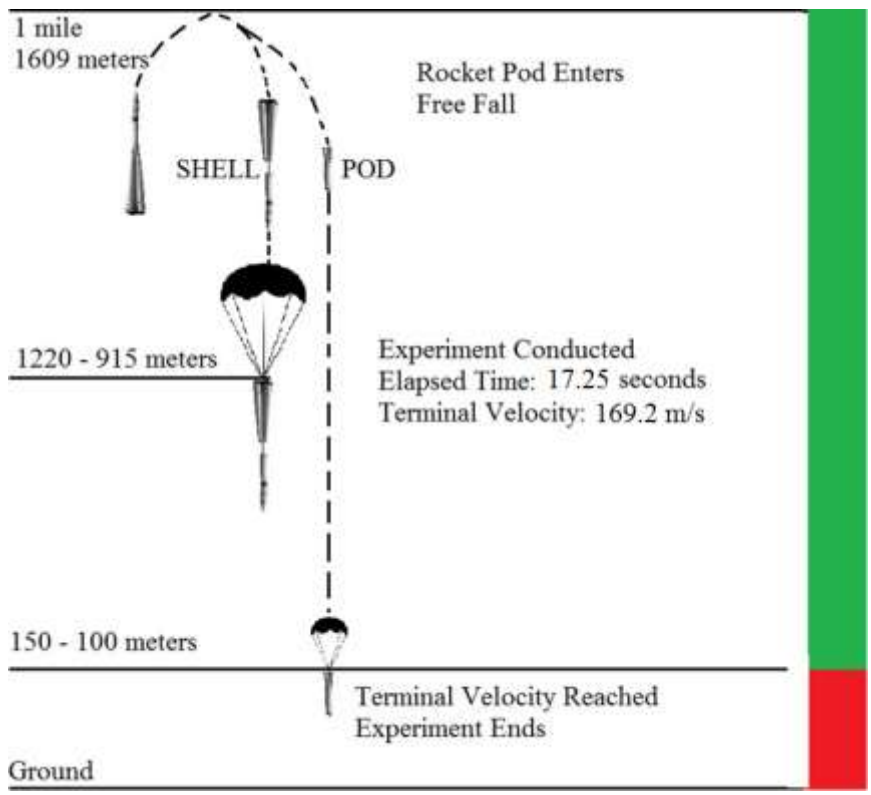

Figure 2: Rocket launch and recovery cycle for the proposed microgravity porous plug cryogenic fluid phase separation experiment.

Conclusions

The state-of-the-art with respect to conventional space-based power generation technologies was outlined in this paper. Since none of the current technologies poses all three attributes critical for future manned interplanetary missions; high power density, longevity, and continuous operation independent of direct sunlight; none are viable for these missions. Some new type of space-based power generation technology is needed to enable future planned manned missions beyond Earth orbit. The cryogenic Rankine cycle is a strong candidate since all technologies and techniques needed to implement this power cycle have already been developed and demonstrated. To function correctly, Rankine cycles require liquid/vapor phase separation, a process normally accomplished in terrestrial applications via gravity-driven buoyancy. For a space-based Rankine cycle to be successfully implemented, microgravity phase separation is needed.

NASA and the U.S. military have already demonstrated microgravity phase separation of non-superfluid cryogenic liquid-vapor mixtures using porous plugs. This technique will therefore be adapted to implement phase separation for a cryogenic Rankine cycle. To select the best combination of porous plug parameters to minimize pressure losses (and parasitic power losses) in the cycle a series of experiments will be conducted to test the phase separation efficacy of several porous plug varieties. An experimental apparatus to measure phase separation efficacy will be launched on a sounding rocket and allowed to free fall, producing microgravity conditions for 17.25 seconds during which the phase separation efficacy of each porous plug sample will be tested and evaluated.

Using the DOE technique following Taguchi's method for experiment reduction, the best performing combination of porous barrier parameters (material selection, void fraction, and internal capillary size) will be identified that demonstrates the most effective nitrogen liquid/vapor phase separation in microgravity. This experiment will provide the final technology demonstration needed to fully implement a cryogenic Rankine power cycle for space-based power generation applications.

References

[i] NASA, "Space Radioisotope Power Systems Multi-Mission Radioisotope Thermoelectric Generator," URL: http://solarsystem.nasa.gov/docs/MMRTG_Jan2008.pdf, accessed 8/15/2013.

[ii] R. E. Martin, "Lightweight Fuel Cell Powerplant Components Program," Report NASA-CR-161412, United Technologies Power Systems Division, February, 1980.

[iii] *Fuel Cell Power Plants*, url: http://spaceflight.nasa.gov/shuttle/reference/shutref/orbiter/eps/pwrplants.html , last accessed 8/15/2013.

[iv] *Facts and Figures*, url: http://www.nasa.gov/mission_pages/station/main/onthestation/facts_and_figures.html#.Uf8A2JLVB8E , last accessed 8/15/2013.

[v] R. T. Lahey, V. Dhir, "Research in Support of the Use of Rankine Cycle Energy Conversion Systems for Space Power and Propulsion," Report NASA/CR-2004-213142, 2004.

[vi] L. G. Fréchette, C. Lee, S. Arslan, Y.-C. Liu, "Design of a Microfabricated Rankine Cycle Steam Turbine for Power Generation," Paper IMECE2003-42082, *Proceedings of IMECE '03 the 2003 ASME International Mechanical Engineering Congress & Exposition*, Washington, D.C., November 16-21, 2003.

[vii] *Cryogenic Power Generation System Recovering LNG's Cryogenic Energy and Generating Power for Energy and CO_2 Emission Savings*, url: http://www.osakagas.co.jp/en/rd/technical/1198907_6995.html , last accessed 8/15/2013.

[viii] J. E. McKeathen, R. F. Reidy, S. K. S. Boetcher, M. J. Traum, "A Cryogenic Rankine Cycle for Space Power Generation," AIAA Paper Number 2009-4247, *Proceedings of the 41st AIAA Thermophysics Conference*, San Antonio, TX, June 22 - 25, 2009.

[ix] L. Lin, X.-L. Yu, Z. Xin, X.-Z. Zhang, "Thermal Cycle Design of Liquid Nitrogen Engine," *Journal of Zhejiang University*, Vol. 40, No. 11, 2006, pp. 1989-1993.

[x] D. M. Althausen, F. D. Quinn Jr., C. T. Bunnell, N. E. Daidzic, "Porous Media Condensing Heat Exchanger with Integral Gas Liquid Separation for Space Flight Use," *Proceedings of the 44th AIAA Aerospace Sciences Meeting*, American Institute of Aeronautics and Astronautics Inc., Reston, VA, 2006, pp. 16186-16196.

[xi] M. J. DiPirro, R. F. Boyle, O. Figueroa, D. Lindauer, D. C. McHugh, P. J. Shirron, "Superfluid Helium Heat Transfer," *AIAA/ASME Thermophysics and Heat Transfer Conference*. Published by ASME, New York, 1990.

[xii] M. J. DiPirro, J. Zahniser, "Liquid/Vapor Phase Boundary in a Porous Plug," *Proceedings of the 1989 Cryogenic Engineering Conference*, Vol. 35, Part 1, 1990, pp. 173-180.

[xiii] M. J. DiPirro, R. F. Boyle, O. Figueroa, D. Lindauer, D. C. McHugh, P. J. Shirron, "The SHOOT Cryogenic System," *Superfluid Helium Heat Transfer*, United Engineering Center, New York, NY, 1990, p. 29.

[xiv] M. J. DiPirro, J. Zahniser, "The Liquid/Vapor Phase Boundary in a Porous Plug," *Advances in Cryogenic Engineering*, Vol. 35, Plumum Press, New York, NY, 1990, pp. 173–180.

[xv] V. G. Baranov, A. I. Vinnikov, M. I. Gutkin, "A Study of the Operation of a Helium Vessel Phase Separator," Translated from *Khimicheskoe I Neftaynoe Mashinostroenie*, No. 8, August 1976, pp. 12–13.

[xvi] M. J. DiPirro, D. C. McHugh, J. Zahniser, "Phase Separators for Normal and Superfluid Helium," *Proceedings of the Twelfth International Cryogenic Engineering Conference - ICEC 12*, 1988, pp. 681-689.

23rd Annual Conference
Part Seven

Planetary Geology & Astronomy

Lassen Volcanic Fumaroles and Hot Springs: Analog for Mars

Lindsay J. McHenry[1], Teri L. Gerard, Gabrielle L. Walters
Department of Geosciences, University of Wisconsin- Milwaukee

Abstract

We are conducting a pilot study on the hydrothermal alteration of lavas at Lassen Volcanic National Park as an analog for potential hydrothermal deposits on Mars. Lassen has hot springs and fumaroles that have altered its lavas into silica, sulfates, and phyllosilicates, all mineral types also identified on Mars. Hydrothermal environments were likely common on Mars (due to evidence of early aqueous and a long record of volcanic activity), and such environments could have remained habitable long after the surface cooled and desiccated. However, some hydrothermal environments are more habitable than others, and being able to distinguish between the deposits of hostile acid-sulfate fumarole and more accommodating near-neutral hot spring environments can provide clues to habitability. Lassen hydrothermal environments produce silica by both acid-sulfate leaching and precipitation from neutral hydrothermal waters, both of which have been suggested as potential origins for deposits in Columbia Hills of Gusev Crater on Mars.

Objectives

The objectives of this study are to:

1. Determine the mineralogical and geochemical patterns of lava alteration associated with acid-sulfate leaching at Lassen hot springs and fumaroles, and contrast them with the patterns associated with more neutral, Cl-rich hydrothermal fluids at fumaroles and hot springs within Lassen park.
2. Compare these results to the mineralogy and geochemistry of hydrothermal deposits observed in the Columbia Hills of Gusev Crater, and determine if either scenario is more consistent with the observations.
3. Determine what mineralogical and geochemical evidence for hydrothermal alteration is most likely to be preserved in the rock record by analyzing samples from the hydrothermally altered lavas of Pleistocene Brokeoff Volcano (in Lassen park) and comparing them to samples from the active fields.

Introduction

One of the most fascinating discoveries about Mars over the last decade has been the presence of extensive sulfate and phyllosilicate alteration products on its surface, potentially indicating the long-term interaction between liquid water and Mars' volcanic crust (e.g. Bibring et al., 2005; Murchie et al., 2009). This suggests a warmer, wetter Mars during its early history, followed by eventual desiccation and cooling. If life ever emerged on Mars, it likely did so during this early period. However, wet, warm environments conducive to life likely persisted in "hydrothermal" environments associated with volcanic activity long after the surface became inhospitable (Walter & Des Marais, 1993; Schulze-Markuch et al., 2007). Likely mineralogical and geochemical evidence for hydrothermal activity on Mars has been observed by the Mars Exploration Rover (MER) Spirit at Gusev Crater (e.g. Yen et al., 2008), and through remote sensing from the Mars Reconnaissance Orbiter (MRO, e.g. Ehlmann et al., 2009).

[1] The authors would like to acknowledge the Wisconsin Space Grant Consortium for their ongoing financial support of this project, and the National Park Service for granting permission to conduct field research at Lassen Volcanic National Park.

Earth has similar deposits in volcanically active areas, and by studying the active processes and deposits created in diverse terrestrial environments, we can better interpret the context of Martian deposits. What mineralogical and geochemical changes occur when hydrothermal fluids interact with volcanic material? How much of this signature is preserved in the rock record? Can these mineralogical and geochemical alteration patterns be used to determine the nature of the fluids (pH, temperature, salinity, etc.) involved, which could help determine potential habitability? All of these questions can be addressed through terrestrial analog studies.

We are conducting an analog study on fumarole and hot spring related hydrothermal alteration at Lassen Volcanic National Park in the southern Cascades of California. While the underlying volcanic composition is different from Mars (dacitic, not basaltic), the overall mineralogical and geochemical alteration patterns appear similar, with alunite (an aluminum sulfate), phyllosilicates, and silica. Sampling older, "fossil" hydrothermal deposits within the park (e.g. Pleistocene altered rocks from Brokeoff Mountain: Rose et al., 1994, Crowley et al., 2004; John et al., 2004; Janik and McLaren, 2010) will allow us to examine the long-term preservation potential of this kind of deposit.

Geological Background

Mount Lassen, in the southern Cascades of Northern California, last erupted in 1914-1915 (Day and Allen, 1925). It has the largest active hydrothermal field in the Cascades, with fumaroles, hot springs, and mud pots (Janik and McLaren, 2010). Volcanic activity in the Lassen area began 825,000 years ago and a series of volcanoes: dacitic Rockland caldera, then andesitic Brokeoff volcano 590,000 years ago, then dacitic Lassen ~27,000 years ago (Janik and McLaren, 2010).

The modern hydrothermal system near Lassen likely had its origin either with the onset of silicic volcanism in the Lassen area ~315,000 years ago, or as recently as 100,000 years ago (Crowley et al., 2004). Currently active steam discharge areas include Bumpass Hell (solfatara: sulfur-rich fumaroles), Sulphur Works, and Devil's Kitchen. Most are acid-sulfate, steam-heated systems, though Little Hot Springs valley shows evidence for more neutral, chlorine-rich hydrothermal fluids (Muffler et al., 1982; Thompson et al., 1985). Most of the hydrothermal waters are isotopically consistent with local meteoric waters suggesting a local source, though some signatures of Mantle-derived volatiles are observed at Sulphur Works (Janik and McLaren, 2010). Figure 1 is a map of the park, highlighting the location of the hydrothermal areas.

These currently active solfataras and other hydrothermal vents have altered the surrounding and underlying rock, which includes dacite (Sulphur Works, Bumpass Hell areas) and andesite (Devil's Kitchen). Less altered rocks are also present at a distance from the hydrothermally altered parts, allowing us to compare fresh and altered rock compositions to help reconstruct the patterns and pathways of alteration. Valley cuts expose a depth profile of the Pleistocene Brokeoff volcano fossil hydrothermal system, which altered both andesites and dacites (Janik and McLaren, 2010). This will allow us to compare ancient (~590,000 year) and modern hydrothermal deposits to help constrain what signatures of past hydrothermal activity are most likely to be preserved, and how such deposits vary with depth.

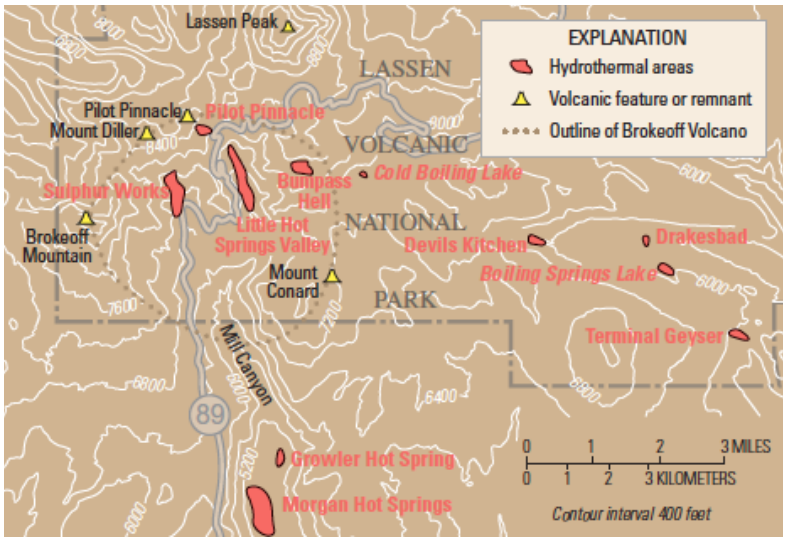

Figure 1: Map of Lassen hydrothermal field, adapted from Clynne et al., 2003.

The products of alteration in these areas include abundant hydrothermally-derived clays (montmorillonite and kaolinite), silica, and alunite (aluminum sulfate). The initial descriptions of these deposits (Day and Allen, 1925; Anderson, 1935) pre-date X-ray Diffraction, and it is likely that other minerals were not identified. Interestingly, silica-rich hydrothermally altered lavas in Lassen hydrothermal fields appear to have formed through both leaching (in acid-sulfate contexts) and precipitation of silica as a sinter (in the near-neutral, Cl-rich hydrothermal deposits: Janik and McLaren, 2010). A mineralogical and geochemical comparison between these two could help identify "fingerprints" for each environment that could be applied to sites on Mars (e.g. Gusev) where both processes have been proposed (Ruff et al., 2011).

Background: Mars Hydrothermal Alteration

The Planetary Decadal Survey (2011) recognizes the importance of Mars' hydrothermal environments: "In all epochs, the combination of volcanism and water-rich conditions might have sustained hydrothermal systems in which life could have thrived." Hydrothermal environments such as fumaroles and hot springs provide sources of heat, energy, and water for life (Walter & Des Marais, 1993; Schulze-Markuch et al., 2007), even when it is too dry or cold for life to persist nearby. A hydrothermal origin has been proposed for some Mars surface features, including the mineralogy and geochemistry of some outcrops and soils studied by MER Spirit at Gusev (e.g. Yen et al., 2008), channels carved by flowing water that likely originated from melting of subsurface ice or release of hydrothermal fluids (e.g. Farmer et al., 1996), and potential hydrothermal mineral assemblages identified from orbit (e.g. Ehlmann et al., 2009). Chojnacki & Hynek (2008) attribute some of the widespread Valles Marineris sulfate deposits to high temperature basalt alteration. Schulze-Makuch et al. (2007) outline targets for Martian hydrothermal environments, and Bishop et al. (2008) even propose hydrothermal activity as a possible explanation for mineralogical features of one of four finalist 2011 MSL landing sites: Mawrth Vallis. Gale Crater, the selected MSL landing site, has abundant sulfates and phyllosilicates (Milliken et al., 2010), likely formed in part by basalt alteration. Mawrth Vallis (or Nili Fossae, another potential hydrothermal site: Ehlmann et al., 2009) could be targeted for a future mission (e.g. ExoMars, Mars 2020).

Since the surface of Mars is largely volcanic (McSween et al., 2009), evidence for hydrothermal activity lies in the alteration products and element mobility patterns produced when hydrothermal fluids interact with volcanic materials. Geochemical and mineralogical evidence can help distinguish hydrothermal from ambient temperature fluid-rock interaction, which can help reconstruct potentially habitable environments. The MER sites show evidence for hydrothermal and low temperature fluid-basalt interaction. Likely hydrothermal features have been discovered in Gusev's Columbia Hills (e.g. Schmidt et al., 2008). While Meridiani Planum has some features consistent with hydrothermal alteration (McCollom & Hynek, 2005), it is generally interpreted as a dirty evaporite-derived eolian deposit later altered by groundwater (e.g. McLennan et al., 2005).

Hydrothermal deposits at Gusev. Deposits in outcrops and soils in Gusev's Columbia Hills are interpreted as hydrothermal because of elevated silica and Ti (likely a sinter or leached deposit) and high S, Cl, and Br concentrations often associated with hydrothermal fluids (Squyres et al., 2007; Schmidt et al., 2008; Yen et al., 2008). The presence of Fe-sulfate minerals and partitioning between Cl and S suggest saline-acidic hydrothermal fluids (Squyres et al., 2007, 2008), potentially fumaroles (Squyres et al., 2007; Schmidt et al., 2009) or warm liquids (Squyres et al., 2008). Water-rock interaction explains the transport of non-volatile elements (e.g. Al, Na, Fe: Squyres et al., 2008) in the Si-rich soils (e.g. Eastern valley: Morris et al., 2008), but isochemical alteration of some rocks (e.g. Watchtower: Morris et al., 2008) suggests low water-rock ratios (Wang et al., 2008), consistent with gaseous (potentially fumarolic) alteration. Ruff et al. (2011) argue that Gusev silica is not consistent with acid-sulfate fumarole leaching but rather with precipitation of a Si-rich sinter from near-neutral fluids. The extent of the Gusev alteration products is unknown since most soils were trenched from the sub-surface by Spirit's wheel and have not been detected remotely; hydrothermal deposits may thus be more widespread than orbital data would indicate (Arvidson et al., 2008). The interpretation of these deposits depends on our ability to distinguish between the products of low and high-T alteration under varied aqueous and fumarolic conditions, which can be addressed in part by studying analog environments on Earth.

Methods

Field methods. In September-October 2012, Dr. Lindsay McHenry, Ph.D. student Teri Gerard, and undergraduate student Gabrielle Walters visited Lassen Volcanic National Park. Our team first visited Sulphur Works and Bumpass Hell, two sites dominated by acid sulfate fumarolic alteration, followed by Devil's Kitchen, Boiling Springs Lake, and Drakesbad Hot Springs, which include both acid-sulfate fumarole and more neutral thermal waters. Finally, our team climbed Brokeoff Mountain to collect samples of a "fossil" hydrothermal system.

At Sulphur Works, we collected a transect of mineral precipitates with increasing distance from a fumarole vent. Yellow sulfur crystals were collected directly adjacent to where the vapors were escaping. The color and texture of the precipitates changed with distance, changing from yellow to white and grey and finally to orange away from the vent. Each mineral zone was collected in turn. Figure 2 is a photograph of this deposit.

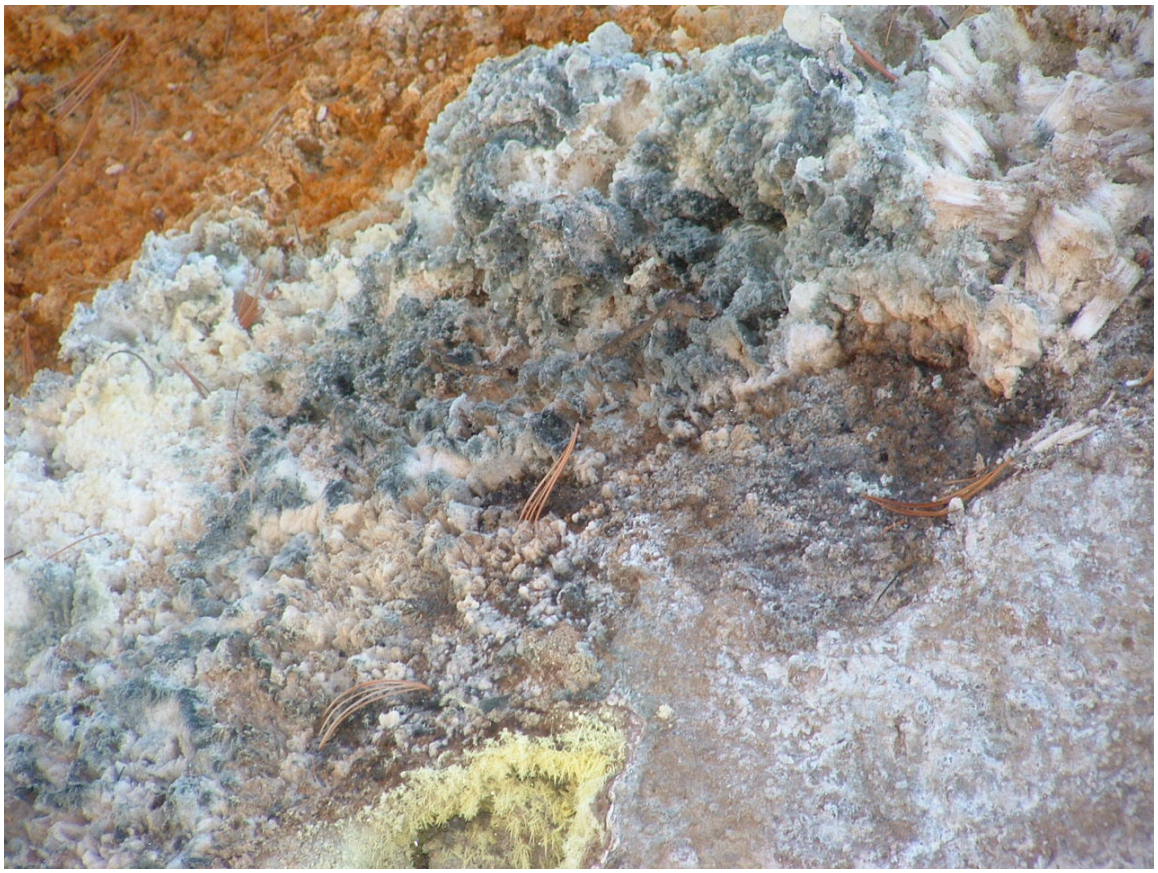

Figure 2: Sulphur Works fumarole mineral deposits. Yellow sulfur crystals (lower center) surround the vent, surrounded in turn by white and grey and then orange mineral deposits. Pine needles provide an approximate scale.

Mineral precipitate and altered rock coating samples were collected at all sites. Where such deposits were located in inaccessible or unsafe areas, a 1.6-meter pole with a can wired to the end was used to collect samples. Where possible, we measured the distance of each sample from its associated vent, or took pictures of the sampling spots with field equipment for scale. Samples were selected based on color and textural changes.

Water temperature and pH measurements were taken using a field pH probe at Sulphur Works, Bumpass Hell, Devil's Kitchen, Boiling Springs Lake, and Drakesbad Spring. Water samples were collected and filtered at Sulphur Works and Drakesbad Springs only.

Laboratory methods. Select samples were air dried and then powdered for X-Ray Diffraction (XRD) by hand using a mortar and pestle. Since soluble and temperature-sensitive sulfate minerals were anticipated, we did not use a shatterbox, micronizing mill, or heat lamp during preparation, nor did we use water or acetone to aid in the grinding process. This results in a powder that is coarser than normal for XRD analysis (and thus not suitable for quantitative phase analysis) but more likely to represent the original mineralogical composition. Each powdered sample was mounted as a random powder for analysis using a Bruker D8 Focus X-Ray Diffractometer. Samples were run using Cu Kα radiation, 1 s per 0.02° 2**θ**, 2°–60° range, and a Sol-X energy dispersive detector following the methods of McHenry, 2009.

The resulting XRD patterns were matched against the ICDD PDF database using Bruker's EVA software to identify the minerals present. Relative abundances (e.g. abundant, common, rare) were determined using relative peak heights. Amorphous silica was provisionally identified based on its characteristic "hump."

Results

Water analysis results. The results of the in-situ water analyses are reported in Table 1. Thermal and non-thermal waters covered a range of pH from highly acidic (pH < 2) to near neutral, in some cases over very short distances (within 2 meters).

Table 1: Field pH and temperature measurements of hydrothermal waters

Site	Description	pH	T (°C)	Sample?
Sulphur Works				
	bubbling pool	2.08	68.5	Yes
	nearby stream	6.90	12.0	Yes
Bumpass Hell				
	bubbling pond	2.45	81.0	
	aqua colored pond	3.00	15.5	
Devil's Kitchen				
	boiling clear water	6.40	93.4	
	nearby milky water	2.30	86.1	
	bubbling muddy pool	5.82	75.5	
Boiling Springs Lake				
	W edge of clear lake	1.88	46.0	
	clear boiling pot	2.93	86.5	
	boiling mud pot	3.84	87.0	
	S edge of clear lake	2.34	49.0	
Drakesbad Hot Spring				
	Warm stream	6.79	56.0	Yes

X-ray diffraction results. The results of the preliminary XRD study are presented in Table 2. Sulfur-bearing minerals are ubiquitous in all samples but SW-12-2, which is a sample of altered substrate. Elemental sulfur is present in samples from Sulphur Works, Bumpass Hell, and Devil's Kitchen, generally near the center of the fumarole where they form in direct contact with the fumarolic vapors. Sulfate minerals become more abundant with distance from the direct vapors, and include Fe-sulfates (jarosite, rhomboclase), Al-sulfates (alunite, alunogen), and mixed sulfates (natroalunite). Calcite and the Ca-sulfate mineral gypsum were so far only

observed in the coating from a rock in the stream at Drakesbad Hot Spring. The Fe-sulfide minerals pyrite and marcasite were so far only observed at Bumpass Hell, and indicate reducing conditions in the stream water at that site. The "rotten egg" smell at Bumpass Hell is consistent with H_2S gas rather than SO_2, which is also consistent with more reducing conditions.

Table 2: Mineral assemblages, based on X-Ray Diffraction

Sample	SiO2 minerals				Igneous		Clay minerals			Sulfates						Sulfides		Other	
	Quartz	Cristobalite	Tridymite	Amorphous	Feldspar	Pyroxene	Kaolinite	Montmorillonite	Halloysite	Jarosite	Rhomboclase	Alunite	Allunogen	Natroalunite	Gypsum	Pyrite	Marcasite	Sulfur	Calcite
Sulphur Works																			
SW-12-1	XX																	XXX	
SW-12-2				XX	X	X													
SW-12-14	XXX				+		X	+		X			+						
Bumpass Hell																			
BH-12-4	X	XXX	X	X										X					
BH-12-5		XX					X				X	X	+			XXX	X	X	
Devil's Kitchen																			
DK-12-3	XX	XXX	XXX						XX	XX									
DK-12-5	XXX	XXX	X	X			X	X				X						XX	
Drakesbad																			
BS-12-7				XX	X										XXX				X

XXX = abundant, XX = common, X = rare to common, + = rare.

Clay minerals were observed in samples from Sulphur Works, Bumpass Hell, and Devil's Kitchen. Halloysite and kaolinite are typical alteration products formed by acid hydrothermal leaching of feldspars or other igneous minerals, while montmorillonite (a smectite) can form under a wider range of conditions.

The SiO_2 mineral assemblage varied considerably between samples, including quartz, tridymite, cristobalite, and an amorphous phase likely consistent with amorphous silica. While quartz could be a primary igneous component of the dacitic substrate, the fact that it is not observed in the samples that yielded feldspars and pyroxenes (other primary dacitic constituents) makes it more likely related to the secondary and precipitated minerals. Cristobalite and tridymite are also phases associated with altered volcanics.

Amorphous silica can form during hydrothermal alteration, either by leaching under acidic conditions or direct precipitation under neutral sinter conditions (e.g. Ruff et al., 2011). It is likely that both processes took place in the Lassen hydrothermal system (e.g. Janik and McLaren, 2010); the amorphous phase in the altered substrate sample from Sulphur Works likely formed by acid-sulfate leaching, while the amorphous phase in the rock coating at Drakesbad probably

resulted from sinter precipitation. Future Scanning Electron Microscopy (SEM) analysis of these samples will help confirm the presence of amorphous silica (as opposed to glass or another amorphous phase).

Future Work

We will continue to analyze our 2012 samples by XRD to determine spatial patterns of alteration and precipitation around Lassen fumaroles. We will additionally analyze select samples by X-ray Fluorescence (XRF) Spectroscopy to determine their major and minor element compositions, tracking changes in bulk composition between more and less altered samples. Select samples will also be analyzed by SEM to help identify amorphous phases (such as amorphous silica or glass) and determine the textural relationships between the different minerals within samples, particularly in sample coatings and crusts.

In September-October 2013 we will visit Lassen Volcanic National Park a second time. We will re-visit Bumpass Hell and Devil's Kitchen to collect additional mineral and water samples, and will also visit Little Hot Springs Valley to expand our collection of near-neutral sinter deposits and associated water.

Once we have completed the field and laboratory phases of this project, we will assess which environmental parameters (e.g. temperature, pH, water composition, substrate composition) exert the greatest influence on the resulting alteration mineralogy and geochemistry, identifying "signatures" of specific conditions. This data, and our interpretations, will then be compared to published mineral and geochemical interpretations for potential Martian hydrothermal deposits (e.g. at Columbia Hills, Gusev Crater).

References

Arvidson, R.E., et al., 2008. Spirit Mars rover mission to the Columbia Hills, Gusev Crater: Mission overview and selected results from the Cumberland Ridge to Home Plate. JGR 113: E12S33.

Anderson, C.A., 1935. Alteration of the lavas surrounding the hot springs in Lassen Volcanic National Park. American Mineralogist 20: 242-253.

Bibring, J.-P., et al. (2005). Mars surface diversity as revealed by the OMEGA/Mars Express observations. Science 307: 1576-1581.

Bishop, J.L. et al., 2008. Phyllosilicate diversity and past aqueous activity revealed at Mawrth Vallis, Mars. Science 321: 830– 833.

Chojnacki, M., Hynek, B.M., 2008. Geological context of water-altered minerals in Valles Marineris, Mars. JGR 113: E12005.

Clynne, M.A., Janik, C.J., Muffler, L.J.P., 2003. "Hot water" in Lassen Volcanic National Park-Fumaroles, steaming gound, and boiling mudpots. U.S. Geological Survey Fact Sheet 101-02.

Crowley, J.K., Mars, J.C., John, D.A., Muffler, L.J.P., Clynne, M.A., 2004. Hydrothermal mineral zoning within an eroded stratocone: remote sensing spectral analysis of Brokeoff Volcano, California. In: King, P.L., Ramsey, M.S., Swayze, G.A. (Eds.), Infrared Spectroscopy in Geochemistry, Exploration Geochemistry, and Remote
Sensing. Mineralogical Association of Canada Short Course, vol. 33. Ontario, London, pp. 215–226.

Day, A.L., Allen, E.T., 1925. The Volcanic Activity and Hot Springs of Lassen Peak. The Carnegie Institution of Washington, Washington, 190pp.

Ehlmann, B.L., et al., 2009. Identification of hydrated silicate minerals on Mars using MRO-CRISM: Geologic context near Nili Fossae and implications for aqueous alteration. JGR 114: E00D08.

Farmer, J.D., 1996. Hydrothermal systems on Mars: an assessment of present evidence. In: Bock, G. Goode, J. (eds.), Evolution of Hydrothermal Ecosystems on Earth (and Mars?). Wiley, NY. 273-299.

Janik, C.J., LcLaren, M.K., 2010. Seismicity and fluid geochemistry at Lassen Volcanic National Park, California: Evidence for two circulation cells in the hydrothermal system. Journal of Volcanology and Geothermal Research 189: 257-277.

John, D.A., Briet, G.N., Lee, R.G., Diles, J.H., Muffler, L.P., Clynne, M.A., 2004. Fossil magmatic-hydrothermal systems in Pleistocene Brokeoff volcano, Lassen Volcanic National Park, California. *Eos Trans. AGU, 87*(52), Fall Meet. Suppl., Abstract V53A-1745.

McCollom, T.M., Marcucci, E, Hynek, B.M., 2010. Combined experimental and theoretical study of acid-sulfate alteration of basalt for interpretation of sulfate-rich deposits on mars, 41st Lunar and Planetary Science Conference, abstract 1380.

McHenry, L.J., 2009. Element mobility during zeolitic and argillic alteration of volcanic ash in a closed-basin lacustrine environment: Case study Olduvai Gorge, Tanzania. Chemical Geology 265, 540-552, doi: 10.1016/j.chemgeo.2009.05.019

McLennan, S.M., et al., 2005. Provenance and diagenesis of the evaporite-bearing Burns formation, Meridiani Planum, Mars. EPSL 240: 95-121.

McSween, H.Y.J., Taylor, G.J., Wyatt, M.B., 2009. Elemental composition of the Martian crust. Science 324: 736-739.
Milliken, R.E., Grotzinger, J.P., Thomson, B.J, .2010. Paleoclimate of Mars as captured by the stratigraphic record in Gale Crater. GRL 37: L04201.

Morris, R.V., et al., 2008. Iron mineralogy and aqueous alteration from Husband Hill through Home Plate at Gusev Crater, Mars: Results from the Mössbauer instrument on the Spirit Mars Exploration Rover. JGR 113: E12S42.

Muffler, L.J.P., Nehring, N.L., Truesdell, A.H., Janik, C.J., Clynne, M.A., Thompson, J.M., 1982. The Lassen Geothermal System. Proceedings of the Pacific Geothermal Conference 1982. University of Auckland, New Zealand, pp. 349–356.

Murchie, S.L., et al. (2009). A synthesis of Martian aqueous mineralogy after 1 Mars year of observations from the Mars Reconnaissance Orbiter, Journal of Geophysical Research 114: E00D06.

National Research Council (NRC), Committee on the Planetary Science Decadal Survey, 2011. Vision and voyages for planetary science in the decade 2013-2022. The National Academies Press, Washington, D.C., 400 pages.

Ruff, S.W. et al., 2011. Characteristics, distribution, origin, and significance of opaline silica observed by the Spirit rover in Gusev crater, Mars. Journal of Geophysical Research 116: E00F23.

Schmidt, M.E., et al., 2009. Spectral, mineralogical, and geochemical variations across Home Plate, Gusev Crater, Mars indicate high and low temperature alteration. Earth and Planetary Science Letters 281: 258-266.

Schmidt, M.E., Ruff, S.W., McCoy, T. J., Farrand, W.H., Johnson, J.R., Gellert, R., Ming, D.W., Morris, R.V., Cabrol, N.A., Lewis, K.W., Schröder, C., 2008. Hydrothermal origin of halogens at Home Plate, Gusev Crater. JGR 113: E06S12.

Schulze-Makuch, D. et al., 2007. Exploration of hydrothermal targets on Mars. Icarus 189: 308-324.

Squyres, S.W., et al., 2008. Detection of silica-rich deposits on Mars. Science 320: 1063-1067.
Squyres, S.W., et al., 2007. Pyroclastic activity at Home Plate in Gusev Crater, Mars. Science 316: 738-742.

Thompson, J.M., 1985. Chemistry of thermal and nonthermal springs in the vicinity of Lassen Volcanic National Park. Journal of Volcanology Geothermal Research 25: 81–104.

Walter, M.R., Des Marais, D.J., 1993. Preservation of biological information in thermal spring deposits: developing a strategy for the search for fossil life on Mars. Icarus 101: 129-143.

Wang, A., et al., 2008. Light-toned salty soils and coexisting Si-rich species discovered by the Mars Exploration Rover Spirit in Columbia Hills. JGR 113: E12S40.

Yen, A.S., et al., 2008. Hydrothermal processes at Gusev Crater: An evaluation of Paso Robles class soils. JGR 113: E06S10.

Dynamics of One-dimensional Self-gravitating Systems Using Hermite-Legendre Polynomials

Eric I. Barnes[1], Robert J. Ragan

Department of Physics, University of Wisconsin — La Crosse

ABSTRACT

The current paradigm for understanding galaxy formation in the universe depends on the existence of self-gravitating collisionless dark matter. Modeling such dark matter systems has been a major focus of astrophysicists, with much of that effort directed at computational techniques. Not surprisingly, a comprehensive understanding of the evolution of these self-gravitating systems still eludes us, since it involves the collective nonlinear dynamics of many-particle systems interacting via long-range forces described by the Vlasov equation. As a step towards developing a clearer picture of collisionless self-gravitating relaxation, we analyze the linearized dynamics of isolated one-dimensional systems near thermal equilibrium by expanding their phase space distribution functions $f(x, v)$ in terms of Hermite functions in the velocity variable, and Legendre functions involving the position variable. This approach produces a picture of phase-space evolution in terms of expansion coefficients, rather than spatial and velocity variables. We obtain equations of motion for the expansion coefficients for both test-particle distributions and self-gravitating linear perturbations of thermal equilibrium. This development presents the opportunity to avoid time-consuming N-body simulations that are limited by statistical uncertainty and provides a powerful analysis tool for understanding the relaxation to equilibrium.

1. Introduction

Over the past several decades, much evidence has been compiled supporting the idea that the baryonic mass visible in galaxies (stars, gas, and dust) comprises a small fraction of the total gravitating mass of such a system. The earliest evidence comes from observations of galactic motions within larger galaxy cluster systems. Individual galaxies had velocities that were too large to remain bound to the cluster, given the inferred amount of stellar mass (Zwicky 1937). However, the uncertainties associated with this analysis were large, and it took several more decades for more conclusive evidence to emerge. The rotation curves (circular speed versus galactocentric distance) of spiral galaxies are considered to be one

[1]EB gratefully acknowledges support from the Wisconsin Space Grant Consortium Research Infrastructre Program.

of the clearest pieces of evidence for what has become known as dark matter surrounding galaxies. In general, these curves show circular speeds of stars and gas in spiral galaxies following solid-body-like rotation near their centers, then reaching a nearly constant value (Rubin & Ford 1970). This contrasts with predictions based on the observed stellar/gas mass distributions in these galaxies, where the circular speed should peak and then decrease in the outer regions of a galaxy. Further studies of stellar kinematics in elliptical galaxies can hint at the need for dark matter, but the dynamics of such systems are more complex than for spiral galaxies, and interpretations are not as clear (Romanowsky et al. 2003).

In parallel with these inferences from galaxy dynamics, the idea of dark matter has also been supported by cosmological investigations. Numerical simulations of large-scale structure formation in the universe can reproduce the observed filamentary structure of galaxy clusters if dark matter is included (Navarro, Frenk, White 1996; Springel et al. 2005). Observations of the cosmic microwave background reveal features that can be described best when roughly 25% of the mass in the universe is dark matter (Spergel et al. 2003). A third route of evidence for dark matter around galaxies involves observations of gravitational lensing. Locations and magnifications of images of distant galaxies and quasars that form when their light is bent around intervening galaxies (or clusters of galaxies) indicate that the lensing galaxies should have masses larger than what can be accounted for from their visible components (Clowe et al. 2006; Williams & Saha 2011).

The current paradigm assumes that dark matter must act collisionlessly. The argument supporting this assumption is as follows. Observations indicating the presence of dark matter have not shown indications of an edge to the dark matter halo. For example, there are no isolated spiral galaxy rotation curves where the circular speed of gas begins to show a Keplerian decrease at some distance. As a result, it is assumed that the dark matter structures around galaxies have much larger spatial extent than the visible components. The baryons that will eventually form stars (mostly Hydrogen gas) are initially mixed with the dark matter over these larger volumes, but the baryons will self-interact via forces other than gravity. This gives the baryons a cooling mechanism that is unavailable to dissipationless dark matter and allows gas to radiate energy away and sink towards the center of the dark matter structure (typically referred to as a halo). Further, collisional effects would lead to halos with more spherical shapes that observations of galaxy clusters would allow (Mohr et al. 1995).

The previously mentioned cosmological simulations of structure formation have done more than simply suggest the reality of dark matter, they have also predicted its behavior on the scale of galaxies. It is generally agreed upon in the simulation community that dark matter halo mass density profiles have central cusps $\rho \propto r^{-\gamma}$ where $\gamma \approx 1$. The logarithmic density profiles then monotonically steepen as one moves away from the center (e.g. Navarro, Frenk, White 1997; Navarro et al. 2004). The consistency of the density behavior across mass scales, initial conditions, and simulation methods suggests that some simple underlying physics is at play in these self-gravitating collisionless systems. Further investigations into the kinematics of dark matter systems have likewise heightened the suggestion of a fundamental

physical process driving the formation of mechanical equilibrium dark matter halos (Taylor & Navarro 2001; Hansen & Moore 2006; Lithwick & Dalal 2011). Investigations of these three-dimensional (3-d) systems involve a wide range of modes of evolution that contribute to the relaxation from initial conditions to a final equilibrium state. The radial orbit instability (Merritt & Aguilar 1985), along with evaporation and ejection (Binney & Tremaine 1987, Chapter 7), are examples of these modes.

In this paper we will consider a one-dimensional (1-d) self-gravitating collisionless system (which can also be formulated as a "sheet" model (Camm 1950). Compared to 3-d models, the 1-d model is easier to analyze while possessing the essential features of 3-d systems — attractive long range forces and collisonless collective dynamics. However, it lacks some of the features of 3-d systems like angular momentum and tidal forces. Though the model is formulated in terms of continuous distribution functions, it can also be considered as the $N \to \infty$ limit of system of N particles with masses m, interacting via two-body gravitational attraction. The evolution of the phase-space distribution function is described by the the Vlasov equation (or collisionless Boltzmann equation),

$$\frac{\mathrm{d}f}{\mathrm{d}t} = \frac{\partial f}{\partial t} + v\frac{\partial f}{\partial x} + a(x)\frac{\partial f}{\partial v} = 0, \tag{1}$$

where $f(x, v; t)$ is the normalized distribution function

$$\int_{-\infty}^{\infty}\int_{-\infty}^{\infty} f(x, v; t)\,\mathrm{d}x\,\mathrm{d}v = 1.$$

The t argument is implied in what follows. The density is obtained simply by integrating over velocities

$$\lambda(x) = M\int_{-\infty}^{\infty} f(x, v)\,\mathrm{d}v, \tag{2}$$

where M is a mass scale for the system (mass per unit area in the sheet model; the total mass Nm for particles). The acceleration $a(x)$ for 1-d systems is calculated by simply taking the difference of the total masses on each side of x,

$$\begin{aligned} a(x) &= -g\int_{-\infty}^{x} \lambda(s)\mathrm{d}s + g\int_{x}^{\infty} \lambda(s)\mathrm{d}s \\ &= g(M_> - M_<), \end{aligned} \tag{3}$$

where g is the 1-d analogue of Newton's gravitational constant, and $M_>$ and $M_<$ represent the mass to the right and left of any location x, respectively. Note the long-range nature of the interaction, which couples particles through the distance between them. Likewise, the density is non-local in phase space, in that it involves an integral over velocities.

Studies of such 1-d systems have a long history (Camm 1950). In general, much of the work can be categorized by dealing with either cosmological conditions (e.g. Valgeas 2006) where an additional non-self-gravitating potential energy term is included in the Hamiltonian (or periodic boundary conditions are used), or isolated systems where self-gravity is the only source of potential (e.g. Reidl & Miller 1988; Koyama & Konishi 2001; Schulz et al.

2013). Within each of these categories, a variety of initial conditions have been investigated. Broadly speaking, initial conditions are typically near-equilibrium (e.g. Reidl & Miller 1987) or far-from-equilibrium (e.g. Joyce & Worrakitpoonpon 2011). The situations we investigate are isolated systems near thermal equilibrium. Such non-equilibrium systems might be considered to be in the final stages of condensation from uniform cosmological conditions, or perhaps in the aftermath of a collision in which two systems coalesce/pass through one another. We note that the absence of tidal forces in 1-d guarantees that non-overlapping systems can be considered as isolated, so that our discussion also applies to clusters of non-overlapping systems between encounters.

What follows here is a discussion of a method for finding solutions to a linearized version of Equation 1. Our approach is to expand the distribution function in terms of orthogonal functions. This method has been used previously, with Hermite polynomials to describe the velocity aspect of distributions (Reidl & Miller 1988), and Fourier expansions for the position for cosmological models with periodic boundary conditions (Alvord & Miller 2009; Reidl & Miller 1987). The form of the thermal equilibrium distribution function for isolated systems very naturally suggests the use of Hermite polynomials for the velocity and Legendre polynomials in $\tanh(x)$ for the position.

The resulting linear set of equations of motion link the expansion coefficients $c_{m,n}(t)$. In this notation, m and n are the orders of the Hermite and Legendre polynomials, respectively. There are few couplings between the coefficients — in fact, the couplings are local, in that they are only between neighbors on the (m, n) grid. This is rather fortuitous in light of the long-range nature of the forces, and gives a simple local continuity-type evolution of coefficients on the (m, n) grid. Furthermore, the method provides a more efficient route to following the phase-space evolution of modestly perturbed systems, compared to N-body simulations.

2. Thermal Equilibrium

Based on the structure of Equation 1, any function of the single particle energy,

$$\epsilon = \frac{1}{2}mv^2 + m\phi(x), \tag{4}$$

is a time-independent solution. Thermal equilibrium is a special case which case the distribution function has the separable Boltzmann form

$$f_0(\epsilon) = Ae^{-\beta\epsilon} = Ae^{-\frac{\beta m v^2}{2}}e^{-\beta m\phi}, \tag{5}$$

where $\beta \equiv 1/k_BT = 1/\langle mv^2\rangle$ is an energy scale (commonly referred to as the inverse temperature), and A is a normalization constant. Upon substitution of Equations 4-5 into Equation 1, it is straightforward to obtain the thermal equilibrium distribution function, which is commonly written as,

$$f_0(x, v) = A\,\mathrm{sech}^2\,(\frac{\beta gmM}{2}x)e^{-\frac{\beta m v^2}{2}}, \tag{6}$$

where $A = (gM/4)\sqrt{\beta^3 m^3/2\pi}$. The corresponding potential is,

$$\begin{aligned}\phi_0(x) &= \int_{-\infty}^{\infty} g|x-s|\lambda(s)\mathrm{d}s \\ &= \frac{2}{\beta m}\ln\left(2\cosh\frac{\beta gmM}{2}x\right),\end{aligned} \tag{7}$$

from which we obtain the acceleration

$$a_0(x) = -\frac{\partial\phi_0(x)}{\partial x} = -gM\tanh\frac{\beta gmM}{2}x. \tag{8}$$

In terms of the quantities defined, the kinetic energy of the equilibrium state is

$$K_0 = M\int_{-\infty}^{\infty}\frac{v^2}{2}f_0(x,v)\,\mathrm{d}x\,\mathrm{d}v = \frac{N}{2\beta}. \tag{9}$$

The equilibrium potential energy is likewise given by

$$U_0 = \frac{1}{2}\int_{-\infty}^{\infty}\lambda_0(x)\phi_0(x,v)\,\mathrm{d}x\,\mathrm{d}v = \frac{N}{\beta} = 2K_0, \tag{10}$$

as required by the virial theorem for one dimension.

The Boltzmann nature of the one-dimensional self-gravitating system is a vital difference from the three-dimensional case. Mechanical equilibria of realistic three-dimensional self-gravitating systems always contain gradients in the kinetic temperature, $T_{\mathrm{K}} \propto \langle v^2\rangle$, that act as pressure support against gravity. Only the infinite mass and energy isothermal sphere has a constant temperature. This one-dimensional distribution function is a true thermal equilibrium, as the kinetic temperature is uniform throughout the equilibrium system.

For simplicity, we transform to dimensionless coordinates using the definitions,

$$\chi = \frac{\beta gmM}{2}x \quad \text{and} \quad \varpi = \sqrt{\frac{\beta m}{2}}v.$$

The scaled equilibrium distribution function is,

$$\tilde{f}_0(\chi,\varpi) = \frac{2}{\beta gmM}\sqrt{\frac{2}{\beta m}}f_0 = \frac{1}{2\sqrt{\pi}}\operatorname{sech}^2\chi\, e^{-\varpi^2}. \tag{11}$$

where tildes are used to indicate dimensionless functions, when a distinction is necessary. The Vlasov equation transforms to,

$$\frac{\partial\tilde{f}}{\partial\tau} + \varpi\frac{\partial\tilde{f}}{\partial\chi} + \alpha(\chi)\frac{\partial\tilde{f}}{\partial\varpi} = 0, \tag{12}$$

where $\tau = \sqrt{\beta m/2}\,gMt$ is the dimensionless time and $\alpha(\chi) = a/(gM)$ is the dimensionless acceleration function.

3. Orthogonal Polynomials

The form of the equilibrium distribution function suggests a set of orthogonal functions to use as a basis for a polynomial expansion. We consider the expansion,

$$\tilde{f}(\chi,\varpi) = \sum_{i,j} c_{i,j} G_{ij}(\chi,\varpi)\tilde{f}_0(\chi,\varpi), \tag{13}$$

where the $c_{i,j}$ are real expansion coefficients. The G_{ij} are functions defined by

$$G_{ij}(\chi,\varpi) = \sqrt{\frac{2j+1}{2^i i!}} H_i(\varpi) P_j(\tanh\chi), \tag{14}$$

where the H_i are Hermite polynomials of order i, and the P_j are Legendre polynomials of order j. The G_{ij} are constructed to be orthonormal to f_0, which serves as a weighting function,

$$\int_{-\infty}^{\infty}\int_{-\infty}^{\infty} G_{ij}(\chi,\varpi)G_{i'j'}(\chi,\varpi)(\varpi)\tilde{f}_0(\chi,\varpi)\,\mathrm{d}\chi\,\mathrm{d}\varpi = \delta_{ii'}\delta_{jj'}. \tag{15}$$

We routinely use the Hermite polynomial orthogonality condition,

$$\int_{-\infty}^{\infty} H_i(\varpi)H_{i'}(\varpi)e^{-\varpi^2}\,\mathrm{d}\varpi = \delta_{ii'}2^i\sqrt{\pi}i!, \tag{16}$$

where δ is the Kronecker delta. For the Legendre orthogonality condition, we can eliminate the factor $\mathrm{sech}^2\,\chi$ with the change of variables $u = \tanh\chi$ and $\mathrm{d}u = \mathrm{sech}^2\,\chi\mathrm{d}\chi$,

$$\begin{aligned}\int_{-\infty}^{\infty} P_j(\tanh\chi)P_{j'}(\tanh\chi)\,\mathrm{sech}^2\,\chi\,\mathrm{d}\chi &= \\ \int_{-1}^{1} P_j(u)P_{j'}(u)\,\mathrm{d}u &= \delta_{jj'}\frac{2}{2j+1}.\end{aligned} \tag{17}$$

Note that this substitution also maps infinite limits on any χ integral to the interval [-1,1].

At thermal equilibrium, only the $i = 0$, $j = 0$ coefficient is nonzero. For an arbitrary distribution function $\tilde{f}(\chi,\varpi)$ perturbed from thermal equilibrium, the coefficients can be determined from

$$c_{i,j} = \int_{-\infty}^{\infty}\int_{-\infty}^{\infty} G_{i,j}(\chi,\varpi)\tilde{f}(\chi,\varpi)\,\mathrm{d}\chi\,\mathrm{d}\varpi. \tag{18}$$

This equation represents a transformation from phase space to a discrete (i,j) grid of coefficients.

The expansion dictates that all mass must derive from the (0,0) term,

$$\begin{aligned}\tilde{M}_{i,j} \equiv \frac{M_{i,j}}{M} &= \int_{-\infty}^{\infty}\int_{-\infty}^{\infty} \tilde{f}_{i,j}\,\mathrm{d}\chi\,\mathrm{d}\varpi \\ &= \int_{-\infty}^{\infty}\int_{-\infty}^{\infty} c_{i,j}G_{ij}(\chi,\varpi)\tilde{f}_0(\chi,\varpi)\,\mathrm{d}\chi\,\mathrm{d}\varpi \\ &= c_{i,j}\delta_{i0}\delta_{j0},\end{aligned}$$

from which we obtain $\tilde{M}_{0,0} = c_{0,0} = 1$. In a similar fashion, one can see that mass density $\tilde{\lambda}(\chi)$ derives only from $i = 0$ terms,

$$\begin{aligned}\tilde{\lambda}(\chi) &= \int_{-\infty}^{\infty} \tilde{f}_{i,j}\,\mathrm{d}\varpi \\ &= \int_{-\infty}^{\infty} \sum_{i,j} c_{i,j} G_{ij}(\chi,\varpi)\tilde{f}_0(\chi,\varpi)\,\mathrm{d}\varpi \\ &= \sum_j c_{0,j}\sqrt{2j+1}P_j(\tanh\chi)\tilde{\lambda}_0(\chi). \end{aligned} \tag{19}$$

4. Linear Perturbations

We now use the orthogonal polynomials developed in the previous section as a basis to study the dynamics of perturbations from thermal equilibrium. We consider distribution functions of the form,

$$\tilde{f} = \tilde{f}_0 + \delta\tilde{f}_1, \tag{20}$$

where $\tilde{f}_1$ is the perturbing function and $\delta \ll 1$ is an expansion parameter.

Using this perturbed $\tilde{f}$ in Equation 1 produces a modified Vlasov equation for the perturbing function (in terms of the previously defined dimensionless quantities),

$$\frac{\partial\tilde{f}_1}{\partial\tau} + \varpi\frac{\partial\tilde{f}_1}{\partial\chi} + \alpha_0(\chi)\frac{\partial\tilde{f}_1}{\partial\varpi} = 2\varpi\alpha_1(\chi)\tilde{f}_0 \tag{21}$$

where we have used $\partial\tilde{f}_0/\partial\varpi = -2\varpi\tilde{f}_0$. The accelerations are given by

$$\begin{aligned}\alpha_0(\chi) &= -\int_{-\infty}^{\chi}\tilde{\lambda}_0(\chi')\,\mathrm{d}\chi' + \int_{\chi}^{\infty}\tilde{\lambda}_0(\chi')\,\mathrm{d}\chi' = -\tanh\chi, \\ \alpha_1(\chi) &= -\int_{-\infty}^{\chi}\tilde{\lambda}_1(\chi')\,\mathrm{d}\chi' + \int_{\chi}^{\infty}\tilde{\lambda}_1(\chi')\,\mathrm{d}\chi'. \end{aligned} \tag{22}$$

The term $2\varpi\alpha_1(\chi)\tilde{f}_0$ is required by Newton's Third Law. In this equation, it has been written on the right hand side to signify that it is neither a convective nor an advective term. In fact, the right hand side is best characterized as a collision term as it represents the deflection of particles into and out of equilibrium due to the perturbation. Here, we ignore the second-order term describing the self-interaction of the perturbing particles, $\alpha_1\partial\tilde{f}_1/\partial\varpi$.

We now express the perturbing distribution function in terms of the Hermite and Legendre polynomials discussed earlier,

$$\tilde{f}_1 = \sum_{i,j} c_{i,j}\sqrt{\frac{2j+1}{2^i\,i!}}H_i(\varpi)P_j(\tanh\chi)\frac{\mathrm{sech}^2\,\chi e^{-\varpi^2}}{2\sqrt{\pi}}, \tag{23}$$

where $c_{0,0} = 0$ since the equilibrium contribution has already been removed. This guarantees that the perturbations are massless. Using Equation 19 in Equation 22, the perturbing

acceleration is found to be,

$$\alpha_1(\chi) = \sum_j c_{0,j}\sqrt{2j+1}\left[\int_\chi^\infty P_j(\tanh\chi')\frac{\mathrm{sech}^2}{2}\chi'\,\mathrm{d}\chi' - \int_{-\infty}^\chi P_j(\tanh\chi')\frac{\mathrm{sech}^2}{2}\chi'\,\mathrm{d}\chi'\right]. \tag{24}$$

Upon making the substitution $u = \tanh\chi$, $\mathrm{sech}^2\,\chi = 1-u^2$, $\mathrm{d}u = (1-u^2)\,\mathrm{d}\chi$, this simplifies to,

$$\alpha_1(u) = \frac{1}{2}\left[\sum_j c_{0,j}\sqrt{2j+1}\left(\int_u^1 P_j(u')\,\mathrm{d}u' - \int_{-1}^u P_j(u')\,\mathrm{d}u'\right)\right]. \tag{25}$$

In terms of the u variable, the modified Vlasov equation (Equation 21) becomes,

$$\frac{\partial\tilde{f}_1}{\partial\tau} + \varpi(1-u^2)\frac{\partial\tilde{f}_1}{\partial u} - u\frac{\partial\tilde{f}_1}{\partial\varpi} - 2\varpi\alpha_1(u)\tilde{f}_0 = 0. \tag{26}$$

Substituting Equation 23 and canceling a common factor of $\tilde{f}_0$ produces,

$$\sum_{i,j}\left\{\dot{c}_{i,j}H_iP_j + c_{i,j}\varpi H_i(1-u^2)\frac{\partial P_j}{\partial u} - c_{i,j}uP_j\frac{\partial H_i}{\partial\varpi}\right\} - 2\varpi\alpha_1(u) = 0. \tag{27}$$

Applying standard Hermite and Legendre polynomial recursion relations to Equation 27 and using the fact that $P_n(1) = 1$ and $P_n(-1) = (-1)^n$ in the simplification of α_1, results in,

$$\sum_{i,j}\sqrt{\frac{2j+1}{2^i\,i!}}\left\{\dot{c}_{i,j}H_iP_j + c_{i,j}\left[\frac{j(j+1)}{2(2j+1)}H_{i+1}P_{j-1} - \frac{j(j+1)}{2(2j+1)}H_{i+1}P_{j+1} + \frac{ij(j-1)}{2j+1}H_{i-1,j-1} - \frac{i(j+1)(j+2)}{2j+1}H_{i-1}P_{j+1} + \delta_{0,i}\frac{1}{2j+1}H_1\left[P_{j+1} - P_{j-1}\right]\right]\right\} = 0. \tag{28}$$

The term containing the Kroenecker delta corresponds to the $2\varpi\alpha_1(\chi)\tilde{f}_0$ term in Equation 21 and is zero except when $i = 0$. Finally, we obtain the equations of motion for the coefficients by multiplying this expression by $G_{m,n}\tilde{f}_0$, integrating over ϖ and u, and making use of the orthogonality relations Equations 16-17. The resulting expressions have the form,

$$\dot{c}_{m,n} = L_{m,n}^{m-1,n-1}\,c_{m-1,n-1} + L_{m,n}^{m-1,n+1}\,c_{m-1,n+1} + L_{m,n}^{m+1,n-1}\,c_{m+1,n-1} + L_{m,n}^{m+1,n+1}\,c_{m+1,n+1}, \tag{29}$$

where the matrix elements $L^{i,j}_{m,n}$ are given by

$$\begin{aligned}
L^{m-1,n-1}_{m,n} &= \frac{\sqrt{m}(n-1)n - 2\delta_{1,m}}{\sqrt{2(2n+1)(2n-1)}}, \\
L^{m-1,n+1}_{m,n} &= -\frac{\sqrt{m}(n+2)(n+1) - 2\delta_{1,m}}{\sqrt{2(2n+1)(2n+3)}}, \\
L^{m+1,n-1}_{m,n} &= \frac{\sqrt{m+1}(n+1)n}{\sqrt{2(2n+1)(2n-1)}}, \\
L^{m+1,n+1}_{m,n} &= -\frac{\sqrt{m+1}(n+1)n}{\sqrt{2(2n+1)(2n+3)}},
\end{aligned} \tag{30}$$

where $m, n, i, j \geq 0$. The test-particle case is obtained by omitting the Kronecker $\delta_{1,m}$ terms.

Equations 29-30 are the main results of this paper. For *linearized* dynamics the $c_{m,n}$ evolve by coupling to diagonal neighbors only. This is somewhat surprising in light of the long-range nature of the forces, and can be traced back to the recursion relation that replaces the integral over χ in the calculation of α_1. Because of this nearest-diagonal-neighbor coupling, the even parity and odd parity modes completely decouple, where the parity is given by $(-1)^{m+n}$. For simplicity, we shall concern ourselves with the even parity modes only, and set all the odd parity coefficients to zero. This automatically guarantees that the center of mass velocity and position are zero, $\langle \varpi \rangle = \langle \chi \rangle = 0$.

5. Discussion

We have demonstrated that a set of orthonormal polynomial terms based on the equilibrium distribution function is useful for investigating the evolution of one-dimensional, self-gravitating, collisionless systems, at least for small linear perturbations from equilibrium. The polynomial coefficients interact via diagonal-neighbor couplings, producing an alternate view of the evolution of these systems in terms of coefficients $c_{m,n}$ on the (m, n) grid.

This polynomial expansion analysis of the Vlasov equation provides a novel, and useful, view of the behavior of one-dimensional self-gravitating systems. While not in the scope of this introductory work, one can imagine several directions any future investigations using this analysis might take. For example one might study the aftermath of collisions of isolated systems, or the stationary states of one-dimensional systems, or the frequency spectrum of the L matrix. One could extend the analysis to second-order to investigate the onset of nonlinear effects, like stability or chaotic behavior. The nearest-neighbor coupling of the coefficients leads to "local" continuity-type dynamics of conserved quantities like energy and fine-grained entropy on the (m, n) grid that should give further insight into the non-equilibrium thermodynamics of these systems.

REFERENCES

Alvord J., Miller B.N., 2009, in Joint Fall 2009 Meeting of the Texas Sections of the APS, AAPT, and SPS. American Phys. Soc., p. C5.002

Binney J., Tremaine S., 1987, Galactic Dynamics. Princeton Univ. Press, Princeton, NJ

Camm G.L., 1950, MNRAS, 110, 305

Clowe D., Bradac M., Gonzalez A.H., Markevitch M., Randall S.W., Jones C., Zaritsky D., 2006, ApJ, 648, L109

Hansen, S.H., Moore B., 2006, New Ast., 11, 333

Joyce, M., Worrakitpoonpon, T., 2011, Phys. Rev. E, 84, 1139

Koyama, H., Konishi T., 2001, Phys. Lett. A, 279, 226

Landau L.D., Lifshitz E.M., 1951, Statistical Physics – Part 1. Butterworth-Heinemann, Boston, MA

Lithwick Y., Dalal N, 2011, ApJ, 734, 100

Merritt D., Aguilar L.A., 1985, MNRAS, 217, 787

Mohr J.J., Evrard A.E., Fabricant D.G., Geller M.J., 1995, ApJ, 447, 8

Navarro J.F., Frenk C.S., White S.D.M., 1996, ApJ, 462, 563

Navarro J.F., Frenk C.S., White S.D.M., 1997, ApJ, 490, 493

Navarro J.F. et al., 2004, MNRAS, 349, 1039

Noullez A., Aurell E., Fanelli D., 2003, J. Comp. Phys., 186, 697

Reidl, Jr., C.J., Miller B.N., 1987, ApJ, 318, 248

Reidl, Jr., C.J., Miller B.N., 1988, ApJ, 332, 619

Romanowsky A.J., Douglas N.G., Arnaboldi M., Kuijken K., Merrifield M.R., Napolitano N.R., Capaccioli M., Freeman K.C., 2003, Science, 301, 1696

Rubin, V.C, Ford W.K., 1970, ApJ, 159, 379

Schulz A.E., Dehnen W., Jungman G., Tremaine S., 2013, MNRAS, 431, 49

Spergel D.N. et al., 2003, ApJS, 148, 175

Springel V. et al., 2005, Nature, 435, 629

Taylor J., Navarro J., 2001, ApJ, 563, 483

Valageas P., 2006, A&A, 450, 445

Williams L.L.R, Saha P., 2011, MNRAS, 415, 448

Zwicky F., 1937, ApJ, 86, 217

Examining Supernova Remnant GSH054-00+003

Cheuk Man Lo, Dr. Shauna Sallmen

Physics Department, University of Wisconsin- La Crosse

Supernova remnants play a key role in galactic evolution. Therefore, studying them intensively can improve our understanding of the process. In this project, we studied the neutral hydrogen shell GSH054-00+003 located at RA 292.75º and DEC 18.25º that was found in the SETHI dataset. We found its reference velocity to be 3km/s. After matching it with the Galactic rotation curve and spiral structure, we found its distance to be 10kpc away. Based on this and geometry, we estimated its size to be 245 pc. Using computer analysis of its HI spectrum, we determined the expansion velocity to be 8.6km/s. We therefore can calculate its age and kinetic energy. Assuming the number density of the ambient interstellar medium to be 1 atom/cm^3, we calculated its energy to be 1.9×10^{43}J. Through comparison to computer models of shell evolution, we estimated it was formed by approximately 5 to 10 supernovae. A simple age estimation is 14 million years. Although this is an over estimate, the slow expansion and absence of x-ray emission indicate the shell is old. We conclude that a cluster of supernovae formed this old shell.

Introduction

The Interstellar Medium (ISM) is the dust and gas between stars in galaxies. It is filled with shells and bubbles blown by winds from stars and supernova explosions of dying stars. Following these events, the hot star material expands outward forming a shell. It eventually cools, slows down and mixes with the ISM.

Originally, the universe was filled with only hydrogen and helium. Heavier elements such as oxygen and iron (necessary for human life) are made by fusion in stars. Elements heavier than iron are made during supernova explosions. These materials eventually distribute throughout the ISM as shells expand and merge with their surroundings. Ultimately, these new elements add to the ingredients for new stars and planetary systems: that is the reason why we can exist today. Since shell material is included in the formation of new stars and planets, it is important to study interstellar shells to understand the ecology of our Milky Way Galaxy. Although scientists understand the big picture of how shells evolve, there are details that we have yet to explain (eg. see review by Cox 2005). Intensive study of the size, age and energy of specific shells can help us to understand their features and evolution processes better.

Cold neutral hydrogen (HI) emits light with a wavelength of 21 cm, visible with radio telescopes. As supernova remnants look like shells and bubbles, we can search for them in this wavelength as they cool down. In this project, we used the SETHI (Search for Extra-Terrestrial HI) dataset (Korpela et al. 2002, 2004) to examine shell GSH054-00+003. This survey contains images of patches of the sky showing gas moving at different radial velocities. For every velocity slice, it contains 21-cm emission from HI gas, averaged over 1.5 km/s in radial velocity. The Galactic coordinates and radial velocity of a shell determine its name. For the shell GSH054-00+003 that we studied, it is located at Galactic longitude +53.6° and latitude -0.1°. The reference velocity is 3km/s, relative to the Local Standard of Rest. Using the SETHI data, we found the shape, size, location, and expansion velocity of this shell. We then estimated its age and kinetic energy enabling us to explore its history and evolution.

Methods

In this project, we used the computer program kvis (Gooch, 1996) to examine the SETHI shell images at the 21 cm wavelength, and IDL (Interactive Data Language) to analyze the shell's properties. We studied shell GSH054-00+003, which was originally found in the SETHI survey (Sallmen et al., in prep). It is located at right ascension (RA) 19h31m and declination (DEC) 18.25º. We determined the location, mean angular diameter and the reference velocity by examining the SETHI images. The shape of the shell is elliptical. Therefore, we could not measure its diameter directly. We measured the length of the major and minor axes of the shell and averaged them to approximate its mean angular diameter. Figure 1 shows GSH054-00+003 at velocity 3.18 km/s. Observe that there is a black stripe, resulting from dense HI in the spiral arm. This shell was found near the spiral arm.

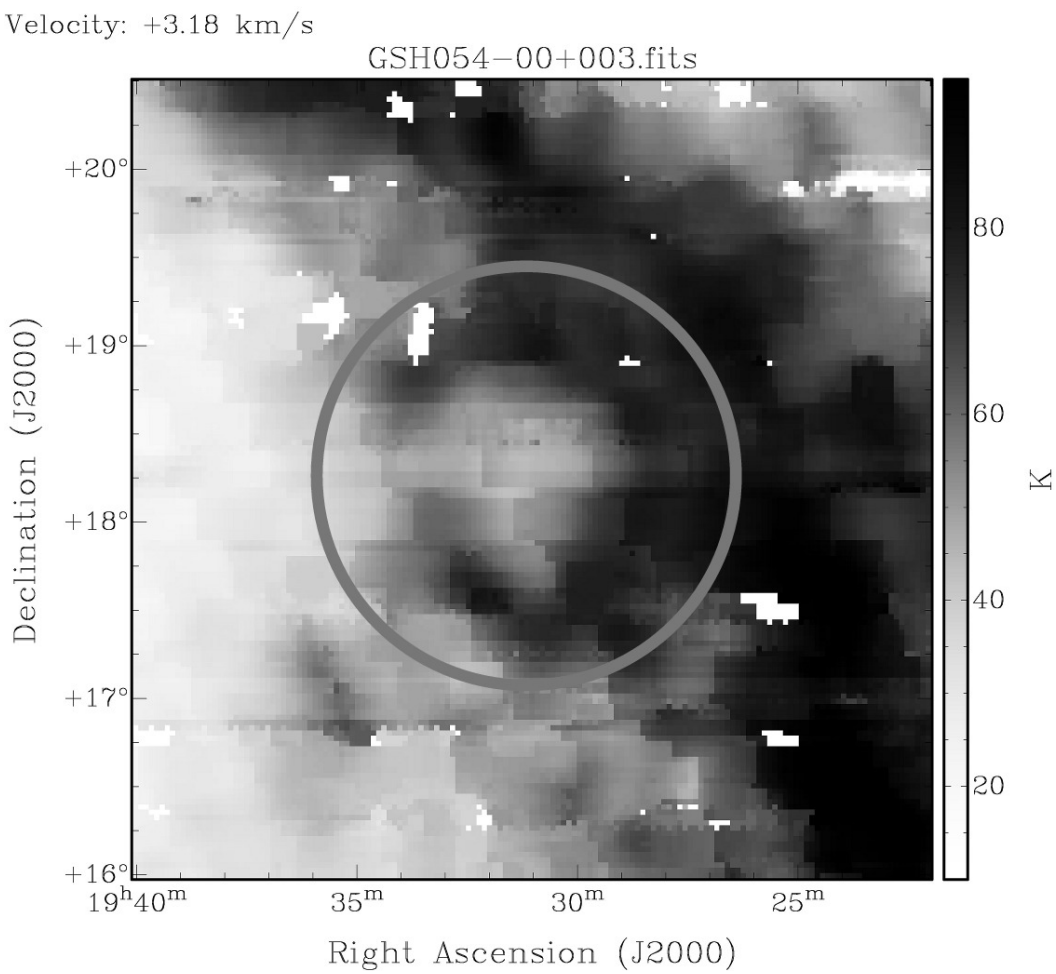

Fig.1 21-cm image of GSH054-00+003 at radial velocity 3.18 km/s. Black areas represent stronger 21cm emission. The shell is indicated by the light grey circle.

Then we used the reference radial velocity to match the rotational velocity of the Galaxy to determine the distance. As the Galaxy is rotating, objects that are in different locations in the Galaxy move at specific speeds. We therefore matched the velocity of the shell with those specific locations that share the same radial velocity in the Galaxy. Figure 2 shows the two matching distances, based on the rotation curve of Brand and Blitz (1993). One is 0.05kpc away and the other one is 10kpc away. Using the fact that the shell is near the spiral arm, we determined its distance is 10kpc away after matching with a map of Galactic spiral arms (Cordes and Lazio, 2003). The 10.0 kpc distance has a lower bound of 9.65 kpc and an upper bound of 10.43 kpc. For the 0.05 kpc distance case, the lower bound is unconstrained and its upper bound is 0.43kpc. The range of distance is determined using the fact that the shell is visible in 6 velocity frames (spanning 7.76 km/s) of the SETHI data.

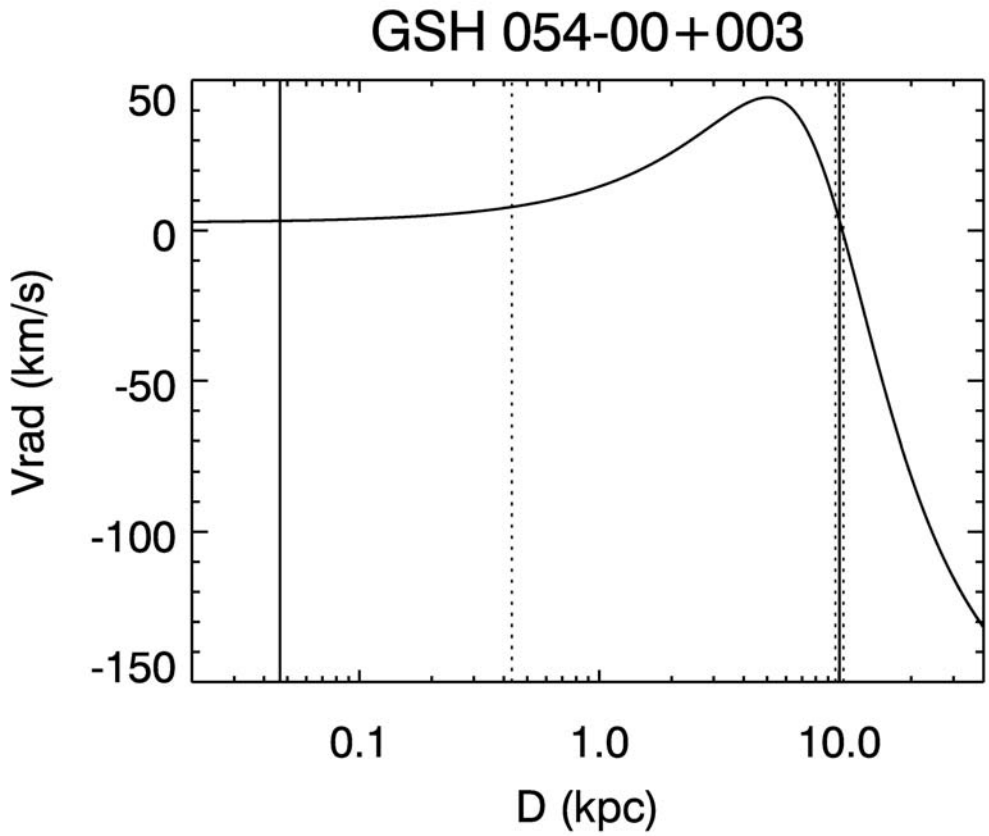

Fig.2 The solid curve represents the radial velocity of the gas along the direction RA 19h31m and DEC 18.25°, according to the Galactic rotation curve (Brand and Blitz, 1993). The vertical solid lines at 10.04kpc and 0.05kpc represent distances at which the shell velocity matches the Galactic rotation curve. The dotted lines represent the error bounds.

After we found the shell's distance, we used geometry to calculate its size. Since we know the mean angular diameter of the shell, the size was calculated as: $S = d \times \theta$, where d is distance, θ is the mean angular diameter (in radians) and S is the size (diameter). To find the expansion velocity, we extracted a spectrum through the center of the shell. We also chose pixels outside the shell at the same Galactic latitude to generate a background spectrum. Figure 3 shows the results for one choice of central and background pixels. In Fig. 3, the solid line is the spectrum at the center of the shell with background subtraction. The dotted line is the spectrum without background subtraction. The dashed line is the spectrum from the surrounding background without any part of the shell. The shell's expansion signature is revealed in the local minimum and surrounding peaks near 3km/s.

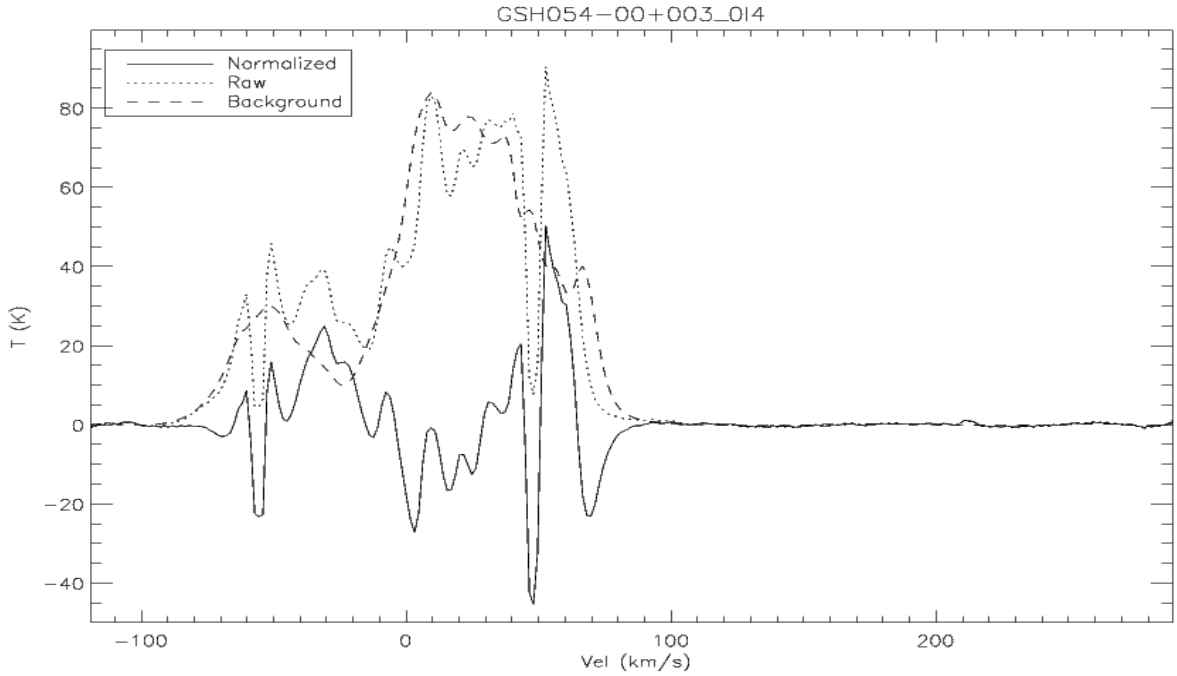

Fig 3. An example of a generated spectrum for GSH053-00+003 (21-cm emission vs. radial velocity). The solid line represents the background reduced spectrum at the center of GSH054-00+003. The dotted line represents the raw spectrum at the center of GSH054-00+003. The dashed line represents the background spectrum. The shell is at about -10km/s to 10km/s.

The background subtracted spectrum was analyzed to determine the expansion velocity as follows. The computer identified the local maxima near the reference radial velocity and set them to be the foreground wall and background wall. Figure 4 is the zoomed in background reduced spectrum. It shows that the computer found the background wall (the wall of the shell that is expanding away from us) at +9.37 km/s and foreground wall (the wall of the shell that is expanding toward us) at -7.65 km/s. We also generated several more spectra using different sets of pixels. For example, we changed the size of the center point, or picked background pixels closer to or farther from the shell. Most of the choices gave results that were consistent with one another. We also compared the results to the shell images at various velocities, to ensure that the background and foreground walls were correctly identified, and not affected by noise in the data or confusion by unrelated gas.

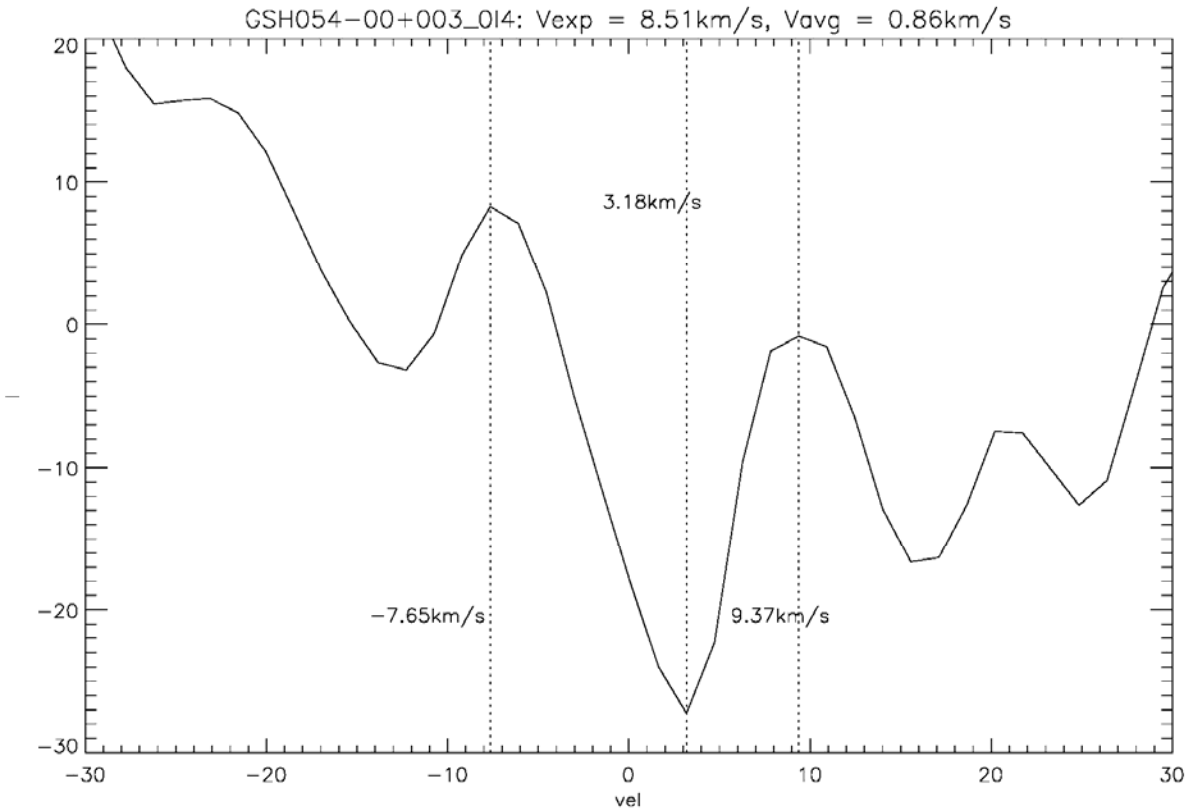

Fig 4. A zoomed in background reduced spectrum of GSH054-00+003. The solid curve represents the background subtracted HI spectrum through the center of GSH054-00+003. The dotted vertical line at 3.18km/s represents the radial velocity of the minimum. The dotted vertical line at -7.65km/s indicates the foreground wall and the one at 9.37km/s indicates the background wall.

With the velocities of the foreground and background walls, the expansion velocity could then be calculated: $V_{exp} = \frac{V_{bg} - V_{fg}}{2}$. Using the expansion velocity of 8.6km/s, we calculated the shell's age and kinetic energy and compared it to models of shell evolution. To find the age we determined how much time it took to expand to its present size: $t = \frac{d}{V_{exp}}$. The result of 14 million years will be an overestimate, because the shell was expanding faster early in its development.

We also wanted to estimate the kinetic energy of the shell. Therefore, we needed both the expansion velocity of the shell and its mass. To find the mass, we assumed that the shell has swept up all the material that was once inside it. The mass m will then be volume times density of ambient material: $m = \frac{4}{3}\pi r^3 \times \rho$, assuming a spherical shell. The mass density of the ambient material is $\rho = m_H n_H + m_{He} n_{He} \approx m_H n_H (1 + \frac{4 n_{He}}{n_H})$. We assumed n_{He}=0.1 n_H, and used a hydrogen number density (n_H) of 1 atom cm^{-3} to calculate the mass of the shell, which was $2.7 \square 10^5$ M_{sun}. We later also tried $10cm^{-3}$. After finding the mass, we calculated the kinetic energy of the shell: $KE = \frac{1}{2} m V_{exp}^2$.

Results:

Table 1 summarizes the information on GSH054-00+003 we gathered and calculated. GSH054-00+003 is located at RA 292.75º and DEC 18.25º with a mean angular diameter of 1.4 º. It is 10.0±0.4 kpc away from us. Using this distance and its bounds, we calculated the size to be 245±10kpc. The shell is moving away from us with radial velocity 2±1km/s, and expanding at 8.6±1.5km/s. The error of the expansion velocity is determined by the resolution of the images. Based on simple assumptions, the age is approximately 14±2.5 million years. We used a hydrogen density of 1 atom/cm^3 to calculate its kinetic energy and got 1.9±0.7□10^{43}J. In the section below, we discuss the implications of the size, expansion velocity, energy, and age estimates.

Table 1. The information of GSH054-00+003

	Calculated/Observed	Error
Location (RA, Dec)	292.75º, +18.25º	~0.25º
Galactic Location (*l, b*)	53.7º, -0.1º	~0.25º
Mean angular diameter	1.4º	~0.1º
Size	245 pc	±10 pc
Central velocity	2km/s	±1 km/s
Distance	10.04 kpc	±0.4kpc
Expansion Velocity	8.6km/s	±1.5km/s
Age	14 million years	+2.5 million years
Energy(density n_H=1/cm^3)	1.9×10^{43}J	$\pm 0.7 \times 10^{43}$J
Mass(density n_H=1/cm^3)	2.7□10^5 M_{sun}	±0.1□10^5 M_{sun}

Discussion:

It is certain that the age we calculate is an over estimate, because the shell was expanding faster before. In addition, it is likely this shell is the result of multiple supernovae from a cluster of stars, which exploded at slightly different times and locations. This possibility is discussed further below. However, it is certain that the shell is old. In online archival x-ray images of the shell (McGlynn et al., 1996), the absence of x-ray emission inside the shell means that it is old and cold. The slow expansion velocity further supports that the shell has been expanding for a long time.

Computer models of supernova evolution suggest that an average old shell with n_H=1 atom/cm^3 that is expanding at ~10 km/s has a kinetic energy of about 3-4 x 10^{42} J (Spitzer 1978; Chevalier 1974; Thornton, 1998). Thornton's computer models suggest that a single shell expanding into material of number density 1 atom/cm^3 (n_H=1) and currently expanding at 9km/s would be around 1.7 million years old, around 70 pc in radius and have kinetic energy 4□10^{42}J. We used this model as a reference. GSH054-00+003 is bigger and contains more energy than this model, so we suspect it to be a cluster of supernovae. We first used the radius to estimate how many supernovae formed GSH054-00+003. Assuming it is a perfect sphere, we calculated its volume to be 2.5□10^6 π pc^3. For a supernova that expands into material with n_H=1, the volume will be 460,000π pc^3. This volume suggests that GSH054-00+003 was made by about 6 supernovae. Then, we compared the kinetic energies. Dividing GSH054-00+003's energy by the model's energy, we get around 5 to 7 supernovae. If we assume the density to be higher, there will be more mass swept up and therefore more energy was needed to form GSH054-00+003. This also means the shell needed more supernovae to form. For a computer model with n_H=10 (Thornton, 1998), a shell expanding at 9km/s will be 6.6 million years old, 30 pc in radius and have kinetic energy around 2.5□10^{42}J. This suggests GSH054-00+003 is made up by 70 supernovae if comparing with radius, and 60 to 100 supernovae if comparing with the energy. It is unlikely that the shell will expand into material with density less than 1 atom/cm^3, because it is near a spiral arm, which is very dense. To conclude, GSH054-00+003 is an old shell, likely formed by a cluster of supernovae.

Acknowledgements:

I would like to acknowledge the use of NASA's SkyView facility (http://skyview.gsfc.nasa.gov) located at NASA Goddard Space Flight Center. In addition, I would like to thank Dr. E. J. Korpela and the SETI@home team for access to the SETHI dataset, which uses data acquired at Arecibo Observatory. The Arecibo Observatory is part of the National Astronomy and Ionosphere Center, which is operated by Cornell University under a Cooperative Agreement with the National Science Foundation.

Reference:

Brand, J. & Blitz, L. 1993, A&A, 275, 67
Chevalier, A. Ap.J., 188, 501, 1974
Cordes, J. & Lazio, J. 2003, arXiv: astro-ph/0301598
Cox, D. P. 2005, ARA&A, 43, 337
Gooch, R. 1996, Astronomical Data Analysis Software and Systems V, 101, 80
Korpela, E. J., Demorest, P., Heien, E., Heiles, C., & Werthimer, D. 2002, Seeing Through the Dust: The Detection of HI and the Exploration of the ISM in Galaxies, 276, 100
Korpela, E. J., Demorest, P., Heien, E., Heiles, C., & Werthimer, D. 2004, How Does the Galaxy Work?, 315, 97
McGlynn, T., Scollick, K., White, N., SkyView: The Multi-Wavelength Sky on the Internet, McLean, B.J. et al., New Horizons from Multi-Wavelength Sky Surveys, Kluwer Academic Publishers, 1996, IAU Symposium No. 179, p465.
Spitzer, L. 1978. Physical Processes in the ISM
Thornton, K. et al. 1998, ApJ, 500, 95

23rd Annual Conference
Appendix A

2013 Program

Wisconsin Space Grant Consortium

&

Marquette University

Present:

the Twenty-Third Annual
WISCONSIN SPACE CONFERENCE

"Global Climate Change Impacts on Lake Michigan"

Marquette University
Milwaukee, Wisconsin

Thursday, August 15 – Friday, August 16, 2013

CONFERENCE 2013 PROGRAM

Thursday, August 16, 2013

8:00-8:45 am **Registration** **McCormick Hall**

Buffet Breakfast

Poster Drop Off (formal poster session at 2:45 p.m.)
Bring posters to registration and staff will set them up in the Engineering Hall foyer

To access Marquette WIFI: Start web browser and when prompted, enter:
Username: W-Conf5 Password: Gold2012

*** Plenary Session ***

9:00-9:30 am **Welcome and Introduction** **Olin Engineering Bldg. 201**

Christopher Stockdale, Associate Professor of Physics, Marquette University

Richard (Rick) Holz, Dean, Helen Way Klinger College of Arts and Sciences, Marquette University

Robert (Bob) Bishop, Opus Dean, College of Engineering, Marquette University

9:30-10:30 am **Session 1: Keynote Address**

Introduction of Keynote:
Michael LeDocq, Chair, WSGC Advisory Council and Instructor, Department of Natural Science, Western Technical College

Prof. J. Val Klump, Senior Scientist and Director, Great Lakes Water Institute, *What Lies Ahead for the Future of Freshwater and Our Great Lakes*

10:30-10:50 am **Morning Break** **outside Olin Bldg. 201**

*** Plenary Session ***

11:00-11:45 am **Session 2: Rocket Teams** **Olin Engineering Bldg. 201**

Moderator: Bill Farrow, WSGC Associate Director for Student Satellite Initiatives, Assistant Professor, Milwaukee School of Engineering

Rocket Team: Second Place – Engineering Division – Team Jarts
Joe Hintz, **Eric Logisz**, **Cameron Schulz**, Undergraduate Students, Department of Mechanical Engineering, Milwaukee School of Engineering, Non-presenting team member: Brett Foster, *The Ripper II – Collegiate Rocket Competition*

Rocket Team: First Place – Engineering Division – Team Whoosh Generator, James Ihrcke, **Eric Johnson**, Undergraduate Students, Department of Mechanical Engineering, Milwaukee School of Engineering, Non-presenting team members: Victoria Falcon, Christopher Larson, Kirsti Pajunen

12:00-12:45 pm **Lunch** **McCormick Hall**

*** Concurrent Sessions -- Research Stream ***

1:00-2:30 pm **Session 3R: Physics** **Engineering Hall 236**

Moderator: Eric Barnes, Associate Professor, Physics Department, University of Wisconsin-La Crosse

Sydney Chamberlin, *When Galaxies Collide: The Search for Low-Frequency Gravitational Wave Backgrounds in the Universe*, Graduate Student, Department of Physics, University of Wisconsin-Milwaukee

Justin Ellis, *Searching for Gravitational Waves with Pulsar Timing Arrays*, Graduate Student, Department of Physics, University of Wisconsin-Milwaukee

Kevin Crosby, *Fluid Mass Gauging in Spacecraft Propellant Tanks Using Modal Analysis*, Professor, Department of Physics, Carthage College

Joseph Krueger, *Conductivity and Optical Transmittance of ZnO/CuO Thin Films*, Undergraduate Student, Department of Physics, University of Wisconsin-La Crosse

Kerry Kuehn, *Physics: A Student's Guide through the Great Texts*, Associate Professor, Department of Physics, Wisconsin Lutheran College

*** Concurrent Sessions -- Education Stream ***

1:00-2:30 pm **Session 3E: K-12 Education & General Public Outreach** **Engineering Hall 136**

Moderator: Karin Borgh, Executive Director, BioPharmaceutical Technology Center Institute

Judy Schieble, *Elementary Rocket Launch II*, Chair, Elementary Rocket Launch/Program, Spaceport Sheboygan.

Todd Treichel, *Rocket Science for K-12 Educators Workshop*, Chairman, AIAA – Wisconsin Section and Senior Systems Engineer, Obital Technologies Corp.

Coggin Heeringa, *Teaching Teachers through Outreach*, Director, Crossroads at Big Creek

Shelley Lee, *The Next Generation Science Standards Are Coming!*, Science Education Consultant, Department of Learning and Content, Wisconsin Department of Public Instruction

2:30-2:50 pm **Afternoon Break** **Engineering Hall foyer (ground level)**

*** Plenary Session -- Poster Session ***

2:45-3:35 pm **Session 4P: Posters** **Engineering Hall foyer (ground level)**

Facilitator: Mike LeDocq, Chair, WSGC Advisory Council, Natural Science Instructor, Western Technical College

Karissa Metko, *Exploring Magnetic Fields around Terrestrial Exoplanets and Potentially Habitable Exomoons*, Undergraduate Student, Department of Astronomy, University of Wisconsin-Madison

Shane Wulf, *Testing Species-Abundance Models of the Hughes Creek Shale (Carboniferous) of Southeastern Nebraska*, Undergraduate Student, Department of Geography and Geology, University of Wisconsin-Whitewater

Daryl Johnson, *Size-Frequency Distribution and Taphonomy of Brachiopoda from the Hughes Creek Shale (Carboniferous) of Southeastern Nebraska*, Undergraduate Student, Department of Geography and Geology, University of Wisconsin-Whitewater

Teri Gerard, *Fumarole Alteration of Hawaiian Basalts: A Potential Mars Analog*, Graduate Student, Department of Geosciences, University of Wisconsin-Milwaukee

Danielle Weiland, *Degassing of FC-72 in Microgravity*, Undergraduate Student, Department of Physics, Carthage College

Tyler Nickel, *Single Photon Detection Using Quantum Dot-Gated RLC Resonant Circuits*, Undergraduate Student, Department of Physics, University of Wisconsin-La Crosse

Eric Ireland, *Zero-gravity Fuel Gauging Using Modal Analysis*, Undergraduate Student, Department of Physics, Carthage College

Balloon Launch and Payload Teams:
Elijah High Altitude Balloon Project, **Trent Cybela** (Payload team only), University of Wisconsin-Platteville; **Dan Kass**, Milwaukee School of Engineering; **Amber Koeune**, Milwaukee School of Engineering; **Nathaniel Pedigo**, Milwaukee School of Engineering; **Alana Tirimacco**, Milwaukee School of Engineering, Non-presenting team member: Danielle Weiland (Launch team only), Department of Physics, Carthage College

3:35-3:50 pm **Group Photograph** **Engineering Hall foyer (ground level)**

*** Plenary Session – Research Session***

4:00-5:00 pm **Session 4R: Chemistry and BioSciences** **Olin Engineering Bldg. 201**

Moderator: Danny Riley, Professor, Department of Cell Biology, Neurobiology, and Anatomy, Medical College of Wisconsin

Philip Gopon, *Low Voltage EPMA of Submicron Fe-Si Metals*, PhD Student, Department of Geoscience, University of Wisconsin-Madison

Vera Kolb, *Coacervates as Prebiotic Reactors*, Professor, Department of Chemistry, University of Wisconsin-Parkside

Rex Hanger, *Freshwater Snails as Indicators of Climate Change and Earth History*, Associate Professor, Department of Geography and Geology, University of Wisconsin-Whitewater

*** Adjourn for Day ***

Friday, August 17, 2013

8:00-8:45 am **Registration** **McCormick Hall**

Buffet Breakfast

8:00-8:45 am **Undergraduate Workshop** **McCormick Hall**

*** Plenary Session ***

9:00-10:00 am **Welcome and Introductions** **Olin Engineering Bldg. 201**
Christopher Stockdale, Associate Professor of Physics, Marquette University

Session 5: Keynote Address

Introduction of Keynote:
Dr. R. Aileen Yingst, Director, Wisconsin Space Grant Consortium and Co-Investigator on the MAHLI Microimaging Camera for Mars Science Laboratory

Prof. Hector Bravo, Chair of Civil Engineering and Mechanics, University of Wisconsin-Milwaukee, *Two Case Studies on Effects of Climate Variability and Climate Change on the Laurentian Great Lakes*

*** Plenary Session***

10:00-10:45 am **Session 6: Team Projects** **Olin Engineering Bldg. 201**

Moderator: Bill Farrow, WSGC Associate Director for Student Satellite Initiatives; Assistant Professor, Milwaukee School of Engineering

Simpson Street Free Press, *Science Learning and Writing Across the Curriculum in Out-of-School Time,* **Deidre Green**, Managing Editor; **Ashley Crawford**, Assistant Editor; **Taylor Kilgore**, Senior Editor

Balloon Payload Team, *The Elijah Project – Exploration with High Altitude Balloons*, **Trent Cybela (**Payload team only), University of Wisconsin-Platteville; **Dan Kass**, Milwaukee School of Engineering; **Amber Koeune**, Milwaukee School of Engineering; **Nathaniel Pedigo**, Milwaukee School of Engineering; **Alana Tirimacco**, Milwaukee School of Engineering; Non-presenting team member: Danielle Weiland (Launch team only), Carthage College

10:55-11:15 am **Morning Break** **Engineering Hall foyer (ground level)**

*** Concurrent Research Sessions***

11:20-12:30 pm **Session 7: Engineering** **Engineering Hall 136**

Moderator: David Bruning, Distinguished Lecturer, Department of Physics, University of Wisconsin-Parkside

Todd Treichel, *Reliability Analysis of Light Emitting Diode Technologies for Cabin Lighting in Manned Space Flight Applications*, Chairman, AIAA – Wisconsin Section and Senior Systems Engineer, Obital Technologies Corp.

Dr. Matthew J. Traum, Assistant Professor, Department of Mechanical Engineering, Milwaukee School of Engineering, *New Capabilities and Discovered Interconnectivities for a Curriculum-Integrated Multicourse Model Rocketry Project*, Non-presenting members: Dr. Vincent C. Prantil, Associate Professor, Dr. William C. Farrow, Associate Professor, Dr. Hope L. Weiss, Assistant Professor, Department of Mechanical Engineering, Milwaukee School of Engineering,

Zhiyuan Yang, Undergraduate Researcher, Department of Mechanical Engineering, Milwaukee School of Engineering, *Dynamic Dynamometry to Characterize Disk Turbines for Space-Based Power*, Non-presenting member: Dr. Matthew J. Traum, Assistant Professor, Department of Mechanical Engineering, Milwaukee School of Engineering,

Roberto J. Fernandez, Undergraduate Researcher, Department of Mechanical Engineering, Milwaukee School of Engineering, *Nitrogen Phase Separation at Terminal Velocity to Inform Design of Future Microgravity Cryogenic Rankine Power Cycles*, Non-presenting member: Dr. Matthew J. Traum, Assistant Professor, Department of Mechanical Engineering, Milwaukee School of Engineering.

11:20-12:30 pm **Session 7R: Planetary Geology and Astronomy** **Engineering Hall 236**

Moderator: Gubbi Sudhakaran, WSGC Associate Director for Research Infrastructure; Chair, Department of Physics, University of Wisconsin-La Crosse

Lindsay McHenry, *Lassen Volcanic Fumaroles and Hot Springs: Analog for Mars*, Associate Professor, Department of Geosciences, University of Wisconsin-Milwaukee

Eric Barnes, *Towards a Better Understanding of Dark Matter*, Associate Professor, Department of Physics, University of Wisconsin-La Crosse

Cheuk Man Lo, *Examining Supernova remnant GSH054-00+003*, Undergraduate Student, Department of Physics, University of Wisconsin-La Crosse

12:45-1:30 pm **Awards Luncheon** **McCormick Hall**

1:30-2:15 pm	**Awards Ceremony**	**McCormick Hall**
	Dr. R. Aileen Yingst, Director, Wisconsin Space Grant Consortium **WSGC Program Associate Directors**	
2:15-2:20 pm	**2014 Conference**	
2:20-2:25 pm	**Christopher Stockdale**	

*** Adjournment ***

WSGC Members and Institutional Representatives

Lead Institution

University of Wisconsin-Green Bay

Scott Ashmann

Affiliates

Aerogel Technologies, LLC
Stephen Steiner

AIAA - Wisconsin Section
Todd Treichel

Alverno College
Paul Smith

Astronautics Corporation of America
Steven Russek

BioPharmaceutical Technology Center Institute
Karin Borgh

Carroll University
Damon Resnick

Carthage College
Kevin Crosby

College of Menominee Nation
Kathy Denor

Concordia University Wisconsin
Matthew Kelley

Crossroads at Big Creek
Coggin Heeringa

Experimental Aircraft Association (EAA)
Bret Steffen

Great Lakes Spaceport Education Fdn.
Carol Lutz

Lawrence University
Megan Pickett

Marquette University
Christopher Stockdale

Medical College of Wisconsin
Danny A. Riley

Milwaukee School of Engineering
William Farrow

Orbital Technologies Corporation
Eric E. Rice

Ripon College
Sarah Desotell

Saint Norbert College
Terry Jo Leiterman

Space Education Initiatives
Jason Marcks

Space Explorers, Inc.
George French

Spaceflight Fundamentals, LLC
Bradley Staats

Spaceport Sheboygan
Daniel Bateman

University of Wisconsin-Fox Valley
Andrew Shears

University of Wisconsin-La Crosse
Eric Barnes

University of Wisconsin-Madison
Gerald Kulcinski

University of Wisconsin-Milwaukee
Ronald Perez

University of Wisconsin-Oshkosh
Nadejda Kaltcheva

University of Wisconsin-Parkside
David Bruning

University of Wisconsin-Platteville
William Hudson

University of Wisconsin-River Falls
Glenn Spiczak

University of Wisconsin-Sheboygan
Harald Schenk

University of Wisconsin-Stevens Point
Sebastian Zamfir

University of Wisconsin-Stout
Todd Zimmerman

University of Wisconsin-Superior
Richard Stewart

University of Wisconsin-Whitewater
Rex Hanger

Western Technical College
Michael LeDocq

Wisconsin Aerospace Authority
Tom Crabb

Wisconsin Department of Public Instruction
Shelley A. Lee

Wisconsin Department of Transportation
Nicole Wiessinger

Wisconsin Lutheran College
Kerry Kuehn

See www.uwgb.edu/wsgc for up-to-date contact information

Wisconsin Space Grant Consortium ■ University of Wisconsin-Green Bay ■ 2420 Nicolet Drive ■ Green Bay, WI 54311-7001
Phone: 920.465.2108 ■ Fax: 920.465.2376 ■ E-mail: wsgc@uwgb.edu ■ Web site: www.uwgb.edu/wsgc